A biomechanical model of foetal head moulding

Rudy Jacques Augusta LAPEER

Queens' College, Cambridge
and
Department of Engineering, University of Cambridge

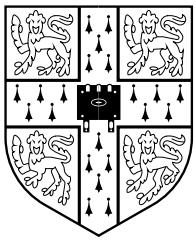

August 1999

A dissertation submitted to the University of Cambridge
for the degree of Doctor of Philosophy

Summary

A biomechanical model of foetal head moulding is presented in this dissertation. The model allows us to evaluate foetal head moulding in a continuous and quantitative fashion rather than the discrete and qualitative assessments which are commonly used in the obstetric and paediatric communities.

Foetal head moulding is a phenomenon which may contribute to satisfactory progress during delivery, as it allows the foetal head to accommodate to the geometry of the passage. In contrast, excessive head moulding may result in cranial birth injuries and thus affect the infant shortly or even long after birth.

Several researchers in the past have designed computer software to simulate human childbirth for diagnostic purposes but did not cover the concept of foetal head moulding in depth. A realistic model of the latter though, would significantly improve the diagnostic value of such a simulation.

Only one group of researchers in the past investigated the biomechanics of foetal head moulding from an engineering point of view, but limited themselves to a static, linear model of the parietal bones.

This research presents a static, non-linear model of the deformation of a complete foetal skull, subjected to pressures exerted by the uterine cervix, during the first stage of labour.

The design of the model involves four major steps: the establishment of the geometry of a foetal skull, the generation of a valid, compatible, finite element mesh, the specification of a physical model and the analysis of the deformation of the foetal skull model. Results of the analysis are validated with clinical experiments on the quantitative assessment of foetal head moulding.

The complex and compound geometry of the foetal skull involves the bones of the cranial vault, which may be considered as thin shells, the membranous fontanelles and sutures, and the relatively solid skull base. The assumption of non-linear, hyperelastic behaviour of the fontanelles and sutures results in realistic overall stiffness of the foetal skull. However, at higher degrees of deformation, convergence problems may occur, mainly because of excessive rotations of the fontanelle and suture elements.

Three models, which differ in terms of speed of processing, stiffness and accuracy, are suggested to solve this problem. The first model assumes linear geometric behaviour of the deforming skull. The analysis for such a model is fast but results in overstiff behaviour when compared to realistic situations. The second model assumes non-linear geometry and utilises polynomial extrapolation of the displacements if convergence halts at a fraction of the applied load. Despite a significant improvement in terms of the degree of deformation, the extrapolated values may prove unreliable. Finally, the third model assumes non-linear geometry and involves removal, stiffening and refinement of the elements which show excessive rotations. Despite the higher demands in terms of processing and user interaction, this model agrees very well with clinical experimental results and displays shapes after moulding which have been reported in previous studies and which are generally known in the obstetric and paediatric communities.

Declaration

This thesis is, unless clear references to other work are cited, my own original work as performed since October, 1995. This work does not include any collaboration with any other group or individual and has not been submitted to any other institution to obtain a degree. The length of the thesis is approximately 54,000 words and contains 89 figures and 32 tables.

Acknowledgements

I wish to thank my supervisor, Dr. Richard Prager for giving me the opportunity to perform this research and providing me with invaluable advice whilst leaving me enough freedom to pursue my own research interests. For proofreading and/or general discussions I am indebted to Drs. Chris Dance, Alonso Peña, Jonathan Carr, Malcolm Sabin and Arul Britto. The latter also for his help and support for the use of the ABAQUS finite element software. Thanks to Patrick Gosling for the support and availability of the computer resources. Thanks to Dr. Robin Richards for the data acquisition of the fetal skull. On the obstetrical front, I have to thank Dr. Kevin Dalton for his general support throughout my stay in Cambridge and the use of many facilities at the Dept. of Obstetrics and Gynaecology and Addenbrooke's Hospital in general, and Prof. Robert Derom for teaching me the basic concepts of obstetrics. Thanks to Prof. Georges De Moor for his constant support and to let me use the facilities at the Dept. of Medical Informatics, during my occasional trips to Ghent. Most importantly, I have to thank my parents, Paul and Erna, for giving me the opportunity to study for as long and in as much depth as I ever desired and especially my mum to be always there whenever I need her. I am most grateful for the financial support as provided by the EPSRC and the Cambridge European Trust. I also wish to thank the members of staff at the Dept. of Ophtalmology at Addenbrooke's Hospital, for their general care and successful treatment to save my eyesight. Finally, thanks to all my friends in the Cambridge Dancers Club, Queens' contemporary dance, the Granta Bar, Queens' College, the SVR-group (past and present) and so many other people, organisations, groups, etc. which I won't mention to avoid that people reading this might wonder how much time I actually spent to do research - don't worry, I never sleep more than seven hours a night! If I forgot anyone, please let me know (pretty soon)!

Contents

List of Figures

List of Tables

Notation

Abbreviations

ad	angular distortion
ar	aspect ratio
bpm	beats per minute
dof	degree of freedom
lhs	left hand side
mqi	mesh quality indicator
rhs	right hand side
AF	advancing front
AP	amniotic pressure
BFD	bifrontal diameter
BFGS	Broyden-Fletcher-Goldfarb-Shanno
BPD	biparietal diameter
BTD	bitemporal diameter
CAD	computer aided design
CCD	charge coupled device
CPU	central processing unit
CSS	constant strain (triangular) shell (element)
CST	constant strain triangle (plate element)
CT	computed tomography
DT	Delaunay triangulation
ESP	Educational + Scientific Products
FD	finite difference
FE	finite element
FEA	finite element analysis
FEM	finite element method
FHCP	foetal head compression pressure
FOV	field of view
HCP	head-to-cervix pressure
HO	homologous object

ICP	intra-cranial pressure
IUP	intra-uterine pressure
LG	linear geometry
LST	linear strain triangle (plate element)
LSTS	linear strain (triangular) thin shell (element)
mNR	modified Newton-Raphson
MaVD	maxillo-vertical diameter
MI	moulding index (Kriewall)
MMI	modified moulding index (Sorbe)
MR	Mooney-Rivlin
MRI	magnetic resonance imaging
MVD	mento-vertical diameter
NLG	non-linear geometry
NI	numerical integration
NN	nearest neighbour
NR	Newton-Raphson
ODE	ordinary differential equation
OFD	occipito-frontal diameter
OOI	object of interest
OrOD	orbito-occipital diameter
OrVD	orbito-vertical diameter
PC	parametric cubic
PDE	partial differential equation
QN	quasi Newton
ROI	region of interest
ROM	rupture of the membranes
SMBD	submento-bregmatic diameter
SOB	suboccipito-bregmatic
SOBD	suboccipito-bregmatic diameter
SOFD	suboccipito-frontal diameter
TPS	thin-plate spline
VDU	visual display unit
VHP	Visible Human Project

Acronyms

conts	contractions
Munits	Montevideo units

Symbol Definitions

Symbols for scalars are lowercase letters, e.g. a.
Symbols for matrices are always boldface capital letters, e.g. $\mathbf{A}$.
Symbols for vectors are usually boldface lowercase letters[1], e.g. $\mathbf{v}$.
Symbols can be any letter of the alphabet except for those listed in the following tables. These symbols are reserved for the definition as specified in the table unless otherwise stated in the text.
Dimensions between parentheses imply that the corresponding variable is only used for theoretical purposes.

Symbols

Symbol	Definition	Dimension
u, v, w	displacement, translational dof	(mm.)
u_x, u_y, u_z	displacement, translational dof	mm.
u_r	rotational deformation	radian
$\mathbf{d}$	nodal displacement vector	mm.
$\mathbf{f}$	external force vector	N
$\mathbf{p}$	internal reaction force vector	N
$\mathbf{r}$	residual force vector	N
C_{ijkl}	the fourth rank elasticity tensor	MPa
C_1, C_2	parameters of *MR* hyperelastic model	MPa (= N/mm^2)
D	dilatation, relative measure as referred to the maximum dilatation of 10 cm.	
E	Young's (elastic) modulus	MPa
$\mathbf{E}$	elasticity matrix	MPa
G	shear modulus	MPa
$\mathbf{K}$	global stiffness matrix	N/mm
P_a	amniotic pressure	mmHg.
Pap	peak-active pressure	mmHg.
Pb	basal pressure	mmHg.
Pp	peak pressure	mmHg.
P_r	radial pressure	mmHg.
$\mathbf{R}$	vector of external forces	N
S_{ijkl}	the fourth rank compliance matrix	(mm^2/N)
Tc	contraction period	(sec.)

[1] Exceptions are *global* vectors in FEA, e.g. $\mathbf{R}$ and $\mathbf{U}$.

Ti	interval period	(sec.)
Tr	rise of pressure period	(sec.)
$\mathbf{U}$	global displacement vector	mm.
V	elastic strain energy	(Nmm.)
W	virtual work	(Nmm.)

Greek symbols

Symbol	Definition	Dimension
α_1, α_2	aspect ratios of a triangle	
β	generalised coordinate	
δ	small increment or variation	
Δ	increment	
γ	ratio of the local and greatest radius of the foetal head	
Γ	boundary, enclosing a ROI for triangulation	
ϵ	one-dimensional strain	
ϵ_{ij}	two-dimensional strain tensor	
$\boldsymbol{\epsilon}$	vector representation of the strain	
κ	parameter used as a control parameter for triangulation	
λ	stretch ratio	
Λ	ROI for triangulation	
μ	parameter used to specify the size of a triangle	
ν	Poisson's ratio	
ξ	barycentric (or area) coordinate	
Π	HCP/IUP pressure ratio	
σ	one-dimensional stress	MPa (= N/mm^2)
σ_{ij}	two-dimensional stress tensor	MPa
$\boldsymbol{\sigma}$	matrix representation of stress	MPa
θ	rotational dof	
υ	diametral strain	

Operators

Operator	Definition
∂	partial differential
$\|.\|$	length of a vector
$\|\|.\|\|$	norm of a vector

$\mathbf{a} \times \mathbf{b}$	vector product
$\mathbf{a}.\mathbf{b}$	dot product
$\det \mathbf{A}$	determinant of matrix $\mathbf{A}$
$\mathbf{A}^T$	transpose of matrix $\mathbf{A}$
$\mathbf{A}^{-1}$	inverse of matrix $\mathbf{A}$

Chapter 1

Introduction

1.1 Engineering and Obstetrics

During the last four decades, major improvements in obstetrical care have led to a significant decrease of foetal and infant mortality and morbidity. The factors which contributed to this improvement originate from multi-disciplinary research and improvements in the fields of pathology, pharmacology, genetics, clinical obstetrics and biomedical engineering. The term 'biomedical engineering' is nowadays accepted for any field of engineering related and applied to biology and medicine. It is especially the field of electrical engineering and in particular, electronics and signal processing, which have made major contributions to obstetrics and medicine in general. Machinery for diagnostic ultrasound, magnetic resonance imaging (MRI) and foetal heart rate monitoring are only a few examples of the wide variety of applications. In contrast with electrical engineering, mechanical engineering has only been popular for a limited range of medical applications, mainly in the field of orthopaedic surgery. It is especially from this field that the term 'biomechanics', used to describe the application of theoretical mechanical engineering to biology and medicine, originates. In obstetrics, mechanical concepts are undeniably of major importance and despite being used for many years, for example the use of mechanical tools such as the forceps and the vacuum extractor for operative delivery, they are usually based on *mechanisms* of labour rather than *mechanics* of labour. Bell [10] considers mechanisms of labour to be primarily concerned with foetal movements of which the majority occurs in the second stage of labour. Knowledge of these mechanisms is important if the clinician is to recognise abnormal foetal positions and therefore needs to extricate the foetus from the birth canal when necessary. The mechanics of labour is however a much wider concept, involving both the first and second stages of labour and focusing on theoretical

mechanical concepts rather than practical issues which are aimed at the delivery of the baby. The following issues are considered to be mechanical concepts of labour:

- Mechanical properties of bony components such as the foetal head and the maternal pelvis.
- Mechanical properties of soft tissue, e.g. the uterus, the cervix, the vagina.
- Interaction of the foetal head with maternal soft tissue and bony pelvis.

Although research involving these concepts has been done for more than a century, very few practical applications have evolved. The ultimate practical application would be to combine all the useful information of past and present research into one single package resulting in some kind of general mechanical model of human parturition. This model could be used to simulate birth, weeks before the actual event. The simulation would be capable of indicating possible complications such as *cephalo-pelvic disproportion* and would thus allow the obstetrician to plan an elective Caesarian section rather than risking an emergency Caesarian section at the time of delivery. Attempts to create such a tool have been made before and are covered in the next section, followed by a discussion on research related to the mechanical concepts of labour. Finally, based on the findings and the assessment of this research, the objective of this work and the strategy to meet it, is described.
Section 1.2 gives an overview of related work done so far and is subdivided into:

- A section on birth simulations: three papers from three different research groups are reviewed and discussed.
- A section describing work on the mechanical concepts of labour. Papers from two distinct researchers are reviewed and their importance to my research is pointed out.
- A section on clinical-obstetrical experiments which describe qualitative assessments of foetal head moulding and its effect on the condition of the newborn.

Readers who are not familiar with the medical/obstetrical terminology may consult the glossary of medical terms in Appendix D.

1.2 Literature review

1.2.1 Research related to childbirth simulation

The combined application of computer science and engineering to simulate the human childbirth process is not a novelty. Since the early 90's several individuals and project teams have been working on this topic. The following sections give a brief overview of their work.

1.2.1.1 Three-dimensional modeling of human organs and its application to diagnosis and surgical planning

In 1993, Bernhard Geiger submitted his Ph.D. thesis [34] on three-dimensional modelling of human organs, based on the concept of the Delaunay triangulation. After outlining the theory in the early chapters, the triangulation model is illustrated in a simulation of a birth process, involving a foetal head sliding through a female pelvis:

- The pelvis is obtained from MRI images of a non-pregnant woman.
- The foetal head is obtained from MRI images of an adult male. It is reshaped and scaled to fit the size and shape of an average foetal head.
- The physical model, i.e. the mechanical model is based on a technique, known in robotics as *compliant motion*.
- During the simulation, the head model is brought into an initial position above the pelvic model. From there it is moved step by step downwards. If at any stage, the head-polyhedron penetrates the pelvic polyhedron, the resulting force[1] and moment about the centre of gravity are calculated. The head is then rotated and translated to minimise this force. If the force cannot be reduced to zero, then the head will not be able to pass without deformation.

Comments on Geiger's work Despite the interesting findings of the movement pattern which the head follows during simulation, there are limitations of this research for clinical applications:

The head is a scaled and reshaped model of an adult head. There is no clear explanation upon which these operations are based. Despite the fact that the shape of the head is of crucial importance in a birth simulation, no

[1] Note that forces are just volumes of interpenetration rather than physical forces.

particular attention has been given to it in Geiger's work.
The foetal head is considered to be an object consisting of a single material of which the material properties have not been taken into consideration. In his simulation, this is not strictly necessary since the physical model is not based on the physical strength of a material. Nonetheless, in reality, the outer part of the foetal head is a composition of several biological materials, i.e. skin, bone and membranous soft tissue.

The physical model involves volumes of interpenetration of the two polyhedrons in contact as *surrogate* contact forces. Moments are considered about the centre of gravity. The interaction between the head and the pelvis during delivery is a quasi-static mechanical contact process. Contact mechanics is an area which has evolved fast during the last decades but is tedious because of the complex mathematical concepts. The model specified by Geiger, though simple, is thus far from realistic. Although it is correct to assume that deeper penetrations will correspond to larger contact pressures, deformation is not considered in the model. It is obvious that the kinematics of the moving object, i.e. the head, will be considerably different when deformation is involved. States, during the sliding contact of the two objects, which are invalid for the simple model, could still be valid for a complex model which includes deformation.
Moments, calculated about the centre of gravity of the head are poor approximations since the centre of gravity is not the centre of rotation. The cervical spine, of which the atlanto-occipital point is the true centre of rotation, should be modelled, irrespective of increasing the complexity.

The trajectory Geiger claims that the trajectory of the foetal head, in his model, corresponds to the trajectory as described in the literature, for all tests. Considering the lack of constraints in his model by neglecting the spine, contact friction and deformation of both the head and pelvis, it seems more likely that many trajectories, of which only a few are realistic, were found.

Conclusion The childbirth simulation of Geiger has interesting concepts despite its simplicity. The idea that the path followed by the head (and basically the entire foetus), for an occiput-anterior vertex presentation, is determined by the minimisation of forces and moments to which the head is subjected is a plausible theory. In Section 1.2.2, more theories based on experiments, some of which were developed as early as the beginning of the century, will be outlined. The poor model of the head and subsequent neglect of its deformation is a

major shortcoming. As a practical application, to be used in a clinical environment, the model is therefore insufficient, not only because of inaccuracies but also because practical issues such as speed of rendering and minimal human intervention have not been considered.
Finally, it is obvious that the simulation was added to the thesis rather to illustrate the utility of the reconstruction model, than to build an accurate, realistic model of human parturition.

1.2.1.2 The prevention of human birth trauma: computer aided simulation of delivery by means of Magnetic Resonance Imaging and Finite Element Analysis

In this paper, Wischnik et al. [107] describe a birth simulation as part of a three-year project in Mannheim-Germany (1992-94).

Overview MR images (T1), of the pelvic area and foetal head of a 29 year old primipara, suspected of cephalo-pelvic disproportion, were taken two weeks before expected delivery. Each pixel of an image consists of 12 bits (4096 grey-levels) which are converted into 256 colours to improve the identification of the geometry. The marching cubes algorithm [64] is used to reconstruct the geometry. The physical model is based on the finite element (FE) method, motivated by the difficulties which could occur when trying to model states of stress and deformation by a non-linear partial differential equation (PDE). Material constants are obtained from [38, 77, 105, 108].
Software:

- custom-built software for MRI processing,
- I-DEAS FE and mesh generation software,
- ABAQUS FE software.

Hardware:
A CRAY-XMP computer (64-bit processor). Calculations were performed in double precision (128 bit or 16 byte floating point arithmetic).

Results Different models were tested, one of which included soft tissue. In this configuration the head was considered to show plastic behaviour. As the elastic moduli of bone and soft tissue are significantly different, major differences in values of stress and deformation were found between representations which did and did not involve soft tissue. Large pressures of up to 710 kPa were found in the area of the hypophysis.

Discussion and comments by Wischnik et al.

- A major improvement towards studies such as those described in [38] and [77] is the involvement of dynamic rather than static evaluations of forces, stresses and deformations.
- To point out the significance of the simulation, Wischnik et al. refer to a study of Ludwig et al. [65] on 150 unselected mature newborns which shows that intracranial haemorrhage occurred in 38% of spontaneously delivered babies, 35% of vaginal-operatively delivered babies and only 18% for babies delivered by Caesarian section.
- Stresses up to 820 kPa were found in the lower areas of the pelvis. This may explain the occurrence of several postnatal maternal complications.

Comments on Wischnik's paper

- In contrast to Geiger's approach, this project team has not spent a lot of time to accurately model the geometry of the different body parts involved in the process. The first step, the segmentation of the MRI data, involves conversion of 4096 grey levels to 256 colours to ease the process of manual segmentation. It is unclear how this crucial step is performed, which is important since the factor of information reduction is 16, which could be too high for reliable discrimination of different tissues in the model.
- The consideration of soft tissue is not clearly explained in the paper. As we will show later, the influence of soft tissue is crucial to realistic models of the head (and birth canal) and should therefore be evaluated carefully.
- Values of pressures are sporadically mentioned throughout the paper and seem to be reasonably high compared with, for instance, values found in crash-test simulations [78].

Despite the consideration of soft tissue, the involvement of virtually all the biological components of human childbirth and a physical model based on real material properties, the detail of the paper lacks an accurate description of the methodology, necessary to solve a range of complicated issues related to the simulation.

1.2.1.3 CAD modeling of the birth process

This work is based on a research project at the University of Massachusetts. Liu et al. [61] talk about the critical factors of successful labour or the three P's:

1. Passage: size and shape of the pelvis.
2. Passenger: size and shape of the foetal head, presentation and position of the foetus and moldability of the head.
3. Power: the force of uterine contractions and possible external help.

The main criticism of Liu et al. towards Geiger's work [34]:

- Only one pelvis-head pair was tested (even though the head was scaled to different sizes).
- No consideration was given to the inner structure of the head, nor the effects of soft tissue in the birth canal.
- In the simulation, the foetal head will always pass through the pelvis even when a severe disproportion occurs.

Liu's objectives

1. To treat the foetus as a kinematic chain instead of an isolated head.
2. To minimise possible birth injuries by all means and not just simply predict Caesarian sections but also selectively assisted vaginal delivery.
3. To use atlases, partial scans and a plastic model to reconstruct the head whilst waiting on a data set to become available.
4. To model the neck joint by a spherical joint with limited range of motion.
5. The kinematic model should involve:
    - a geometric phase determining optimal paths and positions of the foetal head sliding through the birth canal, whilst estimating forces using an approximate function based on volume intersection with the depth of interpenetration as an important indicator,
    - a physical phase determining the precise forces on the foetus, using FE analysis, at those positions where high pressures are expected, and based on the approximate calculations in the geometric phase.
6. The method of evaluation should be based on:
    (a) Comparison of scanned objects with models created from the scans: the Visible Human Project (See Section 2.4.4) will allow the authors to comprehensively check the accuracy of the birth canal model. In general, the anatomical CAD models and the simulation process should be validated using existing data.

(b) Comparison with results in the literature, e.g. measurements of forces applied to the foetal head.

Comments on the work of Liu et al. Many interesting concepts are mentioned here:

- The consideration of the foetus as a whole rather than the head/skull only.
- The use of Geiger's model as a first approximation which is then refined using a realistic physical model based on FE analysis.
- The validation of the geometry and stress/deformation calculations based on the literature.

The main concern about this work is again the 'ease' by which difficult problems and their solutions are brought forward. An accurate model of the head only is already a complicated problem, as will be shown during the course of my work. Thus, needless to say that the consideration of an entire foetus with accurate models of the spine, joints and limbs is far from trivial.
To summarise, good ideas and concepts are mentioned in this paper but many of them are too ambitious when considering the complexity of problematic issues such as soft tissue modelling, foetal head moulding and contact mechanics. Furthermore, it is unclear from the paper what the authors actually did achieve.

1.2.2 Research related to mechanical concepts of labour

1.2.2.1 Biomechanics of human parturition: A fundamental approach to the mechanics of the first stage of labour

This work was submitted by Frank Bell to obtain the degree of Doctor in Philosophy at the University of Strathclyde - Glasgow [10]. The thesis of Bell is vast and is mostly a literature review of research related to the mechanics of labour before 1972 and based on this research, a further development of mechanical concepts by the author. Bell's work is focussed on the first stage of labour, i.e. the stage until full dilatation of the cervix is achieved. In this section, an overview of important general concepts as covered in Bell's work, which are relevant to my research, is presented[2].

[2]Some of the literature which Bell refers to has not been consulted. It is referred to in this section by citing the author followed by the year of the reference, between parentheses.

Mechanisms and mechanics of labour In the introductory section, Bell gives a brief overview of previous research and criticises the bias of clinical researchers towards the *mechanisms* rather than the *mechanics* of labour:

- Mechanisms of labour are primarily concerned with foetal movements of which the majority occurs in the second stage of labour, after full dilatation of the cervix. The mechanisms during this stage are important to the obstetrician to recognise abnormal foetal positions upon which he/she can act by operatively removing the foetus when necessary.
- Since the first stage of labour involves about 90% of the entire duration of labour, the foetal movements during this stage, though small, are nonetheless important in relation to the mechanics of the uterus and the kinematics of cervical dilatation. It is this part which has been neglected in most of the earlier clinical research, despite the fact that the first stage of labour is important to the understanding of clinical concepts such as prolonged labour.

Qualitative concepts of the mechanisms of labour Theories about the mode of transmission of the uterine activity to the foetus and the cause of the flexion of the head:

1. Some physicians believed that the uterine activity was transmitted from the uterus to the birth canal by direct contact between the uterine wall and the foetal body. The force was thus transmitted along the foetal spine. The region where the foetal head is connected to the spine acted as a fulcrum. As the back of the foetal head (i.e. the occipital protuberance) is closer to this fulcrum than the forehead, the reactive forces of the birth canal act effectively on this *lever with unequal arms*, resulting in flexion of the head.
2. Other physicians believed that the uterine activity was transmitted evenly over the foetal body by the hydrostatic pressure created in the intrauterine amniotic fluid during contraction. If this was the case then the atlanto-occipital joint would no longer act as a fulcrum. They proposed that the point of application of the reactive force on the back of the head was lower than the point of the reactive force on the forehead, thus creating a flexing torque.

It should be noted that these theories are equally important as an explanation of how the expulsion force is transmitted, irrespective of explaining the flexion

of the head.
Another important concept, involving the kinematics of the second stage, is the pattern of the trajectory which the foetus follows, starting from cephalic presentation at the beginning of the first stage. We discussed already one possible explanation by Geiger [34], based on the minimisation of the contact pressure (or a simplified measure based on interpenetration) between the foetal head and the maternal pelvis.
Experiments as early as 1893 provide alternative explanations:

1. One of the first theories was that the shape of the bony pelvis influences rotations of the foetal head. This was extended with the suggestion that the muscular lining of the pelvis (and specifically, the upper edge of the obturator internus) forms oblique planes which guides the head in a rotational manner. These concepts were abandoned since they did not explain for instance why a small head rotates in a large pelvis.

2. Experiments by Dubois (1900) and Edgar (1893) showed the importance of the soft tissues of the pelvis. Dubois propelled a dead foetus through the birth canal of a woman, who died immediately after labour, and observed rotation of the foetal head. The experiment was repeated three times and each time the head rotated. The fourth time, the head failed to rotate! The experiment was repeated with a larger foetus for which the head rotated in the first two attempts but it didn't in subsequent attempts. Edgar carried out similar experiments but instead of pushing the foetus through the birth canal from above, he pulled it by means of a string attached to the head. His results confirmed Dubois's: initially, the head rotated but after a few complete passages, the rotation ceased. These experiments showed the importance of the passive *elastic* properties of the pelvic floor.

3. Ostermann (1894) assumed that the flexibility of the foetus varies in different directions. This theory was confirmed in the early 1930's, at least with regard to the flexibility between the foetal head and trunk.
   Sellheim's description (1913) of this concept has attracted most attention: he describes the whole concept of labour as being in principle strain and accommodation whereby the foetus is flexed, twisted and deformed in an intimate mechanical interplay with the birth canal. His arguments on the varying flexibility of the foetus involved the effects of the tonus in the musculature of the back and the tension in the ligaments of the neck.

4. Rydberg (1935) claimed that the rotation of the foetal head was also

influenced by the asymmetrical shape of the head. His argument was that since the head is kidney or bean shaped and the birth canal is a bent tube, this would result in minimum distension (stretching) when the curvatures of the head accommodate the curvatures of the birth canal whilst other positions would be relatively unstable.

Bell's comments on these theories:

- Very little has been added to these theories since the 1930's.
- The importance of the asymmetric shape of the skull (Rydberg) is true but so general as to be almost meaningless.
- Bell claims that simulations using models may not always be representative to the in-vivo process since the flexibility of the newborn changes with time after birth and may be different in the uterus and during labour. The experiments by Dubois and Edgar demonstrated that the rotational movement is not solely dependent on a an in-vivo process but they did not explain the causes of the movement in a quantitative fashion.
- In todays obstetrics, obstetricians might not be too concerned with the causes of foetal movements because forceps delivery has been skillfully developed, radiology allows confirmation of suspected abnormal presentation and Caesarian section is an alternative to difficult vaginal birth and carries less risk than it did in the past. The causes of foetal movements thus seem to be more of academic interest than of practical concern.

Comments

- The experiments as performed by Dubois and Edgar are interesting but unfortunately vague in terms of conclusions because of their qualitative nature. The fact that both researchers, independently, found similar results adds to the credibility of their theory.
- The theory based on varying flexibility of the foetus is a possible explanation but hard to prove.
- Bell's comment on the danger of using models to derive conclusions of an in-vivo process such as labour is something to take into account. For instance, consider the properties of the foetal head which change very shortly after birth. If it would be ethically justified to assess these properties from a stillborn baby just after delivery, limited time would be available to derive relevant results.

- The comment by Bell on the lack of interest from obstetricians in the causes of foetal movement is based on ill-informed arguments. It is true that the cause of the kinematics of the foetus is not of practical concern because of possible operative alternatives but in no way is this a valid reason not to try to find a realistic explanation. At the end, such an explanation could contribute significantly to the process of decision making a long time before delivery, which would lower the risk of critical decisions such as emergency Caesarian section.

Uterine activity - labour forces - amniotic pressure A significant portion of Bell's literature review and further developments are about histological studies which investigate the structure of the uterus and the physiological causes of uterine contractions. Since the effect of the contractions rather than their origin is important in my work, I will not elaborate on this topic.
A first attempt to assess forces in labour by Kristeller (1861), involved the insertion of a spring measuring device in a pair of forceps. Subsequent investigations involved the insertion of balloons into the uterus via the vagina. Initially these were quite large (80 cc.) but it was very soon realised that the presence of these large balloons influenced uterine behaviour and smaller balloons (2 cc.) were used at the end of the century (1893). Some important considerations were:

- The need to simultaneously record intra-abdominal pressure and intra-uterine pressure.
- The disturbing influence of the device.
- The relevance of the foetal membranes in estimating the forces of labour.

Uterine activity and coordination Alvarez and Caldeyro-Barcia (1948) used a transabdominal technique whereby a cannula, connected to a pressure recording device, was introduced into the amniotic fluid through the abdominal wall. Small pressure transducers were introduced into the mass of uterine muscle at various sites via the abdominal wall. The recorded data presented evidence to support the concept of *fundal dominance*, earlier found by Reynolds (1948): contractions of the uterine fundus are stronger and last longer than those of the mid-section and no contractions occur at the lower uterine segment. The term 'pacemaker' (McIntyre (1939)) was used to define a region of the uterus from which excitation or contractile waves originate and spread over the uterus. According to Caldeyro-Barcia and Poseiro (1966) there are two common sites at which the pacemaker may exist adjacent to the uterine ends

of the uterine tubes. Usually only one of the pacemakers predominates and originates nearly all of the waves. If not, interference would result which would lead to abnormal uterine coordination. From the pacemaker area, the normal contraction spreads throughout the uterus at a speed of 2 cm/sec, invading the whole organ within 15 sec. Once a given area of the uterus has been reached by the contractile wave, the *systolic* phase of the contraction takes 30 to 60 sec. to reach its maximum. In normal contractile waves, the activity of different parts of the uterus is so well-coordinated that the peak of the contraction is attained almost simultaneously in all parts, despite the fact that the wave has reached them at different times. Consequently, the further the site from the pacemaker, the shorter the duration of the systolic phase of the contraction. The synchronous relaxation of all parts of the uterus allows the amniotic pressure to fall to a minimum in between contractions, i.e. to the level of the normal *tonus*.

Intra-uterine pressure (IUP) cycle Figure 1.1 shows an idealised intra-uterine pressure cycle. To obtain the component of IUP due to uterine activity solely, the intra-abdominal pressure must be simultaneously measured and subtracted from the total IUP. The latter can be approximately derived if the position of the pressure transducer is known.
The IUP curve shows the following characteristic parameters:

- The minimum pressure in the IUP cycle is called the tonus, resting pressure or basal pressure, Pb.
- The maximum pressure or peak pressure, Pp.
- The difference between maximum and minimum pressure is called the intensity, amplitude or peak-active pressure, Pap.
- The frequency of the cycle is usually quoted in contractions per hour or contraction per ten minutes. The inverse of the frequency is called the period or the interval.
- The duration of the contraction is called the contraction period, Tc.
- The duration of the interval in between contractions is called the interval period, Ti.
- The duration of the interval in which the pressure is increasing is referred to as the period of rise of pressure, Tr.

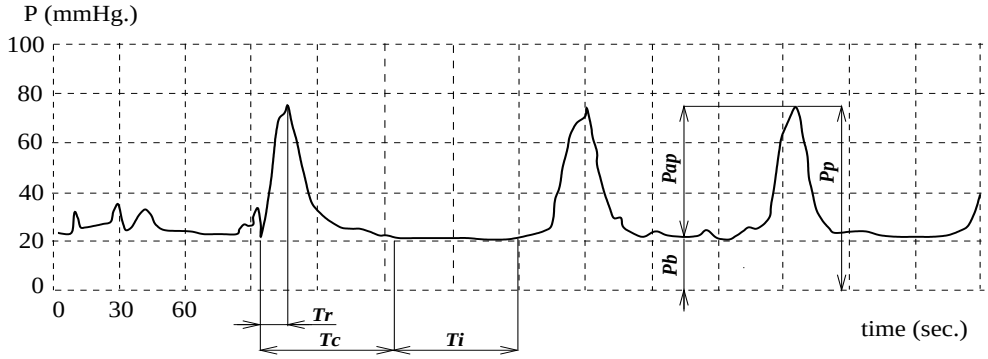

Figure 1.1: An intra-uterine pressure (IUP) pattern.
Pp = peak pressure, Pap = active peak pressure or intensity, Pb = basal pressure or tonus, Tc = contraction period, Ti = interval period, Tr = rise of pressure period. Source: Lindgren 1966 [58].

Caldeyro-Barcia and Alvarez (1952) did not find the horizontal line in between contractions in their measurements, hence the interval period was zero and contractions immediately followed one another. Note that the upstroke of the pressure wave is often close to a vertical line whilst the downstroke is rather of a hyperbolic shape. Turnbull (1957) [101] found three types of intra-uterine pressure patterns (See Figure 1.2):

Type I: Contractions are regular in intensity, frequency and form.

Type II: Contraction pattern shows some irregularity in strength and frequency or abnormal forms re-occur at intervals.

Type III: The pattern is completely irregular and most of the contractions are of an abnormal type.

Turnbull found all three types to occur in normal labour: 60% of 'normal' cases studied, showed contractions of Type II, 30% showed contractions of Type I and 10% showed contractions of Type III. Shulman and Romney (1970) [91] confirmed these results by finding irregular rhythmicity of amniotic pressure waves from 20 'normal' labours. They expressed surprise at the variations which exist in intensity, frequency and duration of the uterine contractions during apparently normal labours. Also, Caldeyro-Barcia (1959) reported wide variations of uterine activity, expressed in Montevideo[3] units, during normal labours.

[3] 1 Montevideo unit or Munit is the product of 1 mmHg. of Pap and 1 conts/10 mins of contraction frequency. For example a Pap of 60 mmHg. and a contraction frequency of 3 conts/10 mins yields a uterine activity level of 180 Munits.

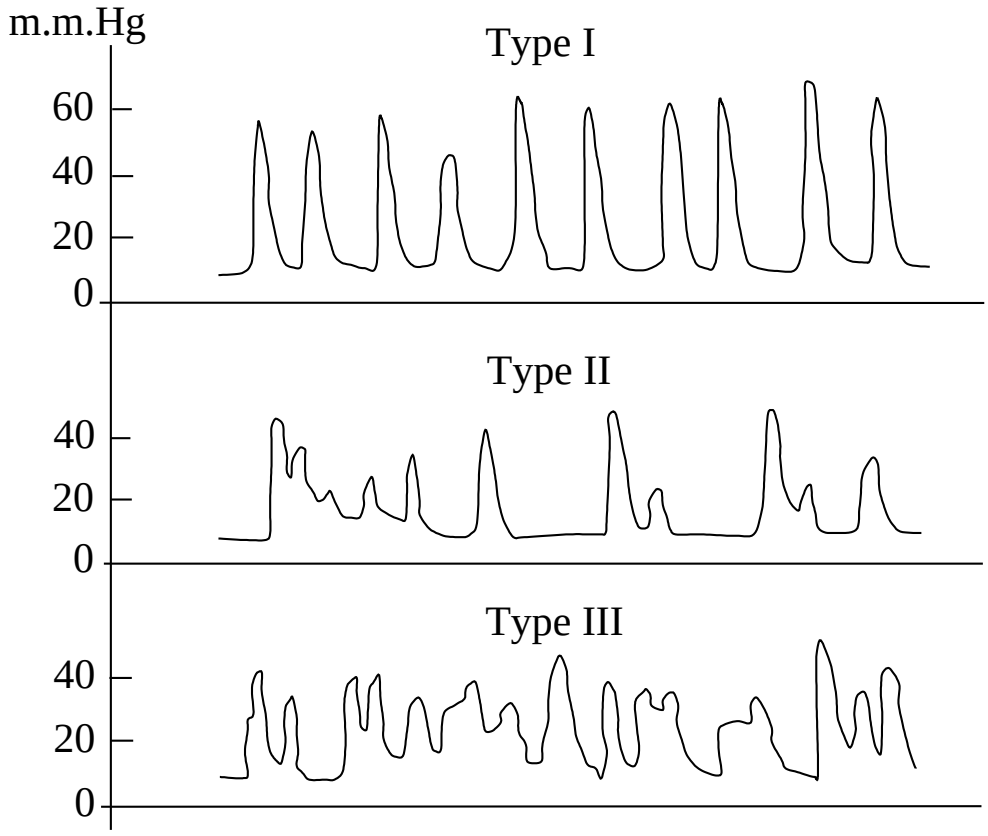

Figure 1.2: Three types of intra-uterine pressure (IUP) patterns according to Turnbull [101].

Intra-uterine pressure variations in labour The *IUP* pattern varies with:

- The parity of the patient: Turnbull (1957) [101] found that the intensity of *IUP* was about 40% higher for primiparas than for multiparas:
  primiparas: range 20-80 mmHg., mode 40-60 mmHg.
  multiparas: range 15-60 mmHg., mode 20-40 mmHg.

- The position of the patient: according to Caldeyro-Barcia and Poseiro (1966), the average frequency of contractions is higher when the mother is lying on the back as opposed to upright position (0.7 conts/10 mins on the average). The average intensity is then lower (7.6 mmHg. on the average) which can be explained by the effect of the uterine weight and the abdominal cavity constraints on the shape of the uterus.

- The state of the foetal membranes. Contradictory findings on the effect of rupture of the membranes (ROM) on the *IUP* pattern: Lindgren (1959) [53] found an increase of frequency of contractions, an increase of intensity of the *IUP* and no change of the tonus. Krapohl et al. (1970) [44] only found a significant decrease of the tonus.

- The degree of cervical dilatation (ranging from 0-10 cm.): findings by Zambrana (1960) showed slight increase of the tonus (starting from 7 mmHg. at dilation 0 up to 12 mmHg. at dilatation 10), higher increase of the intensity (26 mmHg. up to 46 mmHg.), increase of the frequency of contractions (2 conts/10 mins up to 5 conts/10 mins) and an increase of the uterine activity (50 Munits at dilation 0 up to 230 Munits at dilatation 10).

- The influence of the foetus: the size and position of the foetal head and the compressibility of the foetal body.

- The size and shape of the uterus.

Lightening and engagement During *lightening*, the level of the fundus in the abdomen drops and during *engagement*, the foetal presenting part, which is contained within the uterus, enters the pelvic inlet. Both lightening and engagement are probably due in part to the increase in uterine weight and the concomitant increase in the forces on the uterine supports and in part to the changes in the connective tissue in the body. Whilst engagement of the head is almost always described with reference to the pelvis, engagement into the lower uterine pole is, mechanically, of much more interest in understanding the process of labour.

Cervical dilatation In labour, contractions of the uterine tissue act upon the cervical tissue by direct traction along the uterine wall and by creation of the radial pressure via the amniotic fluid, foetus and foetal membranes. During labour, the foetal head is in direct contact with the lower uterine pole and the tissue is distended around the foetal presenting part with a subsequent increase in the diameter of the cervix. Pressures can be greater than the *IUP* and the largest pressure occurs at the largest diameter of the foetal head and decreases at lower levels below this diameter up to the external *ostium*. The assumption that the cervix is elastic would mean that it would return to its original diameter in between contractions which is not the case. If one assumes purely plastic behaviour then there would be no transient recovery of the diameter in between contractions. Therefore the assumption of visco-elastic behaviour of the cervix during dilatation seems to be the most reasonable explanation.
Contradictory findings concerning the shape of the dilatation-time curve were found. Friedman (1954) [30], found a sigmoid-shaped curve with a deceleration phase near the end of the first stage whilst Hendricks et al. (1970) [39] found an exponential-shaped curve with no deceleration phase at the end. In both cases a final cervical dilatation of 10 cm. was found and was not stated as a mean derivation. The caliper device used by Friedman to measure the dilatation was attached across the cervix. The fact that this would interfere with normal dilatation, might explain a possibly incorrect deceleration phase at the final stage.

Rupture of the membranes The rupture of the foetal membranes (ROM) may influence the mechanics of labour according to two apparent mechanisms:

1. Reduction of the intra-uterine volume by the loss of amniotic fluid will tend to reduce the tensile forces in the uterine wall. As the radii of the uterus tend to decrease, the resulting pressure may decrease or increase depending on the uterine wall properties and the uterine radii.

2. The average contact pressure between the foetal head and the lower uterine pole will increase. The subsequent redistribution of force on the foetal head would tend to increase the moulding of the head and consequently reduce the largest diameter.

1.2.2.2 The structure and bending properties of foetal cranial bone

In the early 80's, Gregg McPherson and Timothy Kriewall investigated the bending properties of foetal cranial bone [46, 70, 71] and used a finite element

(FE) model of the parietal bone to investigate foetal head moulding [70, 72] (we discuss this in the next section). It will become clear in the further course of this work that their research is an important basis for the investigation of foetal skull moulding. In this section we summarise the important concepts of their work. Actual results are found in Chapters 5 and 6.

The structure of foetal cranial bone At birth, the skull of the infant is not rigid but consists of separate, relatively rigid bones connected by flexible membranes known as sutures. The cranial bone is relatively homogeneous through its thickness and varies from roughly 0.5-1.5 mm. [70]. This homogeneity across the thickness differs from adult cranial bone which consists of three distinct layers, i.e. the inner and outer layer and the diploë (middle layer) which consists of cancellous bone. A second difference between the structure of the foetal/newborn and adult skull is the orientation of the grain structure which has a definite orientation for the former [70].

The elastic modulus of foetal cranial bone [71] To experimentally derive the elastic modulus, 86 specimens of foetal cranial bone obtained from 6 newborns, with an estimated gestational age ranging from 25 to 40 weeks were tested in three-point bending. The possible influences of gestational age, specimen location and bone fibre orientation on the elastic modulus were investigated too. In addition, 12 specimens from a 6 year-old calvarium were tested for comparative purposes. The average thickness of the bones of the cranial vault varied between 0.71 and 0.86 mm., with a standard deviation of 0.15 mm., for term foetuses. For the preparation of the specimens, the following procedures were followed:

- After post-mortem examination, performed within 12-24 hours after death, the cranial bones of the vault with attached septa and dura mater were removed in one piece and placed in a container of cold buffered saline. The material was preserved under refrigeration (temperature between -10°C and -20°C) until the time of specimen preparation. The membranous sutures holding the bones of the vault together were excised whilst the inner and outer membranes covering the bone were carefully removed. The bones were kept wet by periodic bathing in a separate saline-filled container.

- The size of the specimens was based on the fact that the theory of flexure is most accurate for long thin beams and therefore a length-thickness ratio of 20 was suggested. Assuming a bone thickness of 1 mm. and

the necessity of excess length to ensure easy support of the specimen, an overall length of 25 mm. was chosen. The width of the specimens was 2 mm.

- The excised specimens of 2×25 mm. were cut in a manner to obtain preferred fibre orientations, either parallel or perpendicular to the long axis of the bending specimen because of the orthotropic nature of foetal cranial bone.

- The effects of varying thickness and the curvature of the bone were assessed. The effect of the initial curvature, assessed by the comparison of bending responses of a straight beam using Euler-Bernouilli beam theory and an initially curved beam using FE analysis, was proven to be small enough to be ignored.
  FE analysis was performed to evaluate the effects of varying thickness across the length of the specimen (beam). The error between a model of varying thickness and a model with (averaged) constant thickness in the calculated deflection was 18%. This result indicated that it would not be appropriate to ignore the variation in the thickness of the bone. Therefore, the thickness for each specimen was measured at five equally-spaced locations to the nearest 0.01 mm.

Preliminary investigations were performed:

- To evaluate the effect of multiple load-unload cycles on specimen response. Fung [31] found differential response of biological tissue with multiple-cycle loading. This implies that biological tissue needs to be exercised or preconditioned through several loading cycles before repeatable material response is obtained. McPherson and Kriewall found that after three loading cycles, repeatability was established.

- To evaluate the effect of testing with the specimen immersed in warm saline as opposed to testing in room air. After preconditioning the specimens, McPherson and Kriewall found that the specimen's stiffness for tests in normal saline was slightly less than for tests in room air (4.4%), but not statistically significant. Since testing in a warm saline bath poses difficulties, all specimens were tested at ambient room conditions.

The bending test experiment involved:

1. centering the specimen on the bending supports with the convex surface upwards,

Table 1.1: Values of the elastic modulus in bending, E_b (MPa), of foetal cranial bone as reported in [71]. The values in parentheses are standard deviations. n = the number of specimens.

Gestational age group	Elastic modulus in bending, E_b (MPa)		Statistical Significance
	Parallel fibres	Perpendicular fibres	
Preterm	1650 (1170) $n = 23$	145 (62) $n = 11$	$p < 0.001$
Term	3880 (780) $n = 22$	951 (572) $n = 16$	$p < 0.001$
Statistical Significance	$p < 0.001$	$p < 0.001$	

2. cycling the specimen three times to a midspan deflection of 0.25 mm. at a crosshead speed, for both loading and unloading, of 0.5 mm/min.,

3. loading the specimen to a midspan deflection of 1.5 mm. at a crosshead speed of 0.5 mm/min. followed by unloading at the same speed,

4. removal of the specimen from the fixture and returning it to its storage container.

The resulting calculations of the elastic modulus are based on a model divided into four sections yielding the formula of deflection:

$$\delta = \frac{Pl^3}{768E}[\frac{1}{I_1} + \frac{1}{I_2} + \frac{1}{I_3} + \frac{1}{I_4}] \tag{1.1}$$

where P is the midspan load, l is the span length, E is the elastic (Young's) modulus and I_i is the area moment of inertia for a section i.
Table 1.1 shows the mean values of the elastic modulus in bending, E_b, for preterm foetuses (specimens of gestational age between 24 and 30 weeks) and term foetuses (specimens of gestational age between 36 and 40 weeks) as reported in [71]. All results are significantly different following a paired Student t-test ($p < 0.001$).

Discussion by McPherson and Kriewall

- Because of the discretisation of the continuous variation in thickness of the specimens by a beam model, consisting of four elements, some error in the final result must exist.

- The fibre pattern of foetal cranial bone is radially oriented within each bone and the focus of the pattern lies at the centre of ossification. This means that the fabrication of a specimen with finite width will never have all fibres running either parallel or perpendicular to the long axis of the specimen. Whilst every effort to minimise this variation was taken, the variation does exist and has been ignored throughout the analysis.

Conclusions

1. The mean value of the elastic modulus is significantly different for preterm bone as compared to term bone.
2. The mean value of elastic moduli for each of the previously mentioned classes are significantly different for parallel and perpendicular fibre oriented specimens.
3. The difference with fibre orientation was still significant for the 6 year-old cranium but is not evident with adulthood. Wood [109] was able to show no such difference existed for the adult skull, a finding which is supported by the homogeneous grain structure of adult cranial bone as opposed to the orthotropic structure of foetal cranial bone.
4. The significant differences in properties which exist between the preterm and term bones could be one factor in the explanation as to why preterm infants are more at risk for cerebral trauma than term infants.

1.2.2.3 The biomechanics of foetal head moulding

This work by McPherson and Kriewall [72], published in 1980 in the Journal of Biomechanics, is possibly the only work which involves a quantitative analysis of mechanical behaviour of the foetal skull.
McPherson and Kriewall created an idealised model of a foetal skull using orthogonal radiographs. Their study was focussed on the behaviour of the parietal bones when subjected to the contact pressure of the cervix. The bone dimensions and material properties were derived from previous research [71]. The pressure distribution between head and cervix was based on the findings of Lindgren [54] and improvements of this work by Bell [10].
The diametral strains for both term and preterm parietal bone were evaluated using linear FE analysis, a justified approach according to the authors, because of the small strains and stresses which their model predicted.
The resulting deformations were qualitatively similar to those seen in radiographs of the foetal head, taken during labour.

Preterm cranial bone showed deformations, 2-4 times larger than deformations of term parietal bone for the same load distribution.
Numerical results of their work are given in Chapter 6.

1.2.3 Clinical research related to the physiological consequences and the qualitative assessment of foetal head moulding

1.2.3.1 The physiological consequences of foetal head moulding

Foetal head moulding is an important phenomenon of human parturition, not just from a purely mechanical point of view but also as a possible indicator of obstructed labour, the latter which can influence the general condition of the foetus during delivery and possibly even for the rest of its life.
The pre-occupation with the problem of obstructed, non-progressive or prolonged labour has haunted mankind throughout history. In Europe, from the time of the renaissance onwards, obstetricians and midwives had nothing more to offer than feto-destructive procedures [24]! The chance of survival of the foetus increased significantly during the 18th. century when the forceps became available. It soon became apparent that not just survival but also the quality of life could be affected by the obstetrician's acts. Today, the obstetrician is well aware of the dangers of birth and its possible neurological consequences.
The harmful effects of prolonged labour during the second stage can be due to:

1. the interference with the foetal oxygenation (acidosis),

2. the mechanical effects on the foetal head (moulding, pathological moulding).

The degree of acidosis results from bearing down by the mother during contractions, which possibly diminishes the placental blood flow, whilst the umbilical cord may be locally compressed between foetal parts and soft tissue of the birth canal. Also, the increase of mechanical pressure on the brain and its blood vessels can cause acidosis. A prolonged expulsion can turn the moderate respiratory acidosis in the foetus, that normally resolves rapidly after birth, into a potentially dangerous metabolic acidosis [24].
Amiel-Tison et al. [4] point out that the pressure on the skull may affect the cerebro-vascular circulation, hence causing hypoxaemia. The unequal resistance of the bony skull towards contact pressures, as a result from expulsion and abdominal forces, results in moulding of the head which calls for adaptation of the internal structures such as the blood vessels. From a severe increase of head compression and decrease of cerebral perfusion, brain edema may result, which

subsequently yields a significant increase of the intra-cranial pressure (ICP). Due to the combination of increased ICP and foetal hypoxia, bradycardia may result.
In most of the literature, describing foetal head moulding and/or the measurements of pressures between the head and maternal tissue, it is commonly agreed that severe moulding of the foetal head can cause serious brain damage. Lindgren [53] reports from a study on 23,836 children at the Sabbatsbergs Hospital in the period 1949-1959, that 647 children died perinatally of which 112 (17.3%) showed rupture of the tentorium cerebri which might have been caused by moulding of the foetal skull. The latter being a plausible cause of cerebral haemorrhage as well. Rempen and Kraus [85] point out that strong head compression is assumed to cause serious brain damage of the child mainly because of two pathogenetic mechanisms:

1. the possible elevation of ICP which reduces the cerebral perfusion, leading to ischemia, edema and haemorrhage,

2. moulding of the foetal skull resulting in cerebral trauma with rupture of the blood vessels.

On the contrary, Svenningsen et al. [97] did not find any correlation between foetal head compression pressure, $FHCP$, and the following measurements/tests to assess the condition of the neonate:

- the umbilical cord pH, two minutes after birth,
- Apgar score at 1 and 5 minutes,
- neuro-behavioural testing within 24 hours and classified in four groups ranging from normal neuro-behaviour to serious conditions such as abnormal reflexes, poor visual/auditory habituation and hyper-alertness,
- assessment of retinal haemorrhage within 24 hours and subdivided in four classes of increasing degree of severity.

Svenningsen et al. found a significant correlation between the arterial pH and the duration of expulsive contractions, a phenomenon to which acidosis is commonly associated. He therefore concluded that this condition may have to be considered potentially more dangerous than the effects of relatively short periods of very high degrees of head compression. Also, the 'objective' measurements carried out in his study failed to support the common theory that retinal haemorrhage in the newborn may be used as a subtle indicator of the degree of

cerebral compression during birth. Furthermore, no significant correlation between Apgar scores and *FHCP* was found, a finding supported by Moolgaoker [74]. However, care has to be taken with the findings by Svenningsen et al. [97]. The assessment based on Apgar score is known to be relatively unreliable in statistical terms, as it is the result of five independent observations. Svenningsen did not investigate severe cases of foetal head moulding: it is probably true that cases of *normal* head moulding will not result in adverse effects but this is not so for cases of *pathological* head moulding as a possible consequence of cephalo-pelvic disproportion and/or vacuum extraction and forceps delivery.

1.2.3.2 Qualitative assessment of foetal head compression pressure (*FHCP*)

Several researchers in the past have measured the pressures on the foetal head [3, 5, 9, 33, 35, 52–54, 74, 85, 86, 97]. A significant variance amongst their findings exists, of which a portion can be accredited to different samples of different populations being examined. Also the location where the pressure is measured differs amongst different researchers, e.g. the measurements of Rempen and Kraus [86] are only taken during the second stage, whilst Lindgren's measurements are taken during the first stage before full dilatation. More attention to this material will be given in Chapter 5.

1.2.3.3 An index for foetal head moulding

Kriewall et al. [47] and Sorbe and Dahlgren [94] studied the moulding of the foetal head by measuring principal diameters shortly after birth and three days later to allow for restitution. Their results, which are covered in depth in Chapter 5, will prove to be of crucial importance to the validation of a FE model of foetal head moulding.

1.3 Summary and Objective

Section 1.2.1 gave an overview of projects involved in the simulation of the birth process from the onset of labour until the delivery of the foetus/newborn. Such a simulation, when modelled accurately, could allow the obstetrician to assess possible problems or risks and thus plan interventions to avoid last-minute decisions. For instance, if the simulation could show that vaginal delivery is virtually impossible because of geometrical incompatibility of the maternal birth canal and the foetus, an elective Caesarian section could be planned, thus avoiding

the risk of emergency Caesarian section. Although these projects have outlined important concepts, none of them have covered the phenomenon known as foetal head moulding, a concept necessary to make the simulation realistic. McPherson and Kriewall [46, 71, 72] did work on the assessment of the moulding of the foetal skull but this has been limited to a linear analysis of the parietal bones. Mechanical concepts they used were based on the work of Lindgren [53] and Bell [10] which was discussed in Section 1.2.2.
The importance of foetal head moulding as an important risk factor to the general well-being of the foetus or newborn was outlined in Section 1.2.3.
Based on the knowledge, gathered in the research as discussed in the previous sections, my research will focus on the development of a valid model of the biomechanical behaviour of the foetal skull when it is subjected to labour forces because:

1. It is an important concept for a successful and complete simulation of human parturition.

2. It extends the linear model of the biomechanical behaviour of the parietal bones, as suggested by Kriewall and McPherson, to a non-linear model of the entire skull.

3. It provides a basic model to investigate post-natal pathological conditions caused by excessive head moulding.

The first point illustrates the shortcoming in previous birth-simulation models by overlooking the head moulding phenomenon. Without considering it, a mechanical model of the birth process cannot be realistic.
The second point illustrates the necessity of modelling the behaviour of the entire skull, rather than individual bones. The anatomy of a foetal skull is complex, thus non-linear analysis of the complete geometry is necessary.
Finally, a realistic model of a foetal skull is not only useful in terms of a mechanical childbirth simulation but can also be used for the research on trauma and pathological conditions caused by excessive head moulding during delivery, a problem especially of interest to the paediatric community.

1.4 Plan

To arrive at a realistic model of the deformation of a foetal skull when it is subjected to labour forces, the following tasks need to be accomplished:

1. Accurate recovery of the shape of a foetal or newborn skull.

2. The creation of an accurate, valid and compatible mesh model for FE analysis.

3. Analysis of deformation using the FE method based on a realistic model of loading conditions, boundary conditions and material properties.

The next six chapters of this work are designed around these three requirements as follows:

Chapter 2 Shape modelling of the foetal skull.
The shape recovery and initial mesh generation of two skulls from two different data sources is described in detail.

Chapter 3 Mesh generation and optimisation.
A triangulation algorithm with mesh interpolation and mesh refinement properties and additional techniques for mesh optimisation are presented.

Chapter 4 Important concepts of finite element analysis (FEA).
General concepts of FEA which are crucial to its correct and successful application, are covered. A simple example on the bending of a plate illustrates some of these concepts.

Chapter 5 Analysis of deformation of the foetal skull: The Model.
A model is established which specifies load and boundary conditions and material properties of foetal cranial bone, fontanelles and sutures. Furthermore, a model for validation is outlined.

Chapter 6 Analysis of deformation of the foetal skull: The Experiments.
The first experiment involves the parietal bones only and aims to assess the effects of mesh refinement and geometry. The second experiment assesses the behaviour of the complete skull when subjected to pressures of the cervix during the first stage of labour.

Chapter 7 Conclusion
Results, applications and further research are discussed.

Chapter 2

Shape modelling of the foetal skull

2.1 Introduction

The objective of this work is to analyse the mechanical behaviour of a foetal or newborn skull[1], subjected to labour forces. The first important step towards a successful analysis involves the accurate reconstruction of the shape of the foetal skull. The foetal skull is a complex object, merely consisting of independent bones, connected by sutures. This complex, compound anatomy is the major determinant of the elastic behaviour of the skull. Before outlining the process of shape recovery, we will discuss the anatomy of the foetal skull to give an insight into its overall structure and structural components.

2.2 Anatomy of the foetal skull

The human skull consists of two parts: the **neurocranium** and the **viscerocranium**. The main function of the *neurocranium* is the protection of the brain. It is further subdivided into a cartilaginous and membranous portion. The cartilaginous neurocranium, also called *chondrocranium*, consists initially of a cartilaginous base of the developing skull which forms by fusion of several cartilages. Later endochondral ossification of the chondrocranium forms the bones of the base of the skull. Intramembranous ossification occurs in the mesenchyme at the sides and top of the brain, forming the cranial vault (calvarium) [37]. The *viscerocranium* is the main skeleton of the jaws. The bones of the cranial vault of the foetal skull are held together by dense membranous tissue

[1] During the further course of this dissertation, we will use the term *foetal* skull rather than *newborn* skull.

called sutures. The large areas where the sutures meet are called fontanelles[2].
Appendix B shows the anatomy of the foetal skull in detail.
Figure 2.1 shows the individual bones of the cranial vault.
Figure 2.2 shows a foetal skull subjected to an internal light source. The figure shows that all the bones of the neurocranium and parts of the viscerocranium, except for the maxilla and mandible, are very thin indeed. They are merely shells, which are kept in shape by the intra-cranial pressure (*ICP*) and underlying structures. The ossification centres and the (radially) orthotropic structure of these bones are clearly illustrated in this picture.

2.3 Data acquisition

In finite element analysis (FEA), an accurate geometric model of the shape of the object to be analysed, is of crucial importance. In most finite element (FE) applications, the object is designed (e.g. CAD), hence its shape and dimensions are known in the finest detail. In our case, we do not control the design of the object of interest (OOI), hence we are dealing with a reverse engineering problem. If we were to physically measure the shape and size of an existing object, then the accuracy of the measurements would decrease with increasing geometric complexity. When we are dealing with *in vivo*, internal biological organs, physical measurements would become virtually impossible. In medical applications, rather than physically measuring the organ, we create a 3D image of it using a medical imaging technique.
The oldest technique to image the human body is **X-ray based projective radiography**. An X-ray source projects a fan-beam through the object onto a screen of X-ray film. The X-rays emerge more or less omnidirectionally from the source and as they pass through the subject they are attenuated through photo-electric and Compton scattering processes, both of which depend on the spatially inhomogeneous distribution of bone and soft tissue within the subject's body. The X-rays then expose the film, which is developed to yield a non-linear record of the X-ray exposure [7]. The major drawback of the X-ray images is that it is merely a projection of a 3D object and determination of the full 3D structure of the subject's body is difficult and virtually impossible if only one image is available.
A more advanced technique, also based on the attenuation of X-rays in biological tissue, is **computed tomography** (CT). The X-ray source is collimated to a thin-pencil beam that passes through the patient's body and is detected by a

[2]In the later stages of this work, the importance of fontanelles to the mechanical behaviour of the foetal skull will become apparent.

Figure 2.1: The bones of the cranial vault as individual components: 1 = frontal bones, 2 = parietal bones, 3 = occipital bone. Source: *Life Before Birth* by M.A. England [26].

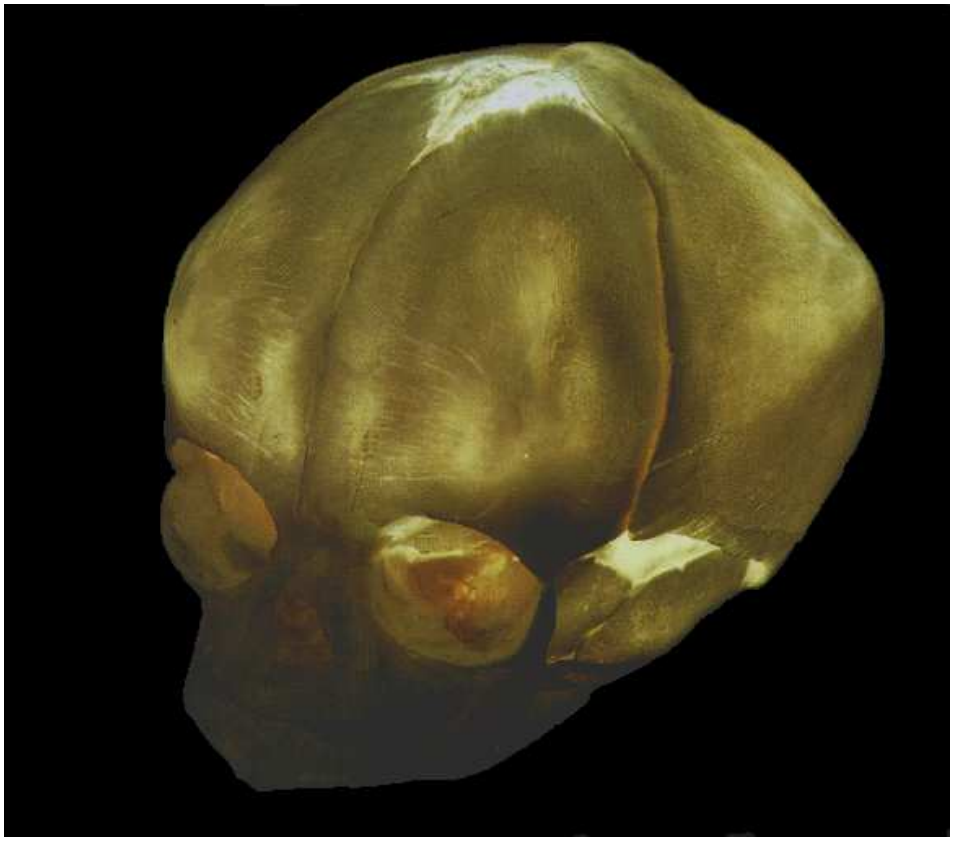

Figure 2.2: Lighted foetal skull: the bones of the cranial vault appear to be relatively thin. Observe the ossification centres and orthotropic structures. Source: *Life Before Birth* by M.A. England [26].

collimated detector aligned with the pencil beam [7]. The detector is not an imaging detector like a piece of film so it yields only a single number for a fixed position of the source-detector assembly. In older systems, to acquire a complete dataset, the assembly is translated so that the aligned source-detector assembly remains in the same orientation but moves laterally. After one translation the source-detector assembly is rotated over typically 1 degree and another translation is performed. The process is repeated until 180 degrees have been covered. In modern CT systems, a fan beam of X- rays and a linear array of detectors are used so many line integrals are measured simultaneously and no translation is necessary. Since only a thin slice of the body part is irradiated, only data of this slice will be acquired [7]. To obtain a set of slices over the entire object, scans in different steps in the direction perpendicular to the plane of the slice are taken, which yields a 3D dataset of voxels[3]. The height of the voxel (often referred to as the z-axis slice dimension) is determined by the slice width and the square base (x and y image dimensions) by the pixel size. The pixel size is related to the display field of view (FOV) and the image matrix[4]:

$$\text{Pixel size} \quad = \quad \text{FOV/matrix size}$$

For example, for a 25 cm. display FOV or reconstruction circle and a 512×512 acquisition matrix, the pixel size is slightly less than 0.5 mm. On most scanners, a range of slice widths can be selected between 1 and 10 mm. [51]. CT images are ideal for the reconstruction of bony objects since the image exhibits a unique grey-value for bone. Drawbacks of CT imaging are the relatively high cost and the radiation hazard from X-rays. Exposure to excessive doses of radiation may cause inhibition of cell division, damage to chromosomes, gene mutation and in the worst case cell destruction [104].

Another tomographic technique is **magnetic resonance imaging** (MRI). Very simply, MRI is an interaction between an external magnetic field, radiowaves and hydrogen nuclei in the body which behave like little magnets. When the subject's body is placed in a magnetic field, it will be temporarily magnetised, i.e. the hydrogen nuclei align with the magnetic field. At equilibrium, the net magnetisation is parallel to the z-axis (along the subject's longitudinal axis) of the external magnetic field. This is called *longitudinal magnetisation* [95]. A radiofrequency (RF) pulse tips the longitudinal magnetisation into the transverse plane, creating *transverse magnetisation*. Longitudinal magnetisation recovers partially between RF pulses, applied at intervals, TR, with time constant T1. Precession of transverse magnetisation induces an electrical signal in the wire

[3] A voxel or 3D volume element is a right square prism.

[4] Also referred to as acquisition matrix [51].

coil, which decays at time constant T2 [95]. The imaging volume is restricted to a slice of a certain thickness by specific frequencies in the RF pulse and the magnetic field gradient. More in depth coverage on the physics of MRI can be found in [95], which also includes clinical applications and [93] for a more mathematical, theoretical approach. Excellent resolution in MRI is obtained with for example an acquisition matrix of 256×256, combined with a FOV of 8 to 10 cm. Note that the increase of planar resolution causes a decrease of signal volume, resulting in a lower signal-to-noise ratio (SNR). The major disadvantage of MRI is the high cost. Health hazards include tissue heating when exposed to excessive RF power, vertigo as a result of exposure to fields, higher than 2 Tesla, and peripheral nerve stimulation when strong gradients are changed too rapidly [95].

A relatively inexpensive and presumably harmless imaging technique is **3D ultrasound**. Acquisition of image data is based on the same technique as *2D ultrasound*: a piezoelectric crystal is excited as to produce a short ultrasound pulse and the resulting echoes are recorded. The intensity and timing of the echoes gives information about the structures along the direction of the ultrasound beam. If the beam is swept through a plane, a 2D image can be created. Because the echo intensities are converted into *brightness* for display, the 2D image is called a B-scan [89]. In depth coverage of 3D ultrasound technology can be found in [79, 89].

Another, relatively inexpensive technique is **laser-scanning**: a laser beam is fanned out into a line and projected onto the object which rotates around its axis. As a single line represents the local curvature of the surface when viewed obliquely by a CCD camera, a matrix of points on the object surface can be obtained. The technique is limited to surface reconstruction.

Stereo-based 3D reconstruction is a popular technique in computer vision and robotics: a visible surface is reconstructed from images obtained with two stereo-vision cameras. The approach has also been found useful in medical applications, for example during cranial surgery, to register the head of a patient with 3D data reconstructed from MR images, two stereo cameras are used to render the visible surface of the patient's head [18]. A disadvantage is that the technique can only be employed for visible surfaces ($2\frac{1}{2}$D).

Discussion Keeping the objective in mind of recovering the shape of a foetal skull, CT images are probably the best option because they exhibit a unique grey-value for bone tissue. MR images do not possess this property, hence the segmentation of foetal cranial bone would pose considerable problems. To obtain a complete skull from 3D ultrasound would be a difficult task as well

because of the size and complexity of the object, which would require several acquisitions. Moreover, since the acquisition needs to be done *in vivo*, the required registration to compensate for foetal movement would yield poor accuracy. In Section 1.2.2.2 it was pointed out that the thickness of foetal cranial bone was of the order of 0.5-1.5 mm. of magnitude. Accurate representation of the geometry would thus require a resolution of at least 0.1 mm. Conventional CT scanners have a typical intra-planar resolution of 0.5 mm. which is insufficient to model the thickness with the required accuracy. However, the availability of CT images of a foetal skull poses the major problem. For ethical, financial and political reasons, CT images of a newborn or foetus are scarcely available and if so, they are difficult to obtain.
Considering the many practical and especially ethical problems related to the acquisition of foetal skull data from medical images, we decided to reconstruct a shell-based surface model only. This decision is justified by the sole fact that the bones of the cranial vault of the foetal skull are very thin, as was illustrated in [71] and was clearly shown in Figure 2.2. Two surface models of a foetal skull were thus developed, based on the following techniques:

1. Using atlas images of a foetal skull and a 3D adult skull, obtained from CT images, specify corresponding landmarks and warp the shape of the adult skull into the shape of a foetal skull using thin-plate spline (TPS) interpolation.

2. Laser-scan a model, either a real skull or the exact replica of a real skull and reconstruct the outer surface.

In the next two sections each technique is covered in depth. Finally, the chapter is closed with a discussion of the results and a summary.

2.4 Foetal skull model *I*: 3D warping using thin-plate splines

The alternative of reconstructing the shape of a human body-part from orthogonal images or pictures, is a cheap solution which only requires the availability of a homologous object (HO). The HO is fully determined in 3D space and is used to interpolate the missing structure of the object of interest (OOI). To do this, we specify a set of landmarks in 3D space for both objects. These pairs of data points allow us to derive a smooth interpolation function to recover the 3D shape of the OOI. In other words, we *warp* the shape of the HO into a plausible shape of the OOI. The thin-plate spline (TPS) is preferred as the basis of the

warping function because it minimises the bending energy of a thin-shell object [12]. The degree by which the shape of the warped OOI will agree with the shape of the true OOI depends mainly on the number of interpolation points used.
Biological objects have a limited set of landmarks, e.g. for the human skull, Riolo et al. have determined this to be 45 [88]. In [50] we used 38 of these[5] to arrive at the 3D shape of a foetal skull, using a 3D adult skull from CT images, obtained from the Visible Human Project (VHP), as the HO. It was observed that this number was insufficient to fully recover the curvature from the cranial vault. Therefore, in the future we will specify the curves between the landmarks as well, which after discretisation, just yield an extra set of points.

2.4.1 Morphometrics, homology and homeomorphic surfaces

Morphometrics is the study of covariances of biological form [12]. The most effective way to analyse forms of whole biological organs or organisms is to record the geometric locations of landmark points. Landmark points are typically determined by a name, e.g. bridge of the nose, and a geometric location. This is necessary to imply true *homology* [12]. In theoretical biology, homology is known to be the correspondence between two body-parts of different creatures, for example the correspondence between a human arm and a chicken wing. However, for the case of warping one object to the other, the homology between these two is not sufficient to assure a successful mapping. Another property known as *homeomorphism* is required: two surfaces are homeomorphic if one can be converted to the other by continuous distortion, i.e. bending, stretching and squashing, in other words, *warping*, but without points being torn apart or *glued* together [28]. In the strictly theoretical sense, the outer surface of a foetal skull and an adult skull are not homeomorphic because of the presence of the fontanelles which can only be inversely created by tearing the sutures of the adult skull apart.

2.4.2 Ray-casting from a set of planar CT images

To allow us to specify landmarks on the HO[6], we can visualise it by *ray-casting*. Ray-casting is a visualisation method which determines the visibility of surfaces by tracing imaginary rays of light from the viewer's eye to the objects in the scene [29]. Ray-casting can be implemented in a variety of ways, which differ in terms of complexity, quality of visualisation and speed of the algorithm.

[5] Some points cannot be located in 3D from the orthogonal images.
[6] Which is in our application a 3D adult skull, available as a set of transverse CT images.

Since speed is not a crucial factor, a relatively simple ray-casting algorithm was implemented which involves the following steps:

1. segmentation[7] of voxel data to isolate the OOI,
2. creation of a Z-buffer (depth-buffer) to render an image of the object, viewed from a particular angle,
3. ray-casting the Z-buffer using a shading model.

Tri-linear interpolation is used during the thresholding operation to obtain resolution at sub-voxel level and to resolve the difference between inter-planar and intra-planar resolution. *Phong's illumination model* for gray-scale images is used to visualise the surface from the Z-buffer [29].
Surface normals are calculated from *Z-buffer gradient estimation*. The alternative approach is *object-space gradient estimation*, which estimates grey-level gradients at voxel level and yields more realistic visualisation but requires extra storage for the grey-level differences of each point on the surface and extra processing time to calculate them[8].

2.4.3 Thin-plate splines as a model for warping

At the root of the thin-plate spline (TPS) analysis lies the function [11]:

$$f(x, y) = -U(r) = -r^2 log(r^2) \tag{2.1}$$

where

$$r = \sqrt{x^2 + y^2} \tag{2.2}$$

or the Euclidean distance from the point (x,y) to the origin.
Bookstein shows that the form of an infinite, previously flat, steel plate which is bent and fixed at a point above or below the original surface, will be described by Equation 2.1 whenever the displacements are sufficiently small. Subject to more constraints, the form of the plate will be described by a linear combination of terms: $r_i^2 \log(r_i^2)$ [12].
We extend the formulation to the 3D case. If we consider displacements of n points in a regular 3D mesh to points in a deformed 3D mesh, the TPS function can be specified as:

$$f(x, y, z) = a_1 + a_2 x + a_3 y + a_4 z + \sum_{i=1}^{n} w_i U(|p_i - (x, y, z)|) \tag{2.3}$$

[7]Because the grey-level range for bone in CT data is unique, simple thresholding within this range is sufficient to segment the skull.

[8]The 'less realistic', sharper edges, typical for Z-buffer gradient estimation, are preferred because they ease the process of landmark determination.

The first part is an affine transformation representing the behaviour of $f(x, y, z)$ at infinity, whilst the second part is the weighted sum of root functions $U(r)$ of the spline. In matrix notation (without the affine part):

$$\mathbf{CR} = \mathbf{Y} \tag{2.4}$$

Where $\mathbf{C}$ = the $n \times n$ matrix:

$$\begin{bmatrix} U(r_{1,1}) & ... & U(r_{1,n}) \\ ... & ... & ... \\ U(r_{n,1}) & ... & U(r_{n,n}) \end{bmatrix} \tag{2.5}$$

where

$$r_{i,j} = |p(x_i, y_i, z_i) - p(x_j, y_j, z_j)| \tag{2.6}$$

or the Euclidean distance between two points p_i and p_j in the 3D space of the original mesh[9].
The $n \times 3$ matrix of TPS parameters:

$$\mathbf{R} = \begin{bmatrix} w_{1x} & w_{1y} & w_{1z} \\ ... & ... & ... \\ w_{nx} & w_{ny} & w_{nz} \end{bmatrix} \tag{2.7}$$

and the matrix of coordinates of the n points in the displaced mesh:

$$\mathbf{Y} = \begin{bmatrix} x'_1 & y'_1 & z'_1 \\ ... & ... & ... \\ x'_n & y'_n & z'_n \end{bmatrix} \tag{2.8}$$

The spline parameters are then obtained from:

$$\mathbf{R} = \mathbf{C}^{-1}\mathbf{Y} \tag{2.9}$$

The affine part can be added to the matrix C yielding the $(n + 4) \times (n + 4)$ matrix:

$$\mathbf{L} = \begin{bmatrix} \mathbf{C} & \mathbf{A} \\ \mathbf{A}^T & \mathbf{0} \end{bmatrix} \tag{2.10}$$

where the $n \times 4$ matrix

$$\mathbf{A} = \begin{bmatrix} 1 & x_1 & y_1 & z_1 \\ ... & ... & ... & ... \\ 1 & x_n & y_n & z_n \end{bmatrix} \tag{2.11}$$

The matrix $\mathbf{0}$ is a 4×4 matrix of zeroes.

[9]Note that the elements on the main diagonal are 0.

2.4.4 Ray-casting an adult skull from CT images obtained from the Visible Human Project

The adult skull used as the HO for the foetal skull or OOI, is obtained from the Visible Human Project (VHP). The VHP is an initiative from the Library of Medicine in Bethesda, Maryland. A full set of CT images, MRI images and photographs of cryo-sections are available from a male and a female volunteer, who donated their bodies to medicine after their deaths. CT images of the visible male were used to raycast the 3D adult skull. The original dataset was tri-linearly interpolated at steps of 0.25 mm., within the plane and between planes[10]. Figure 2.3 shows the result after ray-casting from four different viewing directions.

2.4.5 Specification of a point-distribution in 3D space from principal landmarks of the skull

To specify a point distribution of the foetal skull in 3D space, we developed an interface in a hybrid C, Tcl/Tk environment [80, 106], which allows us to register images from two or more orthogonal viewing directions and to specify landmarks and connecting curves. The approach is based on orthographic projection [87]. Figure 2.4 shows three atlas images of a foetal skull from orthogonal viewplanes [69], organised in a manner to allow easy matching of points from one image to the other. We distinguish three stages to arrive at a point distribution:

1. alignment of images according to a reference point,
2. registration of the images using 2D warping,
3. specification of landmarks and curves yielding a point distribution in 3D space.

Alignment ensures that the images from different viewplanes have at least one point in the same position.
Registration is only necessary when the images are proportionally different. If the disproportion is linear it can be resolved by scaling. Non-linear disproportions can occur when the images are drawings with the relative positioning of the landmarks being correct and consistent in the topological sense but not in terms of exact position. For pictures, different camera properties and lighting artifacts may cause non-linear inconsistencies. To solve these problems we

[10]The inter-planar distance of the VHP CT dataset is 1 mm. and the pixel size or intra-planar resolution is 0.527344 mm.

(a) Anterior view

(b) Posterior view

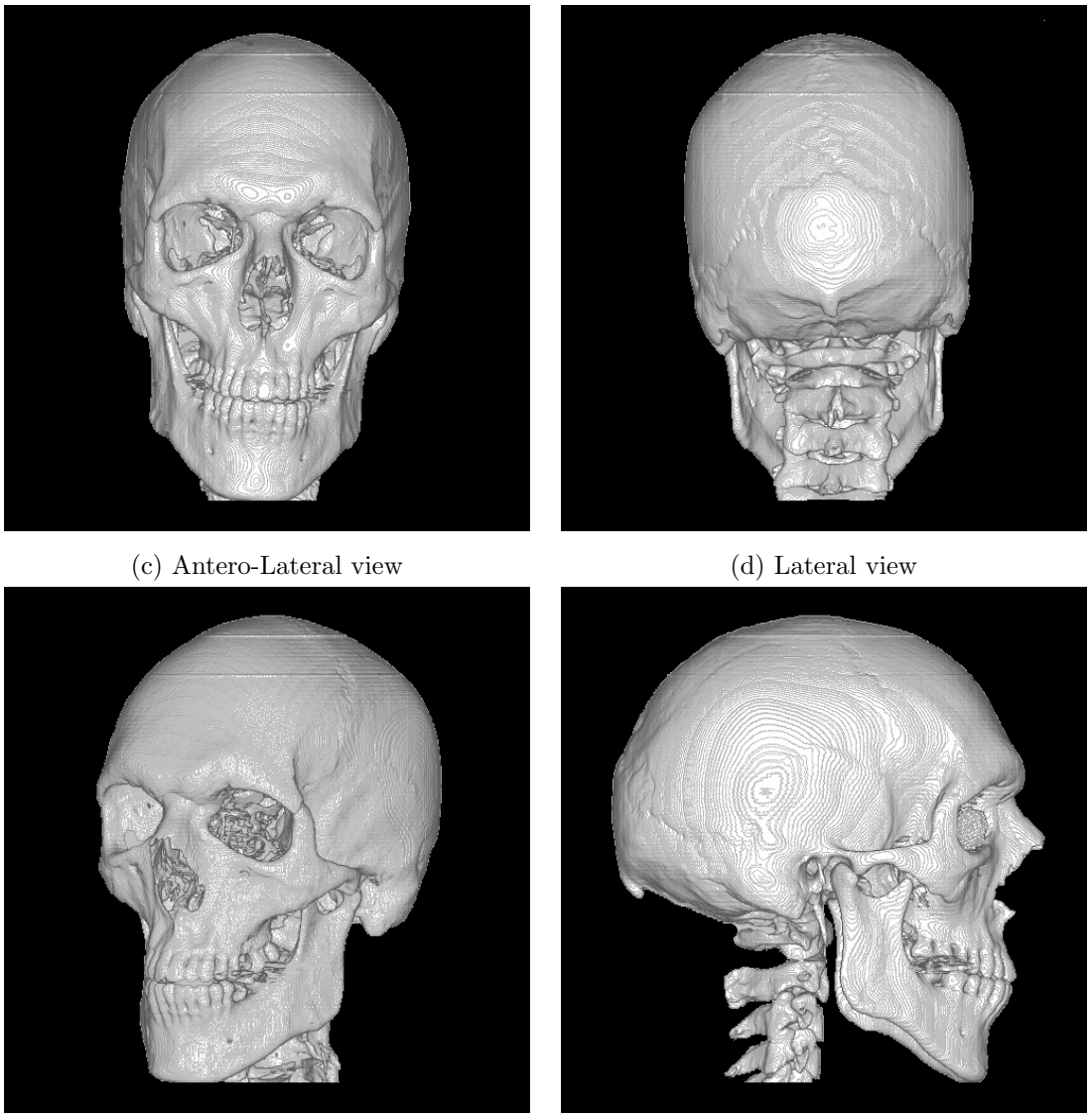

(c) Antero-Lateral view

(d) Lateral view

Figure 2.3: Ray-casted images of the visible male's skull.

specify corresponding landmarks on a *master* image and a *slave* image and subsequently warp the *slave* image to make it correspond to the *master* image.
The final step involves the *specification of corresponding landmarks* in 3D space. In [50], a first warping experiment, strictly using landmark points, is described. In the experiment, 38 landmarks were specified on both the HO and OOI. The result was poor because the principal curves of the OOI were not preserved. Therefore we adapted the interface to match curves as well as points. The segmentation of curves from the images is based on an approach as described in [63]: a rough polygon around the area of interest is drawn. A dynamic model based on internal, external and damping forces will then automatically align the polygon to a boundary curve in the image. The model is defined by:

$$F_i = w_{ex}F_{ex,r_i} + w_{in}F_{in,i} + F_{damp,i} \tag{2.12}$$

with

$$F_{damp,i} = w_{damp}v_i \tag{2.13}$$

where

i	The index of a vertex of the polygon.
F_i	The resulting force on vertex i of the polygon.
F_{ex,r_i}	The radial component of the external force acting on a vertex i.
w_{ex}	The external weighting factor.
$F_{in,i}$	The internal force acting on a vertex i.
w_{in}	The internal weighting factor.
$F_{damp,i}$	The damping force acting on a vertex i.
w_{damp}	The damping weighting factor.
v_i	The velocity of a vertex i.

The external force, F_{ex}, is obtained from the *energy* of the image. The energy is a potential function of the image and can take several forms with an affinity for darkness or brightness. Two different potential functions are considered, i.e. either the original image or this image convolved with a Gaussian function with standard deviation σ. On the lhs of the interaction panel shown in Figure 2.5 we observe the buttons to select the type of the potential function and sliders to change the darkness and, in the case of Gaussian convolution, to set the size of the convolution mask and standard deviation. The external force is taken as the negative gradient of the energy:

$$F_{ex} = -\nabla E \tag{2.14}$$

This definition implies that the external force pulls the contour in the direction of lower energy.
The internal force, F_{in}, is included to obtain a smooth curve.
The damping force, F_{damp}, regularises the oscillation caused by internal and external forces working in opposite directions.
Figure 2.6 shows a polygon settled around the cranial vault-curve starting from the *nasion*[11] and ending approximately at the *opisthion*[12] [12, 88]. The initial polygon was roughly placed on the image (in *Add* mode) by clicking points. To match the curve with a corresponding position in the other images a sliding ruler is activated (*Ruler* button). The corresponding landmark (nasion) in the example, can be spotted in the lower-left image, showing a frontal view of the skull. Since the curves are piecewise linear, the final result is a set of points in 3D space.
A total of 15 curves, resulting in a total of 237 corresponding points, were specified for both skulls.

2.4.6 Warping from homologous object (HO) to object of interest (OOI)

After specification of corresponding landmarks on the adult skull and the foetal skull respectively[13], we can calculate the warping function as formulated in Equation 2.3.
The warping function can be either:

1. a forward transformation, warping from HO space to OOI space,

2. a backward transformation, warping from OOI space to HO space.

Forward warping poses a problem when the coordinates of the warped object (OOI) have to be mapped back to an integer grid for display. Since the coordinates of the warped OOI are real, they have to be rounded if mapped back to an integer grid which may result in the visualised object containing gaps. *Backward warping* solves this problem because integer coordinates from the OOI space are processed through a *backward warping function* yielding real coordinates in the HO space, which are rounded. The grey-values of these rounded coordinates are then allocated to the integer coordinates in the OOI space[14].

[11] See Appendix C.

[12] Posterior-most point of the foramen magnum.

[13] An extra set of 26 anchor points was necessary to fix the corners and sides of the data cube.

[14] Note that backward warping becomes ill-posed if two or more points are mapped to one point or points with nearly the same location [6].

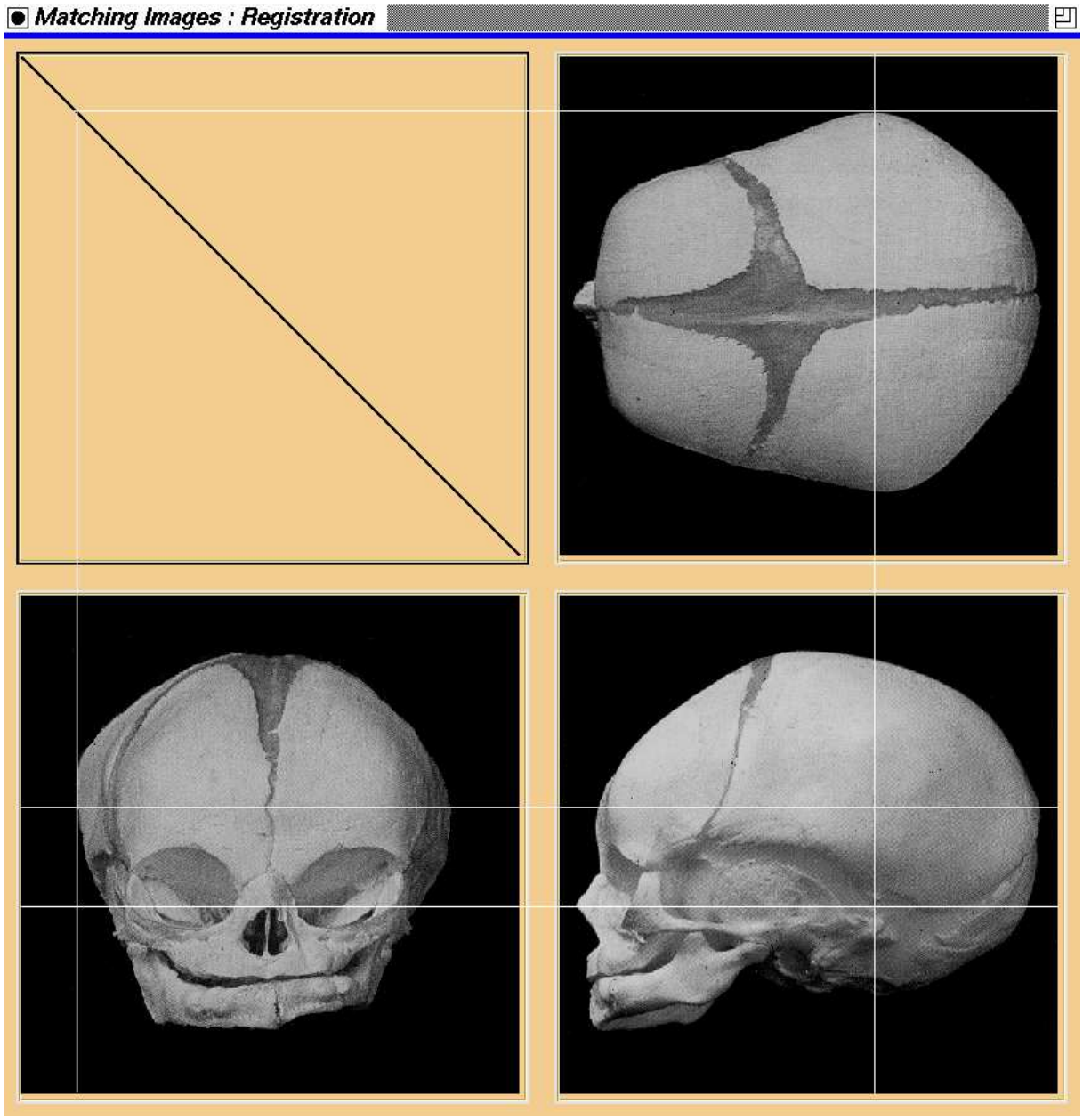

Figure 2.4: The interface in 2D warping mode to register images from three orthogonal viewplanes. The original images of the foetal skull are obtained from [69].

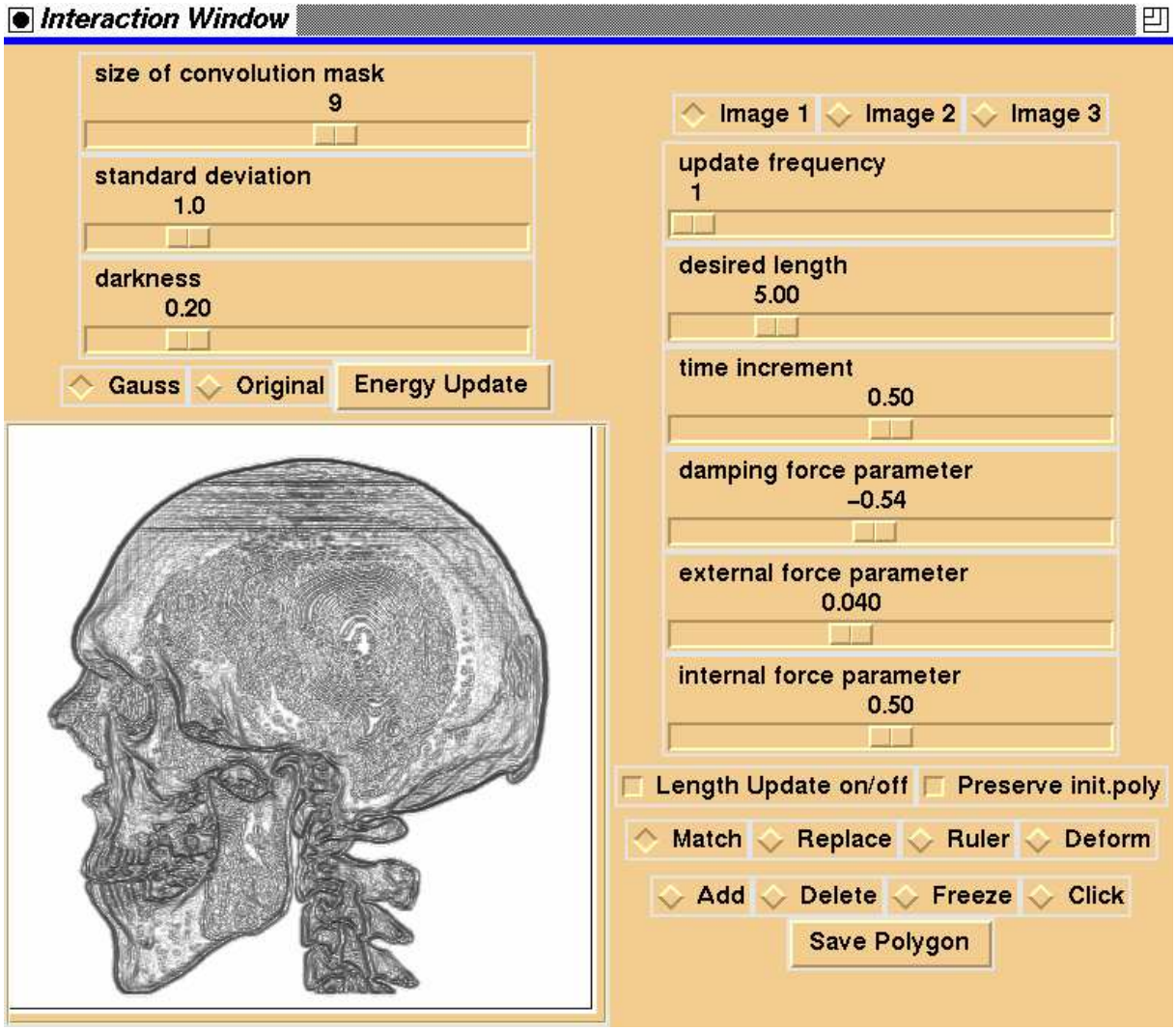

Figure 2.5: The interaction panel to specify landmarks and curves (with energy image of a lateral view of the adult skull).
GUI options include:
- Weighting factors for each of the forces, set, using the sliders on the right hand side of the interaction panel.
The three top sliders have the following functions:
- The first slider sets the period to update the positions of the vertices of the active contour.
- The second slider sets the length of a polygon element in pixels. The length is automatically adapted during deformation of the polygon (activated with the *Deform* button).
- The third slider sets the time increment.
Furthermore, there are buttons to *Add* and *Delete* a polygon and to *Replace*, *Freeze* and *Click* a vertex of a polygon. The *Ruler* button displays a ruler for matching, whilst matching across different images is activated in *Match* mode.

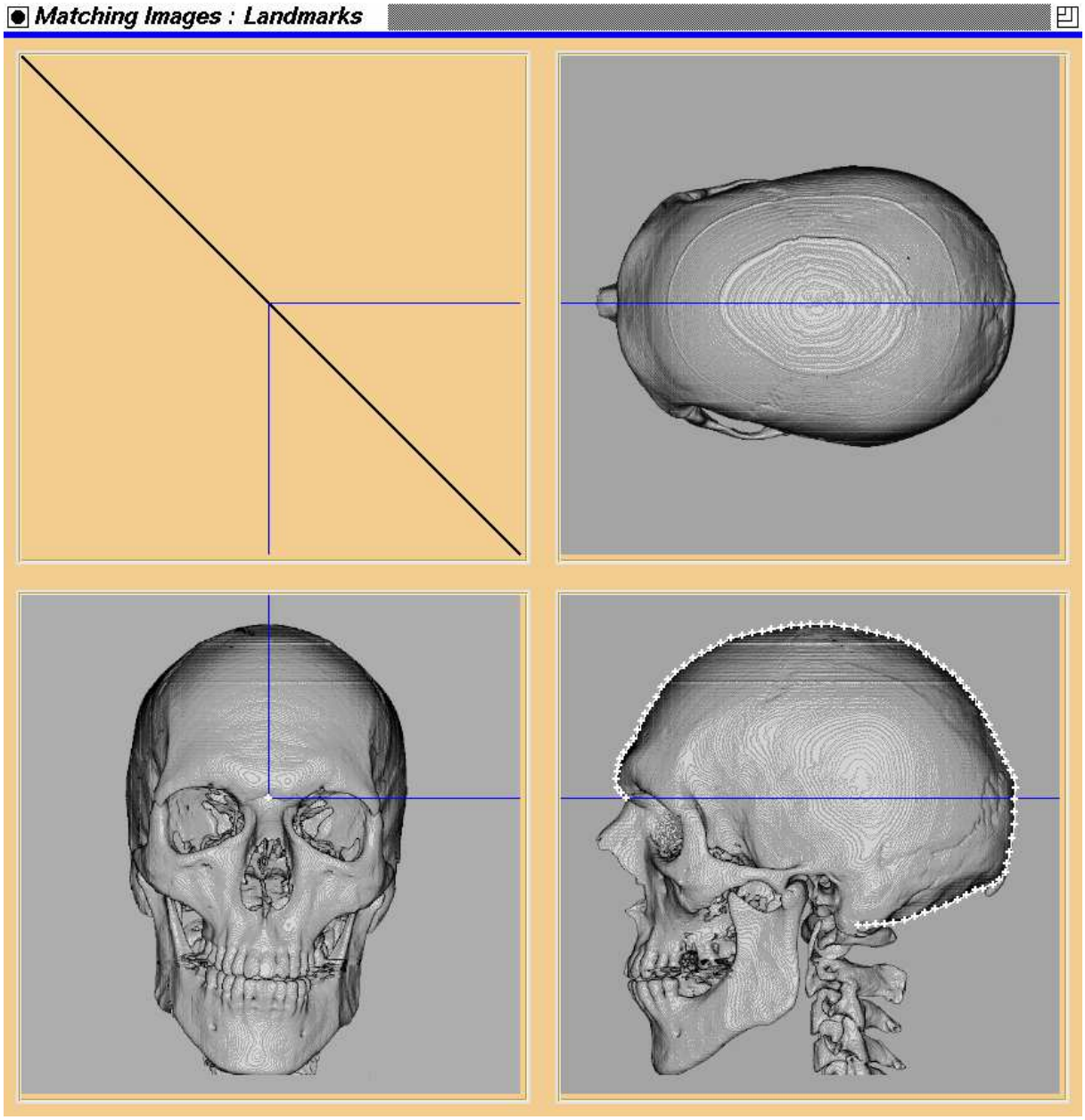

Figure 2.6: The interface to specify landmarks and curves in 3D space: orthogonal images of the ray-casted adult skull. The ruler provides easy matching of corresponding landmarks across the images.

Results The results in Figure 2.7 show lateral, top and frontal views of the warped foetal skull. Note that the fontanelles are missing at this stage. We mentioned in Section 2.4.1 that it is not possible to create the fontanelles in the foetal skull using the warping approach because the fontanelles cannot be created without tearing or cutting the HO. Since the outer surface of the skull has the correct shape, we can locate the fontanelles on the 3D foetal skull by mapping them on the surface. Before we perform this operation, we first create an initial mesh.

2.4.7 Creation of an initial mesh

The ray-casted image of the foetal skull is only a 3D visualisation of the object. If we want to study the mechanical behaviour of the foetal skull we will need to create a mesh model.
An initial mesh was created using the Delaunay triangulation (DT) algorithm for planar data as described in [34]. The reconstruction algorithm is implemented in C and is part of the free software package called *NUAGES*.

Results Figure 2.8 and Figure 2.9 show a snapshot of the 3D mesh-model of the foetal skull with and without the boundary edges and after mapping the fontanelle structures onto the mesh. Figure 2.10 shows the posterior fontanelle.

2.4.8 Discussion

When looking at Figure 2.7b and d we observe an accurate shape of the boundary curves when compared with the original images as displayed in Figure 2.4. We wouldn't expect anything else because these boundary curves have been used to derive the spline function.
Figure 2.7c shows the anterior view. Although the boundary of the skull in the image is correct, for known reasons, facial details are not because:

- The mandible and maxilla are obviously different between adult and foetus because of the absence of teeth for the foetus[15]. Small imperfections such as the teeth and the fontanelles illustrate the fact that the surfaces of a foetal skull and an adult skull are not strictly homeomorphic.

- Since the adult skull and the foetal skull are not from one and the same person, matching of 'simple' structures like the cranial vault is relatively straightforward but more 'complex' structures such as the facial features

[15]Note that the mandible is of no real importance with regard to the moulding of the foetal skull.

(a) Right-Lateral view

(b) Top view

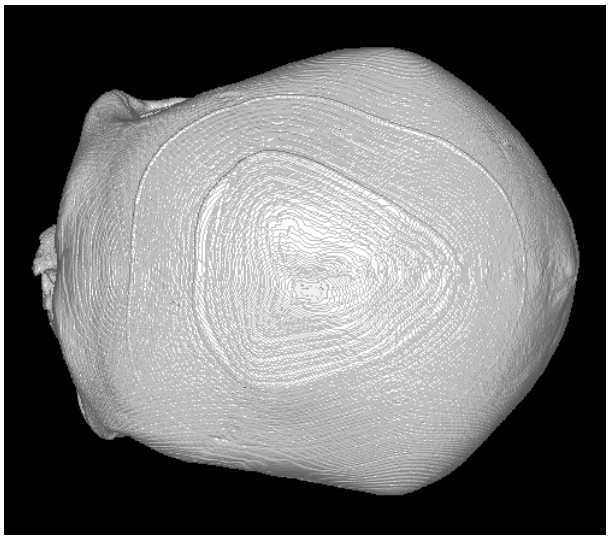

(c) Anterior view

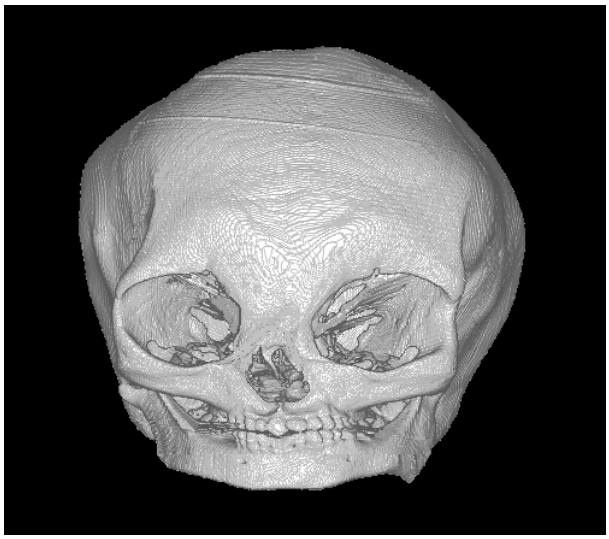

(d) Left-Lateral view

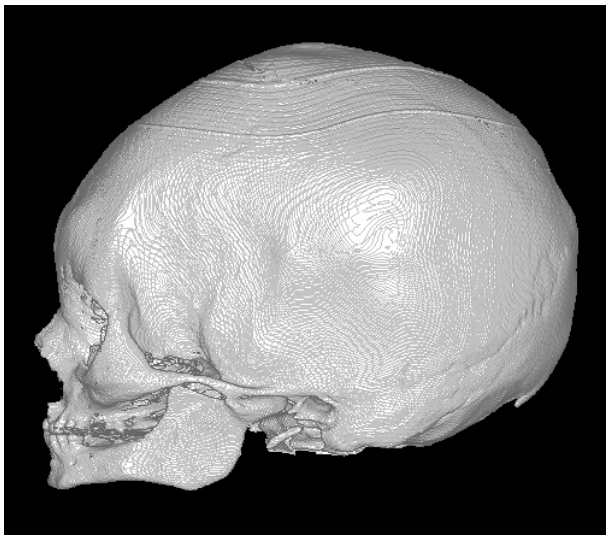

Figure 2.7: Ray-casted images of the warped foetal skull.

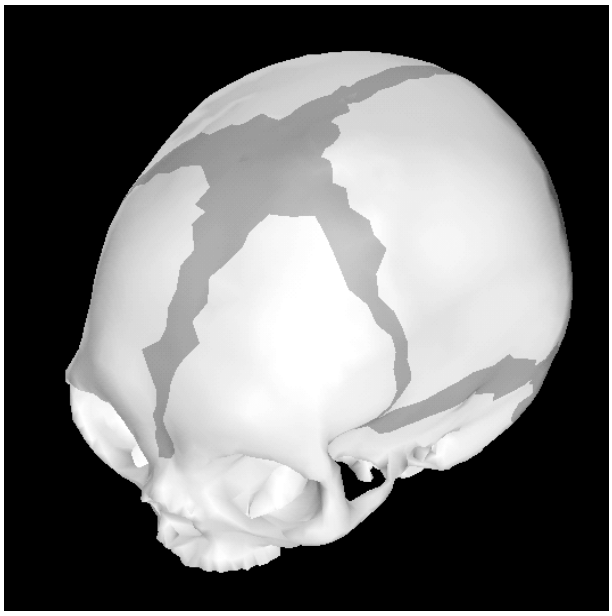

Figure 2.8: 3D view of the reconstructed foetal skull with mapped fontanelles (visualisation in Geomview 1.6.1 [84]).

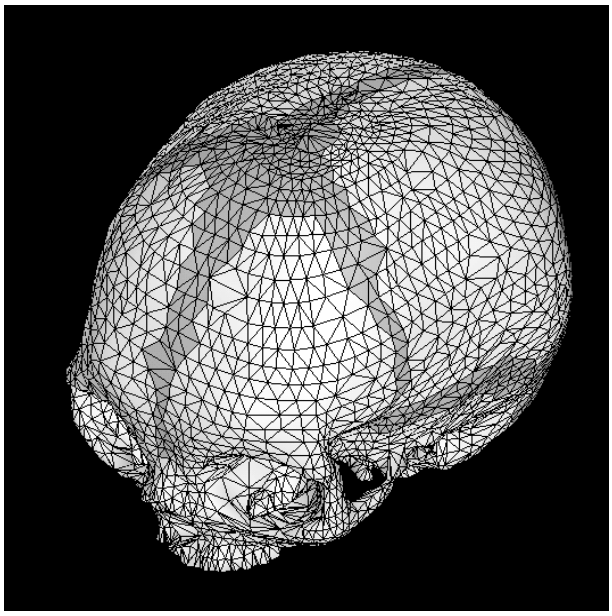

Figure 2.9: 3D view of the reconstructed foetal skull: triangular mesh (visualisation in Geomview 1.6.1 [84]).

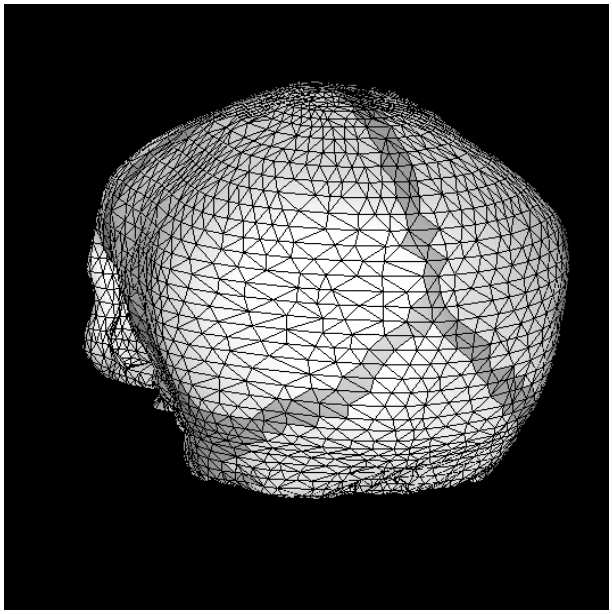

Figure 2.10: 3D view of the reconstructed foetal skull: posterior fontanelle (visualisation in Geomview 1.6.1 [84]).

will show discrepancies. The degree of resemblance depends on the number of points specified, however over-specification could result in tears or overlaps in the surface.

We have illustrated the method to recover the shape of the OOI from a HO by warping the latter into the former, onto the shape recovery of a foetal skull. Obviously this method can be used for many other applications:

- The method allows us to visualise an object in 3D from conventional radiograph (X-ray) images, provided the relative orientation of the images is known. In their study on foetal head moulding, McPherson and Kriewall [72] used orthogonal radiographs to manually reconstruct the parietal bone. Our method provides a better model because of the more accurate TPS interpolation.

- When insufficient imaging data is available, i.e. the set of images is small, relative to the size of the object, important parts of the object can be missed out. Our approach can provide smooth interpolation with a realistic curvature in those areas where no data is available.

- A dataset from a malformed or damaged biological organ can be corrected using the warping technique. A similar approach for cranio-plastic surgery has been shown in [15].

- For educational purposes, images from atlases and medical text- or specialist books, of which the relative orientation is known, can be visualised in 3D provided a library of homologous objects is available. This library of organs is currently available from several collaborators of the Visible Human Project.

A more in depth coverage of the warping technique and the application to the shape recovery of a foetal skull can be found in [48].

2.5 Foetal skull model *II*: laser scanning of a replica model obtained from a natural specimen

The first foetal skull model, obtained by warping the outer shape of an adult skull to the outer shape of a foetal skull using TPS interpolation is a good approximation but the true anatomy at the bone/suture connections is highly dependent on the atlas images. Therefore the model can show the following inaccuracies:

- In a realistic model, the fontanelles and sutures are embedded, i.e. the bones of the skull and in particular the parietal bones, have an inwards curving tendency near sutures and fontanelles. Since the atlas images are usually obtained from a real model of which the original fontanelles and sutures are replaced by a glue-like substance to keep the loosely connected bones together, the inwards curvature of the bones near the sutures has vanished.

- For the same reason, the fontanelles and sutures are usually larger than they used to be in their original state.

The laser-scan approach, which is outlined in this section, aims to improve these shortcomings.
Figure 2.11 shows a picture of a replica model of a foetal skull. The model is manufactured in poly-urethane and originally developed by ESP Ltd. It is a true model of a natural specimen. The model shows clearly the non-smooth transitions between bones and fontanelles/sutures. The inside of the model is incorrect but since we made the assumption of the skull to be a shell-based object, only the outer surface is of importance. This outer surface is accurate considering the fact that the model is an exact mould of a natural specimen.
The first step is to digitise the skull model to obtain a computerised surface model. We used the laser-scanning technique to solve this problem. The laser-scanning technique provides a set of surface data points which are organised in

Figure 2.11: Foetal skull model (manufactured by ESP Ltd.).

rows of vertical arrays. This provides us with a structured matrix of data points of which triangulation of the scanned surface is a straightforward procedure.

2.5.1 The principle of laser-scanning

The laser-scanning system from the Department of Medical Physics and Bioengineering at University College London (UCL) was used to scan the foetal skull model as shown in Figure 2.11. The laser-scanning system was developed as early as 1978 with the objective of providing 3D prediction and simulation for maxillo-facial surgery. This was at the time merely based on 2D methods involving the dissection and rearrangement of facial and profile photographs. Over the years the laser-scanning system was developed for acquiring 3D data of the facial surface [59]. These days it is used for practically all parts of the body and a range of applications in surgery, diagnostic radiology, prosthetics, clinical growth studies, forensic science, archeology and psychology. Commercial interests have included sculpturing and advertising. It should be noted that diverse types of 3D laser-scanners are available on the market of which many are of the free-hand type, i.e. the object is scanned using a hand held device, which is pointed at and moved across the object. The scanner at UCL is fixed and the acquisition of data is based on triangulation [60]. It operates according to the following principle: a beam of laser light is fanned out into a line and projected onto the object surface. When the line is viewed obliquely by a CCD camera,

it is curved, reflecting the shape of the surface at the intersection with the laser beam. An arrangement of mirrors ensures the line is viewed from opposite directions. The resulting image, which is displayed on a VDU, shows the double *mirrored* surface curve. This approach is necessary to avoid the loss of signal due to occlusion of parts of the facial surface by the prominence of the nose. The video signals of the camera are pre-processed by a purpose built printed circuit board which is fitted into a slot of a personal computer. For each video frame, the board outputs a set of numbers which represent the midpoints of the pulses on the video scan lines produced by the projected laser line. To obtain a scan of the entire surface of the object, the latter is rotated on a platform. Up to 256 profiles may be recorded per scan and the angles at which these are recorded can be set. This ensures a maximum rate of acquisition over areas of the anatomy where greatest detail is required such as the mid face. Resolution may thus be matched to surface detail and curvature. The collected dataset usually consists of between 20,000 and 60,000 3D coordinates of points lying on the anatomical surface. Individual data points can be recorded with a precision of less than 0.5 mm. The triangulation of the data points is straightforward because they form an ordered grid or matrix of points on the object surface[16].

2.5.2 Laser data of the foetal skull

One shortcoming of the laser-scanning system is that the top and bottom parts of the object cannot be scanned. This is not hard to understand since the principle is based on scanning the object in a cylindrical fashion, hence a surface of revolution is obtained. Also, data points which are close to the top or bottom can be inaccurate. Therefore multiple scans of the foetal skull are necessary to obtain accurate data over the entire object. Figure 2.12 shows scans obtained from different positions according to the placement of the object on the turntable. The following *defects* occur:

1. gaps, caused at the locations where datapoints are *out of reach*,
2. noise, due to interfering objects, e.g. on Figure 2.12a, noise at the left side is from the supporting table, noise at the bottom is from the supporting metal bar,
3. inaccurate data, typically near locations where data points cannot be acquired,

[16]Contrary to our first model in which the creation of an initial mesh model was less trivial, the mesh of the laser-scanned model can be made instantly available because a regular matrix of points is *wrapped* around the object.

4. false or incorrect connections: a big gap is bridged by long and narrow triangles because no datapoints are available in between the connecting points[17],

5. incorrect patterns on the surface because of vibration of the object during scanning,

6. unclosed gap between the first and last array of scanned points.

In total, four datasets, scanned from different positions of the object on the turntable, were acquired.

To arrive at a single, complete and valid shape model of the foetal skull using the acquired laser-scan data, the following operations are required:

1. Removal of noise for each dataset.

2. The selection of datasets to be used for the final model.

3. The registration of the selected datasets.

4. The selection of relevant parts of each dataset, to be used for the final object.

5. The connection of these parts to obtain a valid and complete object.

The **removal of noise** is mainly aimed at reducing the size of the dataset. Since the object was scanned at the best possible resolution, the datasets contain around 60,000 faces of which a significant number are noise. For example, the metal bar in Figure 2.12a comprises over 15,000 triangles. Custom-built software, developed by the author and called the the interactive mesh-modelling toolkit, *immtk*, can deal with noise removal in a straightforward way, using cut-off planes and individual removal of triangles[18].

Selection of the datasets is based on careful examination whilst keeping in mind the following two guidelines:

- Keep the individual parts to a minimum but not at cost of accuracy.

- Only select accurate parts, i.e. parts of which the data is correct. It is difficult to quantify this concept but any moderately trained observer could tell immediately which points on the reconstructed model are reliable and

[17] This yields a poor approximation of the original surface.

[18] The *immtk* software is developed in a hybrid Tcl/Tk, C environment. It provides tools for mesh adaptation and optimisation, measurements of object dimensions and selection of relevant parts for finite element analysis.

(a) Scan of the skull supported by a metal bar and in face-forward position.

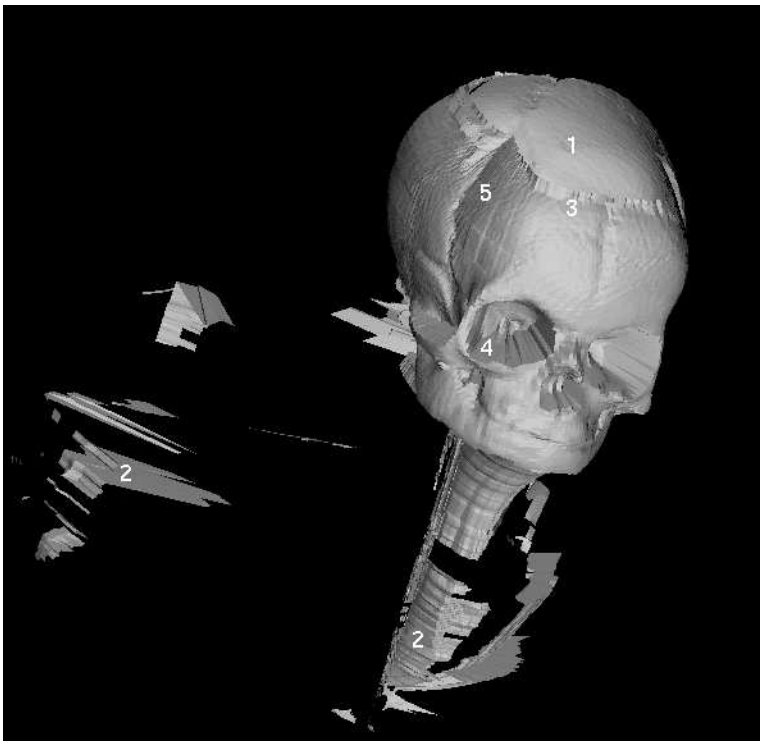

(b) Same scan as in (a) but viewed from the backside.

(c) Scan of the free skull model in face-down position.

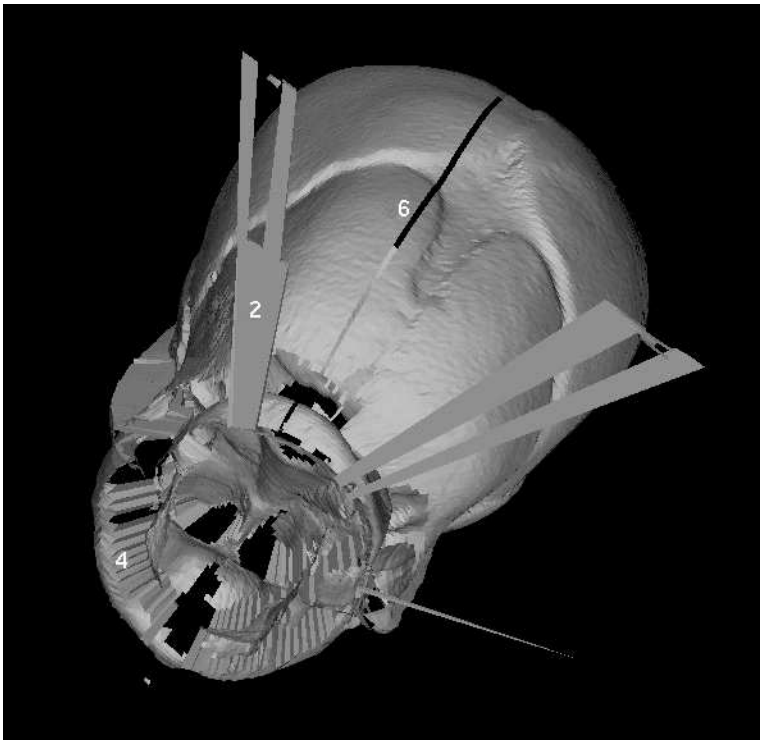

(d) Same scan as in (c), showing the detail of the triangular mesh near the anterior fontanelle.

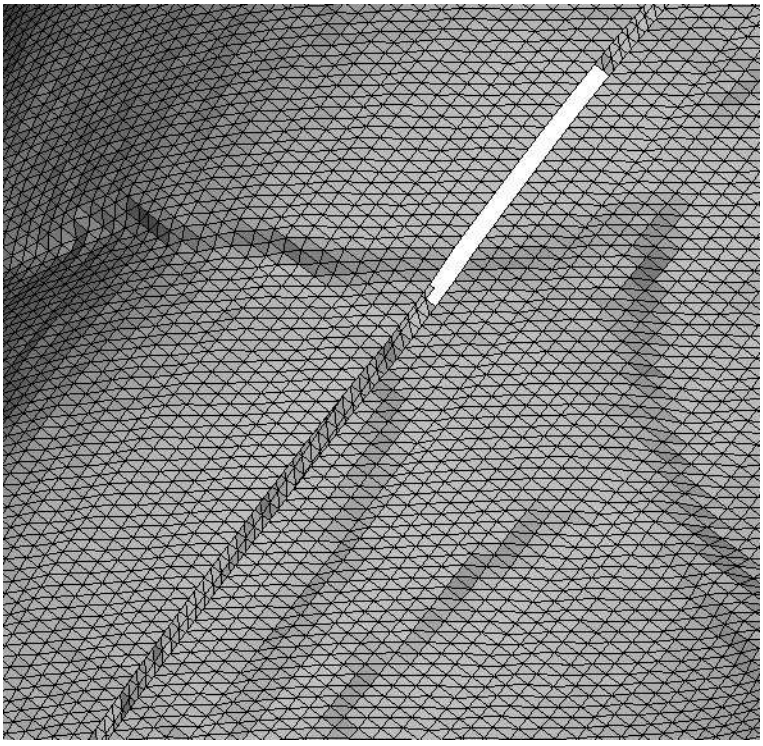

Figure 2.12: Raw models after laser-scanning a foetal skull model from different positions on the turntable. 1 = gaps, 2 = noise, 3 = inaccurate data, 4 = false or incorrect connections, 5 = incorrect patterns, 6 = unclosed gap (see text for further explanation).

which are not. Taken into account that the true object is available for comparison makes this task easier.

Registration of the selected datasets. This is a well-known problem in almost any of the fields of medical imaging and is tedious, especially when moving body parts are scanned. Since we are dealing with a fixed object and the laser-scanned data acquisition system does not yield any significant non-linear disturbances, a conventional approach such as landmark matching, followed by least-squares parameter estimation for a coordinate transformation, is sufficient. The approach is outlined in the next section.
The final steps include the **selection of relevant parts** using the *immtk* software and the **connection of the selected parts**, based on the following methodology:

1. Selection of datapoints and the boundary of the region to be connected.
2. Fitting of a TPS surface to interpolate the regions where no data points are available, i.e. in between the edges of the parts, to be connected. This requires a transformation of the original coordinate basis to the basis of principal directions.
3. Triangulate the surface lying in between the region's boundary.

This methodology is covered in depth in Chapter 3.

2.5.3 Registration of datasets

The concept of registering the datasets is based on matching landmarks.

Linear transformation and homogeneous coordinates Homogeneous coordinates are a powerful concept to describe a set of linear transformations [103]. Translation, rotation, scaling, perspective projection and any possible combination can thus be represented in a single transformation matrix. With homogeneous coordinates, 3D coordinates are extended with a fourth coordinate of value α yielding the 4D vector:

$$\mathbf{x} = \begin{bmatrix} \alpha x & \alpha y & \alpha z & \alpha \end{bmatrix} \tag{2.15}$$

Thus the original 3D coordinates can be derived from the homogeneous coordinates by dividing the first three components by the fourth. In general a coordinate transformation can be represented as:

$$\mathbf{x}' = \mathbf{A}\mathbf{x} \tag{2.16}$$

where $\mathbf{x}$ is a vector of original coordinates, $\mathbf{x}'$ is a vector of transformed coordinates and $\mathbf{A}$ is a general transformation matrix consisting of a concatenation of simpler matrices that perform the elementary transformations of translation, scaling, rotation and perspective projection.

Least squares solution The landmark sets of the two datasets (objects) to be registered are supposed to coincide. However, the transformation, which includes rotation, translation and scaling requires 12 parameters. Since the number of landmarks can be anything >= 3, a least squares solution is required. We wish to transform the landmarks of dataset 2 to approximately coincide with the landmarks of dataset 1. The following set of equations represents the solution:

$$\underset{4\times n}{\begin{bmatrix} \hat{x}_{2,1} & \hat{y}_{2,1} & \hat{z}_{2,1} & 1 \\ \dots & \dots & \dots & 1 \\ \hat{x}_{2,i} & \hat{y}_{2,i} & \hat{z}_{2,i} & 1 \\ \dots & \dots & \dots & 1 \\ \hat{x}_{2,n} & \hat{y}_{2,n} & \hat{z}_{2,n} & 1 \end{bmatrix}^T} = \underset{4\times 4}{\begin{bmatrix} a_{11} & a_{12} & a_{13} & a_{14} \\ a_{21} & a_{22} & a_{23} & a_{24} \\ a_{31} & a_{32} & a_{33} & a_{34} \\ a_{41} & a_{42} & a_{43} & a_{44} \end{bmatrix}} \underset{4\times n}{\begin{bmatrix} x_{2,1} & \dots & x_{2,i} & \dots & x_{2,n} \\ y_{2,1} & \dots & y_{2,i} & \dots & y_{2,n} \\ z_{2,1} & \dots & z_{2,i} & \dots & z_{2,n} \\ 1 & 1 & 1 & 1 & 1 \end{bmatrix}} \tag{2.17}$$

and in matrix notation:

$$\hat{\mathbf{X}}_2^T = \mathbf{A}{\mathbf{X}_2}^T \tag{2.18}$$

where the matrix $\hat{\mathbf{X}}_2$ contains the estimated coordinates of the landmarks of the first dataset, the matrix $\mathbf{A}$ is the general transformation matrix and the matrix $\mathbf{X}_2$ contains the true coordinates of the landmarks of the second dataset. The least squares condition aims to minimise the error between the estimated coordinates of dataset 2 and the real coordinates of landmarks of dataset 1:

$$\frac{dE}{d\mathbf{A}} = \frac{d}{d\mathbf{A}}(\hat{\mathbf{X}}_2 - \mathbf{X}_1)(\hat{\mathbf{X}}_2 - \mathbf{X}_1)^T = 0 \tag{2.19}$$

where the squared error, $E = (\hat{\mathbf{X}}_2 - \mathbf{X}_1)(\hat{\mathbf{X}}_2 - \mathbf{X}_1)^T$.
Working out Equation 2.19 with substitution of Equation 2.18 yields the solution:

$$\mathbf{A}^T = ({\mathbf{X}_2}^T\mathbf{X}_2)^{-1}{\mathbf{X}_2}^T\mathbf{X}_1 \tag{2.20}$$

where the expression $({\mathbf{X}_2}^T\mathbf{X}_2)^{-1}{\mathbf{X}_2}^T$ is known as the pseudo-inverse.

Results After careful consideration, based on the noise factors as shown in Figure 2.12, two datasets were selected. Several trials were performed with

landmark	x_{res}	y_{res}	z_{res}
1	0.2019	0.1233	-1.2954
2	-0.1424	-0.0566	0.9915
3	0.4897	1.2442	-0.7115
4	-0.5660	-1.4431	0.8096
5	-0.3728	-1.2688	-0.2851
6	0.3896	1.4010	0.4908

Table 2.1: Residuals (mm.) of six landmarks (see Figure 2.13a) used for registration of datasets 1 and 2.

a varying selection of 25 available landmarks before a satisfactory match of the two selected datasets was found. Some important factors for successful matching are:

- A small set of accurate landmarks is preferred over a large set with a significant number of relatively inaccurate landmarks.
- Landmarks should be distributed across the object and not localised. This is in accordance with the previous item: a large number of localised landmarks is useless.
- The sum squared error does not always reflect the goodness of fit, e.g. when one landmark is more accurate than the others the overall error could be low, but since the fit is biased towards the particular landmark, the overall fit is not optimal.

The final set contained just six landmarks (see Figure 2.13a) which, after solving Equation 2.20, yielded the transformation matrix:

$$\mathbf{A}^T = \begin{bmatrix} -0.9734 & -0.1073 & -0.1901 & 0.0000 \\ 0.1905 & 0.0033 & -0.9466 & 0.0000 \\ 0.1388 & -0.9798 & 0.0391 & 0.0000 \\ 13.3588 & 33.7066 & -26.3516 & 1.0000 \end{bmatrix} \tag{2.21}$$

The most significant operation was translation as can be seen from the bottom row of $\mathbf{A}^T$. Scaling appeared to be small which is not surprising considering the fact that properly laser-scanned objects should not display major discrepancies in size and shape. Table 2.1 displays the residuals for each landmark.

A further refinement by user-interaction using the *immtk* software yields the final result of the registration as shown in Figures 2.13.

(a) Lateral view: landmarks 1-6 (odd = lhs, even = rhs).

(b) Anterior view: the blue patches at the rhs near the orbit is noise.

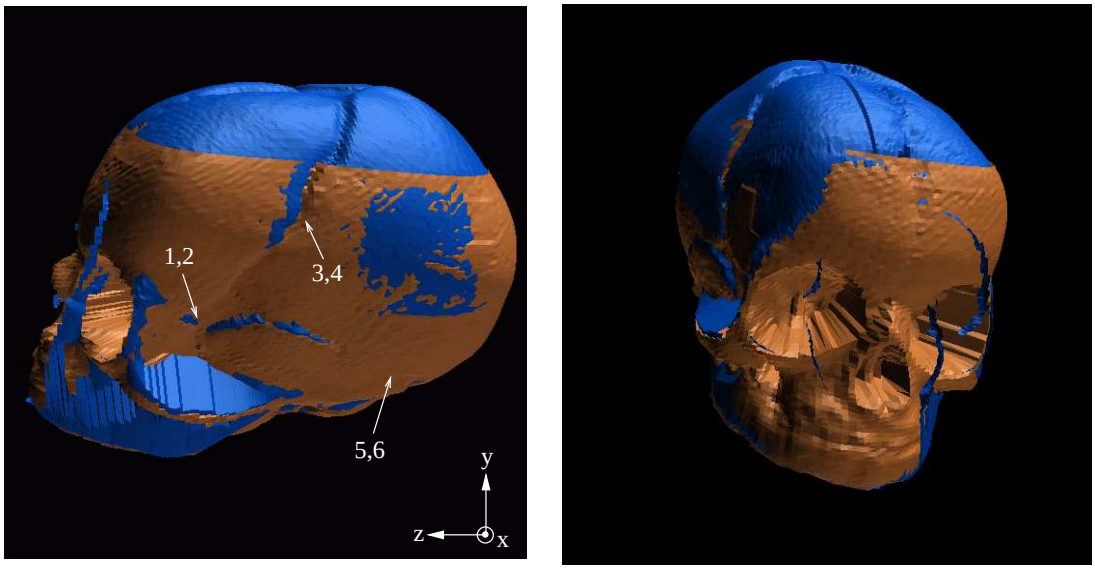

(c) Top-posterior view: perfect match of the sagittal suture of both datasets.

(d) Bottom view: the blue structure, is the base of the skull.

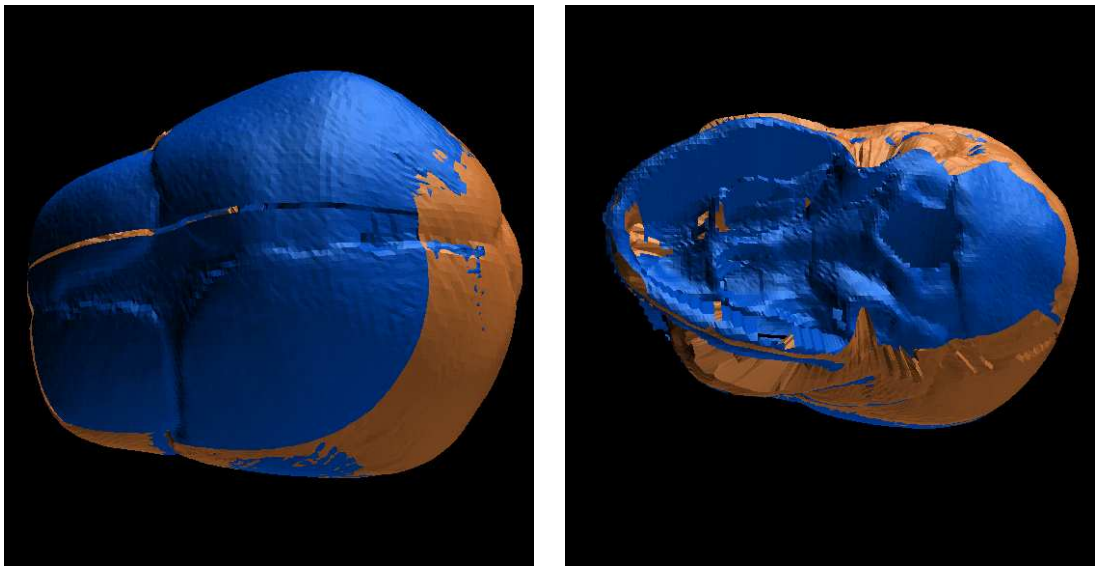

Figure 2.13: Registered datasets: *brown* colour = dataset 1; *blue* colour = dataset 2. Six landmarks were used to register the datasets. Dataset 1 was scanned about the y-axis. Dataset 2 was scanned about the z-axis.

2.5.4 Assembly of relevant parts

We have shown in the previous section how the different datasets can be registered. The selection of relevant parts can be easily done now using the cut-plane option in the *immtk* software. Figure 2.14a shows the mesh of the registered but unconnected skull.

2.5.5 Connection of relevant parts into a single, valid mesh model

The technique to arrive at a valid geometry of the foetal skull is based on TPS interpolation of the unconnected parts. A region across disconnected parts is selected using the *immtk* software. The interior vertices are used to fit the spline surface. The interior region is then re-triangulated according to a user-set triangle size. This technique is described in depth in Section 3.3. Figure 2.14b shows the final mesh model. Figures 2.15 and 2.16 show left lateral and top views respectively, of the original foetal skull and the reconstructed computerised model.

(a) Unconnected, raw mesh model. (b) Final mesh model.

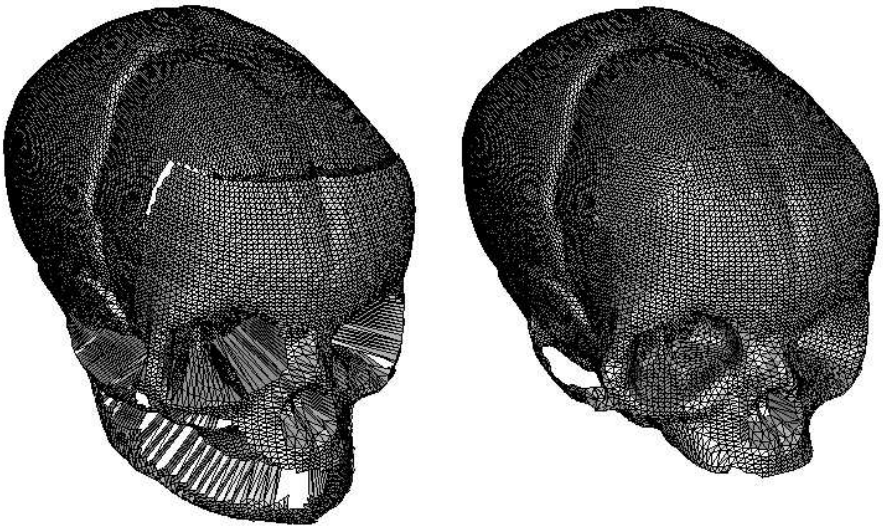

Figure 2.14: Skull models before and after surface interpolation and remeshing.

2.5.6 Discussion

As Figures 2.15 and 2.16 show, the result of the shape reconstruction is successful. Note that the mandible was left out in the computerised model since it is not a fixed part of the cranium and is unlikely to contribute to the moulding

(a) Original foetal skull model.

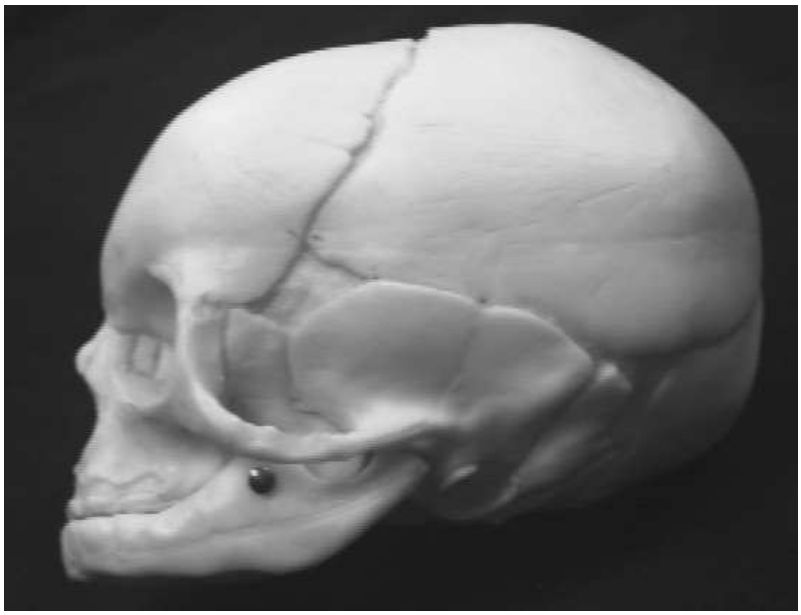

(b) Computerised, reconstructed model.

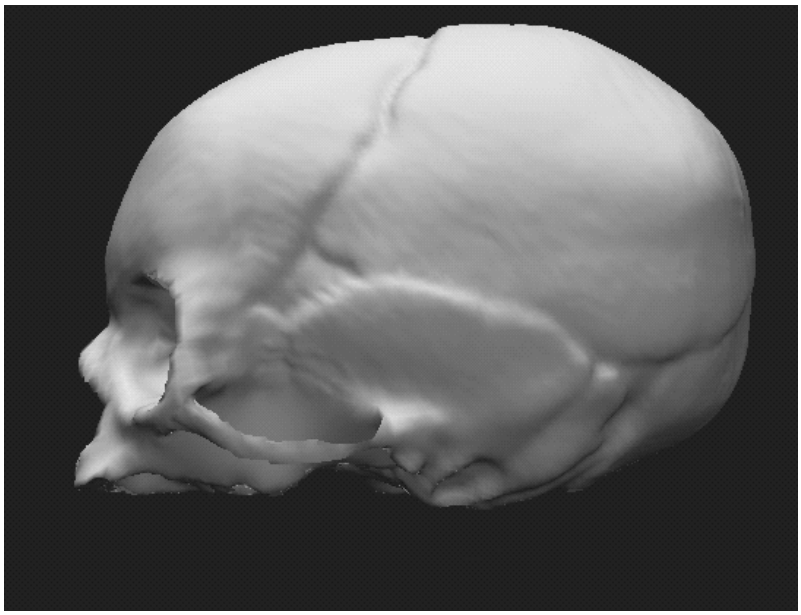

Figure 2.15: Left lateral view of the original and the computerised reconstructed foetal skull model. The image of the original model was captured by a HITACHI KP-180 camera. The image of the computerised model was rendered using the Geomview 1.6.1 software [84]. Note that the mandible is missing in the computerised model.

of the foetal skull. The zygomatic bone was reconstructed using thick shell elements to simulate its thickness because datapoints on the inside of the bone could not be acquired with the laser scanner. The parts underneath the zygomatic bone and mandible were inaccessible as well and were TPS interpolated. After reconstruction, the skull model was rescaled to average size, based on the average value of the biparietal diameter, BPD, and the occipito-frontal diameter, OFD, of a term foetus as reported in [37].

2.6 Summary

In this chapter, two methodologies to recover the shape of a foetal skull, were outlined. Both techniques provide a surface model rather than a solid model. This limitation is justified as the bones of the cranial vault of the skull are thin as compared to their surface dimensions, hence the skull can be modelled as a shell-based object. The first technique illustrated the warping from a 3D adult skull to the shape of a foetal skull. Since this technique cannot recover the fontanelles and sutures, the latter were mapped onto the model after warping. The resulting model was named foetal skull model I. Despite a successful result in terms of the recovery of the surface, foetal skull model I did not possess the embedded configuration of the fontanelles and sutures. Therefore, it was eventually replaced by a model obtained from laser-scanning a replica model of a real foetal skull. This model was named foetal skull model II and will be further used for the analysis of deformation of the foetal skull, subjected to labour forces.

(a) Original foetal skull model. (b) Computerised, reconstructed model.

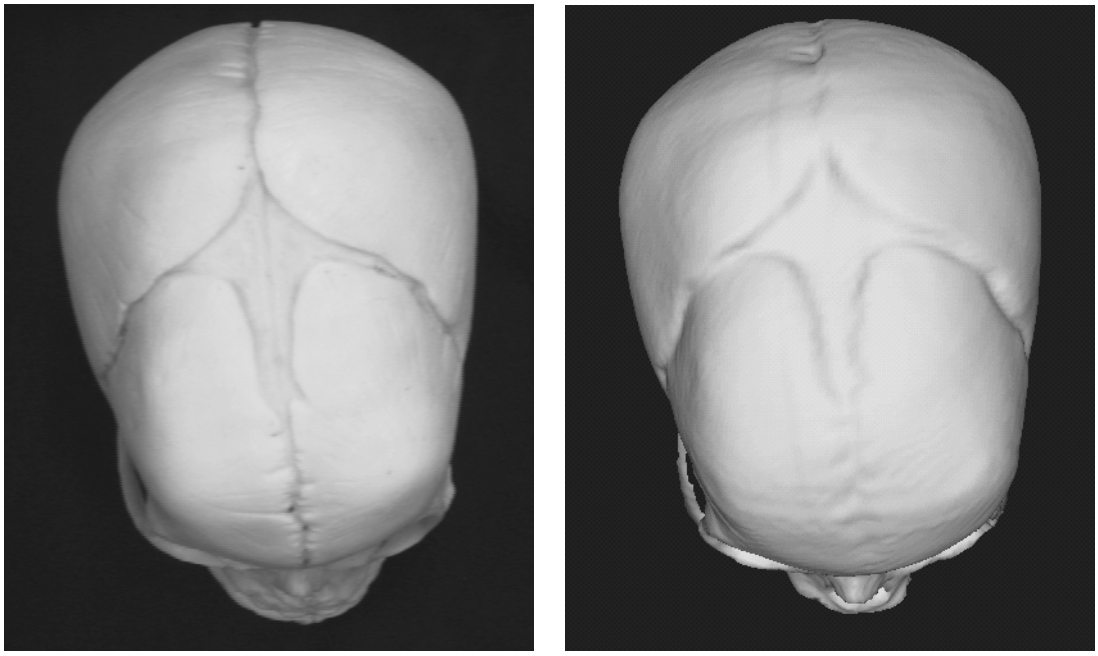

Figure 2.16: Top view of the original and the computerised reconstructed foetal skull model. The image of the original model was captured by a HITACHI KP-180 camera. The image of the computerised model was rendered using the Geomview 1.6.1 software. Note that the mandible is missing in the computerised model (lower part of the image).

Chapter 3

Mesh generation and optimisation

Once the shape of the OOI is determined in 3D space, the next step involves the creation of a mesh model for finite element analysis (FEA).
Elements of different shape are commonly used in FEA. For surface models, the conventional shapes are triangular or quadrilateral. The triangular element is preferred for models of arbitrary, complex shape such as the foetal skull, because it ensures the generation of compatible meshes without violating the geometry. Therefore, in the further course of this work, only triangular elements will be considered.
In Section 3.1 some important properties, related to optimal mesh creation for FE analysis, are covered. These include mesh compatibility, aspect ratio (ar), angular distortion (ad), element size and structure.
In Section 3.2, the advancing front (AF) principle for FE mesh generation is briefly discussed.
In Section 3.3, I suggest a combination of algorithms which allow us:

1. To interpolate missing parts of a surface.
2. To create meshes of arbitrary complexity.
3. To optimise meshes in terms of ar and ad.

3.1 Properties for optimal finite element (FE) mesh creation

The properties discussed in this section are important to guarantee that the FEA yields accurate results. In this chapter, we discuss these properties from

(a) False connection of three first-order elements.

(b) False connection of two first-order elements to a second-order element.

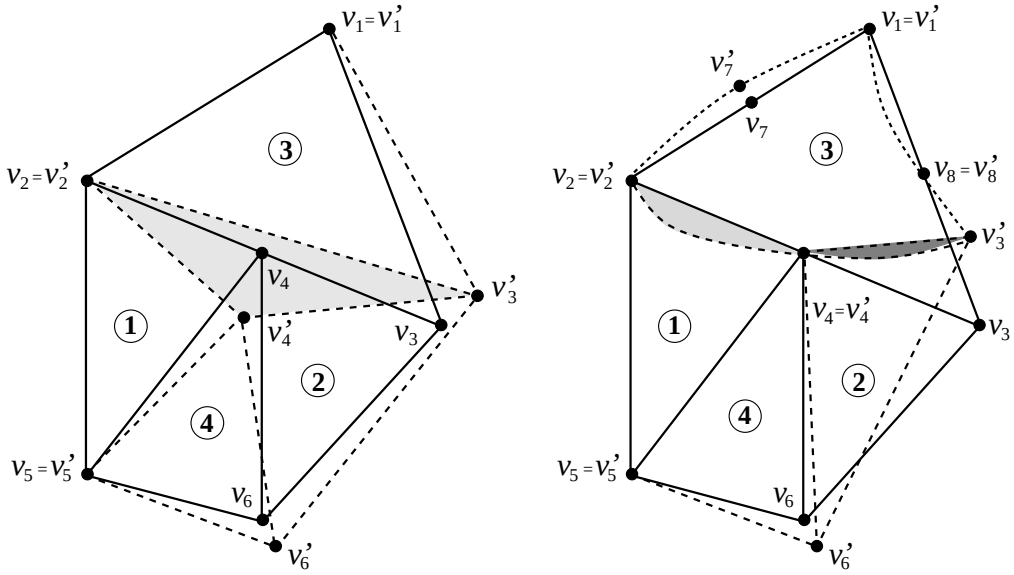

Figure 3.1: Incompatible mesh connections. The deformed mesh is represented by dashed lines.

a geometrical point of view. The theoretical explanation as to why they have to fulfil certain criteria is covered in Chapter 4.

3.1.1 Mesh compatibility

Mesh compatibility is a concept which is related to the order of the shape deformation modes of the element. Figure 3.1 shows two examples of incompatible element connections. In Figure 3.1a, the elements are all first-order. The initially co-linear edges v_2v_4 and v_4v_3 of elements 1 and 2 respectively, are connected to the single edge v_2v_3 of element 3. Since vertex v_4 is not connected to edge v_2v_3, a gap such as $\triangle v_2'v_4'v_3'$ in Figure 3.1a, or overlap, can result after deformation. In Figure 3.1b, the connection involves two first-order elements, 1 and 2, to a second-order element 3. Since the latter exhibits quadratic modes of deformation, even when the common vertex v_4 does not move, gaps or overlaps can occur which are depicted in Figure 3.1b as light-coloured and dark-coloured areas respectively.

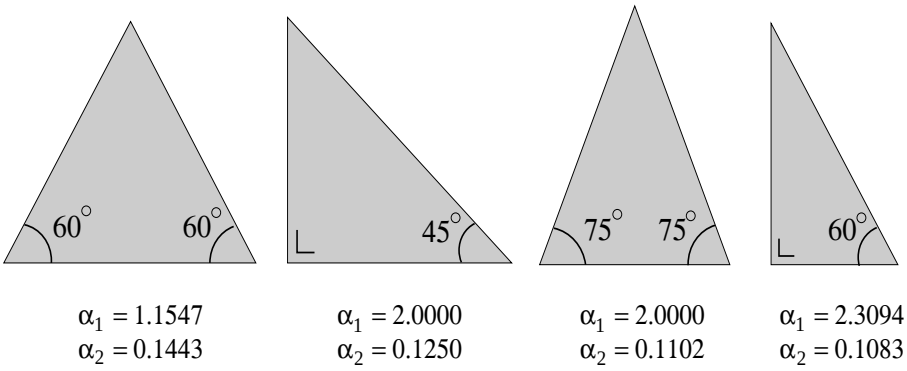

Figure 3.2: Aspect ratios α_1 and α_2 for different shapes of triangles. Note the non-linear relation between α_1 and α_2.

3.1.2 Aspect ratio of a triangle

Two distinct definitions of the aspect ratio, ar, of a triangle are commonly used. The first definition relates the length of the longest side to the shortest height (which is perpendicular to that side):

$$\alpha_1 = \frac{\max |\overrightarrow{v_i v_j}|}{\min |\overrightarrow{v_k m_{ij}}|} \tag{3.1}$$

where

v_i, v_j, v_k are distinct vertices of the triangle with $i \neq j \neq k$,
m_{ij} is a point on the edge $v_i v_j$.

The second definition relates the area of the triangle to the sum of squares of the edge lengths:

$$\alpha_2 = \frac{\frac{1}{2}(\overrightarrow{v_1 v_2} \times \overrightarrow{v_1 v_3})}{|\overrightarrow{v_1 v_2}|^2 + |\overrightarrow{v_2 v_3}|^2 + |\overrightarrow{v_1 v_3}|^2} \tag{3.2}$$

where v_i is a triangle vertex.
Figure 3.2 shows the values of α_1 and α_2 for an equilateral triangle, a right-angled isosceles triangle, an isosceles triangle with top angle of 30° and a right-angled triangle with corner angle of 60°.

The optimum value of the aspect ratio is found for the equilateral triangle. For triangles of degrading aspect ratio, α_2 decreases whilst α_1 increases.
Triangles with bad ar can be categorised as[1]:

Type *I* Right-angled triangles (with long base, short upwards edge and long hypotenuse).

[1] Arbitrary triangles of bad ar can be categorised as a combination of one of these.

Table 3.1: Values of α_1 and α_2 for triangles of Type *I* and *II*. Column 4 gives the ratio of α_1 with the optimal *ar*, i.e. for an equilateral triangle. Columns 6,8 give a similar (but inverse) ratio for α_2. Note that α_1 does not differ for Types *I* and *II* since base and height are used as a reference.

base	height	Type *I*,*II*		Type *I*		Type *II*	
		α_1	α_1-ratio	α_2	α_2-ratio	α_2	α_2-ratio
5	1	5	4.33	0.0481	3.00	0.0633	2.28
10	1	10	8.66	0.0248	5.83	0.0329	4.39
20	1	20	17.32	0.0125	11.57	0.0166	8.69
50	1	50	43.30	0.0050	28.87	0.0067	21.66
100	1	100	86.60	0.0025	57.73	0.0033	43.30

Type *II* Isosceles triangles with one obtuse angle.

Type *III* Isosceles triangles with one sharp angle (and two long edges).

Table 3.1 shows values of α_1 and α_2 for triangles of Type *I* and Type *II* respectively[2].

Although both values are equally valid as a measure for the *ar*, the increasing trend of α_1 for increasing distortion and the corresponding integer representation makes it slightly more favoured than α_2. It is also more commonly used in the FE community. In the further course of this chapter we will use α_1 as a measure of *ar*.

It is not straightforward to define an upper bound of the *ar* for which numerical errors are still within reasonable limits. NAFEMS [76] advises: $\alpha_1 \leq 4$.

3.1.3 Angular distortion

The angular distortion, *ad*, of a triangle is directly related to the aspect ratio α_1. Some finite element packages use this measure as an alternative to α_1 to assess the shape distortion of a triangle. A typical threshold in the ABAQUS FE software, used as a warning for angular distortion of the mesh, is an angle less than 45°. If we consider the guidance by NAFEMS [76] of a maximum *ar* of 4, the minimum allowable angle for a right-angled triangle would be 14°! Thus, 45° seems a rather strict criterion but taking into account that this is issued as a warning and not as an error, it is left to the user to decide whether particular distortions are acceptable or not.

[2]Note that Type *III* triangles tend to become Type *I* triangles as distortion increases.

3.1.4 Triangle size

The size of a triangle in the mesh is obviously an important property. The theoretical arguments for mesh refinement are discussed in Section 4.3.3. Here, we focus on the uniformity of triangle sizes across the mesh rather than their actual sizes.

If we assume that the area A_u of a triangle is an upper bound to the accurate representation of the geometry, then any triangle with area $A_i > A_u$ should be refined until the criterion $A_j \leq A_u$ is reached, where triangles with index j are created from a restricted neighbourhood of the original triangle i.

3.1.5 Structure of the mesh

Meshes which are directionally sensitive, such as the example as shown in Figure 3.3a, should be avoided. For regular meshes the *union jack* motif as shown in Figure 3.3b is preferred. The following example from [76] illustrates why. Assume the dark-coloured triangles in Figure 3.3a are subjected to a pure bending field. If the upper triangle is in horizontal tension then the lower triangle will be in horizontal compression, hence opposite Poisson contractions in the vertical direction result. The problem is alleviated by the combination of two inversely oriented triangles (dark-coloured triangles in Figure 3.3b). A drawback of the mesh with *union-jack* motif is the increase of *bandwidth*[3]. However, state of the art FE packages apply a *wavefront minimisation* algorithm [8, 19] to alleviate this problem. Note that for an *unstructured* mesh or even an 'ideal' mesh consisting solely of equilateral triangles, some degree of directional bias exists when the mesh is not sufficiently refined.

3.1.6 Mesh evaluation

To evaluate the quality and uniformity of a mesh we can:

- Calculate mesh statistics of a mesh quality indicator, *mqi*, e.g. the aspect ratio *ar*.
- Report those elements, exceeding a pre-set threshold of a *mqi*.

Mesh statistics are useful to compare the overall quality of a mesh and can typically be used to evaluate an optimisation strategy. An overall approach such as a histogram is preferred, rather than reporting single statistics which

[3]The bandwidth of a symmetric $m \times m$ matrix $\mathbf{A}$, e.g. the stiffness matrix of a FE structure, is $2w + 1$, if an element $a_{ij} = 0$, for all $j \geq i + w$ (upper triangle) and all $j \leq i + w$ (lower triangle) with $1 \leq i, j \leq m$.

(a) Directionally sensitive mesh pattern. (b) *Union jack* mesh pattern.

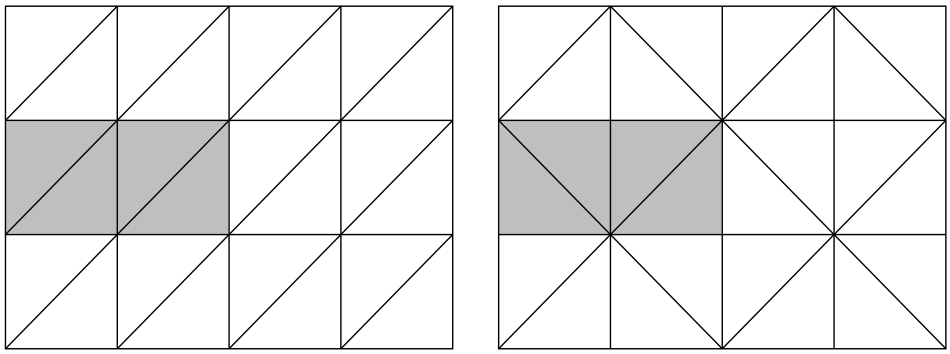

Figure 3.3: Structure of the mesh.

can be misleading. Mesh statistics are however not sufficient to decide whether a mesh is 'fit' for analysis. This has to be based on a criterion, involving the specification of one or more thresholds of a particular *mqi*. For example all the elements with *ar*, exceeding threshold t_1 are reported, whilst elements with *ar* exceeding threshold t_2, where $t_2 >> t_1$, cannot be accepted. In most software packages, the above distinction is characterised by *warning* messages as opposed to *error* messages during the pre-processing phase. A warning message on an *ar*, exceeding a pre-set threshold, will prompt the user to check the element and optimise if deemed necessary. An error message will stop execution and will force the user to adapt the element to satisfy the *ar* criterion.

3.2 The advancing front triangulation for FE mesh creation.

The advancing front (AF) principle was originally developed by Lo in 1985 [62] and has since widely been used in algorithms for FE mesh generation and adaptation.
The principle of an AF is simple (See Figure 3.4):

1. The initial front is the boundary, Γ, surrounding the region of interest (ROI), Λ, to be triangulated. The boundary, Γ, is a closed contour or polygon, consisting of connected vertices. The ROI, Λ, contains the interior nodes.

2. We travel around the boundary in counter-clockwise direction. This implies that points on the lhs of Γ will lie inside the ROI and points on the rhs will lie outside the ROI. This convention is also valid for multiply connected domains.

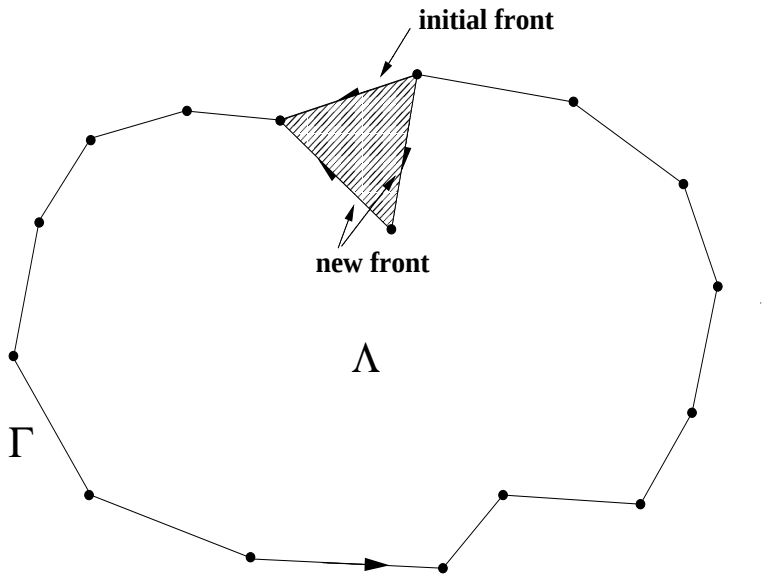

Figure 3.4: Advancing front triangulation: the edge of the initial front is replaced by the new edges of the newly created triangle.

3. We start at an initial edge of the front and connect it to either:

   - a vertex of the boundary, Γ, or
   - a point of the region, Λ.

   The selection is based on a criterion. Lo uses the Euclidean distance and chooses the nearest neighbouring point or alternatively the two nearest neighbours, selecting the triangle with the best ar.

4. If a suitable point is found, the front is updated by removing the original edge and replacing it with the newly created edge(s) of the new triangle. In other words, the newly created triangle lies outside the new front now and is ignored for further processing.

5. We move up one vertex in the front (in counter-clockwise direction) and start the procedure all over again until the front is empty of vertices (edges).

The AF method has become the basis of most meshing algorithms currently used in commercial mesh-modelling software packages.
A directly descended and currently popular approach is adaptive remeshing, originally developed by Peraire et al. [82]. It is based on the AF principle and provides the ability to remesh the model during the analysis. Remeshing is based on the error variation of the variable of interest. If the errors in a region are large compared to some average or minimum value then the region

is refined. Conversely, when the error is small, the region can be made coarser. The advantage of adaptive remeshing is that it saves computational costs by refining the mesh only in those regions where deemed necessary, hence avoiding overall refinement which leads to over-complex meshes.

3.3 A front-based triangulation algorithm for surface interpolation

In the previous section, we did not outline how points in the region, Λ, inside the boundary, Γ, can be created. These internal points or nodes should fulfill the following criteria:

- They should be distributed over the ROI with a density based on the (average) distance between boundary nodes.
- The distances of the internal nodes to the boundary nodes has to be sufficient to avoid excessively small triangles and triangles of bad *ar* near the boundary.

Lo [62] uses a scan-line approach whereby horizontal lines are scanned across Λ to determine the parts inside and outside the boundary, Γ. Nodes are distributed across a line segment inside the valid regions at equal distances, the latter determined by a pre-specified average size of an element. Nodes which are too close to Γ, or to other internal nodes, are omitted. The scan line approach is possibly the best solution for multiply connected regions but the even distribution of points becomes awkward for rather complex boundaries. The method implicitly yields triangles of reasonable size and *ar* but these crucial parameters are not under control. Furthermore, the original algorithm was developed for planar regions.

Controlling the aspect ratio and size parameters during triangulation through specification of valid ranges is desirable but results into instabilities. An algorithm, using this control strategy, is likely to get stuck when no candidate nodes satisfy the constraints.
The set of algorithms which are outlined in this section were developed to solve two problems which occur during the shape/mesh generation of the models to be analysed:

- Interpolation of missing data, a problem which was typical for foetal skull model *II*, obtained from laser-scan data (Section 2.5).
- Generation of meshes with an arbitrary number of elements (a property

which will appear to be useful for the parietal bone test as described in Chapter 6).

The algorithms are restricted to simply connected level-surfaces where the level coordinate z can be represented as a function of x and y: $z = f(x, y)$. Rather than applying the scan-line approach to determine interior nodes, we assume a square grid covering the x-y plane. This idea was tried out earlier by Shaw and Pitchen [92] and Lo [62] but no satisfactory solution to the connection of internally generated triangles to the outer boundary, Γ, was found to satisfy the following conditions [62]:

Condition 1 Minimisation of the processing time spent in testing squares of the grid which are outside the bounded region, Λ.

Condition 2 To ensure that every node generated should lie in the remainder of the region (i.e. the region which has not been covered yet) and well away from existing nodes.

Not being able to find a solution to satisfy these conditions Lo [62] stated:

'In order to tackle domains with irregular boundaries and openings efficiently, the concept of superimposing a rectangular grid has to be abandoned completely.'

Contrary to Lo's claim, I will show that a grid-based approach is feasible including the following features:

- Algorithms of $O(n)$ complexity which thus satisfy Condition 1.
- Satisfying Condition 2 by:
  - Using the *invariant* that generation of interior nodes cannot happen outside the boundary.
  - Specifying a parameter which controls the distance of interior nodes to the boundary nodes.
- Level-surface ($2\frac{1}{2}$D) triangulation as opposed to planar (2D) triangulation.
- The ability to interpolate missing data.
- The ability of arbitrary mesh refinement.

The approach involves the following steps:

1. TPS interpolation is performed on the surface patch.
2. The selected patch (possibly from a larger object and limited by an external boundary) is rotated to its principal axes.
3. Triangles are grown from the centre of the surface towards the surface boundary, creating an internal mesh. The algorithm stops when this internal mesh cannot grow any further without triangles penetrating the surface boundary.
4. The internal mesh yields an internal boundary. This internal boundary is connected to the surface boundary with the *welding* algorithm.

3.3.1 Thin-plate spline (TPS) interpolation

We have discussed the thin-plate spline function in Section 2.4.3 to warp homologous objects. The radial basis function will be used again, though in a different form, suitable for interpolation of a level surface:

$$z = f(x, y) = -U(r) = -r^2 \log(r^2) \tag{3.3}$$

where the coefficient of the radial basis function

$$r = \sqrt{(x^2 + y^2)} \tag{3.4}$$

The matrix $\mathbf{C}$ of which each coefficient is the Euclidean distance between two datapoints, processed through the radial basis function was specified in Equation 2.5.
The linear transformation matrix for n datapoints is specified as:

$$\mathbf{A} = \begin{bmatrix} 1 & x_1 & y_1 \\ ... & ... & ... \\ 1 & x_i & y_i \\ ... & ... & ... \\ 1 & x_n & y_n \end{bmatrix} \tag{3.5}$$

The vector of level points:

$$\mathbf{z} = \begin{bmatrix} z_1 & ... & z_i & ... & z_n & 0 & 0 & 0 \end{bmatrix}^T \tag{3.6}$$

The vector of spline parameters:

$$\mathbf{r} = \begin{bmatrix} w_1 & ... & w_i & ... & w_n \end{bmatrix}^T \tag{3.7}$$

and the linear transformation, $P(x, y) = a_0 + a_1 x + a_2 y$, with parameter vector:

$$\mathbf{a} = \left[\begin{array}{ccc} a_0 & a_1 & a_2 \end{array} \right]^T \tag{3.8}$$

yielding the combined parameter vector:

$$\mathbf{q} = \left[\begin{array}{c} \mathbf{r} \\ \mathbf{a} \end{array} \right] \tag{3.9}$$

Putting $\mathbf{C}$ and $\mathbf{A}$ together yields the $(n+3) \times (n+3)$ matrix:

$$\mathbf{L} = \left[\begin{array}{cc} \mathbf{C} & \mathbf{A} \\ \mathbf{A}^T & \mathbf{0} \end{array} \right] \tag{3.10}$$

with the matrix $\mathbf{0}$ being a 3×3 matrix of zeroes.
The spline parameters can be obtained then from:

$$\begin{aligned} \mathbf{Lq} &= \mathbf{z} \\ \mathbf{q} &= \mathbf{L}^{-1}\mathbf{z} \end{aligned} \tag{3.11}$$

3.3.2 Rotation of the patch to principal axes

Since the interpolated surface is a level surface, i.e. x-y base with dependent variable z, an arbitrary patch or surface in its original coordinate system will need to be transformed into a new base corresponding to the directions of maximum variance of the datapoints. We therefore calculate the principal directions and rotate the patch into its principal base, using the eigenvectors, corresponding to the two largest eigenvalues, as the new x-y base.

3.3.3 The *triangle-growing* algorithm

The suggested algorithm consists of the following steps:

- Find the centre of the boundary, Γ', which is the projection of Γ in the x-y plane.
- Starting from this centre point, create a matrix of boxes which covers the entire domain[4] Λ' and Γ'. The size of the boxes is determined by the user-set variable, μ, which is a fraction[5] of the average edge length, l. The

[4] Λ' is the projection of Λ in the x-y plane.
[5] Conventionally set as $0.5 < \mu < 2$.

corner nodes of the boxes which are inside the region are the candidate nodes for triangulation.

- A queue, consisting of internal nodes to be expanded from the centre outwards to the boundary, is created. The initial node in the queue is the centre node. The *invariant* of the algorithm is that no internal node should be expanded beyond the boundary.
  Starting with the first (current) node in the queue, we expand according to three conditions which ensure that candidate nodes stay a sufficient distance from the boundary:

  C1 If the current node's neighbouring boxes (four) are empty of boundary points, delete the current node from the queue and add its neighbours (maximum eight) to the queue. The current node is accepted for interior triangulation.

  C2 If a neighbouring box contains boundary points, which are at a sufficient distance from the current node, then the current node is accepted for triangulation, but not expanded to the nodes on the vertices of the neighbouring box. The distance by which the current node is allowed to approach the boundary is specified by the user as a fraction, κ, of the box-size $\mu \times l$.

  C3 If at least one neighbouring box contains a boundary point which is too close to the current node, then the current node is not accepted for internal triangulation.

- Note that during the expansion process, *processed* and *invalid* nodes are ignored.

- The algorithm finishes when the queue is empty.

- All accepted nodes in the interior region can now be triangulated in a relatively straightforward fashion.

In Pseudo-code:

Input: → average edge length, l (pre-calculated)
→ user-set box size, μ
→ queue Q, containing centre node, v_c^r
→ a matrix M of boxes of size $\mu \times l$, containing boundary nodes, v^b
→ user-set parameter, κ
Variables: ↔ current node, v_a^r
Output: ← a set of interior nodes, accepted for interior triangulation

```
while Q not empty
    v_a^r ← first node in Q
    if v_a^r is processed or v_a^r is invalid
        continue (while)
    else
        set v_a^r valid
        find the box indices b_i of which v_a^r is the intersection point
        for each b_i (0 < i < 4)
            if M[b_i] contains boundary nodes
                get boundary nodes v_j^b
                for each v_j^b (0 < j < n)
                    if Euclidean distance between v_j^b and v_a^r ≥ κ × μ × l
                        set all neighbouring nodes of v_a^r in b_i invalid
                    else
                        set v_a^r invalid
                        continue (while)
    if v_a^r is valid
        find neighbouring nodes of v_a^r (8) and add them to the end of Q
```

The number of boundary nodes, n, in a box is usually a small number and is in most cases ≤ 1. Note that the last *if* statement is redundant but has been left in for clarity.
After the interior nodes are connected to form a valid interior triangulation, they can be connected to the outer boundary nodes using the *welding* algorithm. This algorithm is described in the next section.
Figures 3.5 a,b,c,d and e illustrate how the *triangle-growing* algorithm operates on a simple example involving an 18-node polygon boundary with elevated centre point (Chinese hat) of which the interior region will be triangulated. In

this example $\mu = 0.95$. *Brown* nodes on the boundary are intersection points with the boxes.

Step (a) The current node (coloured *red*) gets the first node in the queue, which is the centre node. Since the four neighbouring boxes of the current node are empty of boundary points it is expanded into eight neighbouring points (coloured *blue*).

Step (b) The current node (centre node) is accepted for triangulation (coloured *black*). The first node in the queue becomes the current node[6]. Again this node has neighbouring boxes empty of boundary points and is accepted for triangulation and expanded.

Step (c) The remaining seven nodes of the first expansion are all accepted for interior triangulation (coloured *black*). A candidate current node on the lhs has boundary points in boxes 1 and 3. Since the current node is at a sufficient distance of the boundary points it is accepted for triangulation but not expanded[7].

Step (d) The previous current node and the symmetrical right node are accepted for triangulation. The symmetrical top and bottom node are as well (not because of symmetry though!). The node in the upper left corner is now the current node. It contains boundary points in boxes 1,2 and 3 which are too close. The node is rejected for triangulation.

Step (e) The interior triangulation is finished.

Step (f) The internal and external (original) boundaries can be triangulated now with the *welding* algorithm.

3.3.4 The *welding* algorithm

The *welding* algorithm connects or *welds* two closed polygons in space and is based on the advancing-front principle. The algorithm is robust as long as the distance between the boundaries is relatively consistent across the contours and of the same order of magnitude as the lengths of the edges. Besides being used for the second step of the previous method, it can be used independently to connect two patches of an object together.
The *welding* algorithm involves the following basic steps (see Figure 3.5f):

[6]Note that the order of processing nodes has been ignored for ease of illustration.
[7]Nodes outside the region are coloured light-blue.

(a) Centre node expansion (C1 satisfied).

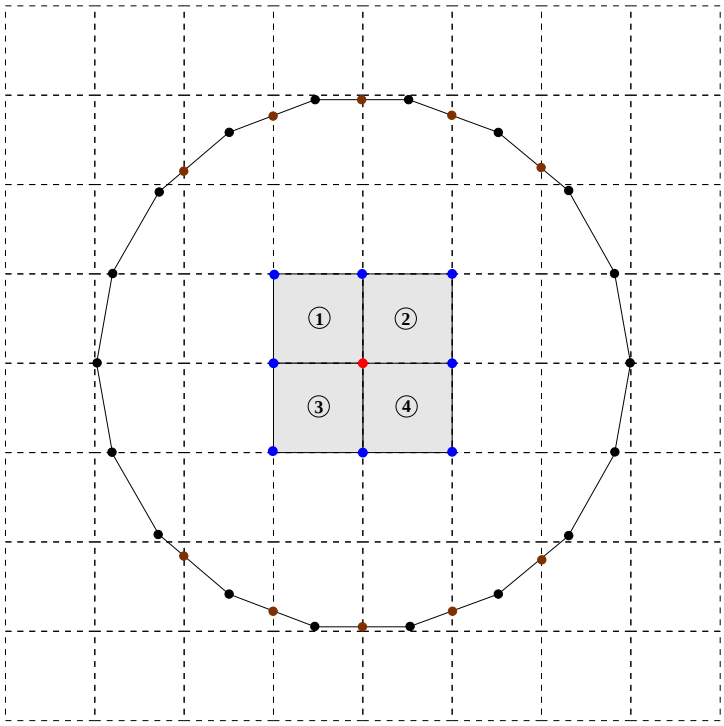

(b) Further expansion (C1 satisfied).

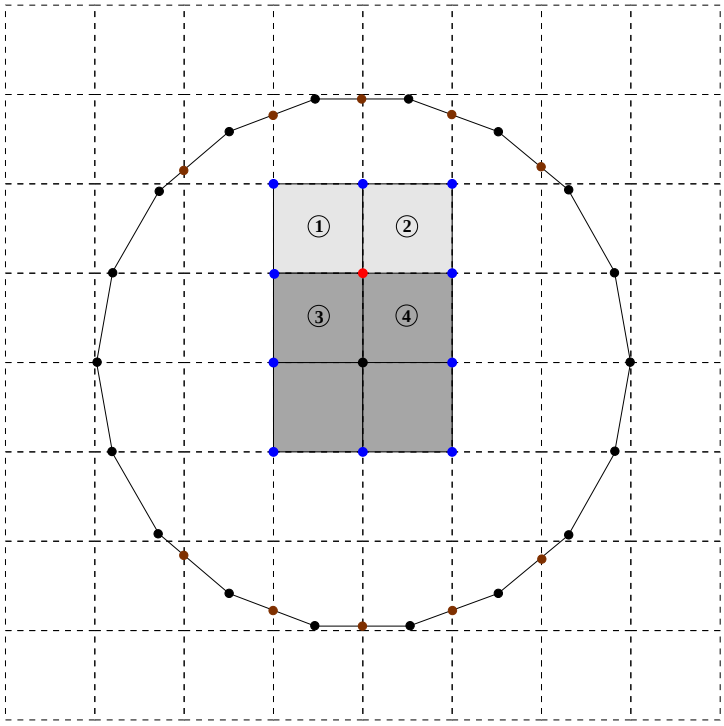

(c) Current node accepted but not expanded (C2).

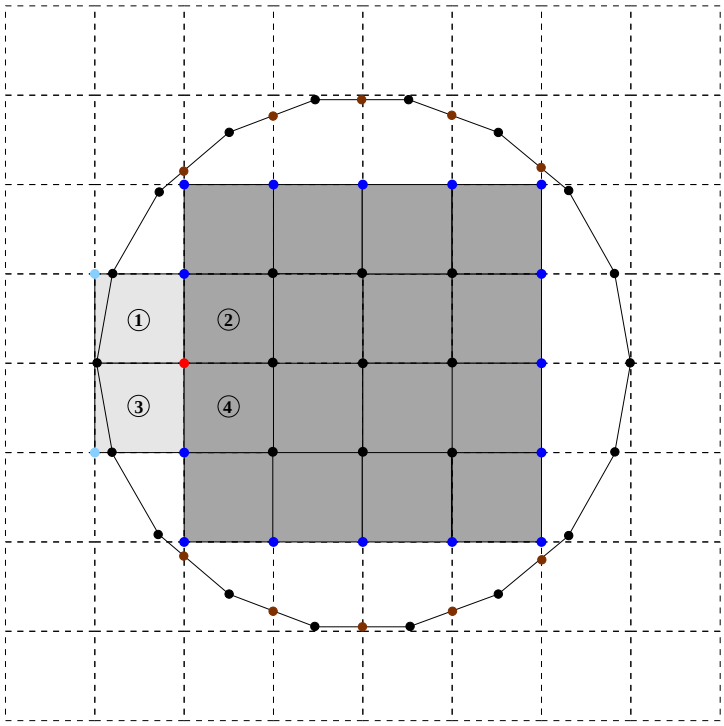

(d) Current node rejected (C3).

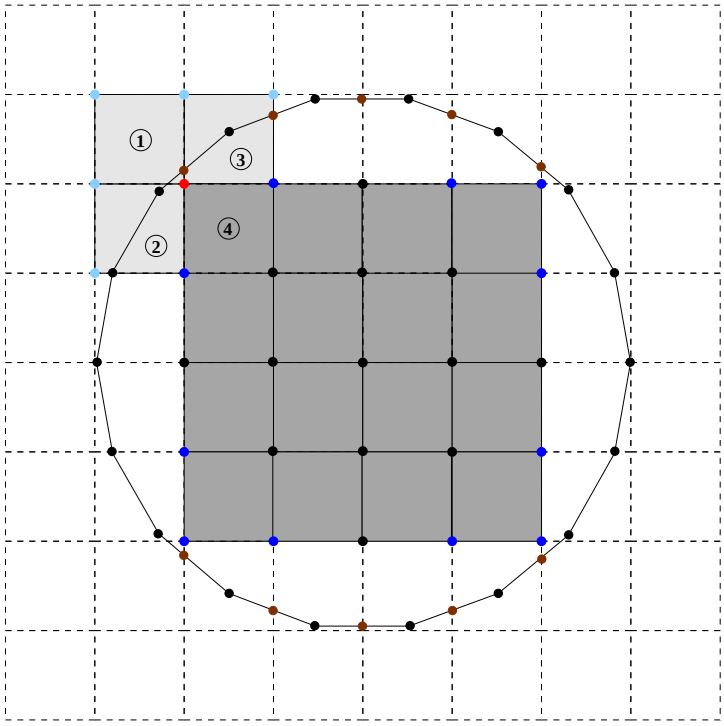

(e) Interior triangulation finished.

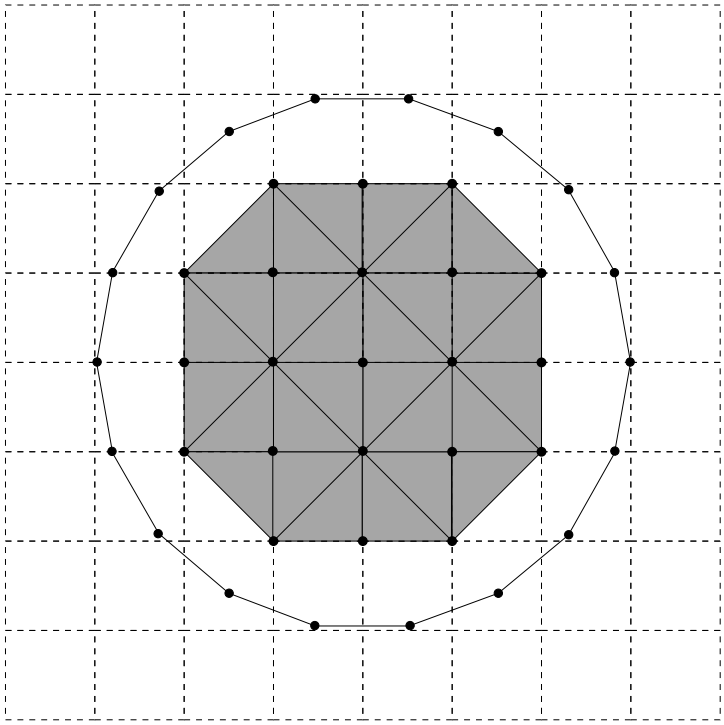

(f) Connecting the boundaries.

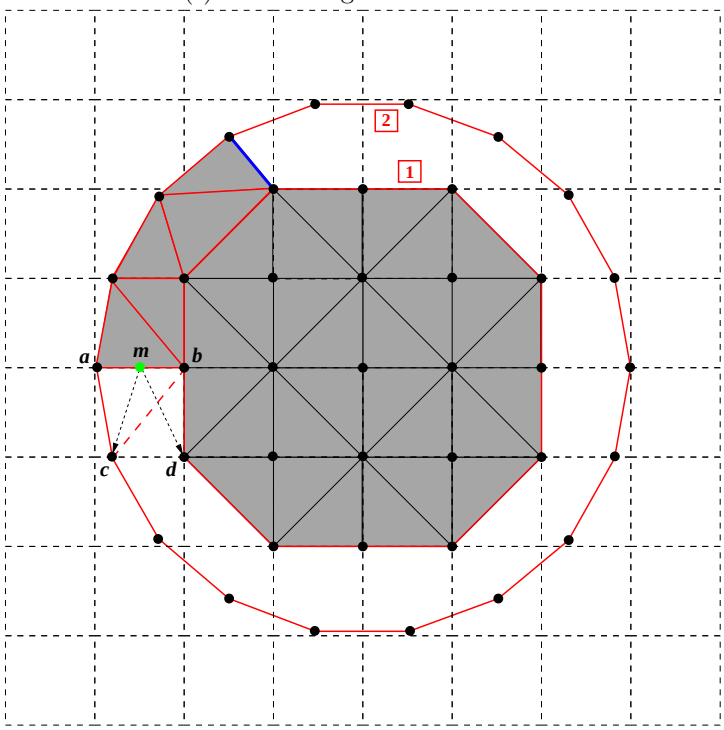

Figure 3.5: Different steps of the *triangle-growing* and *welding* algorithm to triangulate the interior of an 18-node polygon or 'Chinese hat' (see text for explanation).

- Choose an arbitrary initial node on Contour 1.
- Find the node on Contour 2, closest to the initial node of Contour 1.
- The connection of these two nodes is the *initial* leading edge[8] from which the algorithm can be initiated.
- In general, we search the node closest to the midpoint, m, of the current leading edge (nearest neighbour - NN) AND sharing an edge with either a or b. This means that only two candidate nodes, c and d, are considered; one for each contour.
- Since c is closer, we connect it to the node it did not share an edge with (node b in Figure 3.5f).
- Make edge bc the new leading edge of the front.
- Continue until the front is empty of nodes.

Despite its simplicity, the algorithm as it stands is not robust because:

1. Overlapping triangles can be generated, e.g. $\triangle abc$ in Figure 3.6a.
2. *fan*-triangulation can occur: consecutive triangulated nodes all come from the same contour because the node on the opposite contour is remote. Fan-triangulation causes severely disrupted triangles (bad *ar*) and may eventually lead to invalid connections. In Figure 3.6b node b is *starved*, hence fan-triangulation results.

Problem 1 can be solved by consideration of the counter-clockwise convention by which the front moves around the centre C_p (See Figure 3.6a). Nodes are conventionally ordered first on Contour 1, then on Contour 2. Consider the vectors $\vec{v_1}$ and $\vec{v_2}$, where the initial point of both vectors is the candidate node and the endpoints of $\vec{v_1}$ and $\vec{v_2}$ are the nodes of the leading edge, then the cross-product $\vec{v_1} \times \vec{v_2}$ should be positive. On Figure 3.6a, where $\vec{v_1} = \vec{ca}$ and $\vec{v_2} = \vec{cb}$, the cross-product $\vec{ca} \times \vec{cb}$ is clearly negative. The alternative node d should thus be chosen, creating $\triangle abd$ which does satisfy the counter-clockwise condition. Node c is triangulated two steps later through $\triangle aec$.
Problem 2 can be solved by the following condition:

if node v_i of contour $l, l \in [1, 2]$ has not been
updated since n consecutive updates (n is set by the user)

[8] *Blue* edge in Figure 3.5f.

then take node v_i of contour l as the new node to be
connected to the leading edge of the front.

Note that the two conditions to solve problems 1 and 2 overrule the NN condition.

3.3.5 Boundary points and arbitrary mesh refinement

At present, we have assumed that the boundary, Γ, which determines the internal region for triangulation, contains a fixed number of points. The question is whether we can create elements of arbitrary size without changing the configuration of the boundary and if so to what extent? Figure 3.8 shows that we indeed can create elements of varying size by setting the parameters μ and κ. However it is clear that this approach is limited since extreme values of both parameters will yield meshes of bad quality. Therefore, the answer to our question is simple: we do need to alter the configuration of boundary points! In other words, increasing the number of boundary points and correspondingly, the density, will yield finer meshes. Conversely, decreasing the number of boundary points will yield coarser meshes. Just as we used the TPS surface interpolation to preserve the geometry of the surface, we can use spline interpolation to preserve or *estimate* the true geometry of the boundary curve. Since the spline should interpolate the original boundary points, parametric cubic (PC) splines should be used[9]. Once the spline is fitted, a new edge length can be specified and new nodes can be placed on the boundary.

3.3.6 Examples

The following examples illustrate the different properties of the algorithms described in the previous sections.

1. A regular polygon consisting of 18 edges in the x-y plane with raised centre node (one edge length) in the z-direction (Chinese hat). Figure 3.8 shows triangulations using different values of μ and κ.

2. Figure 3.9 shows the left parietal bone of foetal skull model *II*, triangulated at different degrees of mesh refinement.

3. Figure 3.7a and 3.7b show the underlying spline surfaces of the 18-node polygon and parietal bone respectively.

[9]It is shown in [75] that PC splines are a realistic model of a 1-dimensional object (for example a beam) subjected to pure bending.

(a) Overlapping triangle

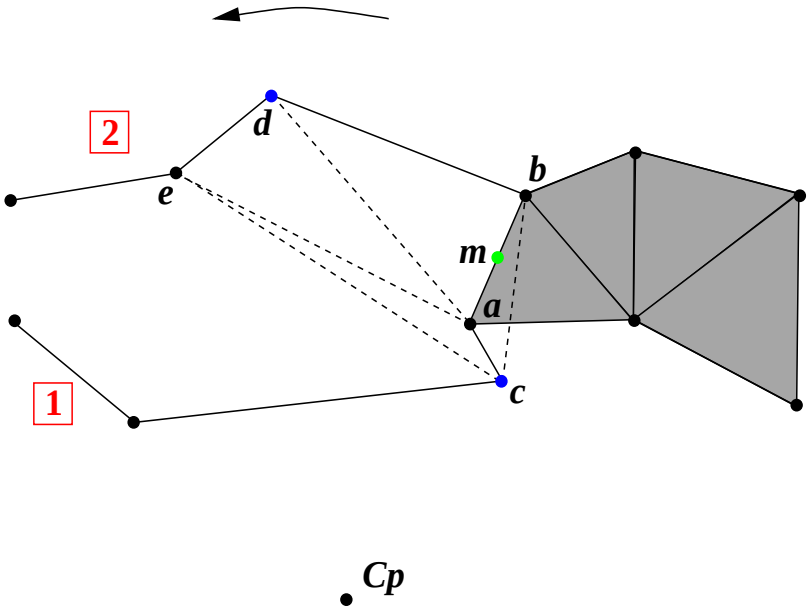

(b) Fan triangulation

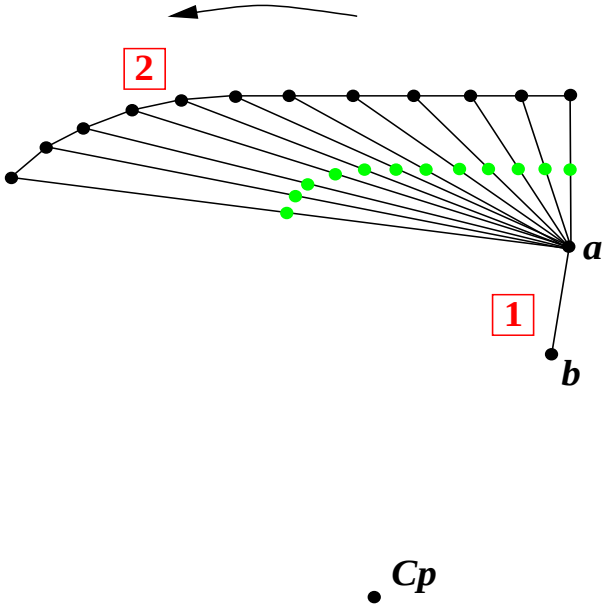

Figure 3.6: Triangulation discrepancies. $\mathbf{C}_p$ is the centre of the external boundary 2. The internal boundary is marked 1. *Green* coloured points are midpoints of edges.

(a) 18-node polygon with elevated centre (Chinese hat).

(b) Left parietal bone of foetal skull model II.

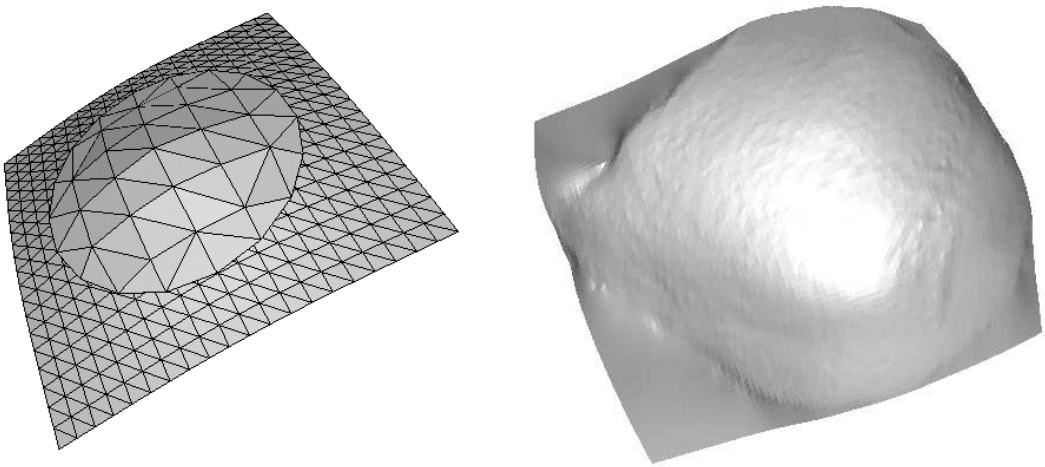

Figure 3.7: Supporting thin-plate spline (TPS) surfaces.

4. A part of a patch from the compound skull from Figure 2.14a as shown in Figure 3.10a is selected. Figure 3.10b shows the result after spline fitting and triangulation.

3.4 Mesh optimisation

Once an initial mesh is created, an optimisation strategy for *mqi*'s such as the aspect ratio (ar), angular distortion (ad) and triangle size as discussed in Section 3.1 can be used. Adaptation of triangle size was covered in the previous section. To improve the ar and the related ad, three techniques are commonly used:

1. Laplacian smoothing: A vertex is moved towards the centre of its surrounding polygon (Figure 3.12). This will generally improve the average ar and ad. The new position of the vertex needs to lie on the surface of the object. This can be dealt with in the following two ways:

   - If the triangulated mesh is part of a level surface, the TPS interpolated surface can be used to reposition the vertices to the centre of their surrounding 3D polygons.
   - If the triangulation is part of a general surface, another way of parametrisation of the surface is required. Since the vertex is only

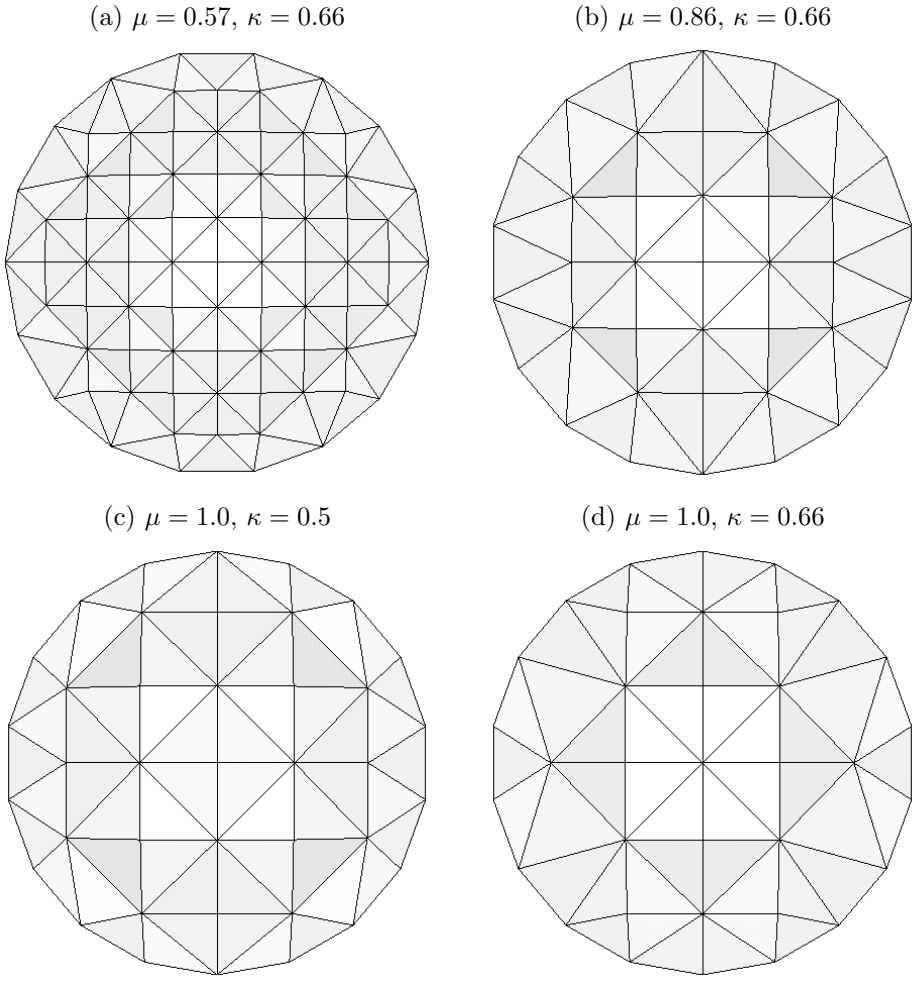

Figure 3.8: Triangulated 3D polygon or 'Chinese hat' with different settings for μ and κ.

moved within the surrounding polygon, a local surface interpolation such as triangular Bezier patches [16, 27], is sufficient.

2. Edge swapping: The common edge shared by two triangles, forming a quadrilateral, is changed to the edge of the two vertices of the quadrilateral which were not previously connected. Figure 3.13 illustrates the technique. Edge swapping can be done automatically but it can be processor intensive for highly refined meshes since each edge needs to be considered. Moreover, one improvement can cancel out a previous one. Since often only a few triangles need to undergo this procedure, we implemented this facility in the *immtk* software. The software has a facility which highlights triangles of bad *ar* or *ad* which can be improved by user-interaction.

(a) Original mesh: 10,537 elements

(b) new mesh: 5,261 elements

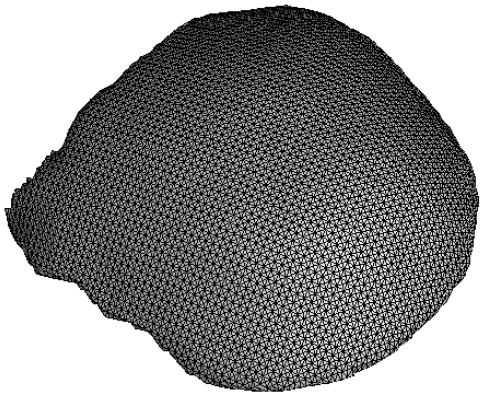

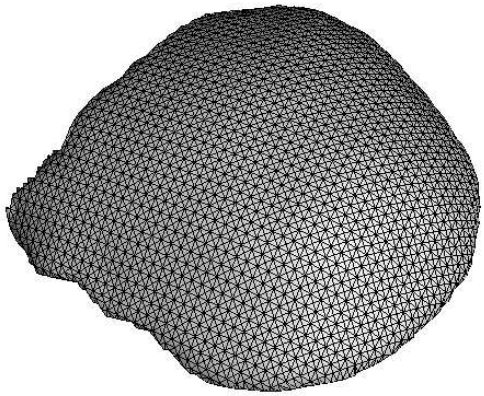

(c) new mesh: 2,604 elements

(d) new mesh: 1,058 elements

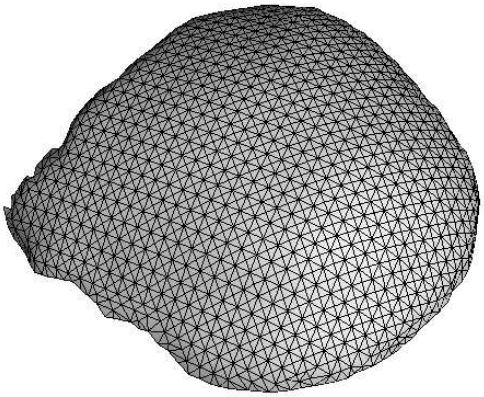

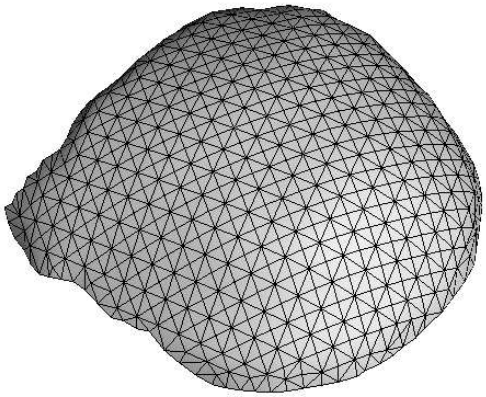

(e) new mesh: 532 elements

(f) new mesh: 277 elements

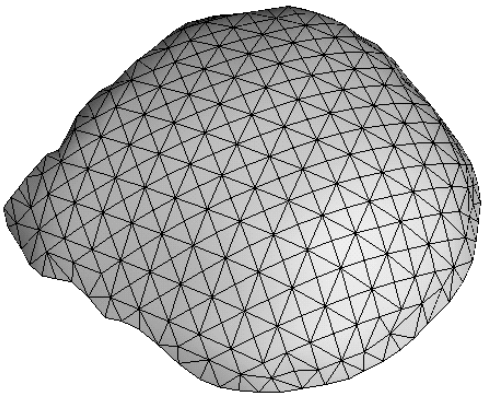

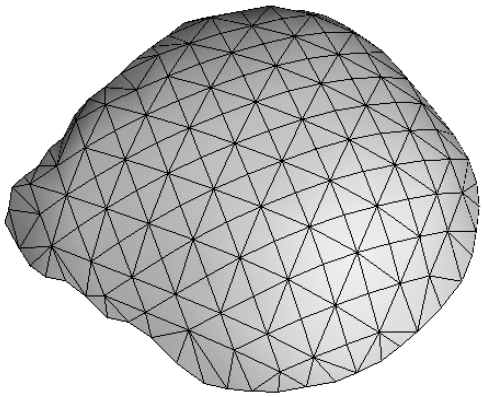

Figure 3.9: Meshes of different complexity for left parietal bone of foetal skull model *II*.

Table 3.2: Mesh statistics of the aspect ratio, α_1, for the original and optimised meshes of the parietal bones of foetal skull model I.

statistic	Original	Optimised
n	1599	1599
mean	1.985	1.680
std.dev.	0.64	0.41
minimum	1.167	1.160
maximum	9.812	5.172

3. Vertex/face addition/deletion: in some cases the two previous techniques are not sufficient to satisfy a pre-set quality criterion hence vertices and/or faces are added and/or deleted. The *immtk* software allows us to perform these operations in a straightforward manner without violating the geometry of the object.

Figure 3.14a shows the example of a parietal bone of foetal skull model I. The initial mesh has been created using planar DT [34]. Figure 3.14b shows the smoothed mesh. Figure 3.11 shows the histograms of the aspect ratio for both cases. From Figure 3.11 and the statistics shown in Table 3.2 it is clear that the mesh after Laplacian smoothing is of significantly better quality than the original[10].

3.5 Discussion

The main subject of this chapter was the introduction of a set of algorithms which allowed us to triangulate simply-connected level surfaces, limited by a relatively arbitrarily shaped boundary and possibly with incomplete data (gaps), to an arbitrary degree of mesh refinement. The approach was used to generate valid mesh models of objects to be analysed during the further course of this research. Many elaborations of the suggested algorithms are possible, some of which have been implemented and tested. The following paragraphs cover elaborations and limitations of the suggested algorithms.

Surface geometry The surface geometry was approximated using TPS surface interpolation. This technique interpolates parts of the surface where no point data is available and works fine for generally smooth surfaces. However, if the data points near a missing part are inaccurate, a not uncommon case

[10]Only 5 triangles have $4 < ar < 6$ in the smoothed mesh, whilst 25 triangles have $4 < ar < 10$ in the original DT mesh.

(a) Original patch (b) Interpolated and triangulated patch

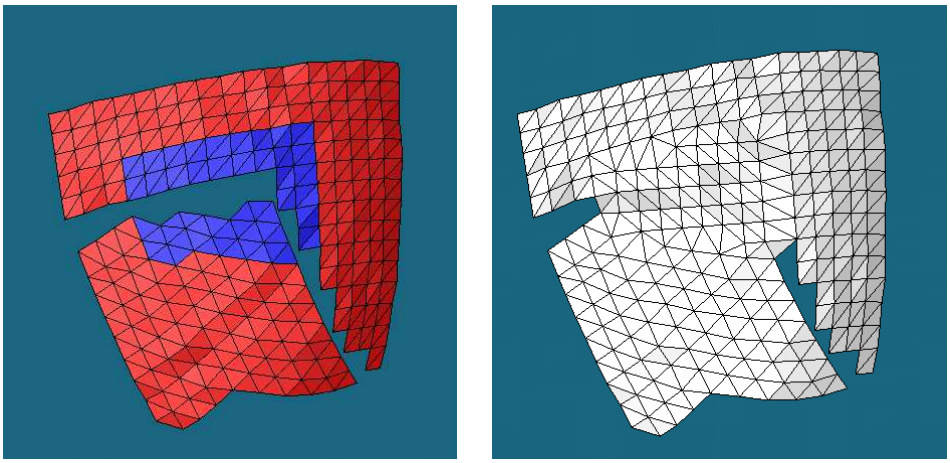

Figure 3.10: Triangulated patch. The *blue* part in (a) is selected from the general mesh (coloured *red*) using the *immtk* software. The missing data is then TPS interpolated and triangulated with the *triangle-growing* and *welding* algorithms of which the result is shown in (b).

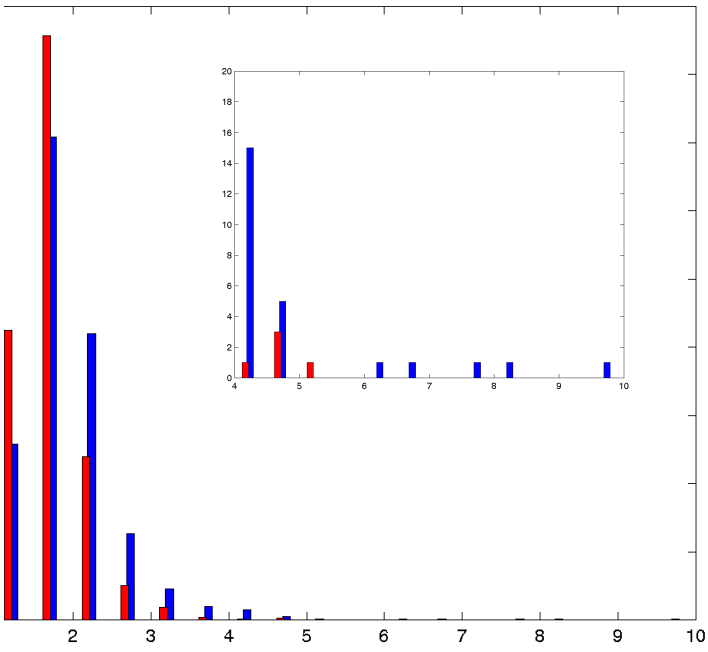

Figure 3.11: Histogram of aspect ratios. The *blue* colour corresponds to the original mesh; the *red* colour corresponds to the optimised mesh.

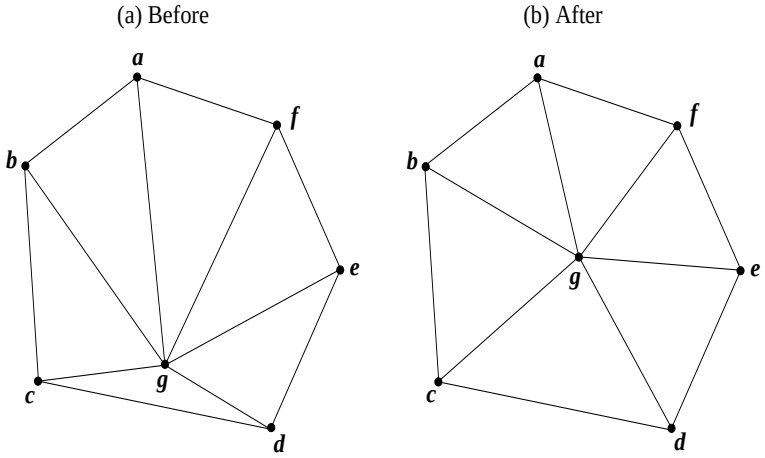

Figure 3.12: Laplacian smoothing: vertex g is moved to the centre of its surrounding polygon which yields overall improvement of the ar and ad.

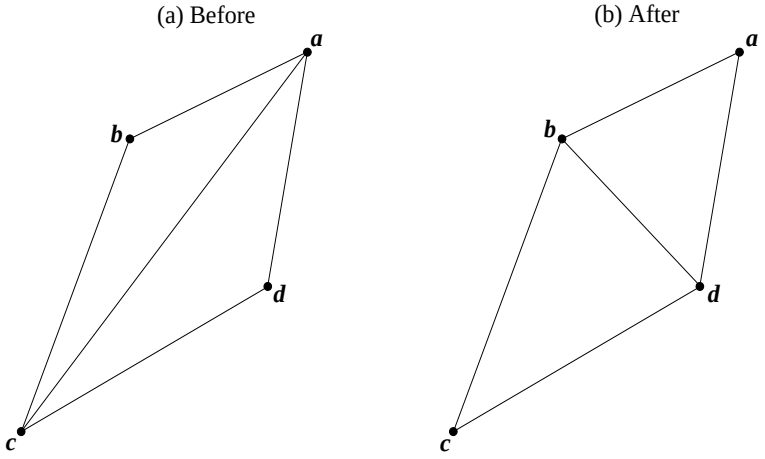

Figure 3.13: Edge swapping: edge ac is replaced by edge bd which yields a better ar and ad for both triangles in quadrilateral $abcd$.

(a) Original mesh (b) After Laplacian smoothing

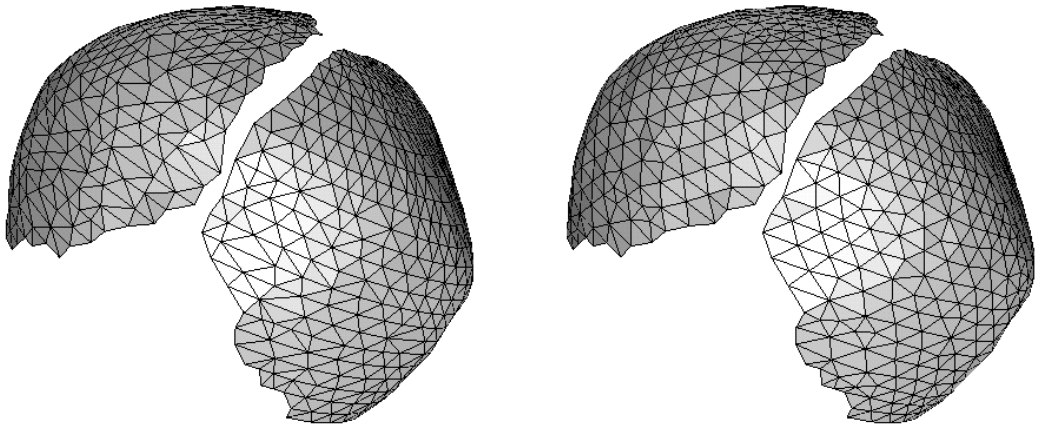

Figure 3.14: Original and optimised mesh models of the parietal bones of foetal skull model I.

for laser-scanned objects, the spline can display unnatural shapes because of its energy minimisation property. To alleviate this problem, inaccurate data points near the gap should be omitted.

Extension for general surfaces The spline interpolation and subsequent triangulation can be extended to general surfaces, if the latter are divided into patches which can be transformed into level surfaces. For the foetal skull, this is straightforward since it is merely a collection of individual shell-shaped parts. Each part can be triangulated separately using the conventional approach. If the boundaries of the different parts conform, i.e. neighbouring patches have common vertices on their common boundary sections, then the collection of the different triangulated parts into the original object is trivial.

Mesh refinement Refinement or coarsening of a mesh can be performed in a straightforward manner. Care has to be taken however with adaptations:

- Coarsening of the mesh as shown in Figure 3.9 involves a risk of altering complex geometries to an extent where it influences the stiffness at certain locations of the object[11]. Despite the use of an underlying surface, the curvature is always affected when a coarser mesh is created. Also, the detail of the boundary is lost, irrespective of spline interpolation. This

[11]This phenomenon will become clear from the results of experiment I in Chapter 6.

can be observed in Figure 3.9 by comparing the level of detail in the boundary geometry at different mesh complexities.

- Adaptive remeshing: although popular in conventional applications of FE analysis, adaptive remeshing has not been considered in the algorithms for reasons similar to the previous issue. Adaptive remeshing alters the mesh during analysis according to an error estimate of the variable of interest to save computational time by avoiding over-complex meshes. In most applications of structural mechanics this variable is stress or strain; in computational fluid dynamics this can be air flow, density or pressure. However, in these fields, the geometry is often 2D, if not, very simple 3D geometries of relatively constant curvature. In our case, the object has a complex curvature. Coarsening the mesh at any location would decrease the level of detail of the geometry. Even if we could adapt the mesh according to curvature in a sensible way, later adaptations for a field variable could disrupt the curvature adaptation. Therefore a sufficiently fine mesh of constant density was preferred: an approach which might result in a slightly over-complex mesh, but nonetheless guaranteed to be accurate!

Mesh optimisation Optimisation of the mesh using Laplacian smoothing is of limited use for meshes created with the *triangle growing* algorithm since the internally grown triangles have vertices which are already in the centres of their surrounding polygons. Laplacian smoothing will have some effect near the boundary triangles, but edge swapping and vertex addition yield in general better results and were thus used to optimise the mesh as shown in Figure 2.14b.

Boundary shape The shape of the boundary is crucial to the success of most triangulation algorithms. The *triangle-growing* algorithm is robust for a large variety of boundary shapes but will fail if the boundary or parts of the boundary have high aspect ratios (e.g. *tentacles* or long, thin rectangular boundaries). The problem here is that triangles cannot grow since the centre node is already too close to the boundary.
The *welding* algorithm works well for boundaries which are at a relatively equal distance compared to the spacing between the nodes. If the relative distance between the two boundaries becomes too large, comparisons of Euclidean distances and calculations of cross-products become unreliable, which results in invalid connections.

It should be noted though that these extreme configurations did not occur in the cases for which the algorithms were originally designed.

3.6 Summary

This chapter has described a set of algorithms for generating valid, compatible, triangulated FE mesh models of an object of complex geometry, in this case a foetal skull. The approach consists of three main algorithms:

1. thin-plate spline (TPS) surface interpolation,
2. the *triangle-growing* algorithm,
3. the *welding* algorithm.

The algorithms provide interpolation across regions where no data points are available and are able to generate meshes of arbitrary complexity. The *triangle-growing* algorithm and the *welding* algorithm have complexity $O(N)$. Their properties were illustrated by several examples, relating to the creation of valid mesh models of the foetal skull and parts of it.
Furthermore, strategies to improve the quality of the mesh were outlined and illustrated.

Chapter 4

Important concepts of finite element analysis (FEA)

4.1 Introduction

The aim of this chapter is to outline important concepts of the finite element method (FEM), necessary to perform a successful analysis of a physical problem. The current availability of commercial FE software saves the analyst or researcher from developing a bulk of error-prone code. Despite this time-saving advantage, there is a potential danger of incompetence by which the user can operate the software without the slightest awareness of possible abuse. Therefore it is essential that the user has a thorough understanding of the problem to be solved so that errors in computed results can be detected and a judgement made as to whether the results are to be trusted or not [19].
The next section gives a brief overview of the history of the FEM, followed by a section describing the concepts of appropriate use. Since the theory behind the FEM is extensive, the content of this section is tailored to the specific problems of the analysis of deformation of the foetal skull.
The reader, unfamiliar with the FEM or in need of a refresh, may consult Appendix A which gives a brief introduction of the basic concepts.

4.2 History

The original idea of the FEM was described in 1943 by the mathematician Courant, in a paper which describes a piecewise polynomial solution for the torsion problem [20]. At the time it was ignored by a majority of conservative, classical analysts, as well as engineers who are known not to be the most diligent readers of mathematical journals! The method became popular in the 1950's, mainly in the aircraft industry since this sector had the strongest mo-

tives for accurately analysing structures of great complexity [76]. A classic paper describing a FE approach in 1956, involved the analysis of delta wings [102], which are too short to be reliably modelled by the classical beam theory. The name *finite element* occurred for the first time in 1960 [19]. The method was at first used for stress analysis of mechanical structures but was soon expanded to the areas of heat transfer, fluid dynamics, magnetic fields, groundwater flow and later on to the field of biomechanics. By the mid-1990's, roughly 40,000 papers and books about the FEM and its applications have been published [19]. Since the early 80's, commercially available software has been developed which currently provides a wide range of options in terms of element types, analyses and pre- and postprocessing facilities. Most of these packages have been updated and improved throughout the years and have thus achieved a high standard of reliability.

4.3 Concepts for the proper use of the finite element method (FEM)

4.3.1 General

The FEM is a convenient tool to solve complex problems which are hard to solve with conventional analytical methods. In most cases, the complexity of a problem is a geometrical one: the object of interest is of such complex geometry that the use of analytical methods results in inadequate solutions. A good example is the modelling of foetal skull moulding using shell analysis. Dym [25] outlined a general theory of shells by describing the equations of equilibrium, the kinematic (or *strain-displacement*) relations and the constitutive (or *stress-strain*) relations for static isothermal loading of isotropic shells. The resulting set of PDE's can be simplified to a set of ODE's, for relatively simple objects of revolution. The set of ODE's can be numerically solved then, using for instance the finite difference (FD) method. However, the geometry of the skull is too complex to be described by an analytical, axisymmetric formulation. Any such attempt would result in approximations far worse than those inherent to the FEM, which involve [19]:

Modelling error which counts for basically any analysis method. When confronted with a physical problem, we do not actually analyse this problem but the mathematical model of it. To arrive at such a model, we make assumptions which do not always reflect the exact behaviour of the problem.

Numerical error The numerical output has been rounded and truncated dur-

ing the course of the analysis. Numerical errors are usually small but some modelling practises can significantly increase them.

Discretisation error This is the typical error of the FEM. The physical structure which we analyse and the mathematical model derived from it, have infinitely many degrees of freedom (dof) whilst the finite element model has a finite number of dof. This implies that the discretisation error will tend to zero as the number of elements increase but will never become zero.

The theory of the FEM includes matrix manipulations, numerical integration, equation solving and other procedures which are carried out automatically by the FE software. This means that the user mainly deals with what is commonly known as *pre-processing* and *post-processing*. Pre-processing involves the description of the geometry, the generation of the FE mesh, the description of loads and boundary conditions, the specification of material properties and the type of analysis which will be performed. Post-processing is another crucial step of the analysis which involves the processing of a bulk of output results which are provided by the FE software.
Despite its convenience and ease of use for arbitrary, complex geometries, FE modelling is more than preparing a mesh, do some pre-processing, wait for the results and subsequently print them! The pre- and post-processing steps are crucial to the reliability of the results and have to be executed with care!
It is also advised to start the analysis with a simplified model and gradually increase complexity as the analysis progresses.

4.3.2 Element shape and aspect ratio (ar)

Element shapes that are compact and regular usually give the greatest accuracy [19]. In Chapter 3, we already mentioned the importance of the ar of a triangular element and the fact that the equilateral triangle exhibits the optimum ar. Distortions or excessive aspect ratios usually reduce accuracy by making the element stiffer, for example a linear strain triangle, LST, with quadratic terms in its displacement field can be reduced to behaving like a first-order, constant strain triangle, CST. In general, distortions usually degrade stresses more than displacements. If strain gradients are sufficiently small than the influence of the ar is minimal.

4.3.3 Convergence with mesh refinement

Monotonic convergence requires:

1. The elements to be complete.

2. The elements and mesh to be compatible.

If these conditions are fulfilled, the accuracy of the results will increase continuously as we continue to refine the finite element mesh [8].
The **requirement of completeness** of an element means that the displacement functions of the element must be able to represent *rigid body displacements* and *constant strain states*. Rigid body displacements are those displacement modes which the body undergoes without stresses being developed in it. The requirement of constant strain states is the ultimate destiny as element sizes shrink to zero. As an example, we calculate the strain fields for a first-order, constant strain triangle (CST) and second-order, linear strain triangle (LST) (see Figure 4.1).

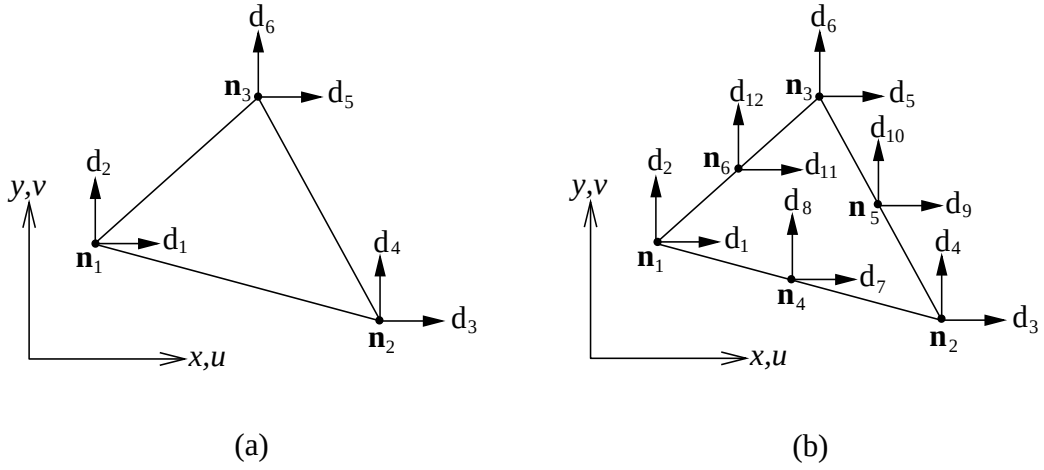

Figure 4.1: (a) First-order, constant strain triangle, CST, and (b) Second-order, linear strain triangle, LST.

For a CST, the displacement field in generalised coordinates β_i is:

$$\begin{aligned} u &= \beta_1 + \beta_2 x + \beta_3 y \\ v &= \beta_4 + \beta_5 x + \beta_6 y \end{aligned} \tag{4.1}$$

The resulting strain field becomes:

$$\begin{aligned} \epsilon_x &= \beta_2 \\ \epsilon_y &= \beta_6 \\ \epsilon_{xy} &= \beta_3 + \beta_5 \end{aligned} \tag{4.2}$$

For a *LST*, the displacement field in generalised coordinates β_i is:

$$\begin{aligned} u &= \beta_1 + \beta_2 x + \beta_3 y + \beta_4 x^2 + \beta_5 xy + \beta_6 y^2 \\ v &= \beta_7 + \beta_8 x + \beta_9 y + \beta_{10} x^2 + \beta_{11} xy + \beta_{12} y^2 \end{aligned} \tag{4.3}$$

The resulting strain field becomes:

$$\begin{aligned} \epsilon_x &= \beta_2 + 2\beta_4 x + \beta_5 y \\ \epsilon_y &= \beta_9 + \beta_{11} x + 2\beta_{12} y \\ \epsilon_{xy} &= (\beta_3 + \beta_8) + (\beta_5 + 2\beta_{10})x + (2\beta_6 + \beta_{11})y \end{aligned} \tag{4.4}$$

It can be readily seen from Equations 4.2 that the *CST* is capable of representing constant strain states. The element gives good results when the strain gradient is small. However, when subjected to pure bending, it yields rather poor results and develops a spurious shear stress [19]. Despite these shortcomings, improved results are obtained as the mesh is repeatedly refined.
The *LST* is capable of representing constant and linear strain states (Equations 4.4) and performs much better in cases of pure bending.

The requirement of compatibility means that the displacements within the elements and across the element boundaries must be continuous. This requirement was illustrated in Section 3.1.1.

Mesh refinement As mentioned before, FE results should converge towards exact results as the mesh is repeatedly refined. We define:

h to be an approximate linear size measure of an element, e.g. for a triangular element, $A^{\frac{1}{2}}$, where A is the area of the element.

p as the degree of the highest complete polynomial in the element displacement field. Thus, for the *CST*, p=1, and for the *LST*, p=2.

Commonly, one refers to **h-refinement** and **p-refinement** in which h or p are changed from the old mesh to the new.

4.3.4 Non-linear geometry

In *linear analysis*, we assume that displacements and rotations are small, supports do not settle, stress is directly proportional to strain and loads maintain

their original directions as the structure deforms [19]. The solution of the displacements are obtained in a single step[1]:

$$\mathbf{U} = \mathbf{K}^{-1}\mathbf{R} \tag{4.5}$$

with $\mathbf{U}$, the global displacement vector; $\mathbf{K}$, the global stiffness matrix; $\mathbf{R}$, the global loading vector. Linear analysis is thus convenient timewise and gives good approximations as long as the earlier mentioned conditions are met. If this is not the case, *non-linear analysis* should be considered.

In non-linear analysis, the principle of superposition does not apply, hence we cannot scale results in proportion to load or combine results from different load cases. The main problem in non-linear analysis is that the governing equations must incorporate conditions which are not fully known until the solution is known.

At all times we are trying to establish the equilibrium:

$$\mathbf{f} - \mathbf{p} = \mathbf{0} \tag{4.6}$$

where $\mathbf{f}$ are the applied loads and $\mathbf{p}$ are the internal resisting forces.

In numerical solutions, an exact equilibrium is never reached and consequently, a *converged state* is sought in which the equilibrium error is acceptably small [41]. A measure of the equilibrium error is provided by the vector of *residual* or *out of balance* forces:

$$\mathbf{r} = \mathbf{f} - \mathbf{p} \tag{4.7}$$

The criterion for convergence is normally expressed as:

$$||\mathbf{r}|| < \phi\,||\mathbf{f}|| \tag{4.8}$$

where ϕ is the error fraction ($\phi \ll 1$).

The most basic solution strategy to a non-linear geometric problem is a *purely incremental* method. Figure 4.2 illustrates the idea behind the method. The entire external load $\mathbf{f}$ is administered to the object in small increments $\mathbf{\Delta f}$. For each increment n, Equation 4.6 becomes[2]:

$$\Delta\mathbf{f}^n - \Delta\mathbf{p}^n = \mathbf{0} \tag{4.9}$$

Assuming linear behaviour within an increment n yields:

$$\begin{aligned} \Delta\mathbf{p}^n &= [\partial\mathbf{p}/\partial\mathbf{d}]_{d^{n-1}}\Delta\mathbf{d}^n \\ &= \mathbf{K}_T^{n-1}\Delta\mathbf{d}^n \end{aligned} \tag{4.10}$$

[1] See Appendix A.

[2] Where $\Delta\mathbf{p}^n = f(\mathbf{d}^n)$ with $\mathbf{d}^n$, the vector of nodal displacements at increment n.

where $\mathbf{K}_T^{n-1}$ is called the *tangent stiffness matrix*. Substitution of Equation 4.10 into Equation 4.9 yields the set of linear equations to be solved at each increment:

$$\mathbf{K}_T^{n-1}\Delta\mathbf{d}^n = \Delta\mathbf{f}^n \tag{4.11}$$

An updated solution for the displacements is then given by:

$$\mathbf{d}^n = \mathbf{d}^{n-1} + \Delta\mathbf{d}^n \tag{4.12}$$

The main drawback of the incremental solution are the increasing load residuals and displacement errors as the load is increased. This *drift off* from the true solution is clearly illustrated in Figure 4.2.

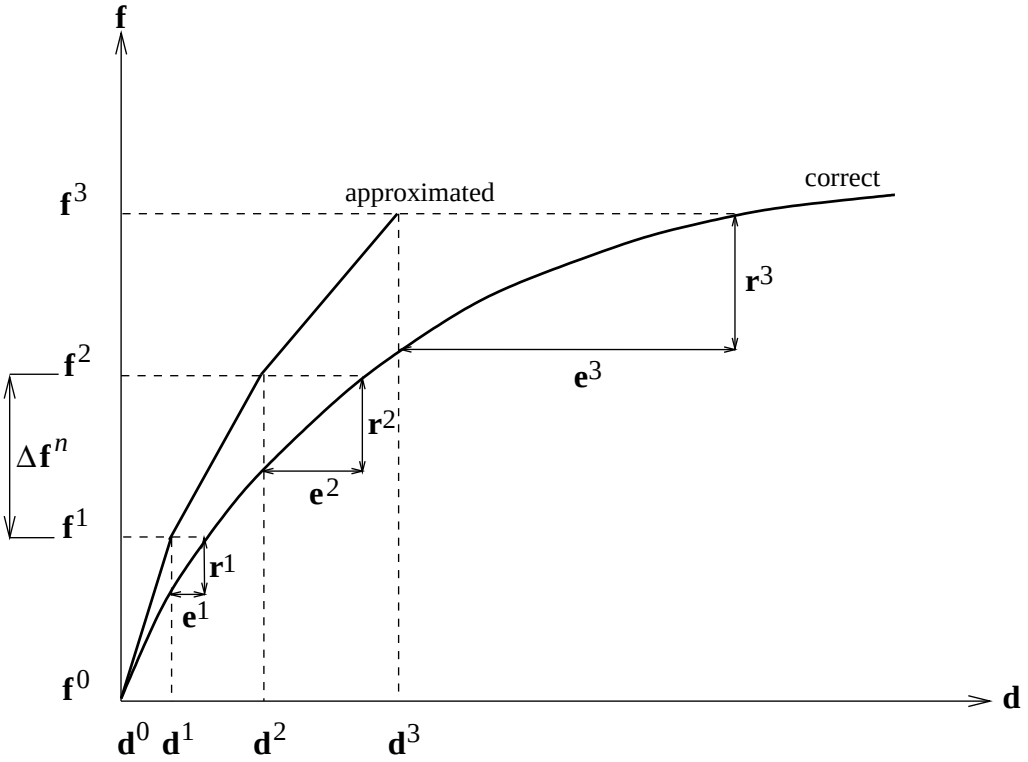

Figure 4.2: Purely incremental solution of a non-linear geometric problem. The continuous curve, or correct equilibrium curve, of applied load $\mathbf{f}$ as a function of displacement $\mathbf{d}$, is approximated by a piecewise linear curve. The latter exhibits residual force errors, $\mathbf{r}^n$, and displacement errors, $\mathbf{e}^n$, at each increment n. These errors increase as the load is increased, hence the approximate solution *drifts off*.

An iterative approach such as the Newton-Raphson (*NR*) method aims to improve this discrepancy. If an approximate solution $\mathbf{d}_i^n$ (starting at iteration $i = 0$) is reached, an improved solution is obtained using a truncated Taylor's

series expansion[3] (neglecting higher-order terms):

$$\mathbf{r}_{i+1}^{n} = \mathbf{r}_{i}^{n} - [\partial \mathbf{r}/\partial \mathbf{d}]_{\mathbf{d}_i^n}\, \delta \mathbf{d}_i^n \tag{4.13}$$

Ideally, we wish the new residual to be zero, hence the current equilibrium equation becomes:

$$\mathbf{r}_{i}^{n} - \mathbf{K}_{T,i}^{n}\, \delta \mathbf{d}_i^n = \mathbf{0} \tag{4.14}$$

with the tangent stiffness matrix, $\mathbf{K}_{T,i}^{n} = [\partial \mathbf{r}/\partial \mathbf{d}]_{\mathbf{d}_i^n}$.
The new and improved update becomes:

$$\mathbf{d}_{i+1}^{n} = \mathbf{d}_{i}^{n} + \delta \mathbf{d}_i^n \tag{4.15}$$

Figure 4.3 illustrates the *NR* method for a single increment. As the figure shows, the residuals $\mathbf{r}$ and the displacement errors corresponding to $\delta\mathbf{d}$ in this case, reduce as the iterative process progresses.

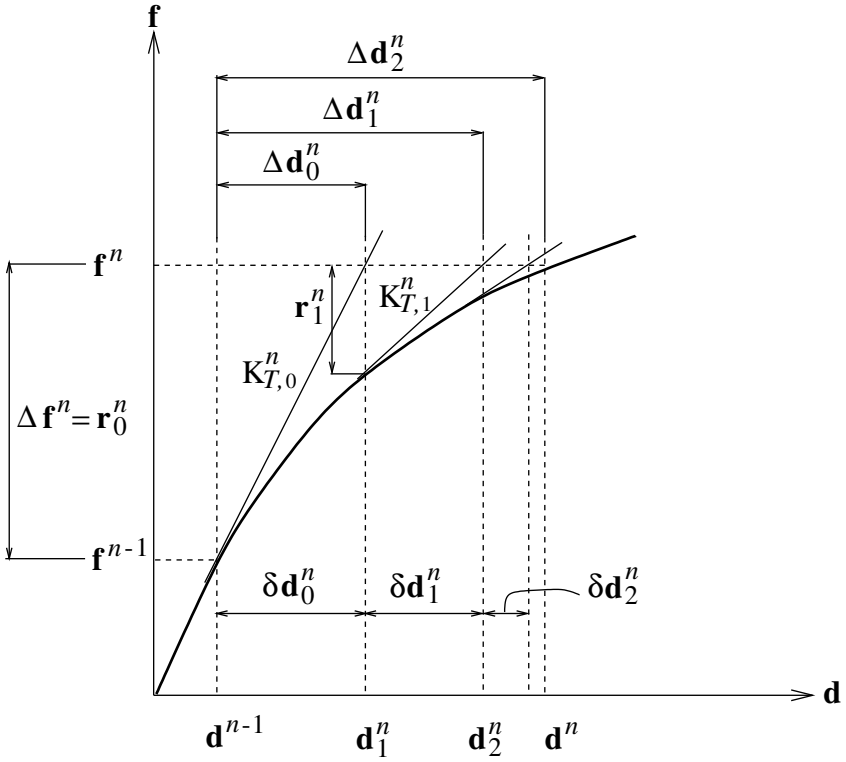

Figure 4.3: The *NR* method for a single increment of the applied force $\mathbf{f}$.

Despite the significantly improved accuracy as opposed to the purely incremental algorithm, the *NR* method is expensive in computational terms as much effort is required in calculation and factorisation of the tangent stiffness matrix at each iteration [41]. To overcome this problem, many modifications of the

[3]Where the residual $\mathbf{r} = f(\mathbf{d})$.

standard *NR* method have been suggested which include the *modified* Newton-Raphson, *mNR*, and the *quasi* Newton-Raphson, *QN*, methods of which the most popular is the Broyden-Fletcher-Goldfarb-Shanno, *BFGS*, method. In depth coverage of these methods can be found in [8, 41].

Convergence control in ABAQUS/Standard

In the ABAQUS/Standard FE software the two main criteria[4] for convergence are [40]:

1. $\mathbf{R}^{\alpha}$, convergence criterion[5] for the ratio of the largest residual, e.g. $\mathbf{r}^{n}$, to the corresponding average flux norm, e.g. $\mathbf{f}^{n}$. The default value is 5×10^{-3}.

2. $\mathbf{C}^{\alpha}$, convergence criterion for the ratio of the largest solution correction, e.g. $\delta\mathbf{d}^{n}$, to the largest corresponding incremental solution value, e.g. $\Delta\mathbf{d}^{n}$. The default value is 10^{-2}.

4.3.5 Example

The effects of h- and p- refinement and *LG*/*NLG* are illustrated by an example of a square plate subjected to a uniform transverse load. The plate is fully built-in and lies in the *x*-*y* plane. The analytical solutions for the maximum deflection and stresses are obtained from Roark's formulas[6][110] and given by:

$$\sigma_{max} = -\frac{\beta_1 q b^2}{t^2} \tag{4.16}$$

$$\sigma_c = \frac{\beta_2 q b^2}{t^2} \tag{4.17}$$

$$u_{z,max} = \frac{\alpha q b^4}{E t^3} \tag{4.18}$$

where σ_{max} is the stress in the middle of an edge, σ_c is the stress at the centre of the plate and $u_{z,max}$ is the maximum deflection (at the centre of the plate). For a square plate: $\beta_1 = 0.3078$, $\beta_2 = 0.1386$ and $\alpha = 0.0138$ [110].
The material of the plate is steel with Young's modulus $E = 370$ MPa. The edge length $b = 100$ mm. and the thickness $t = 5$ mm. The plate is subjected to a constant transverse load across the entire surface, $q = -0.02$ MPa.
The analyses were run with the ABAQUS/Standard software for five models consisting of 8, 32, 128, 512 and 2,048 elements respectively. For each of these

[4]Notation as specified in [40].
[5]Parameter α corresponds to the field variable, e.g. $alpha = 1$ for displacement; $\alpha = 2$ for rotation.
[6]The original theory is worked out in Chapter 6 of [100].

models, the ABAQUS shell elements S3R and STRI65 were used and analysed assuming *LG* and *NLG*, respectively. The S3R element is a general purpose element (suitable for both thin and thick shells), has six dof and can model finite (constant) strain. The STRI65 element is only suitable for thin shell modelling exhibiting small (linear) strain. In the experiments as presented in Chapter 6, the S3R elements will be referred to as constant strain shell (*CSS*) elements and the STRI65 elements as linear strain thin shell (*LSTS*) elements.

Discussion Table 4.1 shows the values of $u_{z,max}$, σ_{max} and σ_c for each analysis. Figure 4.4 shows the trajectories for increasing h-refinement (models 1-5) of $u_{z,max}$, for four different analyses. All curves appear to converge to the same point, which is slightly higher in absolute value than the value as calculated from Roark's formulas[7][110]. The curves for the analyses involving *LSTS*'s (coloured *red* for *LG* and *magenta* for *NLG*) overshoot the true value at less complex models to converge for models of higher complexity. A possible reason why coarser models appear to behave less stiff than finer models, as illustrated in Figure 4.5, is because of the approximate curvature of the surface of model 2 as compared to the true surface curvature, which may cause the midpoint to descend more than for model 5 (which is a more refined model with a curvature closer to the true surface curvature). Figure 4.6 shows the maximum stress, σ_{max}. The curves for the analyses involving *CSS*'s (*blue* and *green* colour) show clearly that first-order meshes require more h-refinement than second-order meshes (*red* and *magenta* colour) for the approximation of stresses. Figure 4.7 shows distinct behaviour between linear geometric analyses (*blue* and *red* curves) and non-linear geometric analyses (*green* and *magenta* curves). The results from the linear analysis converge closer to the value from Roark's formulas for σ_c than the results from the non-linear analysis[8]. A possible explanation may lie in the difficulty of calculating values of stress in a single point of the mesh. In FEA, stress variables are calculated from the integration points of the element. Values at nodes are thus obtained by extrapolation. Again, the value as calculated from Roark's formulas is a numerical approximation and might not be entirely accurate. Finally, Figure 4.8 shows the Mises equivalent stress[9] and the deformation in the z-direction, u_z, for non-linear geometry, *NLG*, second-order elements, *LSTS*, for all five models. The continuity of the stress and

[7]Note that the values from Roark's are obtained by numerical approximation.

[8]For the variables $u_{z,max}$ and σ_{max} the difference between linear and non-linear geometry is small!

[9]The (von) Mises equivalent stress is an invariant stress quantity and is defined as: $\sigma_e = \frac{1}{\sqrt{2}}\sqrt{(\sigma_1-\sigma_2)^2+(\sigma_2-\sigma_3)^2+(\sigma_3-\sigma_1)^2}$ where σ_1, σ_2 and σ_3 are the three principal stresses at the point in question.

Table 4.1: Results of the bending of a fully built-in square plate subjected to a uniform transverse load. The first row shows the values as calculated from Equations 4.16 - 4.18. Subsequent rows show values of models 1-5 with a mesh complexity of 8, 32, 128, 512 and 2,048 elements, respectively. Each model is analysed using *CSS*'s and *LSTS*'s respectively under the assumptions of both *LG* and *NLG*.

Analysis	$u_{z,max}$ (mm.)	σ_{max} (MPa)	σ_c (MPa)
Roark's	-0.5968	+2.4624	-1.1088
1 - *LG* - *CSS*	-0.0281	+6.15E-33	-6.08E-33
2 - *LG* - *CSS*	-0.1304	+0.1406	-0.2026
3 - *LG* - *CSS*	-0.5510	+1.2320	-0.9399
4 - *LG* - *CSS*	-0.6119	+1.8840	-1.0680
5 - *LG* - *CSS*	-0.6234	+2.1830	-1.0950
1 - *LG* - *LSTS*	-0.5730	+1.3810	-1.3190
2 - *LG* - *LSTS*	-0.6621	+2.1340	-1.3460
3 - *LG* - *LSTS*	-0.6422	+2.4250	-1.1660
4 - *LG* - *LSTS*	-0.6338	+2.4370	-1.1180
5 - *LG* - *LSTS*	-0.6301	+2.4730	-1.1070
1 - *NLG* - *CSS*	-0.0281	+6.44E-05	+4.39E-05
2 - *NLG* - *CSS*	-0.1304	+0.1416	-0.2014
3 - *NLG* - *CSS*	-0.5482	+1.2490	-0.9013
4 - *NLG* - *CSS*	-0.6075	+1.9050	-1.0150
5 - *NLG* - *CSS*	-0.6186	+2.2040	-1.0380
1 - *NLG* - *LSTS*	-0.5712	+1.4010	-1.2870
2 - *NLG* - *LSTS*	-0.6558	+2.1580	-1.2720
3 - *NLG* - *LSTS*	-0.6365	+2.4440	-1.1010
4 - *NLG* - *LSTS*	-0.6284	+2.4540	-1.0570
5 - *NLG* - *LSTS*	-0.6248	+2.4890	-1.0470

displacement patterns clearly improves as the mesh is refined.

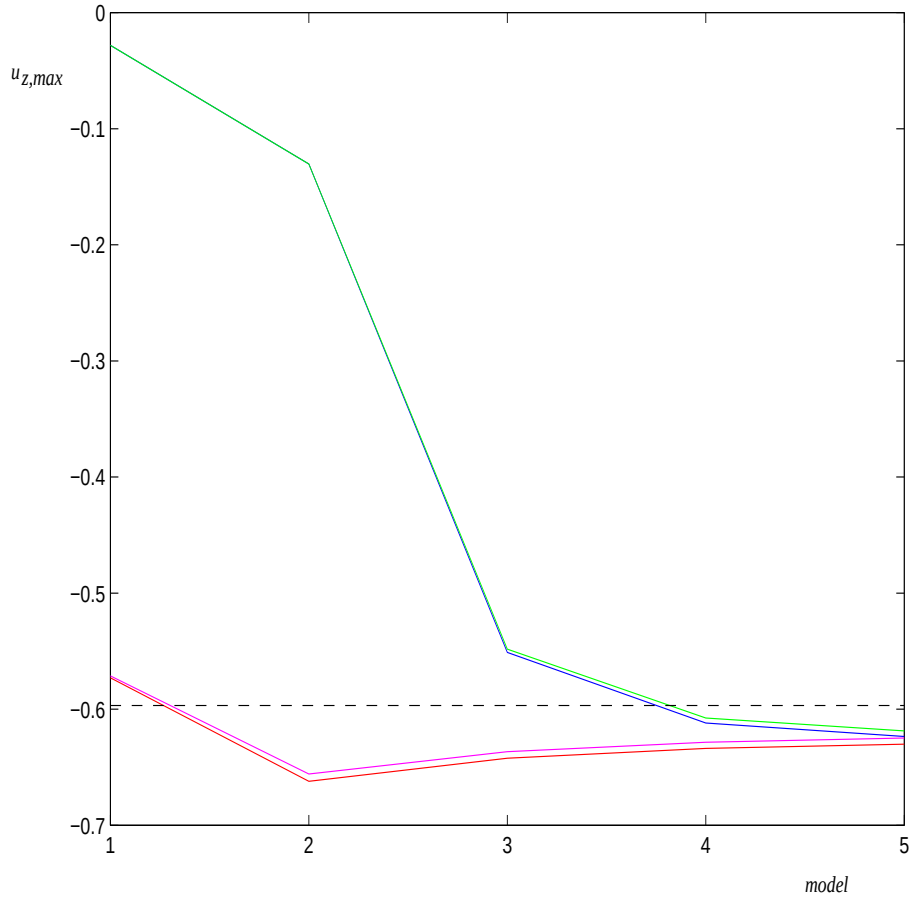

Figure 4.4: Maximum vertical displacement, $u_{z,max}$ (mm.), of the centre of a fully built-in square plate, subjected to a uniform transverse load. Models 1-5 contain 8, 32, 128, 512 and 2,048 elements respectively. Colour code: *blue* corresponds to *LG - CSS*, *red* corresponds to *LG - LSTS*, *green* corresponds to *NLG - CSS*, *magenta* corresponds to *NLG - LSTS*. The dashed line corresponds to the value as calculated from Roark's formulas [110]: $u_{z,max} = -0.5968$ mm.

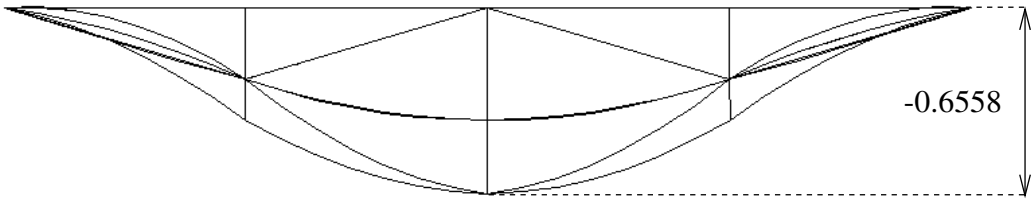

(a) Model 2: 32 elements

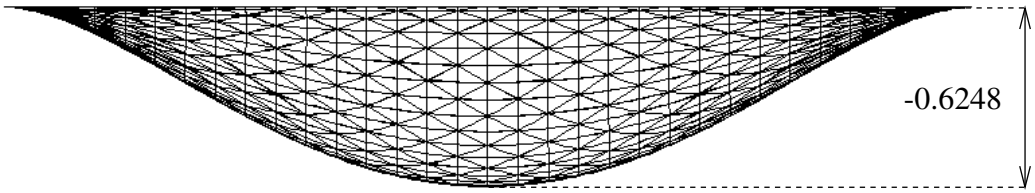

(b) Model 5: 2,048 elements

Figure 4.5: Comparison of the maximum vertical displacement, $u_{z,max}$ (mm.), for two models of different complexity, analysed using *LSTS*'s and assuming *NLG*. The displacement is larger for model 2 despite its coarser mesh (see text for explanation). Deformation magnification = 30.

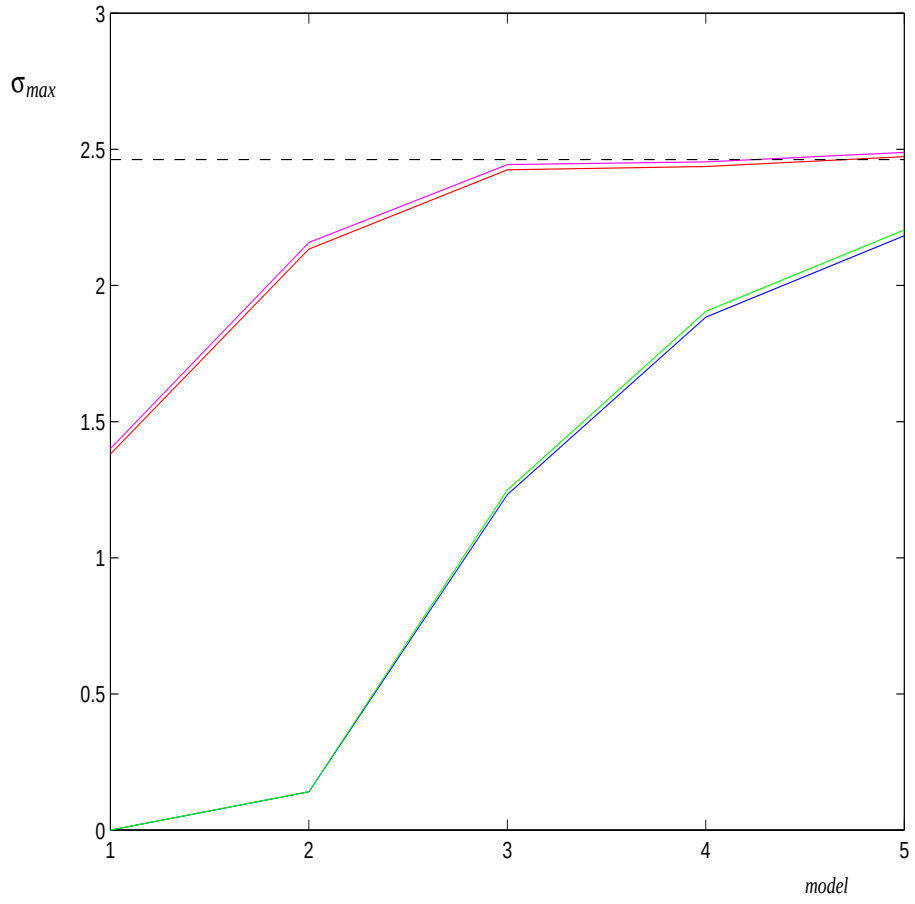

Figure 4.6: Maximum stress at the middle of an edge, σ_{max} (MPa), of a fully built-in square plate, subjected to a uniform transverse load. Models 1-5 contain 8, 32, 128, 512 and 2,048 elements respectively. Colour code: *blue* corresponds to *LG - CSS*, *red* corresponds to *LG - LSTS*, *green* corresponds to *NLG - CSS*, *magenta* corresponds to *NLG - LSTS*. The dashed line corresponds to the value as calculated from Roark's formulas [110]: $\sigma_{max} = +2.4624$ MPa.

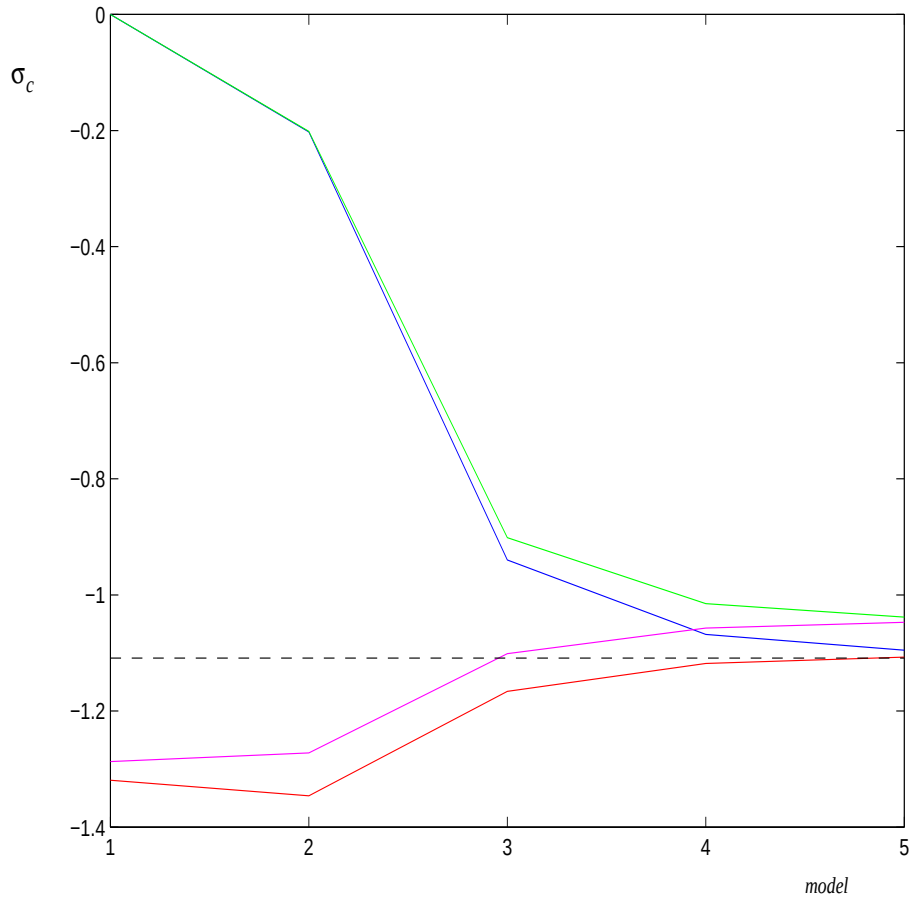

Figure 4.7: Stress, σ_c (MPa), at the centre of a fully built-in square plate, subjected to a uniform transverse load. Models 1-5 contain 8, 32, 128, 512 and 2,048 elements respectively. Colour code: *blue* corresponds to *LG - CSS*, *red* corresponds to *LG - LSTS*, *green* corresponds to *NLG - CSS*, *magenta* corresponds to *NLG - LSTS*. The dashed line corresponds to the value as calculated from Roark's formulas [110]: $\sigma_c = -1.1088$ MPa.

Mises stress (MPa) $\mathbf{u}_z$ (mm.)

Model 1: 8 elements

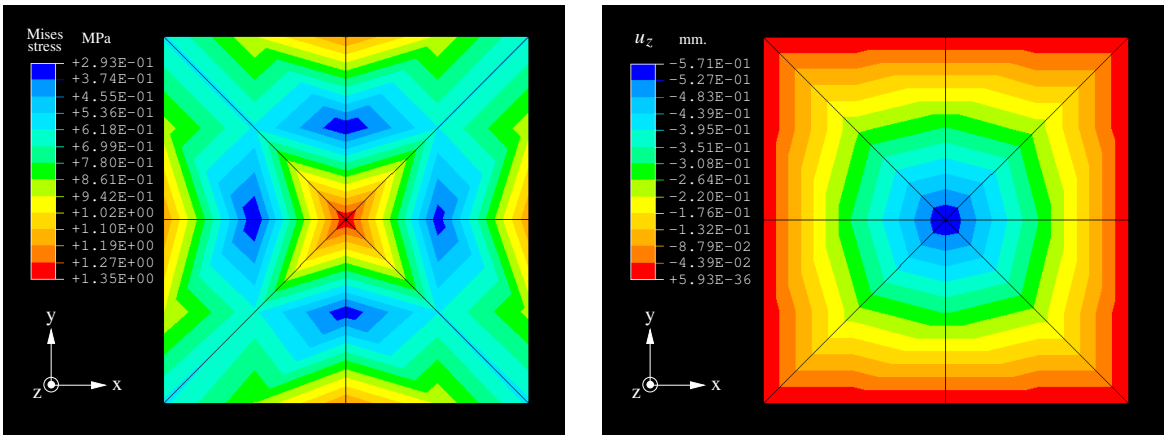

Model 2: 32 elements

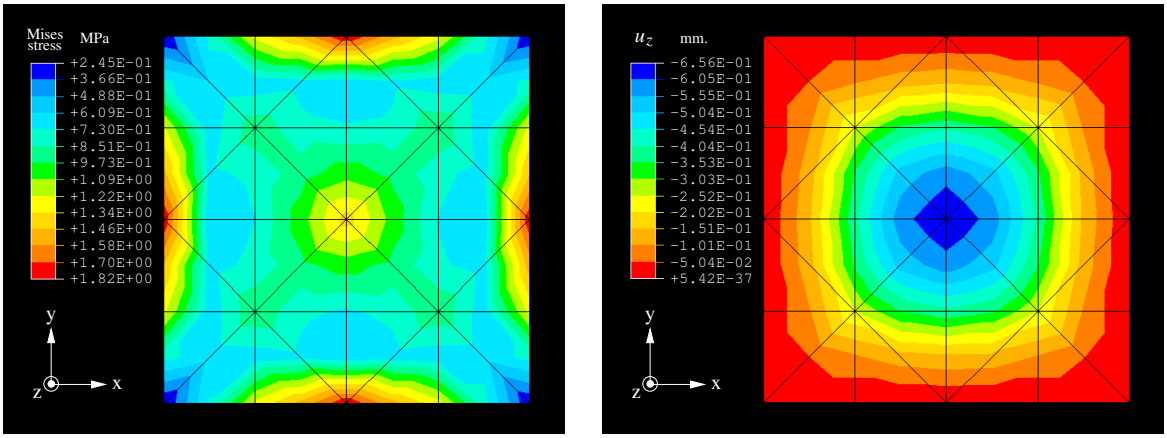

Model 3: 128 elements

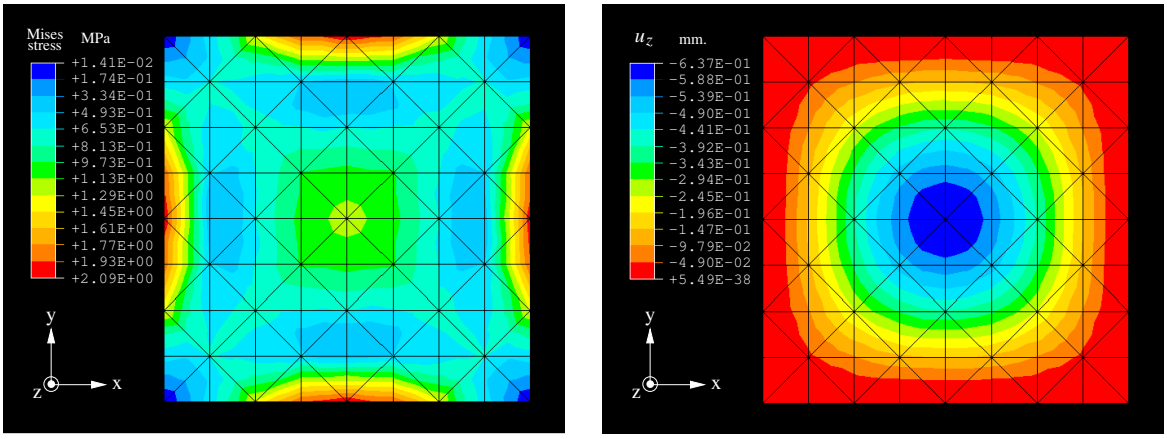

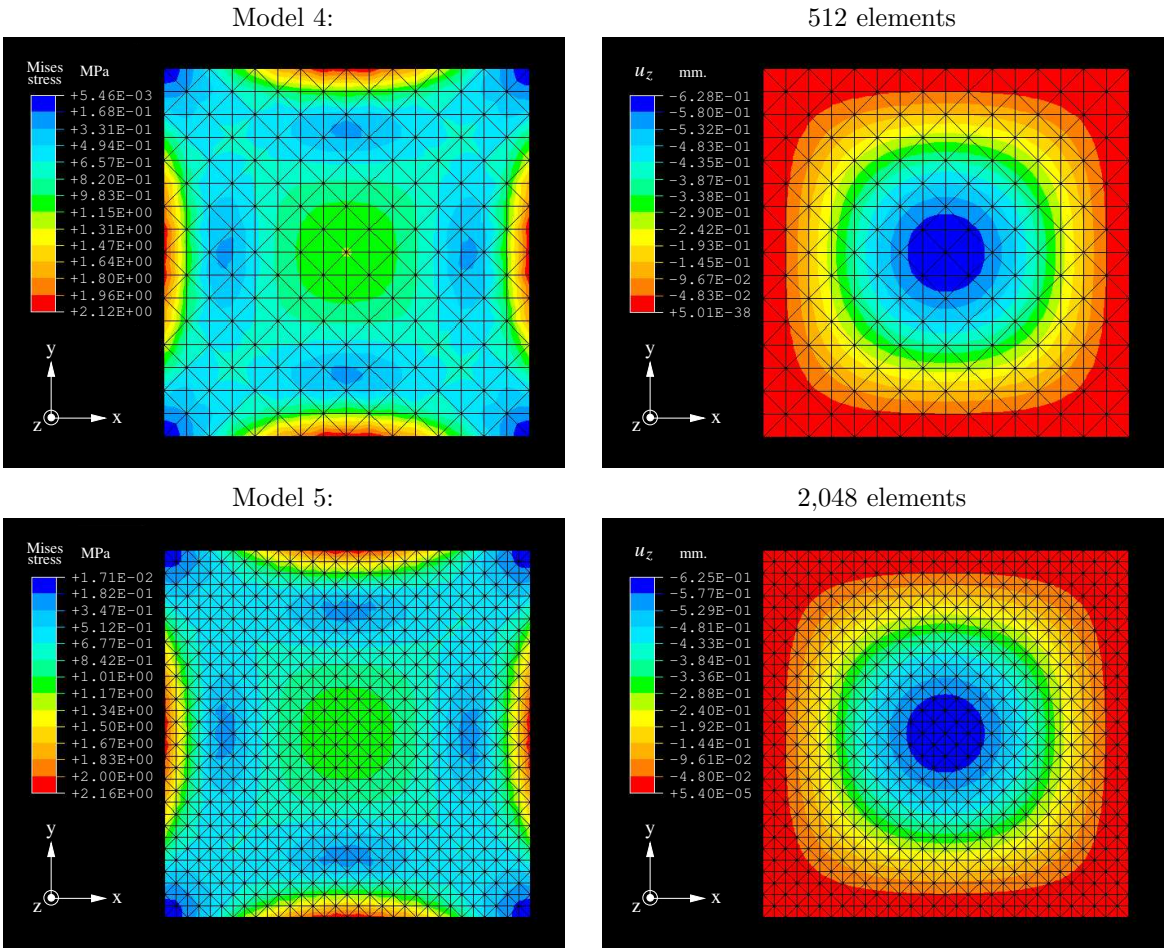

Figure 4.8: Mises equivalent stress (MPa), and displacement, u_z (mm.), for models 1-5 with 8, 32, 128, 512 and 2,048 elements respectively. Note the improved continuity of the patterns as meshes are gradually refined.

4.3.6 Anisotropic materials

The constitutive equations for a *general*, *linearly elastic*, *anisotropic* solid material in tensor notation is given by:

$$\epsilon_{ij} = S_{ijkl}\,\sigma_{kl} \tag{4.19}$$

where ϵ_{ij} is the second-rank strain tensor, σ_{kl} is the second-rank stress tensor and S_{ijkl} is the fourth-rank compliance matrix.
The constitutive relations are usually written for σ as a function of ϵ.
With the fourth-rank elasticity tensor, $C_{ijkl} = S^{-1}_{ijkl}$, we can write:

$$\sigma_{ij} = C_{ijkl}\,\epsilon_{kl} \tag{4.20}$$

For a general 3D anisotropic body, i, j, k, l range from 1 to 3. This means that there are 81 material constants in the elasticity tensor C_{ijkl}. However because of symmetry, there are only 21 independent material constants, necessary to describe full anisotropy.

4.3.7 Hyperelasticity

A material is called *hyperelastic* if it possesses an elastic potential function, V, which is a scalar function of the strain, ϵ, and whose derivatives with respect to one of the strain tensor components yields the corresponding stress tensor component, σ [41] (see Figure 4.9).
In formula form:

$$V = \int_0^{\epsilon_n} \sigma\, d\epsilon$$

or

$$\sigma = \frac{dV}{d\epsilon} \tag{4.21}$$

The most widely used prescription of the specific strain energy potential, for a hyperelastic incompressible material, is the Mooney potential [66]:

$$V = C_1(\bar{I}_1 - 3) + C_2(\bar{I}_2 - 3) \tag{4.22}$$

where $\bar{I}_1, \bar{I}_2$, are the first and second deviatoric strain invariants, respectively, and C_1 and C_2 the corresponding material-dependent constants[10].
The principal stretches, λ_i, for $i = 1, \ldots, 3$, are related to the principal nominal strains, ϵ_i, by:

$$\lambda_i = 1 + \epsilon_i \tag{4.23}$$

[10]This hyperelastic model is also known as the Mooney-Rivlin (MR) model.

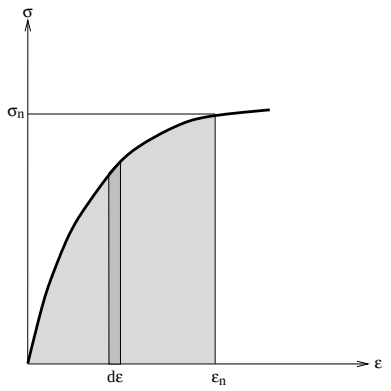

Figure 4.9: Hyperelastic relation between stress σ and strain ϵ.

The deformation gradient, expressed in the principal directions of stretch is given by:

$$\mathbf{F} = \begin{bmatrix} \lambda_1 & 0 & 0 \\ 0 & \lambda_2 & 0 \\ 0 & 0 & \lambda_3 \end{bmatrix} \tag{4.24}$$

Assuming incompressibility and isothermal response we obtain $\det \mathbf{F} = 1$, which implies:

$$\prod_{i=1}^{3} \lambda_i = 1 \tag{4.25}$$

The deviatoric strain invariants in terms of the principal stretches are then given by:

$$\begin{aligned} \bar{I}_1 &= \sum_{i=1}^{3} \lambda_i^2 \\ \bar{I}_2 &= \sum_{i=1}^{3} \lambda_i^{-2} \end{aligned} \tag{4.26}$$

For more in depth coverage of the Mooney potential, see chapter 7 of [66]. General theory on hyperelasticity can be found in the Theory Manual of the ABAQUS FE software [40].

Chapter 5

Analysis of deformation of the foetal skull: The Model

5.1 Introduction

The aim of this chapter is to establish a biomechanical model for the analysis of deformation of the foetal skull when it is subjected to labour forces. This model will be used in the next chapter to perform a series of experiments aimed at the assessment of foetal skull moulding during labour.
In Chapter 4, the importance of how close the physical model should reflect reality was emphasised. A model of sufficient complexity is required to yield a realistic solution but on the contrary, a too complex model should be avoided since it might not produce a solution at all.
The processes involved with the expulsion of the foetus from the uterus and the resulting deformation of the head are complex, hence some simplifications have to be made.
Before making any assumptions, let us first describe the three stages[1] involved during the process of birth:

The first stage starts from the onset of *true labour* characterised by the increase of frequency and intensity of contractions which causes the foetus to be pressed against the lower uterine pole and the cervix to dilate. This stage is completed when the cervix reaches full dilatation. Two phases can be identified: the *latent phase* and the *active phase*. In the *latent phase* the cervical dilatation is less than 3 cm. and contractions may be infrequent. Full dilatation is conventionally taken as 10 cm., a value which is reported by both Friedman [30] and Hendricks et al. [39].

The second stage starts at full dilatation of the cervix. The foetus is expelled

[1] See also Figures D.8 and D.9 in Appendix D.

from the uterus and travels through the vagina. The second stage finishes when the baby is delivered.

The third stage starts at the delivery of the baby and ends when the placenta and membranes are fully expelled and the uterus has retracted firmly to compress the uterine blood sinuses.

The third stage is obviously not within our interest.
The second stage is important with regard to the moulding of the foetal head but requires the knowledge of soft tissue characteristics of the pelvic floor and vagina, which are not commonly known. The position of the head in contact with the birth canal and possibly the bony pelvis is difficult to assess and depends a lot on the cephalo-pelvic proportions. Pressures acting on the head depend on the contact between the head and birth canal and will therefore be non-uniform in time and space. From a mechanical point of view we can classify this situation as a mechanical contact problem which is of a non-linear nature.

This leaves us with the first stage of labour where the foetal head is in contact with the cervix. Lindgren et al. [52–58], did extensive work on the measurement of amniotic pressure and the pressure between the cervix and the foetal head. Bell [10] worked out several theoretical models based upon the findings by Lindgren. More recent work on the measurement of pressures are by Allman et al. [3], Antonucci et al. [5], Beazley [9], Furuya et al. [33], Gough et al. [35], Moolgaoker [74], Rempen and Kraus [85, 86] and Svenningsen et al. [97].

The study of foetal head moulding during the first stage of labour is justified for uncomplicated deliveries which do not involve cephalo-pelvic disproportion. The importance of the first stage to foetal head moulding was pointed out in a study by Lindgren and Smyth [52]. Moreover, the first stage involves in most cases about 90% of the entire duration of labour [10].

Reliable measurements of material properties of the different components of the foetal skull are another important issue for a successful analysis of deformation. The research as performed by McPherson and Kriewall involving the evaluation of the elastic modulus of foetal cranial bone [71], the work by Bylski et al. on foetal dura mater [14] and the work by McElhaney et al. [67, 68] on the material properties of adult skull bones and soft tissue are all major contributions in this context.

In reality, the entire process of expulsion of the foetus is dynamic. However, since uterine contractions change very slowly in time and cervical dilatation, starting from the onset of labour until full dilatation, takes several hours, the assumption of a static model is justified.

Having decided to limit the modelling of foetal head moulding to the first stage of labour plus the availability of data on loading conditions and material properties, we can now design a static model to analyse the deformation of the skull. However, a crucial piece of information is missing: how can we validate the model?
The answer lies in studies done by Kriewall et al. [47] and Sorbe and Dahlgren [94], involving the measurements of several cephalic diameters shortly after birth and three days later to allow for sufficient restitution after moulding. Inverse interpretation of these measurements provides us with data, suitable for validation of our model. Moreover, since the cases studied in [47, 94] involved normal vaginal deliveries without serious complications, the results are suitable for the validation of a model which is restricted to the first stage of labour.
In the next sections, I will describe the necessary pre- and postprocessing steps to perform and respectively evaluate the analysis of deformation of the foetal skull[2]. Each of the sections outlines a concept as described above. Findings from earlier research are interpreted and tailored into a model to be used for analysis. The sections include:

- Establishment of the load distributions and loading conditions.
- The material properties of foetal skull bone and sutures.
- Validation of the results.

5.2 Load distributions and loading conditions

5.2.1 The origin of forces during labour

During pregnancy, the foetus resides in the uterus which is filled with amniotic fluid. The net intra-uterine pressure, IUP, also referred to as amniotic pressure, AP, is fairly low in the early stages of pregnancy with peak pressures up to about 10 mmHg. and a contraction frequency of 2-3 contractions per hour [22]. This pattern gradually increases so that by the third trimester of pregnancy, the contraction frequency may have reached 4-6 contractions per hour with IUP peaks in the range of 20-40 mmHg. [99]. These contractions are painless and may cause a sensation of tightening and pressure which in the latter case are commonly known as Braxton-Hicks contractions. The first stage of labour starts with, what is in obstetrical terms known as, the onset of labour. It is defined as the development of regular, painful uterine contractions producing progressive

[2]Note that the first and most important step of pre-processing is the establishment of a valid geometry, a prerequisite which was covered in Chapters 2 and 3.

dilatation of the cervix [99]. *IUP* peaks can reach values up to about 100 mmHg., and possibly even higher in exceptional cases such as uterine spasms [56], and the contraction frequency increases to about 3-5 contractions per ten minutes.

5.2.2 Intra-uterine pressure (*IUP*) and head-to-cervix pressure (*HCP*) measurements

Measurements of intra-uterine pressure, *IUP*, and head-to-cervix pressure, *HCP*, have been performed by a variety of researchers. One of the main problems in the interpretation and summary of these measurements is the variation in terms of representation. Figure 5.1 shows an idealised curve of the amniotic pressure. The distinction between peak pressure and active peak pressure (peak pressure minus basal pressure) is clear from the figure but unfortunately not always from the reported values in the literature! Other obscurities result from reporting mean and maximum values. Mean values of a population sample of n patients with pressure measurements over m contractions can involve double averaging. Maximum values can be averaged over the number of contractions m and the sample size n or can be absolute maxima. Therefore it is not straightforward to report summary values from a range of investigators. Nonetheless, an attempt was made of which the result is shown in Table 5.1, an extended and more comprehensive version of the summary table as reported by Rempen and Kraus [85] and based on values reported in [5, 33, 54, 74, 85, 97, 101]. The variations of the reported values amongst different researchers is apparent and may also be explained by the following facts:

- For the measurement of *HCP*, it is generally difficult to keep the pressure/force sensors in place between the sliding head and the uterine cervix, thus inaccuracies may result.

- Furuya et al. [33], Moolgaoker [74], Rempen and Kraus [85] and Svenningsen et al. [97] measured the pressure during the *second stage* of labour. Normally, higher peak values could be expected as compared to measurements during the first stage[3]. The accuracy may be lower as well since it is even more difficult to keep transducers in place.

- Factors such as parity, location of measurement, latent or active phase, rupture of the membranes and degree of dilatation influence the pressure distribution[4]. No study takes account of all of them.

[3]Since the amniotic pressure is higher during the second stage because of increased uterine activity and maternal bearing down efforts.

[4]These factors are briefly outlined in Section 5.2.3.

Table 5.1: Head pressure measurements from different sources (mmHg.): basal = average basal pressure (*Pb*); average = average peak active pressure (*Pap*); max. = maximum peak active pressure, during contractions; n = the sample size (* = primiparae only; ** average pressure over the trace i.o. average *Pap*; *** measurements during second stage of labour).

			IUP		*HCP*		
Author	Year	n	basal	max.	basal	average	max.
Turnbull	1957	31	6-16*	20-80*	-	-	-
Lindgren	1960	10	10-11.5	108-121	17.5-76	-	127-312
Moolgaoker***	1979	44	-	-	-	98-150**	357-497
Furuya***	1981	40	21	115.5	30	-	404
Svenningsen***	1988	46	-	-	-	158	390
Rempen***	1991	42	19.5	142	41.5	-	239
Antonucci	1997	6	-	30-75	-	-	235-514

- A series of experiments as performed by Knoke et al. [42] to measure the *IUP* with three intrauterine catheters pointed out the variation due to the random placement of the catheter. The catheters were passed simultaneously into the same uterus during labour. They assessed nine women and reported variation in recorded pressure of the order of 5-10 mmHg.
- Gough et al. [35] points out that in earlier experiments (by Lindgren amongst others), the *HCP* pressure measurements are influenced by the *IUP*.

5.2.3 Perinatal factors influencing the intra-uterine pressure and head-to-cervix pressure

Lindgren's extensive research on this topic is used as a framework and work from other researchers is mentioned where necessary. Factors influencing the intra-uterine pressure, *IUP*, and head-to-cervix pressure, *HCP*, include:

Location

1. The pressure between the rim of the cervix and the head, the *HCP*, is on average greater than the amniotic fluid pressure or *IUP*. It shows an increasing trend from the lower rim towards the greatest diameter [52, 57] as shown in Figure 5.3. Figure 5.2 shows the different locations of the pressure transducers. A similar trend of the *HCP* at different locations of the head was found by Beazley [9] (see further).

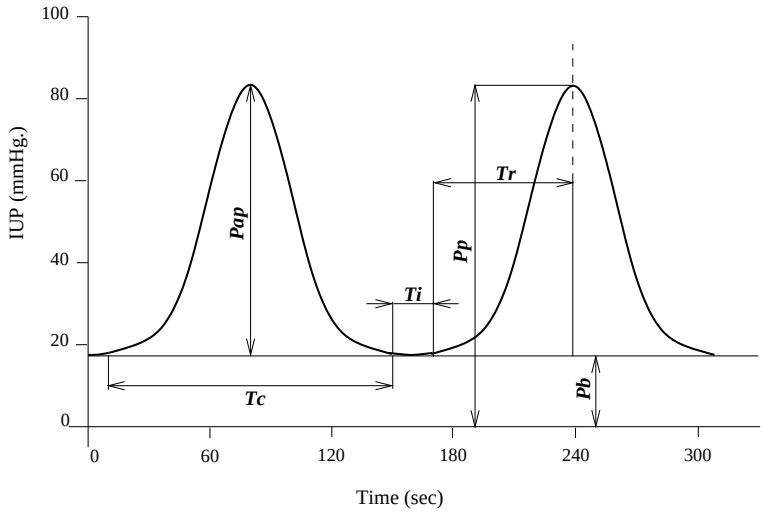

Figure 5.1: The idealised intra-uterine pressure cycle. Pp = peak pressure, Pap = active peak pressure or intensity, Pb = basal pressure or tonus, Tc = contraction period, Ti = interval period, Tr = rise of pressure period.

2. The pressure at the largest diameter of the head is proportional to the square of the increase in diameter for normal cases of labour [52]. This is shown Figure 5.4a. Figure 5.4b shows that the extension of this concept for different levels (i.e. different diameters) on the head of a single case is a plausible assumption.

Rupture of the membranes

Rupture of the membranes (ROM) results in a redistribution of the *HCP*, i.e. greater pressures at the largest diameter (Q') but lower values at 3 cm. below (Q") as compared to the pressure distribution before ROM (see Figure 5.5).

Parity and gravidity

The pressures at levels near the greatest diameter are larger for multiparae for the same *IUP* than for primiparae, according to Lindgren and Smyth [52]. Table 5.2 shows this effect which is valid for both cases of intact membranes and ruptured membranes. Results from Moolgaoker for primigravidae and multigravidae[5] [74] show lower values of the *HCP* for the latter (see Table 5.3). This appears to be in contradiction with Lindgren's results, though care has to be taken in the interpretation since the *IUP* is constant for both groups in his

[5]See Appendix D for the distinction between parity and gravidity. Note that both variables are the same if the patient did not have any abortions or ectopic pregnancies.

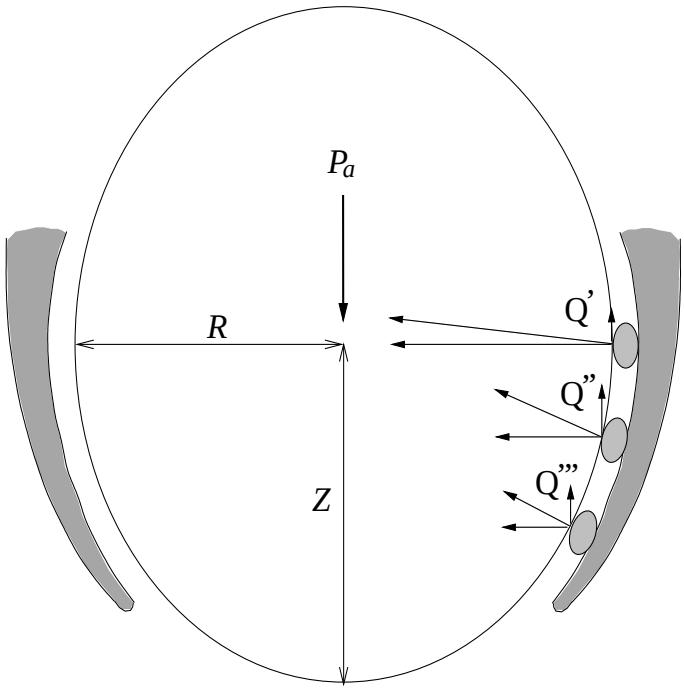

Figure 5.2: Schematic representation of an ellipsoidal foetal head in contact with the cervix, showing the location of the pressure transducers for measurement of the *HCP* (from Lindgren and Smyth, 1961 [52]). P_a is the amniotic pressure or *IUP*.

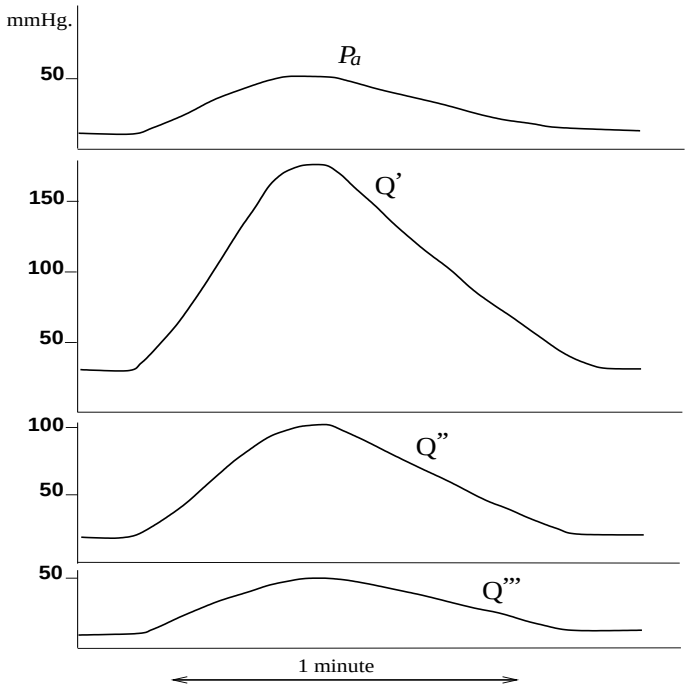

Figure 5.3: Typical values of the *IUP* and the *HCP* at three levels of the foetal head (from Lindgren and Smyth, 1961 [52]). P_a is the amniotic pressure or *IUP*. The corresponding locations of the pressure transducers, Q, are shown in Figure 5.2.

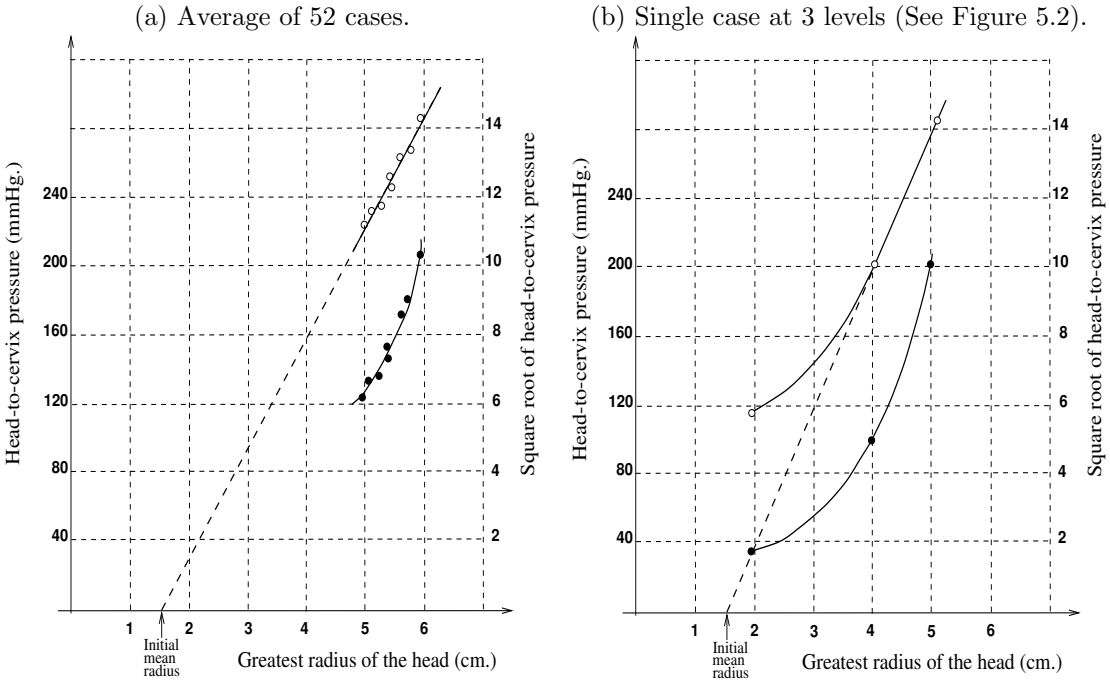

Figure 5.4: Relation of the average *HCP* and the radius of the foetal head (from Lindgren and Smyth, 1961 [52]). • == *HCP*; ∘ == Square root of *HCP*.

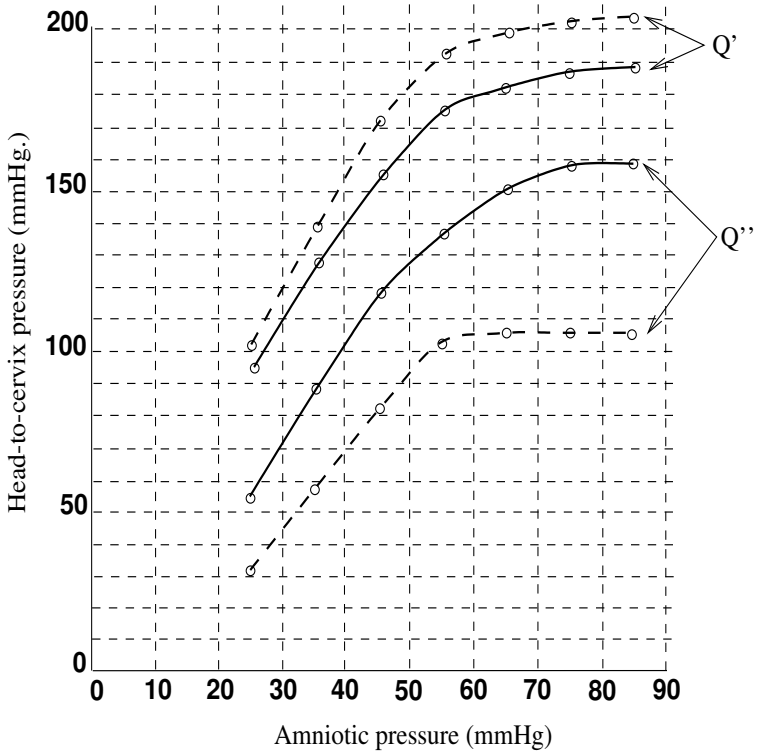

Figure 5.5: Effect of rupture of the membranes (ROM) on the pressure distribution (from Lindgren and Smyth, 1961 [52]). Solid line is before ROM; dashed line is after ROM. See Figure 5.2 for the locations of Q' and Q".

Table 5.2: Comparison of the *HCP* (mmHg.) at different levels of the head for primi- and multiparae (from Lindgren and Smyth, 1961 [52]).

	Primiparae			Multiparae		
Membranes	Q'	Q"	Q"'	Q'	Q"	Q"'
Intact	143	129	101	223	165	52
Ruptured	150	104	82	248	103	26

Table 5.3: Comparison of the *HCP* (mmHg.) at two levels of the head for primi- and multigravidae (from Moolgaoker, 1979 [74]).
aas = at or above spines; *bs* = below spines.

	Primigravidae		Multigravidae	
	aas	*bs*	*aas*	*bs*
n	11	11	11	11
Average	150	124	124	98.3
Maximum	497	445	445	357

results. Turnbull [101] reported higher values of the *IUP* for primiparae as opposed to multiparae, which would agree with Moolgaoker's findings.

Progress of labour

Beazley [9] monitored two patients, one of which showed normal progress during labour (patient A) and one which showed delayed labour (patient B). The different outcome for these patients appeared to be due to the resistance of the cervix which was measured to be 11.8 N for patient A as opposed to 190 N for patient B in the early stage of labour and was also reflected in a higher *HCP* for the latter. Table 5.4 shows the results of pressure measurements using three balloon tipped catheters inserted between the foetal head and cervix, at the levels of the lower rim, intermediate and at the maximum circumference, i.e. the level of the biparietal diameter, *BPD*. For patient B, it can be observed that during the latent phase of labour (i.e. cervical dilatation $\leq$ 3 cm.), the *HCP* is larger at lower levels than at the largest diameter of the head. This is the reverse pattern of what is usually observed during the active phase of labour.

5.2.4 Mechanisms as a cause of the head-to-cervix pressure (*HCP*) distribution

Lindgren and Smyth [52] suggested the following possible causes of the *HCP*:

Table 5.4: *HCP* measurements (mmHg.) by Beazley [9] for two patients: patient A showed normal progress during labour whilst patient B showed delayed labour. The latent phase of labour corresponds to a cervical dilatation ≤ 3 cm. The active phase corresponds to a cervical dilatation > 3 cm. Measurements are at the levels of the lower rim (Low), intermediate level (Int.) and the level of the maximum circumference (*BPD*).

Patient	Latent phase				Active phase			
	IUP	*BPD*	Int.	Low	*IUP*	*BPD*	Int.	Low
A	40	-	-	-	50	90	50	30
B	60	-	125	200	60	165	70	40

- unequalised hydrostatic pressures due to a dilated cervix,
- direct thrust along the foetal axis between the uterine fundus and the cervix and transmitted through the foetus,
- circumferential muscle bands around the largest diameter of the foetal head,
- an effect due to the constriction of the cervix and lower segments as these parts elongate axially,
- extra-uterine forces.

Figure 5.6 shows a diagram of the forces of expulsion according to Lindgren and Smyth. In Figure 5.6a the cervix is closed and the foetus is surrounded by fluid. In Figure 5.6b the cervix has opened, the membranes are still intact and there is no contact between breech and fundus. Pure hydrostatic expulsion causes a force:

$$F_1 = \frac{\pi}{4}(P_a {D_2}^2 - P_f {D_1}^2) \tag{5.1}$$

where P_a is the amniotic pressure or the *IUP* and P_f is the pressure in the forewaters[6]. In Figure 5.6c, the membranes have ruptured and there is direct contact between breech and fundus resulting in the downwards directed force F_2. Force F_1 has increased now because the resisting pressure of the forewaters, P_f, has become zero.

5.2.5 A theoretical model on the relation between the intra-uterine pressure and head-to-cervix pressure

As the results from the intra-uterine pressure and the head-to-cervix pressure measurements, as discussed in the previous sections, show significant intra- and

[6]The amniotic fluid in the bulging part of the membranes below the foetal head.

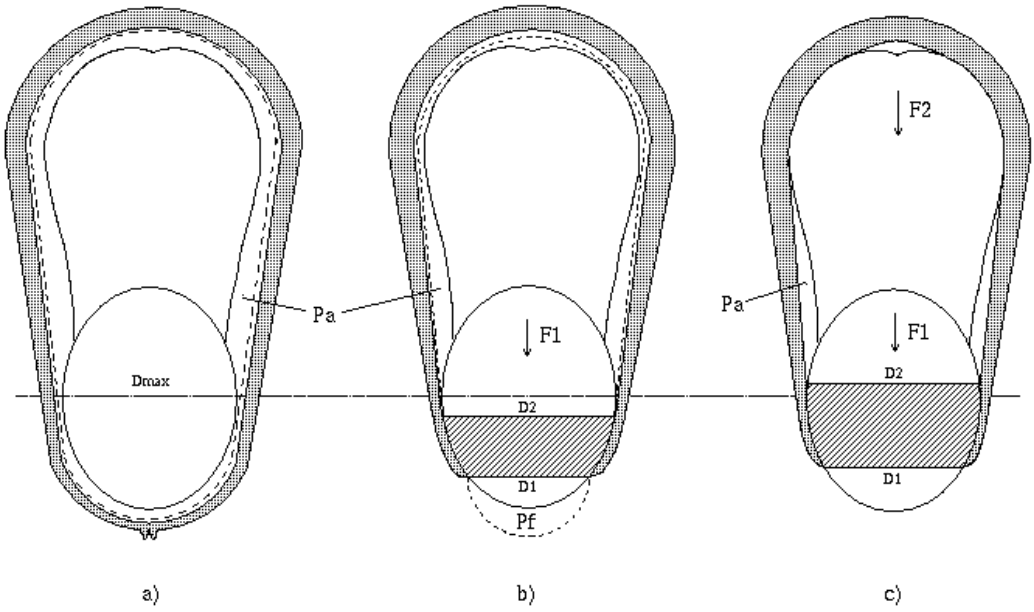

Figure 5.6: Schematic representation of a foetus in utero, subjected to forces of expulsion according to Lindgren and Smyth [52]. The dashed line corresponds to the foetal membranes. D_{max} is the maximum diameter of the foetal head; the hatched area is the area of head-to-cervix contact with lower and upper diameters D_1, D_2, respectively; P_a is the amniotic pressure; F_1 is the resultant force due to pure hydrostatic expulsion; F_2 is the force due to direct contact between breech and uterine fundus; P_f is the pressure in the forewaters. See text for further explanation.

inter-variability amongst researchers, it is difficult to define a load distribution solely based on these experimental values. Moreover, none of the researchers has studied a significant sample of the population nor did they report values over the entire range of cervical dilatation for an individual patient. Therefore a theoretical model, which fits the experimental data to the best possible degree, is needed.

Lindgren's model

Lindgren and Smyth[52] proposed the following theory based on the helicoidal organisation of the fibrous and muscular structure of the lower segment of the uterus and the cervix (Figure 5.7). From Figure 5.7b, calculating the equilibrium of forces based on the principle of virtual work[7]:

$$wL\,P_r\,dR = -\pi R^2 P_a\,dH \tag{5.2}$$

[7]Note that an increase of dR causes a decrease of dH and vice versa. L is assumed to be constant.

with:

R	the radius of the largest diameter of the head,
w	the width of the helix,
L	the length of the helix,
P_a	the amniotic pressure or IUP,
P_r	the radial pressure, exerted by the cervix or HCP.

Since the fibres of the uterus are organised in clockwise and anti-clockwise directions, the structure cannot unwind hence the length L can be calculated from:

$$L^2 = H^2 + (2\pi nR)^2 \tag{5.3}$$

with H, the length of contact in the vertical direction and n, the number of turns. Differentiating Equation 5.3 yields:

$$\frac{dH}{dR} = -4\pi^2 n^2 \frac{R}{H} \tag{5.4}$$

The contact area wL is related to the height H as:

$$H = \frac{wL}{2\pi R} \tag{5.5}$$

Combining Equations 5.2, 5.4 and 5.5 yields an expression for the radial to amniotic pressure ratio:

$$\frac{P_r}{P_a} = \frac{2\pi^2 n^2 R^2}{H^2} \tag{5.6}$$

Equation 5.6 shows that the ratio of the radial pressure, P_r, and the amniotic pressure, P_a, is proportional to the square of the largest radius of the foetal head, R^2, the square of the number of turns, n^2, and inversely proportional to the square of the length of head-to-cervix contact, H^2.
Lindgren's model suffers from the following shortcomings:

- The HCP/IUP ratio is constant for a particular degree of dilatation, thus pressures at different levels of the head are constant. This contradicts Lindgren's claims that the pressure varies at different levels and is largest at the level of the largest diameter of the head.
- Equilibrium had to be based on the concept of virtual work[8].
- Note that Lindgren ignores the force on the buttocks, F_2, as shown in Figure 5.6c.
- The area of contact between the cervical helix and the head is an overestimate since windings will overlap.

[8]Because the resultant forces of P_a and P_r in the model are orthogonal.

(a) Helicoidal structure of uterine and cervical tissue.

(b) Diagram of the cervical helix in contact with the foetal head.

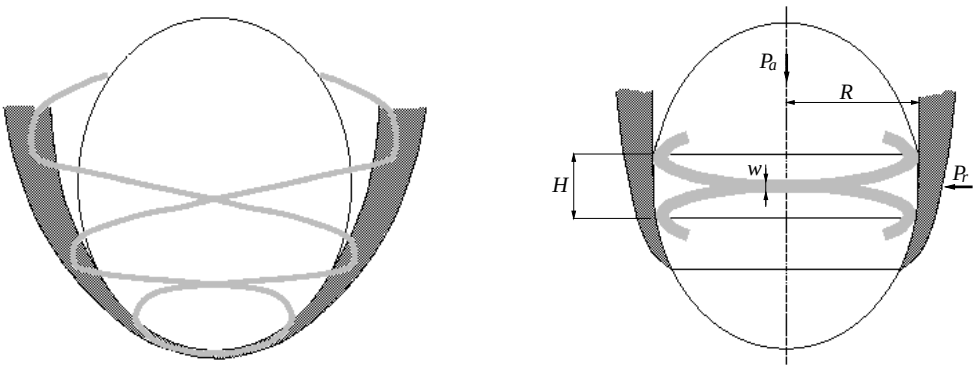

Figure 5.7: Structure of the uterus and cervix (originally from W. Langreder (1956) and reported in [52]).

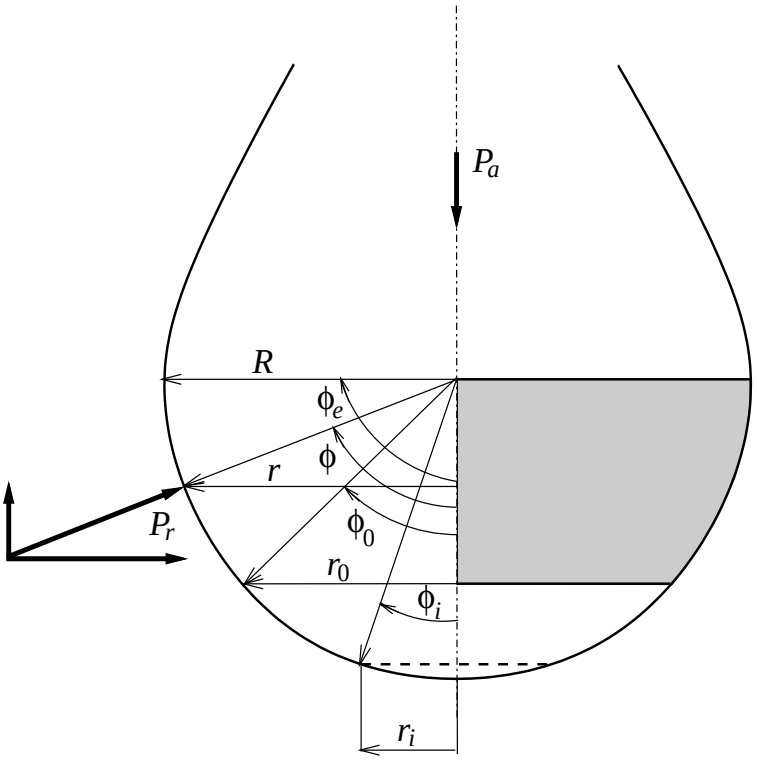

Figure 5.8: Bell's model: a spherical lower pole of the foetal head is in contact with the cervix. The dark-coloured patch shows the right half of the head-to-cervix contact area. P_r is the radial pressure (HCP), P_a is the amniotic pressure (IUP), R is the largest radius of the foetal head, r_i is the radius of initial dilatation and r_0 is the radius of the current dilatation.

Bell's model

Equation 5.6 shows that the radial pressure, P_r, is proportional to R^2 for a constant IUP. Figure 5.4a shows that the pressure in normal cases is related to the square of the *increase* in diameter for different cases. Figure 5.4b shows that this assumption is reasonable for an individual case.
Based on Lindgren's findings, Bell [10] worked out several pressure distributions assuming a spherical lower pole of the head (Figure 5.8).
Two possible configurations based on a quadratic relation between pressure and radius are considered:

- *Pressure distribution 1:* the radial pressure is proportional to the *square of the radius* of the head at all levels.
- *Pressure distribution 2:* the radial pressure is proportional to the *increase of the square of the radius* of the head at all levels.

The equilibrium equation in the vertical direction is given by:

$$P_a \pi R^2 = \int_{\phi_0}^{\phi_e} P_r \cos\phi \, 2\pi r R \, d\phi \tag{5.7}$$

Pressure distribution 1

$$P_r = Cr^2 \tag{5.8}$$

where C is a constant.
Substituting Equation 5.8 into Equation 5.7, using the relation $r = R\sin\phi$ and working out:

$$\begin{aligned} P_a \pi R^2 - 2\pi \int_{\phi_0}^{\phi_e} Cr^2 R^2 \cos\phi \sin\phi \, d\phi &= 0 \\ P_a - 2\int_{\phi_0}^{\phi_e} CR^2 \cos\phi \, \sin^3\phi \, d\phi &= 0 \\ P_a - \frac{CR^2}{2}[\sin^4\phi]_{\phi_0}^{\phi_e} &= 0 \end{aligned} \tag{5.9}$$

Assuming:

$$\phi_e = \frac{\pi}{2} \tag{5.10}$$

and defining the cervical dilatation, D, as:

$$D = \sin\phi_0 = \frac{r_0}{R} \tag{5.11}$$

and the ratio of the local radius and the greatest radius of the head:

$$\gamma = \frac{r}{R} \tag{5.12}$$

then substitution of Equations 5.8, 5.10, 5.11 and 5.12 into Equation 5.9 yields the following expression, relating the radial pressure, P_r, to the amniotic pressure, P_a:

$$\Pi_1 = \frac{P_r}{P_a} = \frac{2\gamma^2}{1 - D^4} \tag{5.13}$$

Pressure distribution 2

$$P_r = C(r - r_i)^2 \tag{5.14}$$

where C is a constant.
Substituting Equation 5.14 into Equation 5.7 and working out:

$$\begin{aligned} P_a \pi R^2 - 2\pi \int_{\phi_0}^{\phi_e} C(r - r_i)^2 R^2 \cos\phi \, \sin\phi \, d\phi &= 0 \\ P_a - 2 \int_{\phi_0}^{\phi_e} CR^2 \cos\phi \sin^3\phi \, d\phi + & \\ 4 \int_{\phi_0}^{\phi_e} Cr_i R \cos\phi \, \sin^2\phi \, d\phi - 2 \int_{\phi_0}^{\phi_e} Cr_i{}^2 \cos\phi \, \sin\phi \, d\phi &= 0 \\ P_a - \frac{CR^2}{2}[\sin^4\phi]_{\phi_0}^{\phi_e} + \frac{4Cr_iR}{3}[\sin^3\phi]_{\phi_0}^{\phi_e} - Cr_i{}^2[\sin^2\phi]_{\phi_0}^{\phi_e} &= 0 \end{aligned} \tag{5.15}$$

Substitution of Equations 5.14 and 5.11 into Equation 5.15 yields:

$$\frac{6P_a}{3R^2(1 - D^4) - 8Rr_i(1 - D^3) + 6r_i{}^2(1 - D^2)} = \frac{P_r}{(r - r_i)^2} \tag{5.16}$$

Finally, setting the initial dilatation:

$$D_i = \frac{r_i}{R} \tag{5.17}$$

and substituting together with Equation 5.12 into Equation 5.16 yields the final expression[9], relating the radial pressure, P_r, to the amniotic pressure, P_a:

$$\Pi_2 = \frac{P_r}{P_a} = \frac{6(\gamma - D_i)^2}{3(1 - D^4) - 8D_i(1 - D^3) + 6D_i{}^2(1 - D^2)} \tag{5.18}$$

Discussion Figure 5.9 shows the two pressure ratios, Π_1 and Π_2, as a function of γ for dilatation, $D = 0.9$, 0.7, 0.5 and 0.3, respectively, and $D_i = 0.3$. Figure 5.10 shows the pressure ratios, Π_1 and Π_2, at the largest diameter of the head as a function of D for $D_i = 0.3$ and $\gamma = 1$. From both figures, it can be seen that pressure distribution 2 has slightly higher peak values than

[9]Note that substitution of $D_i = 0$ yields Equation 5.13.

pressure distribution 1 for all dilatations near the largest diameter of the head. At lower levels closer to the cervical rim, this pattern is reversed thus making distribution 1 less steeper than distribution 2.
Although the difference between the two pressure distributions is small, pressure distribution 2 is preferred as a model for the loading distribution on the foetal skull because:

- It supports Lindgren's theory of the pressure being, in normal cases, related to the square of the increase in diameter.
- The pressure must be zero near the initial mean radius which is effectively larger than 0 and generally considered to be 1.5 cm. (which corresponds to $D_i = 0.3$).
- Peak values near the largest diameter of the head are higher than for pressure distribution 1 (worst case).

Assuming a *IUP* of 50 mmHg., the *HCP* for $D = 0.9$, is slightly more than 300 mmHg. for Π_2 (see Figure 5.10). This value does agree with the maximum value reported by Lindgren as shown in Table 5.1. Higher degrees of dilatation or higher values of the *IUP* would yield maximum values of the *HCP* corresponding to values as for example reported by Antonucci et al. [5] (see Table 5.1).

5.3 Material properties

5.3.1 Material properties of foetal cranial bone

Fibres from foetal cranial bone emanate from the centres of ossification, a property which can be seen from Figures 2.1 and 2.2 in Chapter 2. McPherson and Kriewall [71] showed that foetal cranial bone is an in-plane orthotropic material which displays different material properties in tangential and radial (perpendicular) directions relatively to the direction of the fibres.
From the formulation of a general isotropic material (Equation 4.19), we can derive the constitutive relations for an in-plane (2D) orthotropic material in matrix form (using single indices if the first and second index are the same):

$$\begin{bmatrix} \epsilon_1 \\ \epsilon_2 \\ 2\epsilon_{12} \end{bmatrix} = \begin{bmatrix} \frac{1}{E_1} & -\frac{\nu_{21}}{E_2} & 0 \\ -\frac{\nu_{12}}{E_1} & \frac{1}{E_2} & 0 \\ 0 & 0 & \frac{1}{G} \end{bmatrix} \begin{bmatrix} \sigma_1 \\ \sigma_2 \\ \sigma_{12} \end{bmatrix} \tag{5.19}$$

with E_1, E_2, the elastic moduli in the two in-plane directions, respectively; ν_{12}, ν_{21}, Poisson's ratios; G, the in-plane shear modulus.

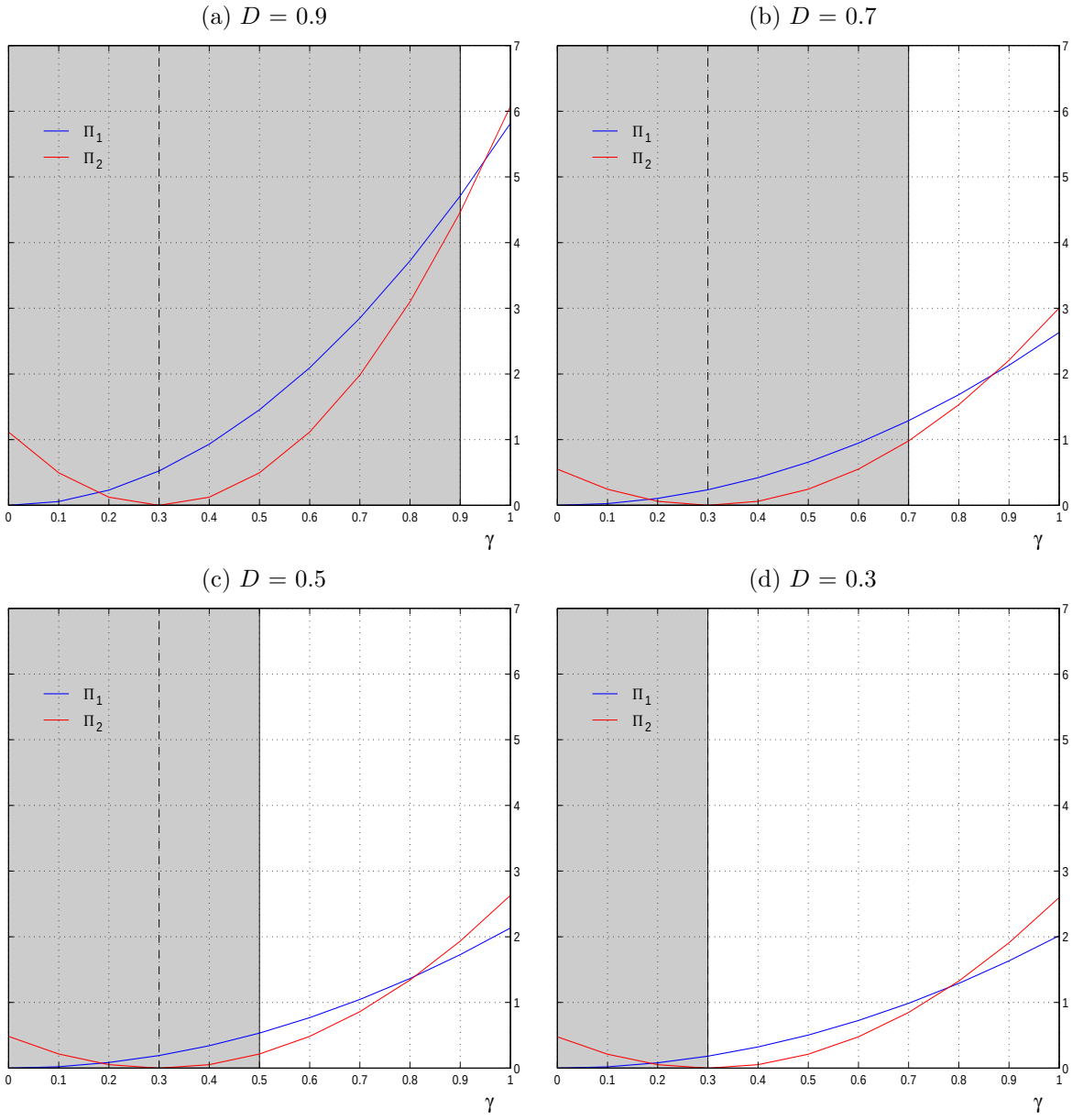

Figure 5.9: Pressure ratios, Π_1 (*blue* colour) and Π_2 (*red* colour), for different dilatations, D, as a function of the ratio of the local radius and the largest radius of the head, γ (the valid region is coloured white). $D_i = 0.3$.

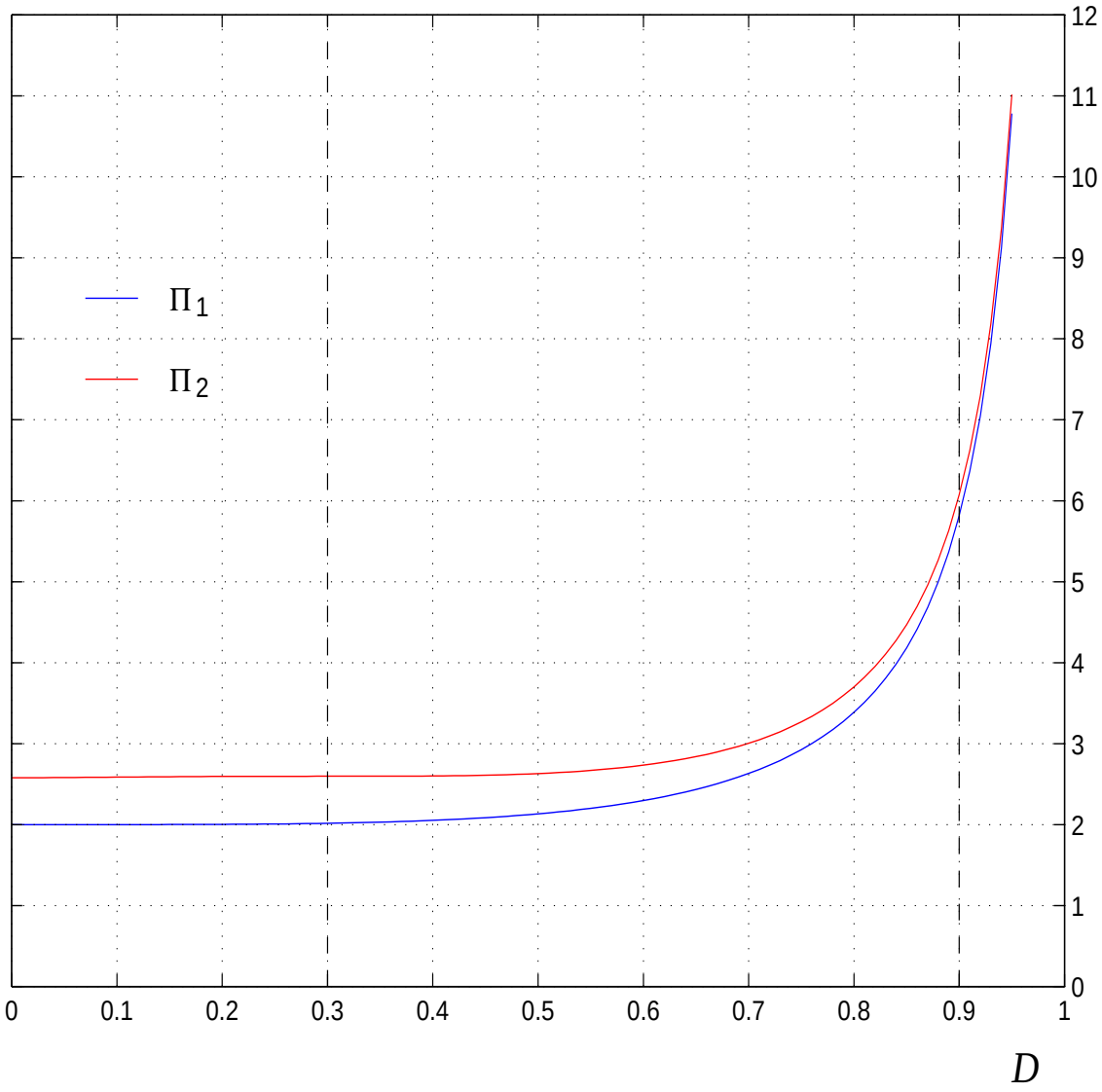

Figure 5.10: Pressure ratios, Π_1 (*blue* colour) and Π_2 (*red* colour), at the maximum diameter of the head as a function of cervical dilatation, D.
$D_i = 0.3$.

Writing Equation 5.19 for σ_{ij} as a function of ϵ_{kl} (Equation 4.20) gives[10]:

$$\begin{bmatrix} \sigma_1 \\ \sigma_2 \\ \sigma_{12} \end{bmatrix} = \begin{bmatrix} \frac{E_1}{1-\nu_{12}\nu_{21}} & \frac{\nu_{12}E_2}{1-\nu_{12}\nu_{21}} & 0 \\ \frac{\nu_{21}E_1}{1-\nu_{12}\nu_{21}} & \frac{E_2}{1-\nu_{12}\nu_{21}} & 0 \\ 0 & 0 & \frac{E_1}{2(1+\nu_{12})} \end{bmatrix} \begin{bmatrix} \epsilon_1 \\ \epsilon_2 \\ 2\epsilon_{12} \end{bmatrix} \tag{5.20}$$

McPherson and Kriewall [72] found the following values for the elastic moduli of foetal cranial bone, with index 1 denoting the direction tangential to the fibres and index 2 denoting the direction perpendicular to the fibres:

$$\begin{aligned} E_1 &= 3.860 \text{ GPa} \\ E_2 &= 0.965 \text{ GPa} \end{aligned}$$

No values of Poisson's ratio were derived for foetal cranial bone. McElhaney et al. [68] reported a value, $\nu = 0.22$, for tangential compression of adult cranial bone. We will use this value as an estimate for ν_{12}.
For a body in plane stress, the in-plane shear stress components on perpendicular faces must be equal in magnitude [21]:

$$\mathbf{E}_{12} = \mathbf{E}_{21} \tag{5.21}$$

which gives us an expression for ν_{21}:

$$\nu_{21} = \frac{\nu_{12}E_2}{E_1} \tag{5.22}$$

which yields, after substitution of E_1, E_2 and ν_{12}: $\nu_{21} = 0.055$.
Having obtained all the necessary constants we can calculate the elasticity matrix, $\mathbf{E}$, from Equation 5.20:

$$\mathbf{E} = \begin{bmatrix} 3.907 & 0.215 & 0 \\ 0.215 & 0.977 & 0 \\ 0 & 0 & 1.582 \end{bmatrix} \tag{5.23}$$

Since shell elements are used to model the foetal skull, shear stresses and strains in the z-direction (direction perpendicular to the shell surface) have to be considered which requires the elasticity matrix, $\mathbf{E}$, to be extended to 3D. Since experimental values are not available, shear components in the z-direction are given the same value as $\mathbf{E}_{33}$ in Equation 5.23. Thus the sparse 3D elasticity

[10] Note that the derivation of the shear modulus, G, is based on the assumption that the material is in-plane isotropic rather than in-plane orthotropic.

matrix becomes[11]:

$$\mathbf{E} = \begin{bmatrix} 3.907 & 0.215 & 0 & 0 & 0 & 0 \\ 0.215 & 0.977 & 0 & 0 & 0 & 0 \\ 0 & 0 & 0 & 0 & 0 & 0 \\ 0 & 0 & 0 & 1.582 & 0 & 0 \\ 0 & 0 & 0 & 0 & 1.582 & 0 \\ 0 & 0 & 0 & 0 & 0 & 1.582 \end{bmatrix} \tag{5.24}$$

5.3.2 Material properties of fontanelles and sutures

McElhaney [67] reported values of Young's modulus, $E = 31.5$ MPa, and Poisson's ratio, $\nu = 0.45$, of adult dura mater, under the assumption of linear elastic behaviour and near incompressibility.

Bylski et al. [14] investigated the material properties of foetal dura mater. They assumed the material to be homogeneous, isotropic, nonlinearly elastic, incompressible and undergoing large deformation when subjected to a static load (hyperelastic). Hyperelasticity was discussed in Section 4.3.7 defining the Mooney-Rivlin (MR) model, which involves the two material constants, C_1, C_2. Bylski et al. reported the following values for foetal dura mater:

$$\begin{aligned} C_1 &= 1.18 \text{ MPa} \\ C_2 &= 0.295 \text{ MPa} \end{aligned}$$

The anisotropic and viscoelastic behaviour, generally displayed by soft tissues [32], was ignored by both authors. This assumption was justified from research by Melvin et al. [73], who reported that the general variability in the adult dura mater tissue tends to overshadow the anisotropic and viscoelastic effects.

5.3.3 Material properties of the skull base and maxilla

Adult cranial bone is a transversely (tangent to the skull surface) isotropic material [109]. Material constants for the skull base and maxilla of the foetal skull have not been reported as yet. We will assume that the foetal skull base and maxilla are similar to adult cranial bone and adopt the values of Young's modulus, $E = 4.46$ GPa, and Poisson's ratio, $\nu = 0.21$, for an adult skull, as reported by McElhaney [67].

[11] The row of zeroes (third row) corresponds to zero stress and strain in the direction, normal to the mid-surface of the shell.

5.4 Validation of the model: experimental data

Validation of the model is based on experimental data as reported by Kriewall et al. [47] and Sorbe and Dahlgren [94].

5.4.1 Kriewall's research

Kriewall et al. examined 38 infants delivered at the University of Michigan Medical Center. Of the total sample, 15 infants were born by elective Caesarian section before the onset of labour, whilst the remaining 23 were delivered vaginally from vertex presentations.
Measurements of each infant were made using obstetrical calipers. The measurement of the biparietal diameter, *BPD*, bitemporal diameter, *BTD*, suboccipitobregmatic diameter, *SOBD*, occipitofrontal diameter, *OFD*, submentobregmatic diameter, *SMBD*, and mentovertical diameter, *MVD*, were made within the first hour of birth and then repeated after 24, 48, and 72 hours, respectively[12].
A moulding index was derived making the following assumptions [47]:

- Consider the foetal head as an ellipsoid with principal axes corresponding to the *BPD*, *MVD* and *SOFD*.
- To define curvature in the three-dimensional sense, the geometric mean is taken from the curvature in the two planes defined by the normals in the direction of the *SOFD* and the *BPD*, respectively.
- This product is made more sensitive by multiplication with the square of the *MVD*.

Resulting in Kriewall's moulding index:

$$MI = \frac{MVD^2}{BPD \times SOFD} \tag{5.25}$$

Results Only the *BPD*, *SOFD* and *MVD* changed significantly over the first three days postpartum. Table 5.5 shows the restitution of moulding over a three day period for each of the three diameters of the moulding index, *MI*. Table 5.6 shows the moulding indices for each group at day 0 and day 3. The moulding indices between groups were significantly different at day 0 but not at day 3.

[12] See Appendix C for the definition of foetal head/skull diameters.

Table 5.5: Restitution of three principal diameters (mm.) after moulding according to Kriewall et al. [47].

Variable	Vaginal delivery (n=23)			Caesarian section (n=15)		
	day 0	day 3	signific.	day 0	day 3	signific.
BPD	93	91	p<0.01	94	89	p<0.01
SOFD	106	108	p<0.01	106	107	-
MVD	139	135	p<0.01	129	132	p<0.01

Table 5.6: Moulding index, *MI*, before restitution (day 0) and after restitution (day 3) (from Kriewall et al. [47]).

Group	n	day 0	day 3	signific.
Vaginal	23	2.00	1.86	p<0.01
Caesarian	15	1.68	1.82	p<0.01

Discussion

- The definition of landmarks within the bregma is difficult, hence measurements show significant inter-observer and intra-observer variability (up to 2 mm. as reported by the author).
- This measurement problem might have contributed to the fact that only three of the seven diameters appeared to change significantly. The fact that the other four diameters did not contribute to the moulding could be explained by the measurement accuracy being insufficient as compared to the changes of these diameters.
- If restitutional changes can be considered in the opposite direction of changes from moulding, then the sensitivity of the moulding index is not optimal. Consider the effects of moulding on the *MVD* and the *BPD*: both variables increase during moulding, however the *MVD* occurs in the numerator of Equation 5.25 and the *BPD* in the denominator.
- Similar effects in restitution for the *BPD* and the *SOFD* occur for both groups, i.e. vaginal delivery and Caesarian section. Only the *MVD* appears to display different restitution between groups. This finding might point out that the group involving Caesarian sections is not an ideal control group [47]. However, the *reverse* moulding behaviour could be due to the amniotic pressure changes before the onset of labour.

5.4.2 Sorbe and Dahlgren's research

Sorbe and Dahlgren [94] investigated 319 vaginal deliveries. They used a photographic method to document the size of the infant's head, immediately postpartum and three days later. Six different diameters were measured, i.e. the biparietal diameter, BPD, the occipito-frontal diameter, OFD, the orbito-occipital diameter, $OrOD$, the suboccipito-bregmatic diameter, $SOBD$, the maxillo-vertical diameter, $MaVD$, and the orbito-vertical diameter, $OrVD$. A modified moulding index MMI was used based on Kriewall's MI [47]:

$$MMI = \frac{MaVD^2}{BPD \times SOBD} \tag{5.26}$$

where the mento-vertical diameter, MVD, in Equation 5.25 is replaced by the maxillo-vertical diameter, $MaVD$, because it can be more accurately measured. The suboccipito-frontal diameter, $SOFD$, is replaced by the suboccipito-bregmatic diameter, $SOBD$. This change was motivated by the fact that in 94.7% of the deliveries in this study, the foetuses were delivered in *occiput anterior vertex* presentation[13], for which the $SOBD$ is the presenting (and maximum) diameter.
Table 5.7 shows the skull diameters immediately postpartum and three days later, for the entire series, primiparas and multiparas, respectively. Table 5.8 shows the modified moulding index, MMI, immediately postpartum and three days later for the same groups.

Discussion

- From both tables, we observe significant changes for the $SOBD$, $OrVD$ and $MaVD$ for primiparas. If we consider moulding as the inverse process of restitution then:
  - The $SOBD$ decreases during moulding.
  - The $OrVD$ increases during moulding.
  - The $MaVD$ increases during moulding.
- Diameters do not show significant changes for multiparas nor does the modified moulding index, MMI.
- The $SOBD$ is the least affected for multiparas whilst it does change significantly for primiparas.

[13] see Figure D.4a.

Table 5.7: Skull diameters (mm.) immediately postpartum and three days later as reported by Sorbe and Dahlgren [94].

Diam.	Day 0		Day 3		
	mean (mm.)	std. (mm.)	mean (mm.)	std. (mm.)	p
The entire series, n=319					
BPD	105.0	4.5	105.0	4.7	0.44
OFD	134.0	6.7	133.6	5.6	0.26
OrOD	131.4	6.2	131.3	4.9	0.38
SOBD	115.4	6.2	117.1	5.7	0.0008
OrVD	129.1	6.8	126.9	6.2	0.0003
MaVD	142.4	6.5	140.5	6.0	0.002
Primiparas, n=202					
BPD	105.1	4.7	105.5	4.6	0.20
OFD	134.3	7.0	134.2	5.4	0.46
OrOD	131.4	6.3	131.7	5.5	0.35
SOBD	115.4	6.4	118.1	6.0	0.0002
OrVD	130.2	6.3	127.8	5.9	0.0006
MaVD	143.3	6.3	141.2	5.5	0.003
Multiparas, n=117					
BPD	105.2	3.9	105.1	4.8	0.40
OFD	133.5	5.3	133.5	5.4	0.49
OrOD	131.5	5.6	130.6	4.0	0.11
SOBD	115.1	5.7	115.6	4.9	0.24
OrVD	127.6	6.6	126.8	6.1	0.21
MaVD	140.7	6.1	139.9	6.0	0.20

Table 5.8: Modified moulding index (*MMI*), immediately postpartum and three days later as reported by Sorbe and Dahlgren [94].

Day 0		Day 3		
mean	std.	mean	std.	p
The entire series, n=319				
1.70	0.16	1.61	0.12	p<0.001
Primiparas, n=202				
1.73	0.16	1.61	0.12	p<0.001
Multiparas, n=117				
1.66	0.15	1.61	0.11	p=0.02

- Contrary to Kriewall's findings, the *BPD* does not significantly change for either of the two groups in this study.
- The *MMI* is again not optimal, in the empirical sense, since the *BPD* does not change and the *OrVD*, which does show significant changes, is not used in the formulation of the *MMI*.

5.4.3 Landmark specification for validation

In the previous section, several diameters were used to assess the change of shape of the foetal head during the moulding process. We will use these diameters and the corresponding landmarks for validation of the results as presented in Chapter 6. Appendix C covers the definition of each diameter and corresponding landmark and shows their location on the foetal head and skull. Some landmarks as shown in Figure C.1 of Appendix C, cannot be used for measurements on the skull because they are located in the centre of a fontanelle or suture. Since we aim to measure deformations of the cranial vault, landmarks should be located on bone rather than fontanelles or sutures. This problem is solved by defining a left and right landmark, symmetrically positioned around the original landmark as is shown in Figure C.2 for the bregma.
Note that the mentum and mento-vertical diameter, *MVD*, cannot be measured because the mandible has been left out in the skull model. The submento-bregmatic diameter, *SMBD*, as reported by Kriewall [47], but not defined, is omitted because the location of the *sub-mentum* is unclear[14].

5.5 Summary

In this chapter, a model for the analysis of deformation of a foetal skull, subjected to labour forces, was presented. The model is limited to the first stage of labour. An idealised model for the pressures acting on the foetal skull, assuming the shape of the lower pole of the skull to be spherical [10], is used. Material properties of foetal cranial bone, fontanelles, sutures, skull base and maxilla were specified, based on reported values from [14, 67, 68, 71, 72]. Finally, a set of diameters and landmarks were defined for validation of experimental results which will be compared with results from clinical experiments as reported in [47, 94].

[14]The *SMBD* is just like the *MVD* of no importance in our model because the mandible is missing.

Chapter 6

Analysis of deformation of the foetal skull: The Experiments

The work presented in this chapter involves a series of experiments aimed at a better understanding of the foetal head moulding phenomenon. Theoretical concepts from FE analysis, as discussed in Chapter 4, will be adopted during the course of this chapter. Different assumptions concerning the load distribution, material properties and validation were discussed in Chapter 5 and will be applied unless otherwise stated.
The first experiment is an extension of the work by McPherson and Kriewall [72] and involves the parietal bones only.
The second experiment involves the entire skull including the parietal bones, the frontal bones, the occipital bone, the temporal bones, the skull base, the maxilla, the fontanelles and the sutures. The mandible is left out since it is not a fixed part of the cranium and is unlikely to contribute to the moulding process. Linear elastic and hyperelastic behaviour of the fontanelles and sutures are evaluated as well as the influence of material properties and pressures to the degree of moulding.
The third and final experiment presents three models of the deformation of the foetal skull, subjected to pressures during the first stage of labour, which differ in terms of speed of processing, stiffness and accuracy.

6.1 Experiment *I*

The first experiment is a parietal bone test similar to the one as performed by McPherson and Kriewall [72]. It was mentioned in Section 4.3.1, that starting the analysis with a simple model is preferred. This is why the first experiment involves the parietal bones only. During the analysis we aim to fulfil the following **objectives**:

1. to compare linear geometric analysis with non-linear geometric analysis,
2. to assess the influence of the number of elements (h-refinement) and the order of the elements (p-refinement) on the degree of deformation,
3. to compare the effect of constant thickness vs varying thickness of the parietal bone on the degree of deformation,
4. to compare the variation between the left and right parietal bone in terms of deformation,
5. to compare the results with those obtained by McPherson and Kriewall [72].

6.1.1 McPherson's parietal bone test

McPherson and Kriewall [72] reconstructed the shape of a foetal parietal bone (lhs) by using orthogonal radiographs of a foetal skull and manual determination of landmarks using orthographic projection[1]. The bone on the rhs was obtained by reflection. The model contains 64 nodes and 63 elements (see Figure 6.1). The elements are arranged in three concentric rings, each ring being of different thickness, decreasing from the centre towards the boundary. These values are based on the findings reported in [72] and we will use them throughout the course of the experiments.
The elements were first-order triangles and quadrilaterals.
The material properties of the parietal bone were considered to be orthotropic and set to $E_1 = 3.86$ GPa, $E_2 = 0.965$ GPa and $\nu_{12} = 0.28$.
Boundary conditions are shown in Figure 6.1. The nodes on the lower edge have only 1 dof, i.e. rotation about the y-axis. The nodes on the upper edge have five dof with displacements in the x-direction inhibited.
The pressure distribution is linearly distributed over the head-to-cervix contact area for dilatation 0.5, with a maximum value of the *HCP*, at the level of the *SOB* plane, of 200 mmHg., and a minimum value at the cervical rim of 50 mmHg. Above the *SOB* plane, an amniotic pressure of 50 mmHg. is present. These values show good agreement, according to the authors, with those reported in [54].
Three *relative diametral strains*, υ_1, υ_2 and υ_3, in % and used to assess the deformation of the model, are calculated from the change of diameters dm_1, dm_2 and dm_3 respectively (Figure 6.1):

[1] A similar approach as the recovery of foetal skull model *I*, as discussed in Section 2.4, but not involving active contour fitting and thin-plate spline interpolation.

Table 6.1: Relative diametral strains (%) of three diameters of the parietal bone after moulding (from McPherson and Kriewall [72]).

υ_1	υ_2	υ_3
-1.33	+1.00	-1.04

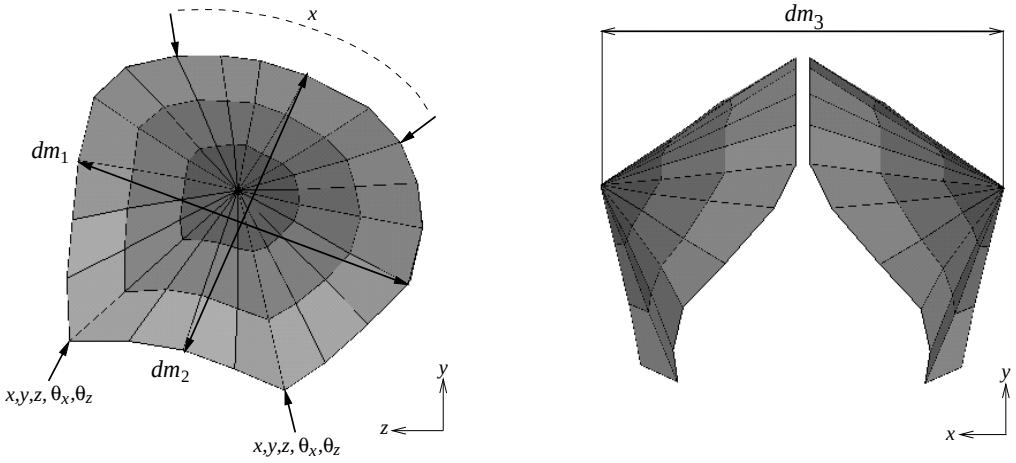

Figure 6.1: McPherson's parietal bone model. The figure on the lhs shows the boundary conditions: two nodes of the lower edge are restricted in all dof, except for rotation about the y-axis; six nodes on the upper edge are only restricted in the x-direction.

$$\upsilon_i = \frac{dm_i - dm_i^0}{dm_i^0} \times 100 \tag{6.1}$$

for $i = 1, \ldots, 3$, with dm_i^0, the original diameter.
The results of their analysis are shown in Table 6.1.

6.1.2 Parietal bone test *I*

Geometry

The left parietal bone of foetal skull model *II* is used. Six models of 277, 532, 1,058, 2,604, 5,261 and 10,537 elements, respectively, are used to assess the effect of h-refinement and were visualised in Figure 3.9. Each of the six models is modelled with first-order, constant strain triangular shell elements, *CSS* (ABAQUS - S3R), and second-order, linear strain triangular shell elements, *LSTS* (ABAQUS - STRI65), respectively, to assess the effect of p-refinement. The thickness of the parietal bone is set to an average value of 0.75 mm., based on results as reported in [72]. The axis directions are shown in Figure 6.2.

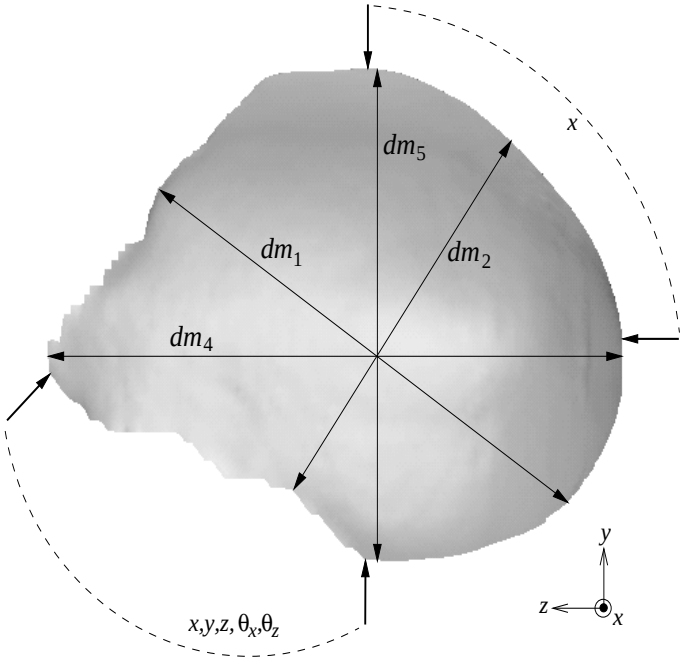

Figure 6.2: Left parietal bone: diameters measured for evaluation of deformation and boundary conditions. The nodes on the lower edge are restricted in all dof, except for rotation about the y-axis; the nodes on the upper edge are only restricted in the x-direction.

Material properties

As specified in Section 5.3.1: $E_1 = 3.86$ GPa, $E_2 = 0.965$ GPa, $G_{12} = G_{13} = G_{23} = 1.582$ GPa, $\nu_{12} = 0.22$ and $\nu_{21} = 0.055$.

Boundary conditions

Figure 6.2 shows the boundary conditions.

Loading

We adopted the linear load distribution from [72], which is shown in Figure 6.3. The *HCP* is 200 mmHg. at the level of the *SOB* plane and linearly decreases to 50 mmHg. at the level of the cervical rim for dilatation $D = 0.5$. The *IUP* (above the *SOB* plane) is 50 mmHg.

Analysis

Both linear geometric, *LG*, and non-linear geometric, *NLG*, static analyses are performed. Strains υ_1, υ_2, υ_4 and υ_5 are measured. The corresponding

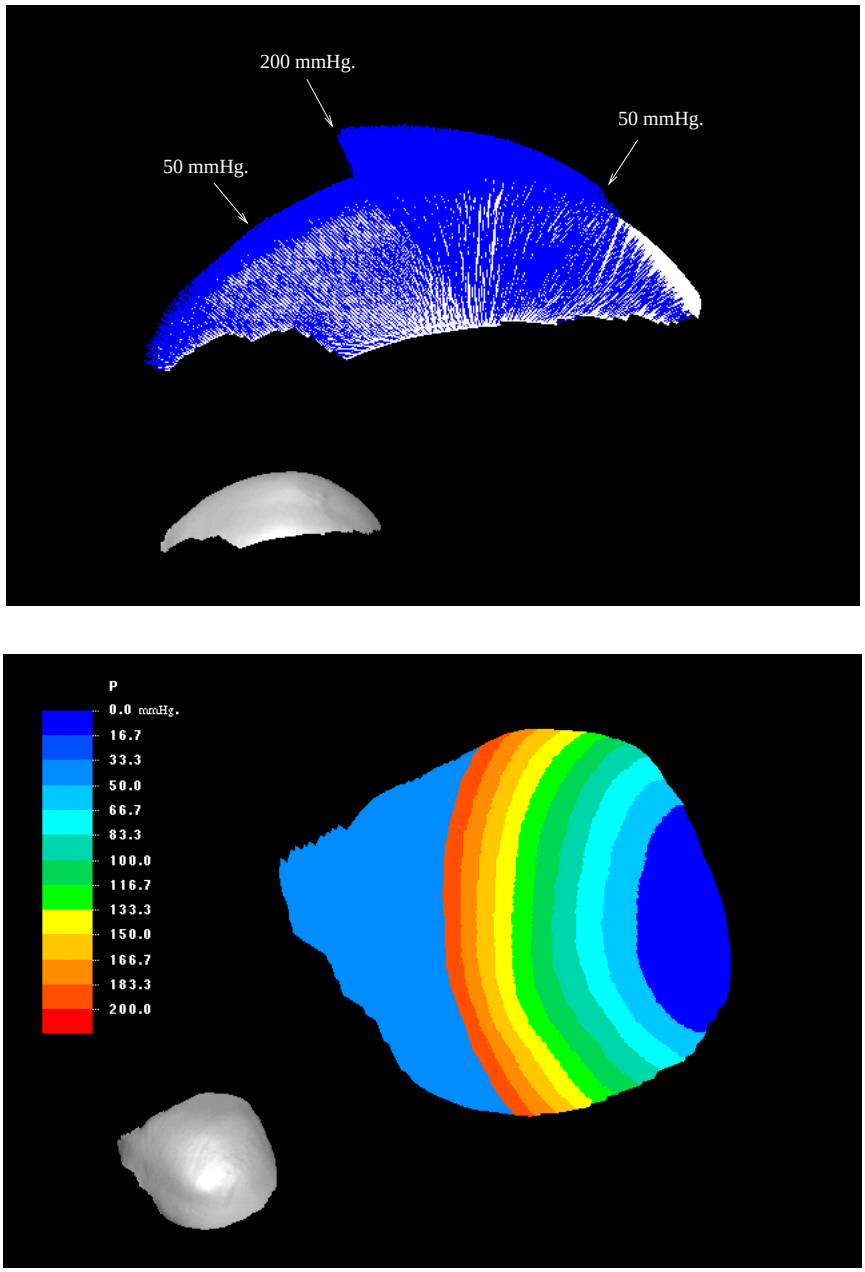

Figure 6.3: Linear pressure distribution on the left parietal bone at dilatation $D = 0.5$. The top figure shows the left parietal bone projected in the x-z plane. The pressure is visualised with normals at each node of the underlying mesh. The location where the pressure increases from 50 mmHg. to 200 mmHg. is determined by the intersection of the bone with the *SOB* plane (see Figure 6.9 for the location of the *SOB* plane on the foetal skull). The bottom figure shows the left parietal bone, projected in the y-z plane. The pressure distribution is visualised using a colour code.

Table 6.2: Parietal bone test I: average diameters and standard deviation of the undeformed models (mm.).

dm_1	dm_2	dm_4	dm_5
73.5 ±0.5	59.6 ±0.3	85.7 ±0.7	67.6 ±0.6

diameters are shown in Figure 6.2. Equation 6.1 explains the relation between strain υ_i and diameter dm_i.

Results

Diameters, before and after deformation, were measured by orthogonally projecting the parietal bone in the y-z plane. Strains can be calculated then by the application of Equation 6.1. The absolute error on the distance measurements is 0.05 mm.
Table 6.2 shows the diameters of the undeformed models.
Table 6.3 shows the strains for linear and non-linear analyses, respectively, for both constant-strain shells, *CSS*, and linear strain thin shells, *LSTS*.
Figure 6.5 shows the original parietal bone (*red* colour) and deformed parietal bone (*blue* colour) for all models, at a deformation magnification of 5.

Discussion

Reliability of results and errors: The results from Table 6.3 are subject to a small relative error based on the absolute measurement error and the accuracy by which landmarks can be located for measurement. The latter depends on the geometry of the boundary which is less detailed for coarser models. The error can be represented by the standard deviation of the original diameters as reported in Table 6.2.

Linear vs Non-linear geometry: The strains υ are, in all the cases, significantly higher for the analyses assuming *NLG*. This implies that the assumption of *NLG* is justified and should be considered in further experiments despite the requirement of significantly longer processing times as is shown in Table 6.4 for model 1. Processes were run on a SGI-Indigo-2 with MIPS R10000 processor. The CPU time is more than 13 times longer for *CSS*'s and more than 16 times for *LSTS*'s. The relative improvement for υ_1 is however more than 100% for both *CSS*'s and *LSTS*'s (Table 6.3).

p-refinement or first-order elements, *CSS*, vs second-order elements, *LSTS*.

Table 6.3: Parietal bone test I: relative diametral strains (%) for six models of decreasing geometric complexity (the relative error is specified as a percentage of the strain!).

υ_1 (relative error = 1%)

model	n	*LG-CSS*	*LG-LSTS*	*NLG-CSS*	*NLG-LSTS*
1	10,537	-2.17	-2.32	-4.83	-5.36
2	5,261	-1.22	-1.46	-1.86	-2.81
3	2,604	-0.93	-1.35	-1.52	-2.18
4	1,058	-1.04	-1.47	-1.58	-2.83
5	532	-1.48	-1.86	-2.91	-4.37
6	277	-1.21	-1.80	-1.93	-3.84

υ_2 (relative error = 1%)

model	n	*LG-CSS*	*LG-LSTS*	*NLG-CSS*	*NLG-LSTS*
1	10,537	+1.56	+1.74	+3.16	+3.64
2	5,261	+0.83	+1.04	+1.18	+1.89
3	2,604	+0.64	+0.81	+0.81	+1.27
4	1,058	+0.68	+0.81	+0.83	+1.56
5	532	+0.87	+1.20	+1.32	+2.22
6	277	+0.72	+1.08	+0.89	+1.77

υ_4 (relative error = 1%)

model	n	*LG-CSS*	*LG-LSTS*	*NLG-CSS*	*NLG-LSTS*
1	10,537	+1.89	+1.99	+2.32	+2.52
2	5,261	+1.09	+1.33	+1.34	+1.72
3	2,604	+1.24	+1.56	+1.43	+1.79
4	1,058	+1.30	+1.64	+1.50	+1.98
5	532	+1.34	+1.94	+1.60	+2.36
6	277	+1.22	+1.80	+1.36	+2.08

υ_5 (relative error = 1%)

model	n	*LG-CSS*	*LG-LSTS*	*NLG-CSS*	*NLG-LSTS*
1	10,537	+2.35	+2.58	+4.74	+5.21
2	5,261	+1.20	+1.60	+2.04	+3.12
3	2,604	+0.86	+1.16	+1.16	+2.28
4	1,058	+0.71	+1.14	+1.39	+3.57
5	532	+1.42	+1.97	+3.01	+4.52
6	277	+0.99	+1.68	+1.62	+3.68

Table 6.4: Analysis times (sec.) for model 1 (10,537 elements).

Time (sec.)	*LG-CSS*	*NLG-CSS*	*LG-LSTS*	*NLG-LSTS*
User time	42.220	580.84	111.05	1895.8
System time	10.800	129.60	24.790	380.23
Total CPU time	53.020	710.44	135.84	2276.0
Wallclock time	62.000	1070.0	203.00	4146.0

The *LSTS*'s show better performance than the *CSS*'s for all cases. The effect of p-refinement is however much smaller than the effect of *LG* vs *NLG*. The relative difference decreases for more complex models as is shown in Figure 6.4 for all strains, obtained from a non-linear analysis. The time spent to analyse second-order elements is higher than for first-order elements which is illustrated in Table 6.4, columns 1 and 3 for linear analysis, and columns 2 and 4 for non-linear analysis.

h-refinement or in this case *h-coarsening* displays a peculiar behaviour as compared to the mainstream belief that models of higher mesh refinement are less stiff than coarser models. It is clearly shown in Figures 6.4 and 6.5 that some coarser models show higher degrees of deformation than corresponding finer models. The answer may lie in the following explanations:

- *Geometry:* When the model becomes too coarse, it tends to behave as a *bent plate* rather than a *shell*. This means the inherent stiffness due to the smooth curvature of the shell is lost. In Section 4.3.5, we observed a similar phenomenon with a square plate subjected to a uniform transverse load. Figure 4.5 showed how a coarser mesh can display less stiff behaviour than a finer mesh.
- *Boundary conditions:* The boundary conditions become less 'strict' for coarser models since they contain less boundary nodes. This may result into larger rotations in between nodes.

6.1.3 Parietal bone test *II*

Most of the conditions and parameter settings are the same as for test *I*. The sole difference is the involvement of the right parietal bone and the *varying thickness* of the bones.

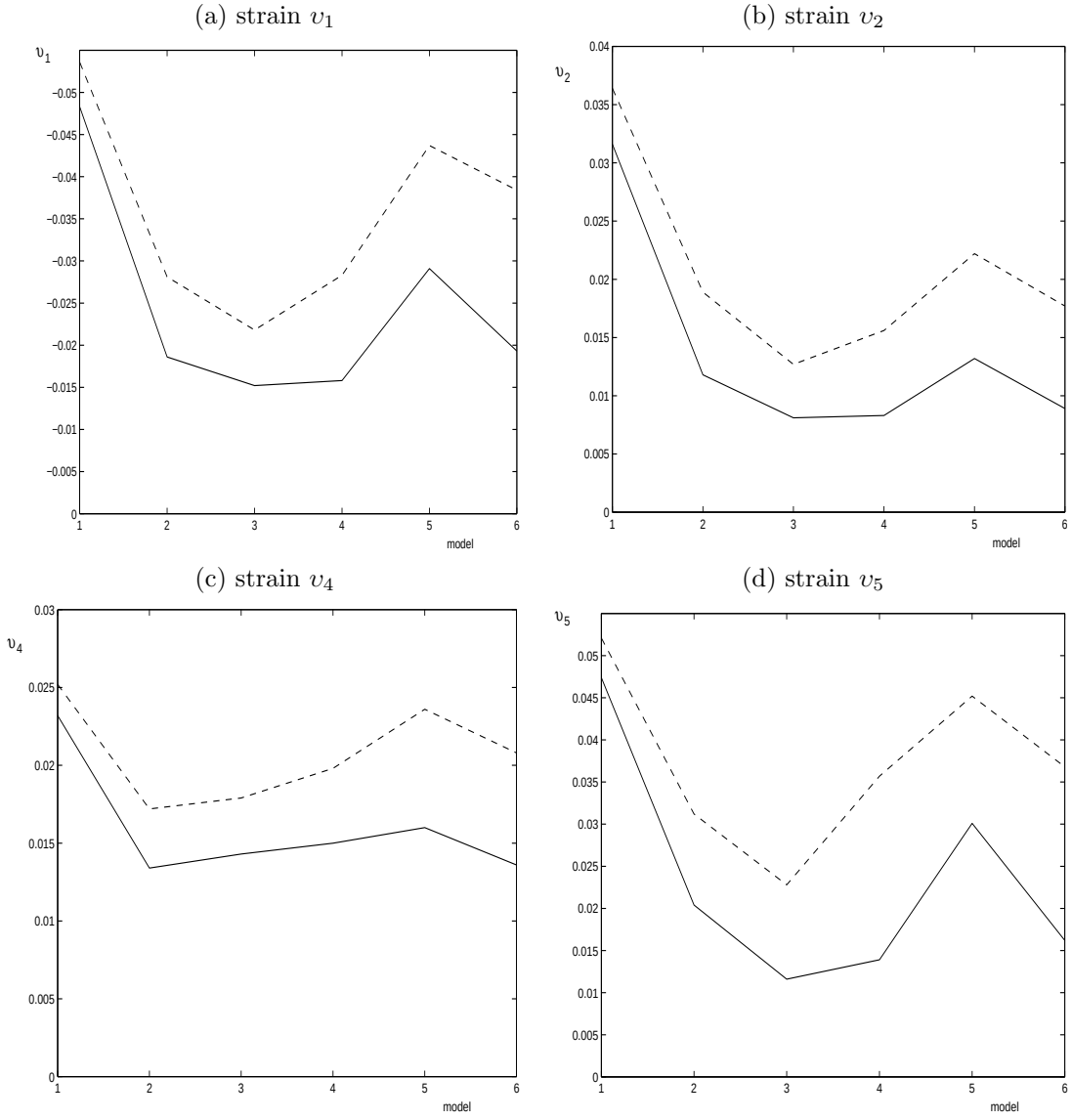

Figure 6.4: Diametral strains as a result of a non-linear analysis. The solid curve represents *CSS*'s; the dashed curve represents *LSTS*'s.

Figure 6.5: Original mesh (*red* colour) and deformed mesh (*blue* colour) for models 1-6, subjected to a linear *HCP* at cervical dilatation $D = 0.5$.
The deformation magnification = 5.

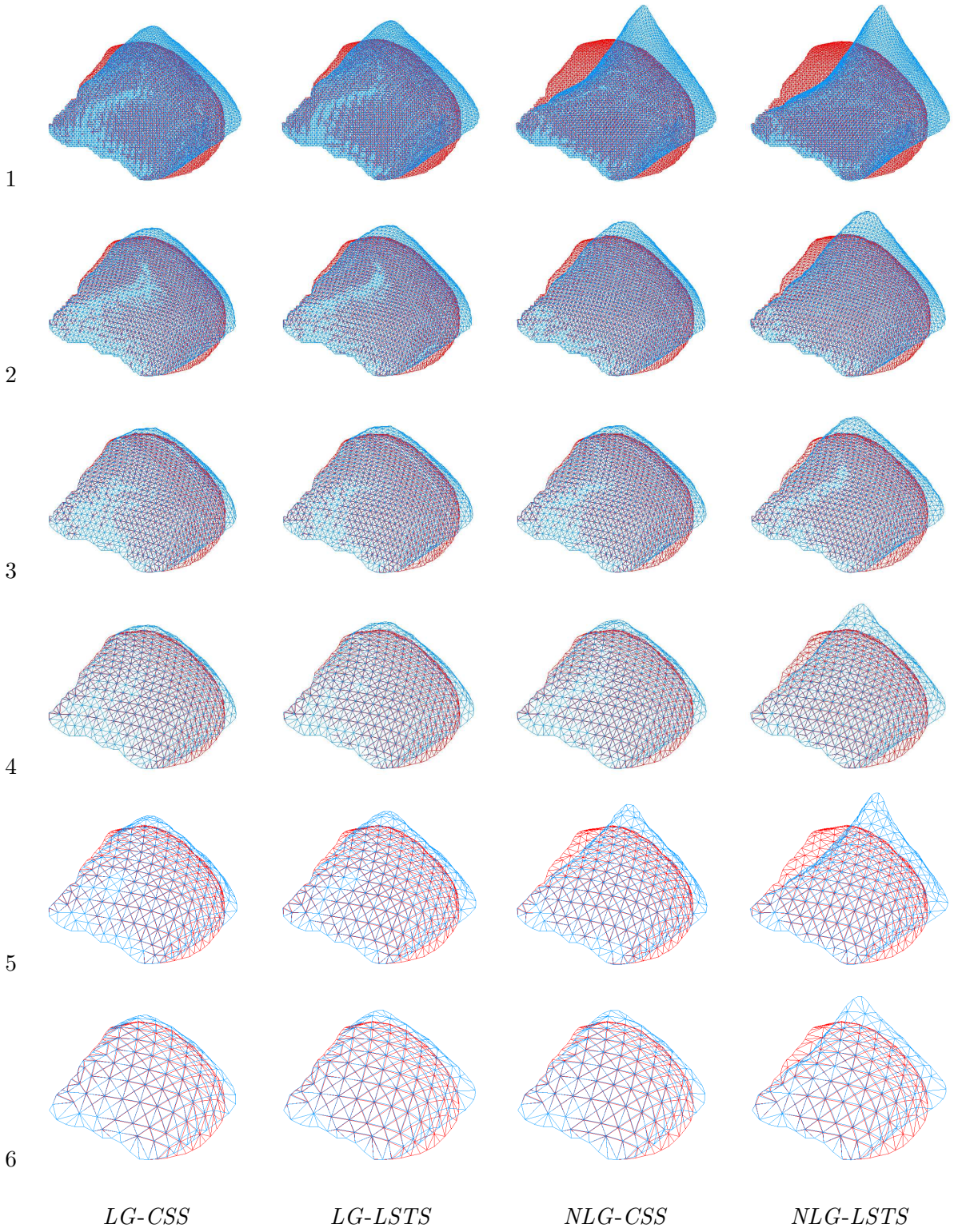

(a) Posterior view of left and right parietal bone (b) Right parietal bone

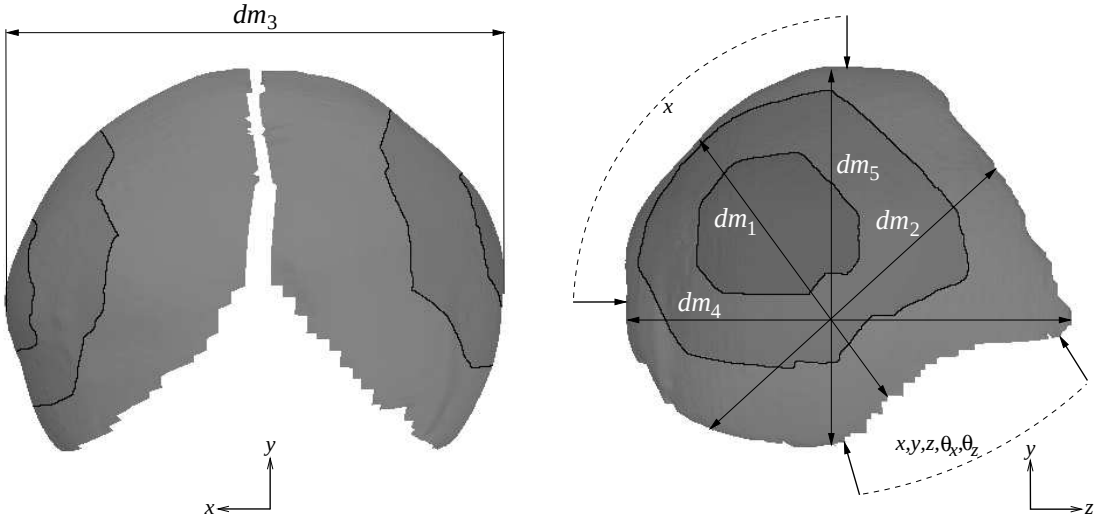

Figure 6.6: Left and right parietal bones: diameters measured for evaluation of deformation and boundary conditions. The nodes on the lower edge are restricted in all dof, except for rotation about the y-axis; the nodes on the upper edge are only restricted in the x-direction. There are three concentric areas of distinct thickness, decreasing from the centre area towards the outer area.

Geometry

A model of the left parietal bone of foetal skull model *II* containing 10,537 elements and a model of the right parietal bone of foetal skull model *II* containing 10,530 elements, were used. Both first-order shells, *CSS* (ABAQUS S3R), and second-order shells, *LSTS* (ABAQUS STRI65), are tested. The thickness of the parietal bones varies over three regions [72]:

- Inner ring: 0.89 mm.
- Middle ring: 0.74 mm.
- Outer ring: 0.61 mm.

The axis directions are as shown in Figure 6.6.

Material properties

The same settings as in parietal bone test *I*: $E_1 = 3.86$ GPa, $E_2 = 0.965$ GPa, $G_{12} = G_{13} = G_{23} = 1.582$ GPa, $\nu_{12} = 0.22$ and $\nu_{21} = 0.055$.

Table 6.5: Parietal bone test *II*: diameters (mm.) of the undeformed models for left and right parietal bones.

Model	n	dm_1	dm_2	dm_3	dm_4	dm_5
Left	10,537	73.7	59.1	90.1	85.7	67.5
Right	10,530	74.6	60.0	90.1	82.4	70.2

Boundary conditions

Left parietal bone: the same as in parietal bone test *I* (See Figure 6.2).
Right parietal bone: nodes corresponding with those of the left parietal bone when mirrored about the y-z plane (See Figure 6.6).

Loading

As before, a linear *HCP* distribution of 200 mmHg. at the level of the *SOB* plane decreasing to 50 mmHg. at the level of the cervical rim for dilatation $D = 0.5$. Amniotic pressure of 50 mmHg. above the *SOB* plane. This distribution covers both the left and right parietal bones.

Analysis

Both linear and non-linear static analyses are performed. All strain measures corresponding to the five diameters as shown in Figure 6.6 are measured. Strain υ_3 corresponds to the biparietal diameter, *BPD*, and is measured across the left and right parietal bone.

Results

Table 6.5 shows the diameters of the undeformed models.
Table 6.6 shows the results for a linear geometric analysis, *LG*, and a non-linear geometric analysis, *NLG*, respectively.
Figures 6.7 and 6.8 show the original meshes (*red* colour) and deformed meshes (*blue* colour) of the left and right parietal bones, respectively, for different analyses. The deformation magnification is 5.

Discussion

Left vs Right parietal bone: The results of the left and right parietal bones are in complete agreement.

Linear vs Non-linear geometry: As in parietal bone test *I*, the analysis assuming *NLG* shows higher degrees of deformation.

(a) *LG-CSS* (b) *LG-LSTS*

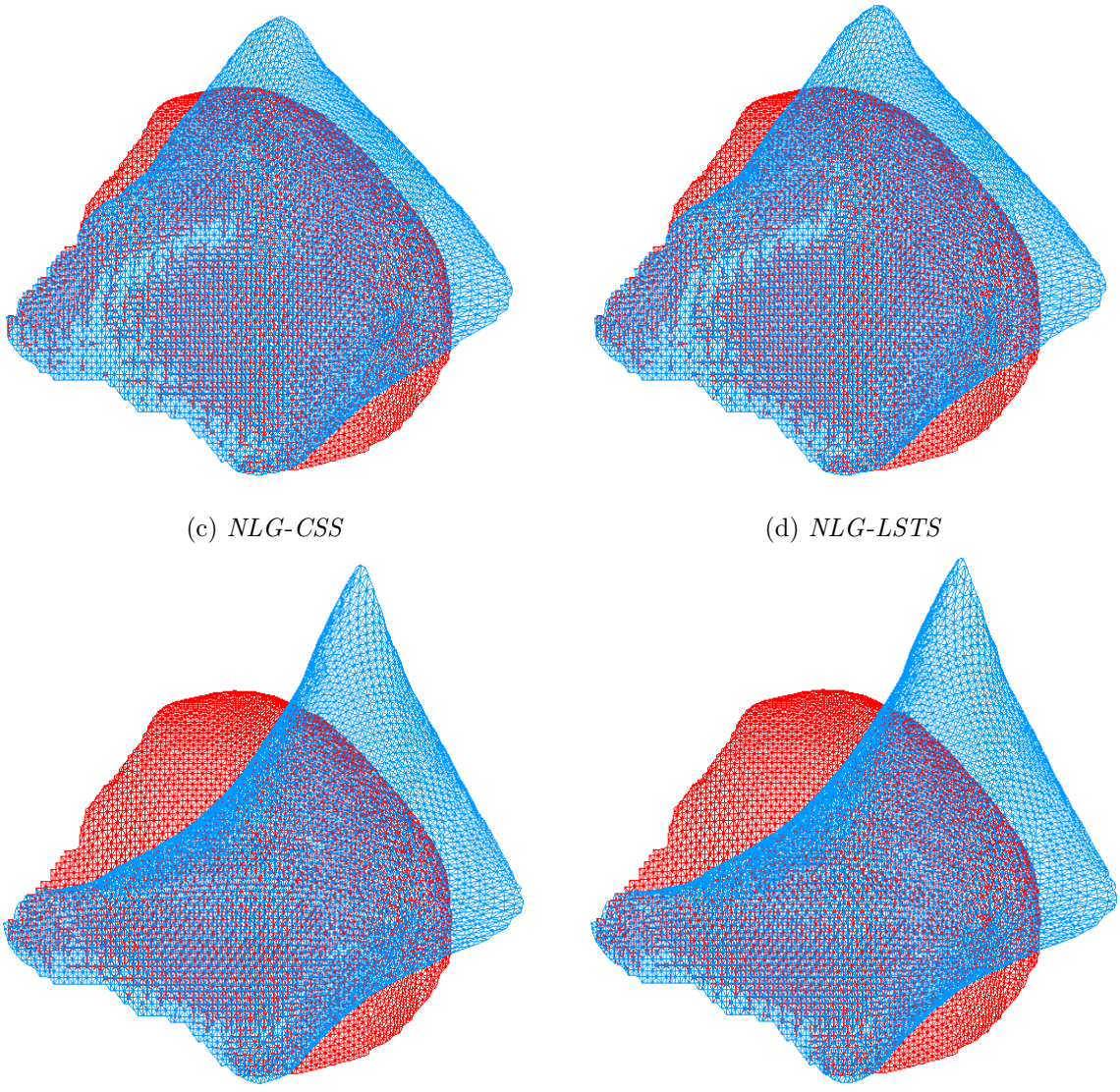

(c) *NLG-CSS* (d) *NLG-LSTS*

Figure 6.7: Original mesh (*red* colour) and deformed mesh (*blue* colour) for the left parietal bone. The deformation magnification = 5.

(a) *LG-CSS* (b) *LG-LSTS*

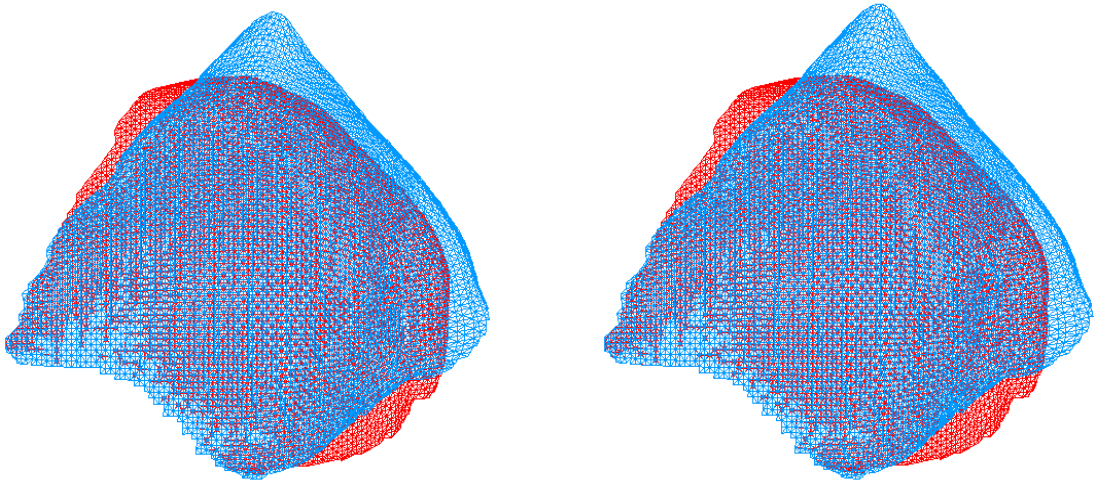

(c) *NLG-CSS* (d) *NLG-LSTS*

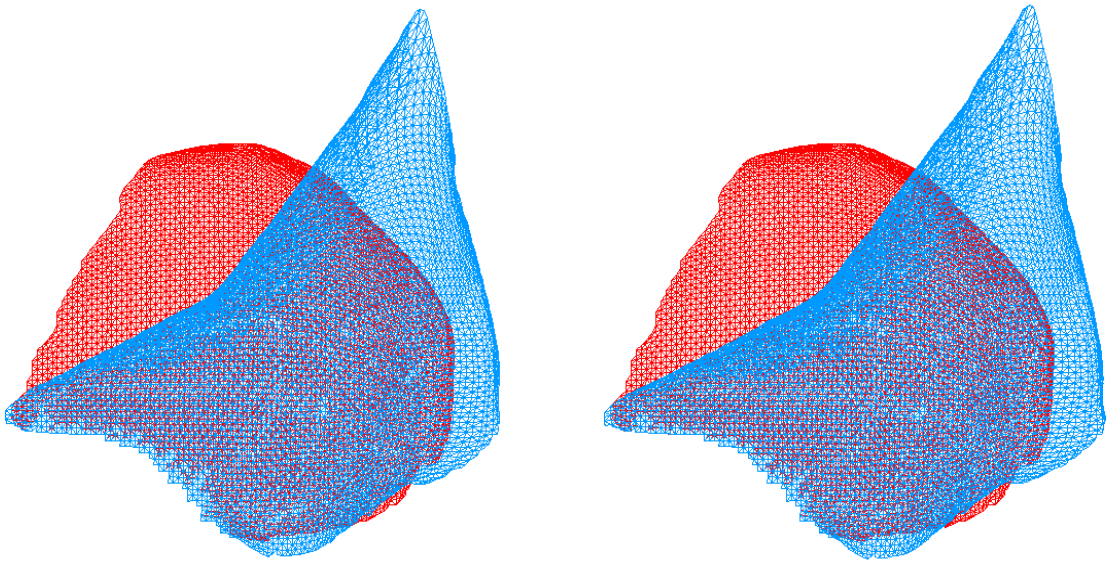

Figure 6.8: Original mesh (*red* colour) and deformed mesh (*blue* colour) for the right parietal bone (mirrored about the y-z plane). The deformation magnification = 5.

Table 6.6: Parietal bone test *II*: relative diametral strains (%) for left and right parietal bones, under the assumption of linear and non-linear geometry, respectively. The relative error is approx. 1% of the strain value.

Linear geometry, *LG*

Model/Elmnt	υ_1	υ_2	υ_3	υ_4	υ_5
Left-*CSS*	-3.07	+2.23	-0.97	+2.70	+3.65
Left-*LSTS*	-3.46	+2.55	-1.06	+2.94	+4.16
Right-*CSS*	-2.27	+1.34		+1.86	+3.08
Right-*LSTS*	-2.61	+1.41		+2.16	+3.52

Non-linear geometry, *NLG*

Model/Elmnt	υ_1	υ_2	υ_3	υ_4	υ_5
Left-*CSS*	-7.06	+4.73	-2.55	+3.20	+6.37
Left-*LSTS*	-7.39	+5.39	-2.75	+3.44	+6.77
Right-*CSS*	-6.70	+5.81		+2.85	+7.56
Right-*LSTS*	-6.70	+5.85		+2.90	+7.56

First-order vs Second-order shells or *CSS* vs *LSTS*: The difference is very small and nearly zero for non-linear analysis of the right parietal bone. However, the CPU time (SGI Indigo - MIPS R10000) for a *NLG-CSS* analysis of the right parietal bone was 1122 sec. as opposed to 5104 sec. for a *NLG-LSTS* analysis!

Varying thickness vs Constant thickness: Comparing the results of the left parietal bone with varying thickness (Table 6.6) with model 1 of the left parietal bone of constant thickness from the first parietal bone test (Table 6.3), we spot a significant increase for the diametral strains of the bones with varying thickness!

The biparietal diameter - dm_3**:** a small decrease of the *BPD* occurs which corresponds with the result from McPherson and Kriewall [72].

McPherson's model: The strains υ_1-υ_3 show the same directional changes for both models, however the strains of the author's model are considerably larger than those of McPherson's model (see Table 6.1). This difference is mainly because of the more accurate geometry of our model in terms of number of elements (10,537 vs 63) and the assumption of non-linear geometry. Nonetheless, McPherson's model is less stiff than one would expect, considering the low number of elements and the assumption of linear geometry. However, in Figure 6.1 we can see that the parietal tuberosity is approximated by a sharp corner point which will cause a significant reduction of stiffness in the y and z-directions. This is why the

factor, by which the *BPD* of McPherson's model differs from the author's, is smaller than the factor for υ_1.

6.1.4 Summary

The parietal bone test was aimed at the fulfilment of a set of objectives as specified in the beginning of Section 6.1.
The first objective involved the comparison of linear geometric with non-linear geometric analysis. The results showed better elastic behaviour for the latter. Less stiff models in FE analysis are considered to be superior to stiffer models if the difference between them is based on the number of elements or the geometry. Objective number two involved the refinement of the mesh in terms of the number of elements (h-refinement) and the order of the elements (p-refinement). H-refinement was inversely applied (h-coarsening) to assess the feasibility of using less complex models to reduce analysis times. We found that the less complex models were more stiff than the original model at 10,537 elements. An exception occurred for the least complex models with 532 and 277 elements respectively, which displayed moderate stiffness as compared to more complex models. Care should be taken with the interpretation of this outcome because the reason is likely to be the poor representation of the original geometry for these models, making them behave like a bent plate rather than a shell. The effect of p-refinement on a sufficiently complex model was minor which was illustrated in parietal bone test *II*, where the improvement using second-order elements was negligible, despite the significantly higher processing time.
Bone of varying thickness, decreasing from the centre towards the boundary, showed a significantly higher relative strain over the entire region as compared to bone of average constant thickness.
No discrepancies were found between the behaviour of the left and the right parietal bone.
The actual values of the diametral strains found in this experiment are difficult to validate so it will be left until Section 6.4 to assess the credibility of the parietal bone model as a plausible model of foetal head moulding. Despite this, the parietal bone experiment has pointed out some important facts, which will be taken into consideration for the next experiment which involves the evaluation of the complete skull model.

6.2 Experiment *II*

Experiment *II* covers the analysis of deformation of the foetal skull when subjected to the pressure of the cervix during the first stage of labour. The next

sections describe the default parameter settings which will not normally change unless otherwise stated.

6.2.1 Pressure distributions

From Chapter 5, pressure distribution 2, as specified in equation 5.18, is considered to be a realistic model of the pressure as exerted by the cervix on the foetal head. Figure 6.9 shows the location of the *SOB* plane of which the intersection with the head corresponds with the location of the cervix in contact with the largest diameter of the head, i.e. the *SOBD*, for an *occiput anterior vertex* presentation. Figures 6.10a-d illustrate the non-linear pressure distribution for dilatations $D = 0.9$, 0.7, 0.5 and 0.3, respectively. The maximum value of cervical dilatation is conventionally taken to be 10 cm. as reported in [30] and [39]. At this degree of dilatation, the cervix loses contact with the head and the second stage starts. Therefore the maximum dilatation for the experiment is set to $D = 0.9$. The active phase of labour starts at 3 cm. of dilatation [17] which corresponds to a minimum value of $D = D_0 = 0.3$. The part of the skull which is in contact with the amniotic fluid, i.e. the part above the *SOB* plane, is subjected to an average amniotic pressure of 50 mmHg. The largest diameter of the skull is set to 90 mm. which corresponds to the average *BPD* as reported in [37] when ignoring the thickness of the skin. The fontanelles are not subjected to any pressures, an assumption which is justified on the basis of the geometry of the foetal skull where fontanelles and sutures are *embedded* into the convex hull of the cranial vault.

6.2.2 Geometry of the undeformed mesh

The landmarks and diameters for validation of the model are defined in Appendix C and displayed in Figures C.1 and C.2. Table 6.7 shows the location of the landmarks on the undeformed mesh. Table 6.8 shows the original diameters. In this experiment, landmarks are represented by a distinct node of the undeformed skull. Deformation is then evaluated on the basis of the displacements of this node from which an absolute diametral strain can be calculated[2]. Figure 6.9 shows the direction of the axes.

[2]The term 'absolute' is used here to indicate a strain with a dimension, e.g. mm., as opposed to a 'relative' strain which is dimensionless. It does not however imply 'absolute value' which would mean that the strain has no sign!

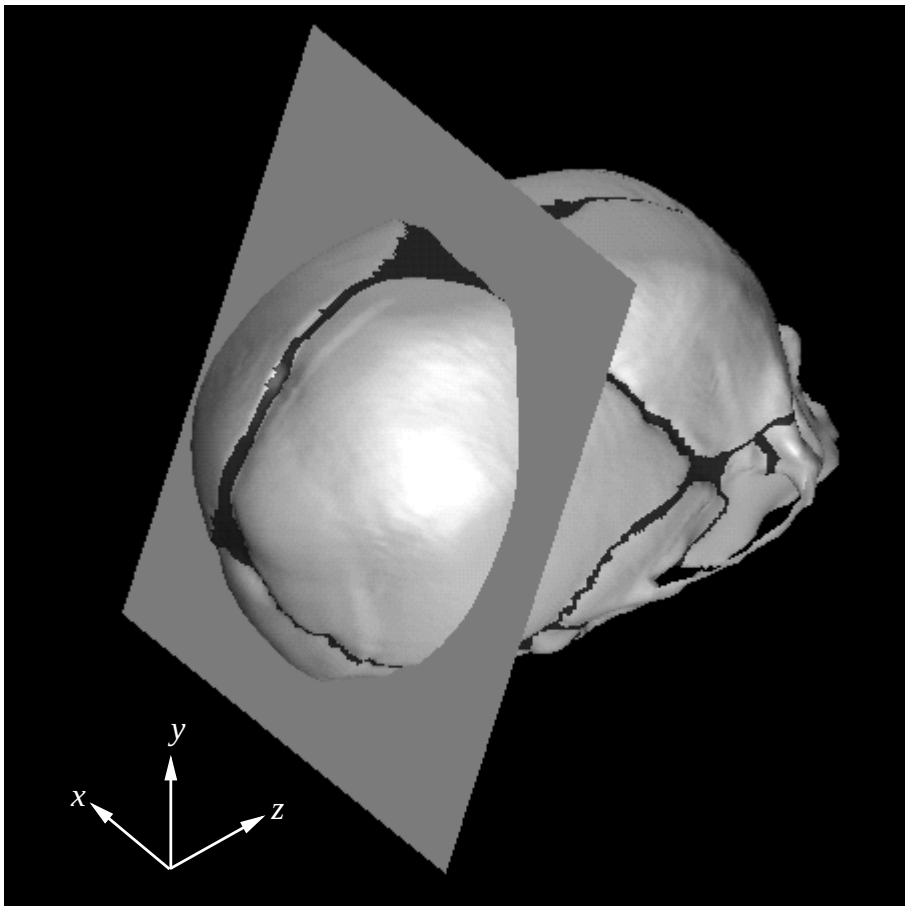

Figure 6.9: Location of the sub-occipito bregmatic (SOB) plane, corresponding to *occiput anterior vertex* presentation and the axis directions for the analysis of deformation of foetal skull model II (see also Figure D.4a).

(a) $D = 0.9$

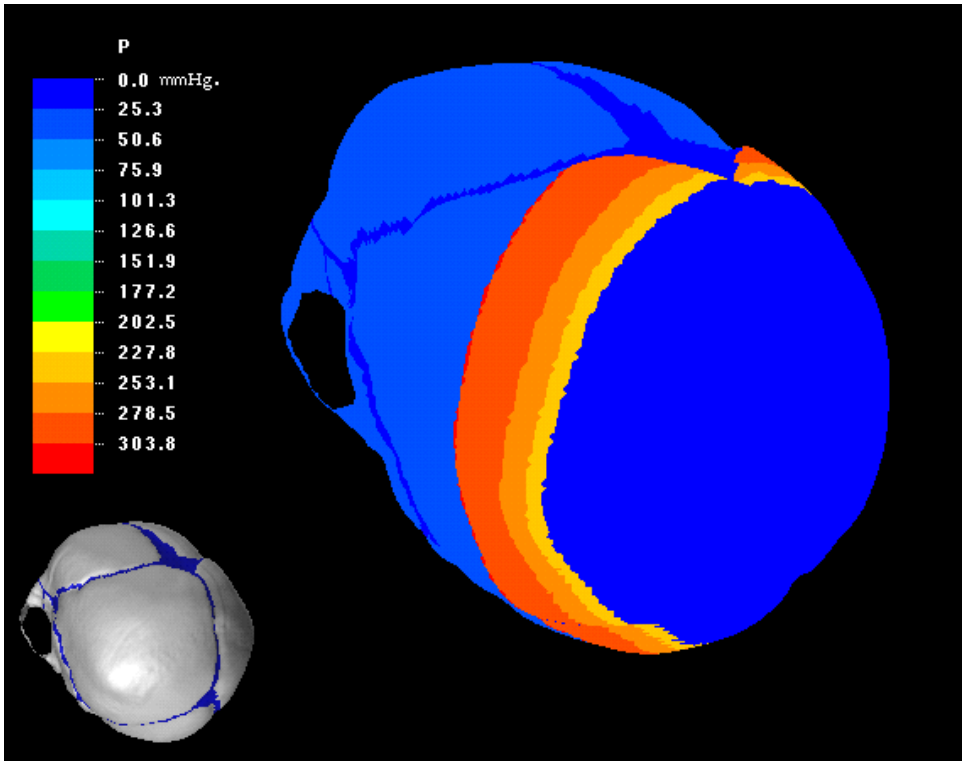
P
0.0 mmHg.
25.3
50.6
75.9
101.3
126.6
151.9
177.2
202.5
227.8
253.1
278.5
303.8

(b) $D = 0.7$

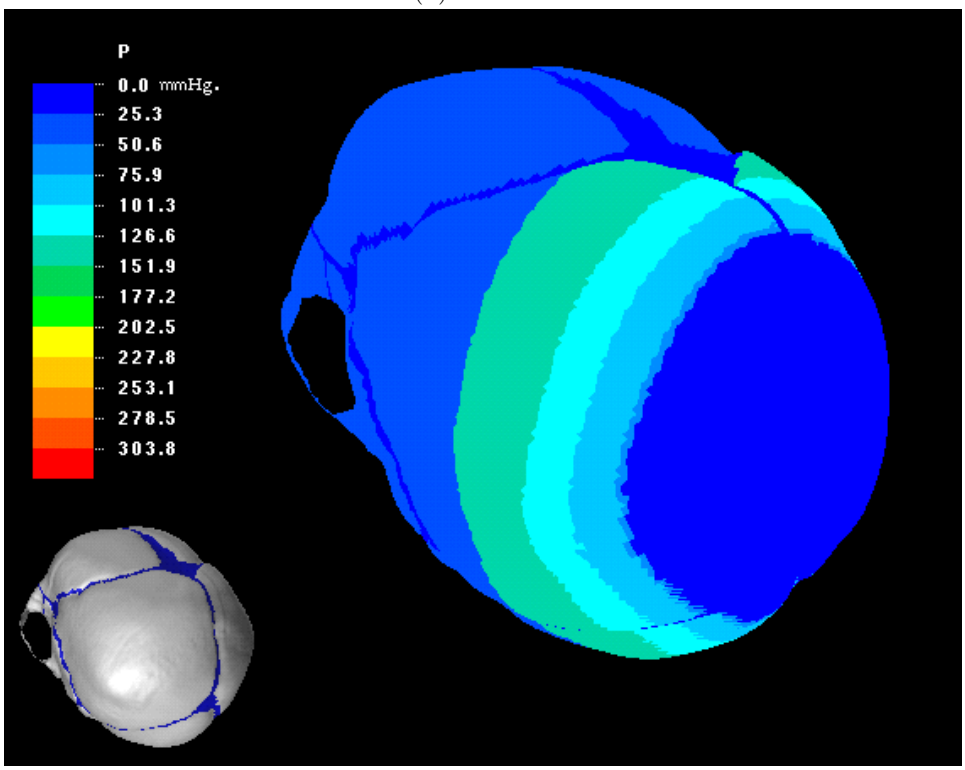
P
0.0 mmHg.
25.3
50.6
75.9
101.3
126.6
151.9
177.2
202.5
227.8
253.1
278.5
303.8

(c) $D = 0.5$

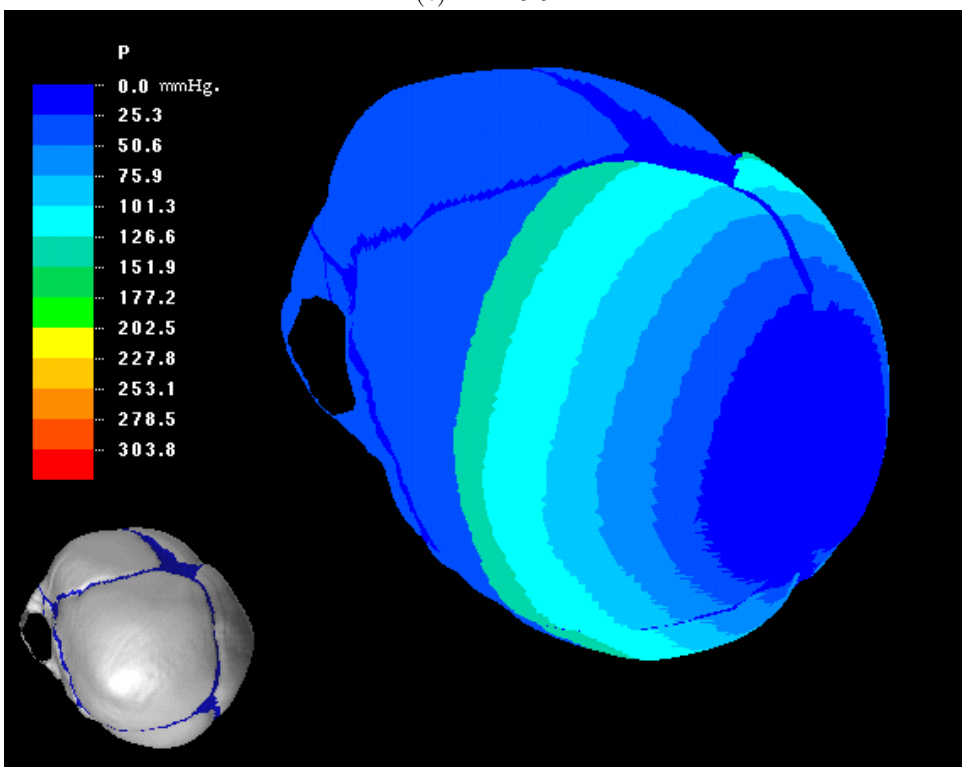

(d) $D = 0.3$

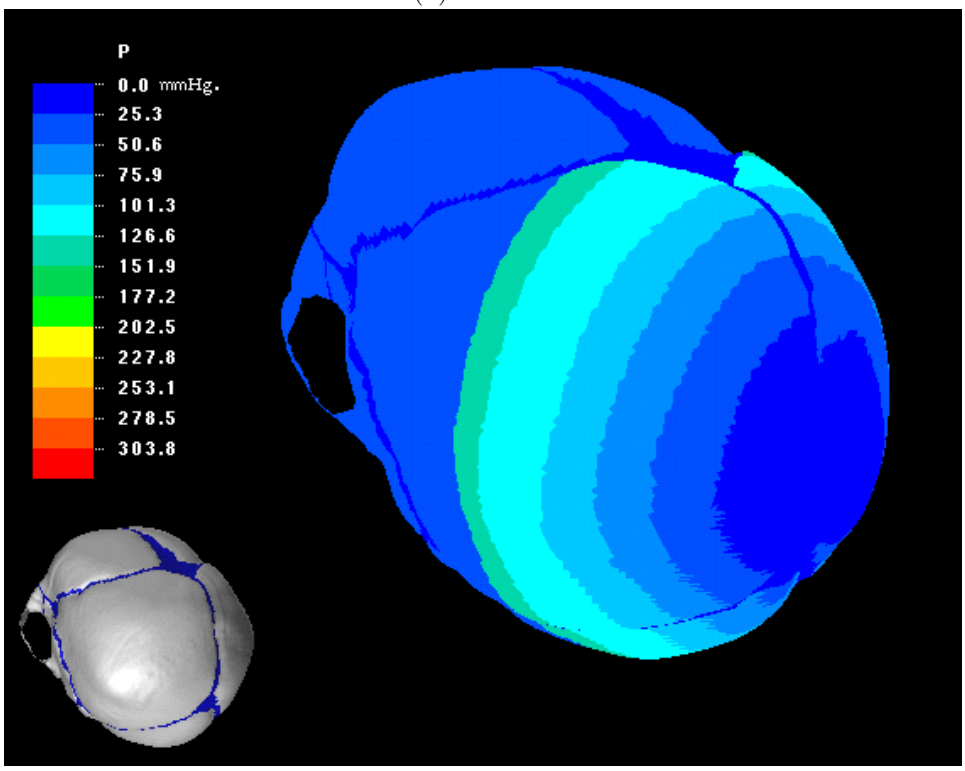

Figure 6.10: Pressure distribution as exerted by the cervix, for different degrees of dilatation.

Table 6.7: Coordinates of landmarks (mm.), used for validation (see Appendix C, for definitions).

Landmark	x	y	z
2	0.43	-25.81	62.53
3	0.91	-4.59	56.76
4L	3.46	1.80	56.28
4R	-2.04	1.59	56.32
5L	1.77	25.87	46.15
5R	-1.28	26.29	46.58
6L	21.19	40.84	-4.22
6R	-22.27	40.84	-3.57
7L	6.26	9.87	-61.59
7R	-3.11	9.30	-61.27
8	1.89	-5.21	-63.17
9	1.36	-31.69	-51.28
10L	45.54	6.78	-26.75
10R	-44.10	8.46	-22.73
11L	24.61	26.30	42.51
11R	-25.93	26.05	36.51
12L	40.67	-12.45	-1.48
12R	-39.88	-9.52	-1.70

Table 6.8: Diameters (mm.) of the undeformed foetal skull. 'Single' implies the measurement of a diameter between two single landmarks. 'Left' and 'Right' implies the existence of left and right landmarks for the same location, thus two diameters are given.

Diameter	Single	Left	Right
MaVD		129.28	128.73
OrOD	119.93		
OrVD		119.35	118.91
OFD		119.66	119.74
SOFD		113.16	113.78
SOBD		88.71	89.97
BPD	89.75		
BFD	50.90		
BTD	80.60		

6.2.3 Basic experiment

Geometry

The foetal skull model contains 63,413 elements. The size of the triangles is 0.94 mm. on the average. The mandible is left out since it is not a fixed part of the cranium and is unlikely to contribute to the moulding process. The zygomatic bone is approximated by thick-shell elements, since the data acquisition process was unable to scan the inner points of this bone. The cranial vault bones, i.e. parietal, frontal and occipital bones are divided into three concentric rings, emanating from the centre of the bone and of variable thicknesses. These are set as reported in [72]:

- Inner ring: 0.89 mm.
- Middle ring: 0.74 mm.
- Outer ring: 0.61 mm.

The locations of the rings were obtained by region growing from the centre of the bone (tuberosities) at equal distances towards the border. The resulting regions were then (manually) adapted according to the fibre structure of the skull model and by comparison to atlas images from [26].
The thickness of the squamosal bones is set to 0.89 mm.
The thickness of the maxilla and skull base is set to 2 mm. - an estimate based on the thickness of the palate of the foetal skull model.
The thickness of the fontanelles/sutures is set to 0.57 mm., an average from values as reported in [14].
Figure 6.11 shows the foetal skull with the regions of different material and thickness properties in different colours.

Material properties

- Foetal cranial bone, in-plane orthotropic:
  $E_1 = 3.86\text{GPa}$, $E_2 = 0.965\text{GPa}$, $G_{12} = G_{13} = G_{23} = 1.582\text{GPa}$,
  $\nu_{12} = 0.22$, $\nu_{21} = 0.055$, from [72].
- Maxilla and skull base, isotropy assumed:
  $E = 4.46\text{GPa}$, $\nu = 0.21$, from [67].
- Fontanelles and sutures: isotropy assumed,
  $E = 31.5\text{MPa}$, $\nu = 0.45$, from [67].

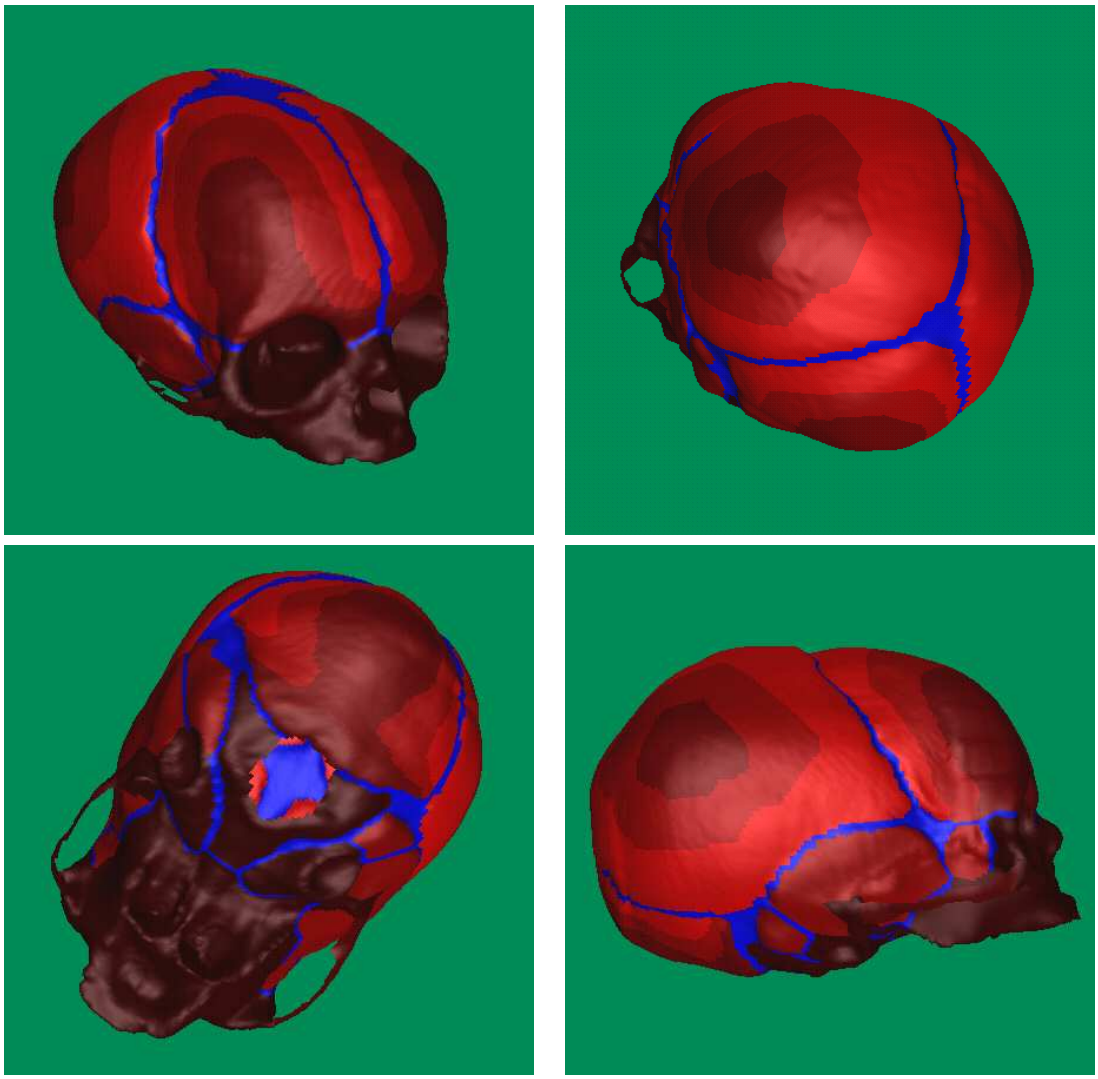

Figure 6.11: Coloured foetal skull model: *red* colour is bone; *blue* colour are sutures/fontanelles. Darker *red* colours correspond to regions of higher thickness values (visualisation in Geomview 1.6.1 [84]).

Elements

First-order elements, *CSS* (ABAQUS - S3R), are used for both bone, fontanelle and suture structures. The S3R shell element in ABAQUS provides accurate results in most loading situations and is valid for thin and thick shell problems. However, due to its constant bending and membrane strain approximations, high mesh refinement is required to capture pure bending deformations or solutions to problems of high strain gradients [40]. The results from experiment I, showed that first-order elements at the highest level of refinement are a justified choice in terms of accuracy and processing time.

Boundary conditions

Three nodes on the base of the skull are fully built-in to avoid rigid body translation and rotation. Additionally, three fully built-in nodes on the facial part of the skull are specified, to avoid rigid body rotation about the x-axis.

Loading

As defined in Section 6.2.1

Analysis

Non-linear geometry, *NLG*, static analysis.

Results

Table 6.9 shows the strains (mm.) of the principal diameters[3]. The first two rows show the values as reported by Kriewall et al. [47]. The third and fourth row show values as reported by Sorbe and Dahlgren [94]. The next rows give the original diameter of the author's results followed by the absolute diametral strains for dilatations, $D = 0.9$, 0.7, 0.5 and 0.3, respectively.
Table 6.10 shows the maximum positive and negative deformations for each dilatation case.

Discussion

From Table 6.9, it can be seen that the resulting strains are direction-wise (i.e. elongation vs compression) in complete agreement with the measurements from

[3](0) indicates the original size of the diameter in mm. Positive strains imply increase of the diameter after deformation or elongation; negative strains imply decrease of the diameter or compression.

Table 6.9: Diametral strains (mm.) of the deformed foetal skull for different dilatations - **basic experiment**. (0) = original diameter. Positive (+) values are tensile strains, negative (-) values are compressive strains. S = single measurement, L = lhs measurement and R = rhs measurement. * are values of the *MVD* rather than the *MaVD*. Note that the values from Kriewall et al. [47] and Sorbe and Dahlgren [94] are averages.

	MaVD	*OrOD*	*OrVD*	*OFD*	*SOFD*	*SOBD*	*BPD*	*BFD*	*BTD*
Kriewall (0)	135.0*	-	-	-	108.0	-	91.0	-	-
Kriewall	+4*	-	-	-	-2.0	-	+2.0		
Sorbe (0)	140.50	-	126.90	-	-	117.10	105.00	-	-
Sorbe	+1.90	-	+2.20	-	-	-1.70	0.00	-	-
Lapeer (0) S/L	129.28	119.93	119.35	119.66	113.16	88.71	89.75	50.90	80.61
R	128.73	-	118.91	119.74	113.78	89.97	-	-	-
D=0.9 S/L	+0.2304	+0.3193	+0.1973	+0.3213	-0.1457	-0.8282	-0.1286	-0.0515	-0.1214
R	+0.1805	-	+0.1531	+0.3148	-0.1443	-0.5122	-	-	-
D=0.7 S/L	+0.1564	+0.0854	+0.1340	+0.0825	-0.1015	-0.3578	-0.0877	-0.0433	-0.1613
R	+0.0984	-	+0.0769	+0.0775	-0.0980	-0.1595	-	-	-
D=0.5 S/L	+0.1183	+0.0027	+0.0996	+0.0002	-0.0946	-0.3106	-0.0632	-0.0375	-0.1457
R	+0.0448	-	+0.0263	-0.0047	-0.0913	-0.1221	-	-	-
D=0.3 S/L	+0.1023	-0.0106	+0.0857	-0.0121	-0.0926	-0.3062	-0.0522	-0.0344	-0.1355
R	+0.0286	-	+0.0124	-0.0170	-0.0896	-0.1194	-	-	-

(a) Displacements in the y-direction, u_y (mm.).

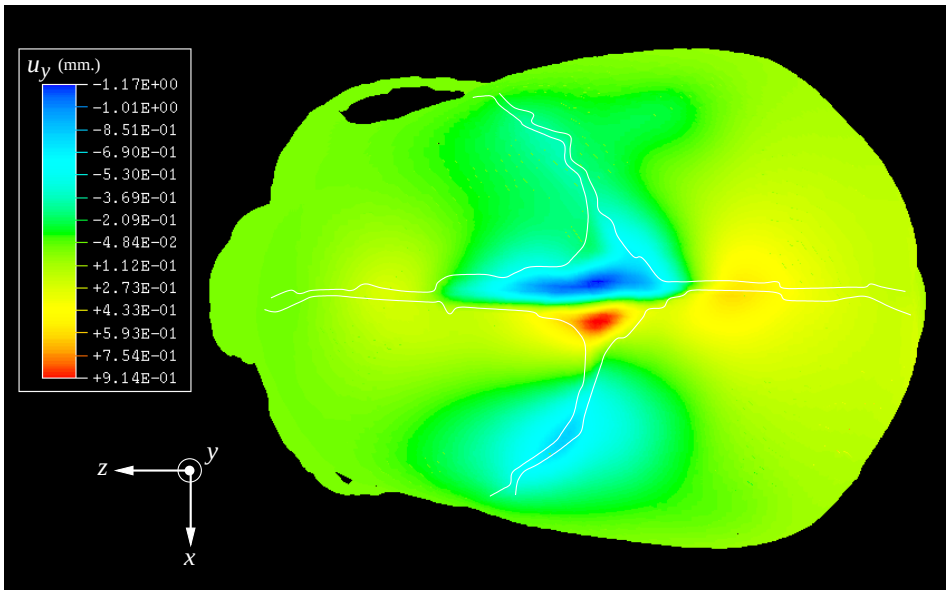

(b) Rotations about the z-axis, u_{rz} (radians).

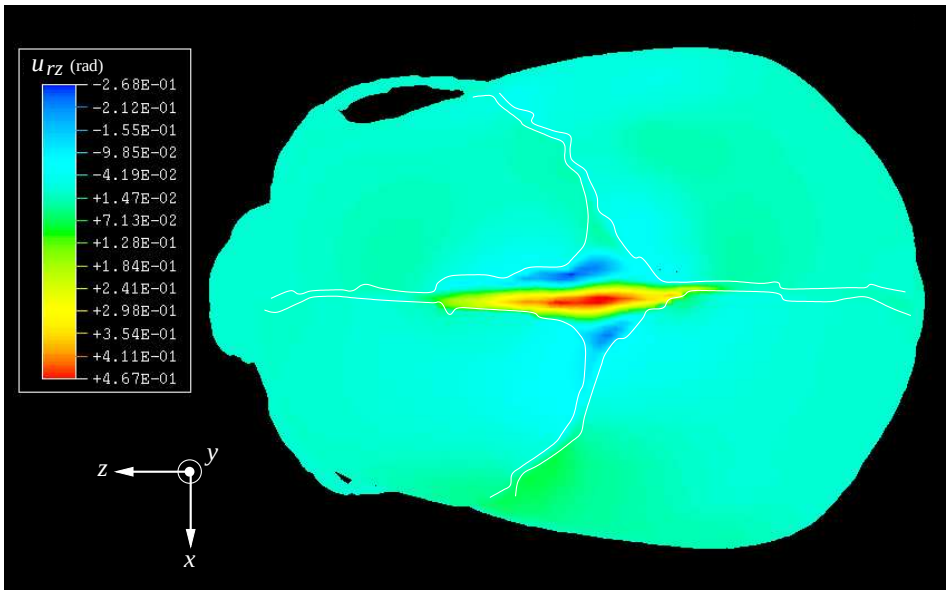

Figure 6.12: Contour plots for basic experiment ($D = 0.9$).

Table 6.10: Maximum deformations (mm.) for each dilatation case for basic experiment.

dof	$D = 0.9$		$D = 0.7$		$D = 0.5$		$D = 0.3$	
	-	+	-	+	-	+	-	+
u_x	-0.9069	0.4956	-0.3052	0.3715	-0.2357	0.3205	-0.2266	0.2948
u_y	-1.1720	0.9144	-0.8817	0.2913	-0.8313	0.2165	-0.8453	0.2003
u_z	-0.6127	1.0260	-0.2646	0.5161	-0.1679	0.4249	-0.1620	0.4092
u_{rx}	-0.2192	0.1710	-0.1094	0.0866	-0.0919	0.0724	-0.0889	0.0705
u_{ry}	-0.1263	0.2308	-0.0478	0.1033	-0.0385	0.0807	-0.0368	0.0766
u_{rz}	-0.2682	0.4673	-0.1728	0.1754	-0.1438	0.1410	-0.1385	0.1360

Kriewall et al. [47] and Sorbe and Dahlgren [94] (except for the *BPD* which will be discussed shortly). However, the magnitude of the strains are significantly smaller. Only the decrease of the *SOBD* for $D = 0.9$ is of comparable magnitude to the value reported by Sorbe and Dahlgren. In general this means that the model behaves realistically in terms of the *shape after deformation* but not in terms of the *degree of deformation*.

Table 6.10 shows the maximum positive and negative deformations for all dilatations. The values of u_y, i.e. the displacement in the y-direction, and the values of u_{rz}, i.e. the rotations about the z-axis, are of particular interest because of their magnitude. Figure 6.12 shows that these large deformations occur within the anterior fontanelle. Elements on the lhs of the centre-line of the fontanelle, bend upwards whilst elements on the rhs bend downwards. This corresponds with a positive rotation about the z-axis of those elements laying in between the up- and downwards moving elements. It will be shown in further experiments that by decreasing the stiffness of the fontanelles and sutures, these rotations may eventually lead to convergence problems.

Except for u_y and u_{rz}, the most significant changes occur for $D = 0.9$. This is not at all surprising if we compare the pressure distributions as shown in Figure 6.10 (and also Figure 5.9). The maximum pressure is higher than 300 mmHg. for $D = 0.9$ and only about 150 mmHg. for $D = 0.7$, 0.5 and 0.3.

Results from Kriewall et al. (Table 6.9) show an increase of the *BPD* of 2 mm! Sorbe and Dahlgren did not find any changes for the *BPD*, whilst the current experiment shows a slight decrease of the *BPD*. The decrease of the *BPD* is in agreement with the results from parietal bone test *II* and reported in [72]. From a mechanical point of view, one would suspect the *BPD* to decrease when

subjected to a pressure distribution as exerted by the uterine cervix. The comparison with real cases has to be treated with care though: other factors might have influenced the results as reported by Kriewall et al. [47].

6.2.4 Elaboration *I*

The results of the basic experiment showed the effect of the cervical pressure on the foetal head under relatively normal conditions, i.e. average values of pressures, material constants, thickness of the cranial bones, fontanelles and sutures. The next set of experiments will focus on the effect of increasing or decreasing each of these values to cause a higher degree of deformation. Values are set according to standard deviations and/or extrema as reported in [71] for the bones and in [14] for the fontanelles/sutures.
Only dilatation $D = 0.9$ is considered since this configuration gave the highest degree of deformation in the previous tests.
Table 6.11 shows the parameter settings for five of the six different analyses[4]:

Analysis 0 is the analysis with the original parameter settings as described in the basic experiment for dilatation $D = 0.9$.

Analysis 1 changes the material properties of the bone which are set to a minimum value of $E_1 = 2.830$ GPa and $E_2 = 0.570$ GPa.

Analysis 2 changes the thickness of the fontanelle/suture to a lower bound value of 0.36 mm.

Analysis 3 changes the thickness of the cranial vault bones to lower bounds of 0.74 mm., 0.59 mm. and 0.46 mm., for the inner, middle and outer concentric areas respectively. The thickness of the squamosal bones is set to 0.74 mm.

Analysis 4 changes the *IUP* to an upper value of 75 mmHg. [5]. Application of Equation 5.18 will subsequently adapt the *HCP* (P_r) distribution to the value of the *IUP* (P_a).

Analysis 5 increases the thickness of the squamosal bones to 2 mm., as if they were part of the skull base.

[4] Analysis 5 does not involve any change of the basic parameters as reported in Table 6.11.

Table 6.11: Basic parameters for five different analyses. t_b = thickness of bone; t_f = thickness of fontanelles and sutures.

Analysis	E_1 (MPa)	E_2 (MPa)	G_{12} (MPa)	G_{13} (MPa)	t_b (mm.)	t_f (mm.)	P_{max} (MPa)
0	3.860E3	0.965E3	1.582E3	1.582E3	0.89-0.61	0.57	-6.66E-3
1	2.830E3	0.570E3	1.160E3	1.160E3			
2	3.860E3	0.965E3	1.582E3	1.582E3		0.36	
3					0.74-0.46	0.57	
4					0.89-0.61	0.57	-9.99E-3

Results

Table 6.12 reports the values of the strains for each analysis. The following analyses did not fully converge to 100% of the load and were therefore extrapolated using polynomial regression:

analysis 2 : 88.8% convergence
analysis 3 : 93.0% convergence

Excessive rotations of the fontanelle/suture elements are the main cause of non-convergence. This potential problem was already illustrated in Figure 6.12 in the previous section. The problem will be discussed in depth in Section 6.3.1.

Discussion

Changing the thickness of the fontanelles/sutures (analysis 2) seems to have the most significant effect on the stiffness of the entire skull. The finding is peculiar since the fontanelle/suture structures behave very much like membranes meaning that they are nearly incompressible and on the other hand very elastic when subjected to tensile forces. Despite this fact, their influence on the general stiffness of the structure appears to be eminent. This effect will be further investigated assuming hyperelastic behaviour of the fontanelles/sutures in the next section.
Changing the thickness of the cranial vault bones (analysis 3) has a slightly smaller effect but nonetheless significant. This doesn't apply however for the squamosal bones since the results of analysis 5 (squamosal bone thickness = 2 mm.) hardly differ from those of analysis 0 (squamosal bone thickness = 0.89 mm.). From this result, one may conclude that the contribution of the squamosal

Table 6.12: Diametral strains (mm.) for **elaboration** *I*. (0) = original diameter. Positive (+) values are tensile strains, negative (-) values are compressive strains. S = single measurement, L = lhs measurement and R = rhs measurement. * are values of the *MVD* rather than the *MaVD*. Note that the values from Kriewall et al. [47] and Sorbe and Dahlgren [94] are averages.

	MaVD	*OrOD*	*OrVD*	*OFD*	*SOFD*	*SOBD*	*BPD*	*BFD*	*BTD*
Kriewall (0)	135.0*	-	-	-	108.0	-	91.0	-	-
Kriewall	+4*	-	-	-	-2.0	-	+2.0	-	-
Sorbe (0)	140.50	-	126.90	-	-	117.10	105.00	-	-
Sorbe	+1.90	-	+2.20	-	-	-1.70	0.00	-	-
Lapeer (0) S/L	129.28	119.93	119.35	119.66	113.16	88.71	89.75	50.90	80.61
R	128.73	-	118.91	119.74	113.78	89.97	-	-	-
analysis 0 S/L	+0.2304	+0.3193	+0.1973	+0.3213	-0.1457	-0.8282	-0.1286	-0.0515	-0.1214
R	+0.1805	-	+0.1531	+0.3148	-0.1443	-0.5122	-	-	-
analysis 1 S/L	+0.3000	+0.4304	+0.2575	+0.4305	-0.2269	-1.3320	-0.0858	-0.0566	-0.0935
R	+0.2391	-	+0.2059	+0.4228	-0.2208	-0.7545	-	-	-
analysis 2 S/L	+0.7229	+0.9981	+0.6674	+0.9867	-0.2934	-3.3296	-0.4353	-0.1119	+0.0925
R	+0.5670	-	+0.5338	+0.9775	-0.2875	-2.6992	-	-	-
analysis 3 S/L	+0.4986	+0.6939	+0.4348	+0.6847	-0.4495	-2.8366	-0.0820	-0.0629	+0.0729
R	+0.3605	-	+0.3151	+0.6747	-0.4283	-1.2533	-	-	-
analysis 4 S/L	+0.4672	+0.6013	+0.4021	+0.5910	-0.3917	-2.9315	-0.1277	-0.0762	+0.0861
R	+0.3508	-	+0.3032	+0.5814	-0.3778	-1.8517	-	-	-
analysis 5 S/L	+0.2317	+0.3209	+0.1992	+0.3222	-0.1440	-0.8271	-0.1225	-0.0504	-0.0604
R	+0.1826	-	+0.1558	+0.3159	-0.1426	-0.5160	-	-	-

bones to the moulding of the foetal skull is negligible.
The effect caused by decreasing the material constants (analysis 1) is relatively small as compared to the effect of decreasing the thickness of bones, sutures and fontanelles. An explanation could be the inherent stiffness of a shell-shaped object.
Increase of the *IUP* and correspondingly the *HCP* to an excess of 50% (analysis 4) has a major non-linear effect on the deformations.
The change of the *SOBD* is larger than the values as reported by Sorbe and Dahlgren [94] for analyses 2,3 and 4. Note however that extremum values were taken and that the proportion of the load absorbed by the skin has not been accounted for.
The left side of the skull appears to be slightly less stiff than the right side. This effect is mainly due to the geometry of the parietal bones.
The *BPD* decreases more than 0.4 mm. when the fontanelles/sutures are decreased in thickness (analysis 2). This effect emphasises the major influence of these structures to the general stiffness of the skull.
A similar study like elaboration *I* is described in [49]. The absolute diametral strains as reported in this study were significantly smaller because the assumption of constant thickness (0.75 mm.) of the cranial vault bones[5]. This finding emphasises the importance of the varying thickness of the cranial bones to the stiffness of the skull.

The aim of the experiment was to assess the effect of lower or upper bound parameter values which cause a higher degree of deformation. That the latter was achieved is not surprising, however, the model is still too stiff as compared to clinical experimental results. This shows that the overstiffness of the model cannot be simply explained by the variation in the model parameters.

6.2.5 Elaboration *II*

In the previous section, the importance of the fontanelle/suture structures to the stiffness of the overall structure was pointed out.
Bylski et al. [14] investigated the behaviour of foetal dura mater under large deformation biaxial tension. They found experimental values for the stiffness coefficients in two directions assuming the Mooney-Rivlin (*MR*) hyperelastic model: $C_1 = 1.18$ MPa and $C_2 = 0.295$ MPa.
In the next experiment all the parameters are set to the same values as for the basic experiment, except for the material properties of fontanelle/suture

[5]Note that the loading distribution in this study was different as well: a constant load of 250 mmHg. over the entire area of head-to-cervix contact, for dilatation, $D = 0.9$, was applied.

structures which are assumed to behave as a hyperelastic medium following the *MR* model, with values C_1 and C_2 as mentioned above.
The experiment is run for dilatations $D = 0.9$, 0.7, 0.5 and 0.3, respectively.

Results

Table 6.13 shows the resulting absolute diametral strains for $D = 0.9, 0.7, 0.5$ and 0.3, for hyperelastic fontanelles/sutures.
The following analyses did not reach full convergence and deformations were thus extrapolated using polynomial regression:

$D = 0.9$: 63.7% of the full load
$D = 0.7$: 75.0% of the full load

Table 6.14 shows the maximum positive and maximum negative deformations for each analysis.

Discussion

Assuming hyperelastic behaviour of the fontanelles/sutures appears to have a significant effect on the entire stiffness of the structure which is shown by comparing the results in Table 6.13 with those in Table 6.9. The cause of this effect might in this case well be due to the more realistic values of the material constants: the values on foetal dura mater as reported by Bylski et al. [14] are more than an order of magnitude smaller than the elastic modulus for adult dura mater as reported by McElhaney [67]!
The following effects on the diameters occur when comparing the current results with those of elaboration *I*.

MaVD The absolute diametral strains have increased considerably. The degree of increase is more eminent for the rhs measurements (mainly due to the displacements of landmark 7R on the right parietal bone). Note that the values at $D = 0.9$ are much closer to the value as reported by Sorbe and Dahlgren [94].

OrOD and OFD These two diameters are very near each other (See Figure C.2) which is reflected in similar displacement patterns across different dilatations for both the basic experiment and elaboration *II*. Peculiar is the trend for dilatations 0.7 and 0.5 from elongation in the basic experiment to compression in elaboration *II*. This is possibly related to the decrease of stiffness of the posterior fontanelle which causes lifting of the parietal bones and the occipital bone. This prohibits the bulging of the

Table 6.13: Diametral strains (mm.) for **elaboration** *II*, assuming hyperelastic behaviour of fontanelles and sutures. (0) = original diameter. Positive (+) values are tensile strains, negative (-) values are compressive strains. S = single measurement, L = lhs measurement and R = rhs measurement. * are values of the *MVD* rather than the *MaVD*. Note that the values from Kriewall et al. [47] and Sorbe and Dahlgren [94] are averages.

	MaVD	*OrOD*	*OrVD*	*OFD*	*SOFD*	*SOBD*	*BPD*	*BFD*	*BTD*
Kriewall (0)	135.0*	-	-	-	108.0	-	91.0	-	-
Kriewall	+4*	-	-	-	-2.0	-	+2.0		
Sorbe (0)	140.50	-	126.90	-	-	117.10	105.00	-	-
Sorbe	+1.90	-	+2.20	-	-	-1.70	0.00	-	-
Lapeer (0) S/L	129.28	119.93	119.35	119.66	113.16	88.71	89.75	50.90	80.61
R	128.73	-	118.91	119.74	113.78	89.97	-	-	-
D=0.9 S/L	+0.9466	+1.0717	+0.8702	+1.0368	-0.2184	-4.8672	-1.1541	-0.2168	+0.4393
R	+1.1179	-	+1.0863	+1.0261	-0.2251	-4.7253	-	-	-
D=0.7 S/L	+0.3194	-0.0553	+0.2761	-0.0756	-0.1837	-1.1974	-0.3795	-0.1387	-0.2166
R	+0.3624	-	+0.3264	-0.0878	-0.1829	-1.1266	-	-	-
D=0.5 S/L	+0.2210	-0.2452	+0.1911	-0.2647	-0.1682	-1.0379	-0.2644	-0.1197	-0.1935
R	+0.2111	-	+0.1818	-0.2750	-0.1665	-0.8181	-	-	-
D=0.3 S/L	+0.1811	-0.2744	+0.1553	-0.2917	-0.1738	-0.9487	-0.2288	-0.1105	-0.1814
R	+0.1521	-	+0.1267	-0.3026	-0.1731	-0.7048	-	-	-

Table 6.14: Maximum deformations (mm.) for each dilatation case - elaboration *II* (hyperelastic fontanelles/sutures).

dof	$D = 0.9$		$D = 0.7$		$D = 0.5$		$D = 0.3$	
	-	+	-	+	-	+	-	+
u_x	-7.488	+5.876	-1.211	+0.8934	-0.8912	+0.8302	-0.7607	+0.7189
u_y	-10.51	+2.342	-2.556	+0.7064	-2.189	+0.5251	-2.102	+0.4694
u_z	-4.187	+2.814	-0.7646	+1.127	-0.6874	+0.9866	-0.5381	+0.9571
u_{rx}	-1.062	+3.072	-0.2761	+0.4649	-0.2826	+0.3463	-0.2791	+0.2962
u_{ry}	-1.748	+1.747	-0.2722	+0.2855	-0.3048	+0.2518	-0.2041	+0.2440
u_{rz}	-0.6255	+3.608	-0.4600	+0.8977	-0.4273	+0.6924	-0.4436	+0.5708

parietal bones in the negative z-direction, a phenomenon which would occur for a stiffer posterior fontanelle. This effect would indeed be more eminent for pressure distributions which cover most of the parietal bones (i.e. for $D = 0.3$ - 0.7).

OrVD The order of magnitude of the elongation for $D = 0.9$ is much closer to the value, reported by Sorbe and Dahlgren. The same effect on the rhs measurements occurs as observed for the *MaVD*.

SOFD The difference between the two experiments is in general less than a factor 2. The diameter hardly changes for either experiment. The values as reported by Kriewall et al. [47] shows a compressive strain of -2 mm.[6]

SOBD The compressive strains are larger for $D = 0.9$ than the value reported by Sorbe and Dahlgren and the difference as compared to the basic experiment is large (almost a factor 10 for the rhs measurement). Also for the lower degrees of dilatation the *SOBD* has changed considerably.

BPD At dilatation 0.9, the biparietal diameter shows a decrease of more than 1 mm. As before, this is in contradiction with the increase of 2 mm. as reported by Kriewall et al. It is however in agreement with the results from parietal bone test *II* and those reported in Table 6.1 [72]. Since we only assess the skull moulding as caused by the head-to-cervix pressure (*HCP*), other effects during the second stage of labour may be involved which cause the *BPD* to increase. On the other hand, Sorbe and Dahlgren did not find any significant changes in the *BPD*.

[6]Note that the accuracy of Kriewall's reported values is only 1 mm.

BFD **and** *BTD* Despite the increase of compressive strains under hyperelastic conditions, the change of the *BFD* is minimal. This is not too surprising since frontal bones are almost entirely subjected to the amniotic pressure (*IUP*) only. A peculiar behaviour is shown by the *BTD* at $D = 0.9$ which changes from a minor compressive strain in the basic experiment to a reasonable tensile strain in elaboration *II*. This effect may be explained as a countereffect to the compression of the *BPD*, since landmarks 12L and 12R, which determine the *BTD*, are not subjected to the *HCP*.

The minimum and maximum values are shown in Table 6.14. Figure 6.13 shows again the displacements in the y-direction and rotations about the z-axis for dilatation $D = 0.9$[7]. The same effect as mentioned in the basic experiment occurs but to a much higher degree. From Table 6.14, the extrapolated value of +3.608 radians implies the element would have warped entirely around itself. This value was +0.873 radians, at the time convergence halted, which corresponds to a deflection of 50°! In the current experiment, displacements of landmarks were extrapolated to 100% of the load. In Section 6.3.1 we will discuss the validity of this approach and possible alternatives.

6.3 Experiment *III*

The final set of experiments presents three models which are all capable of providing a solution of the deformations for full application of the load. One of the models, involving polynomial extrapolation of the deformations, was already discussed in the previous section. In the next section we will point out the advantages and shortcomings of this model and subsequently suggest two other models which vary in terms of speed, accuracy and stiffness.

6.3.1 The convergence problem

Decreasing the stiffness of the fontanelle/suture structures by either decreasing their thickness (elaboration *I* of experiment *II*) or assuming hyperelastic behaviour (elaboration *II* of experiment *II*) has shown to display more realistic behaviour of the deformation of the entire skull. However, higher degrees of deformation have an adverse effect on the convergence of the solution due to excessive rotations of the fontanelle/suture structures or even buckling in the extreme case (corresponding to negative eigenvalues in the tangent stiffness matrix). In the previous experiments we used extrapolation of the deformations corresponding to 100% of the load. It is obvious that care has to be taken with

[7]The values are not extrapolated and correspond to 63.7% of the loading.

(a) Displacements in the y-direction, u_y (mm.).

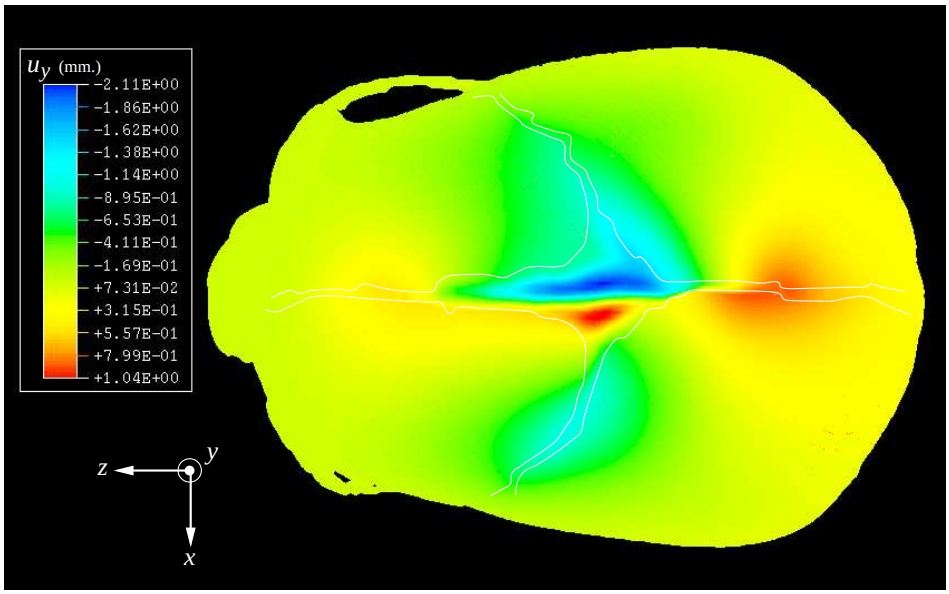

(b) Rotations about the z-axis, u_{rz} (radians).

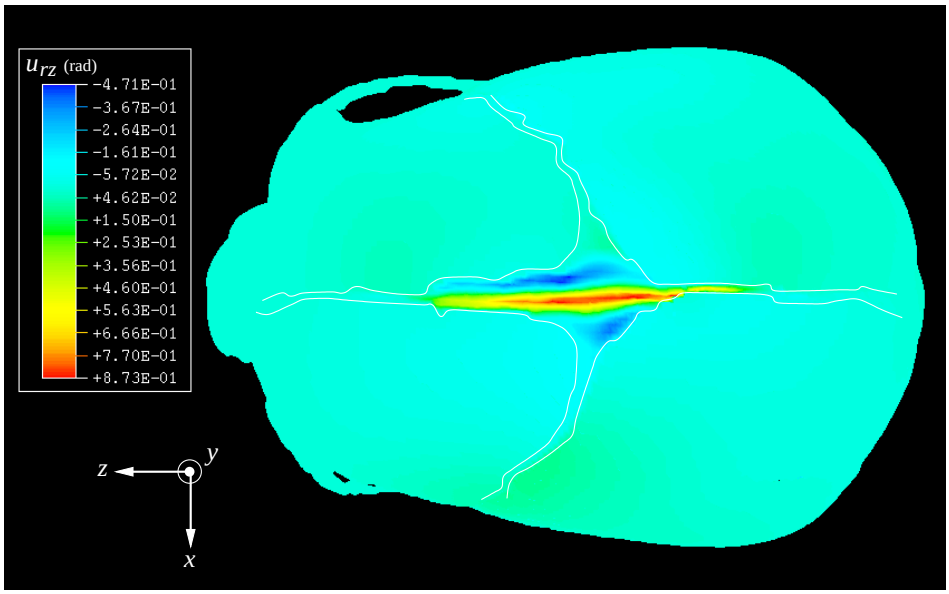

Figure 6.13: Contour plots for elaboration II ($D = 0.9$).

this approach. Figure 6.14 shows a trajectory of a nodal dof with extrapolation using second-, third- , fourth- and fifth- order polynomials respectively. The extrapolated values differ significantly, e.g. more than a factor 2 between quadratic and quintic interpolation! However, to conclude from this result that a higher-order polynomial is preferred is contradicted by the example as shown in Figure 6.15. The quintic polynomial overfits the data and yields therefore an unrealistic extrapolated value.

6.3.2 Alternative solutions to the convergence problem

One alternative solution to the convergence problem is to perform a linear analysis. This is obviously the least time-consuming approach but the accuracy is poor. Results of a linear model with hyperelastic fontanelles/sutures, model I, are given in Table 6.15.
A better solution in terms of accuracy is adapting the model during the analysis: elements which reach zero stiffness are removed or changed as to increase their stiffness or the local neighbourhood around the element is refined. This solution is time-consuming both in terms of use of the CPU as for individual user input since a significant amount of time is spent to inspect results before appropriate decisions can be made. The results are remarkable though as can be seen in Table 6.15 - model *III*: the analysis shows the best agreement with the findings of Sorbe and Dahlgren [94]. In Table 6.15, model *II* corresponds with the extrapolated results from elaboration *II* of experiment *II* for $D = 0.9$. A comparison of the *SOBD* between model *II* and model *III* might indicate that the former overestimates the degree of moulding considering the fact that the value of model *III* corresponds better to the value as reported by Sorbe and Dahlgren.
Table 6.16 shows the times needed for each analysis.
Figures 6.16 - 6.18 show the moulding of the skull for model *III*. The lifting of the parietal bones can be clearly seen from Figures 6.16 and 6.17. This phenomenon was also shown in the parietal bone tests (Figures 6.5, 6.7 and 6.8), is commonly known in the obstetric and paediatric community and was reported in [36, 72].

6.3.3 The moulding index

During the course of this chapter, we have reported results of the analysis by calculating strains of the diameters rather than calculating the moulding indices, as defined by Kriewall et al. (Equation 5.25) and Sorbe and Dahlgren (Equation 5.26). The reason is that the moulding indices hide information

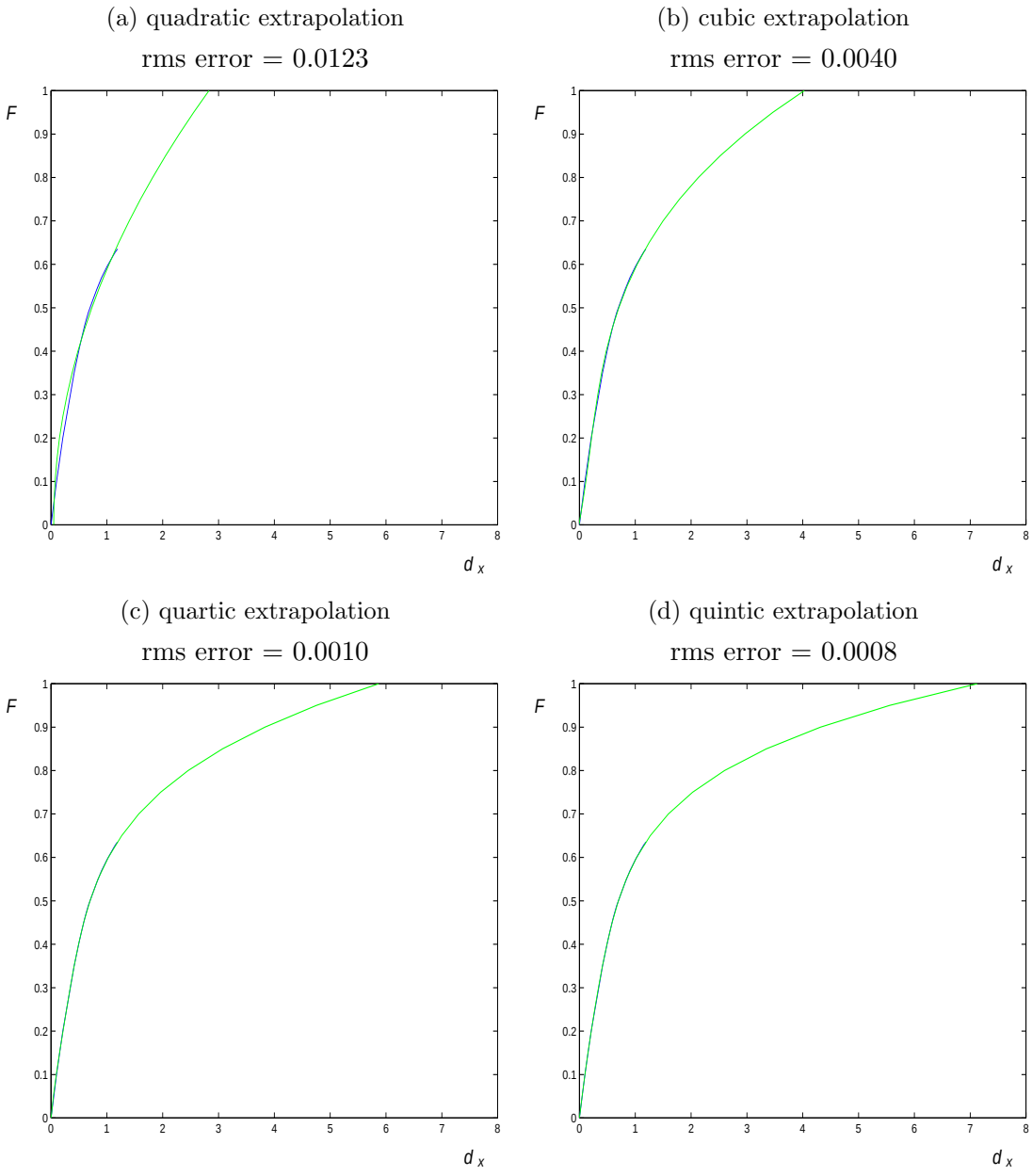

Figure 6.14: Extrapolation of a load-displacement trajectory (d_x in mm.). Convergence halted at 63.7% of the total load ($F = 0.637$). The *blue* line is the original trajectory. The *green* line is the polynomial.

(a) quintic extrapolation

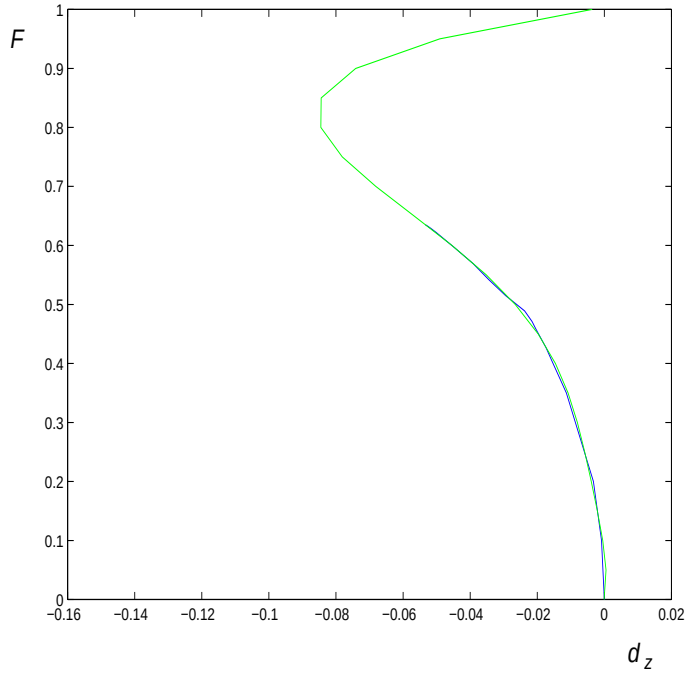

(b) quadratic extrapolation

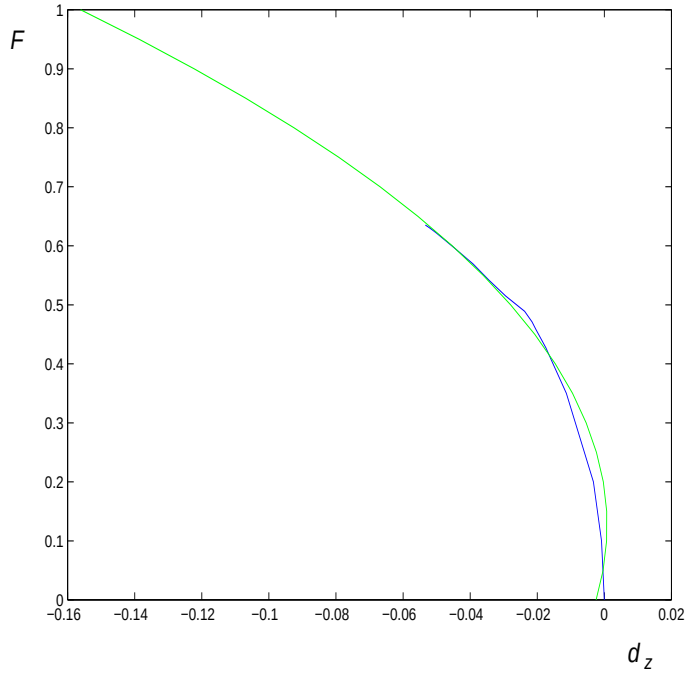

Figure 6.15: Extrapolation of a load-displacement trajectory with overfit (d_z in mm.). Convergence halted at 63.7% of the total load ($F = 0.637$). The *blue* line is the original trajectory. The *green* line is the polynomial. Note the overfitting of the quintic polynomial (a), resulting in an unreliable extrapolated value for d_z.

Table 6.15: Diametral strains (mm.) of three models as a solution to the convergence problem. All models assume fontanelles and sutures to possess hyperelastic properties. Results are for dilatation, $D = 0.9$. (0) = original diameter. Positive (+) values are tensile strains, negative (-) values are compressive strains. S = single measurement, L = lhs measurement and R = rhs measurement. * are values of the *MVD* rather than the *MaVD*. Note that the values from Kriewall et al. [47] and Sorbe and Dahlgren [94] are averages.

	MaVD	*OrOD*	*OrVD*	*OFD*	*SOFD*	*SOBD*	*BPD*	*BFD*	*BTD*
Kriewall (0)	135.0*	-	-	-	108.0	-	91.0	-	-
Kriewall (1)	+4*	-	-	-	-2.0	-	+2.0		
Sorbe (0)	140.50	-	126.90	-	-	117.10	105.00	-	-
Sorbe (1)	+1.90	-	+2.20	-	-	-1.70	0.00	-	-
Lapeer (0) S/L	129.28	119.93	119.35	119.66	113.16	88.71	89.75	50.90	80.61
R	128.73	-	118.91	119.74	113.78	89.97	-	-	-
model *I* S/L	+0.2466	+0.3311	+0.2074	+0.3330	-0.1486	-0.7381	-0.2165	-0.0672	-0.2210
R	+0.1899	-	+0.1538	+0.3257	-0.1491	-0.4793	-	-	-
model *II* S/L	+0.9466	+1.0717	+0.8702	+1.0368	-0.2184	-4.8672	-1.1541	-0.2168	+0.4393
R	+1.1179	-	+1.0863	+1.0261	-0.2251	-4.7253	-	-	-
model *III* S/L	+1.4239	+1.8526	+1.2402	+1.8177	-0.8532	-2.5209	-0.8294	-0.1119	-0.0170
R	+1.0074	-	+0.8830	+1.7804	-0.8458	-2.4859	-	-	-

(a) undeformed skull

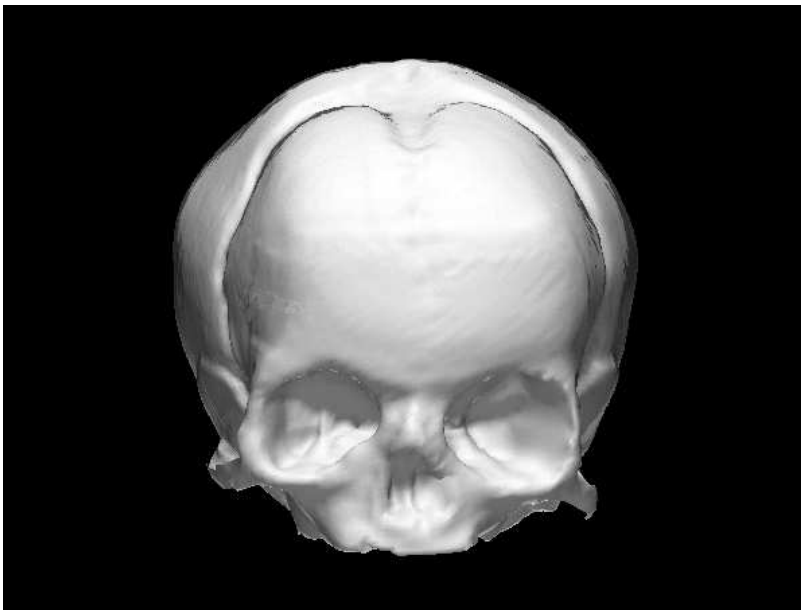

(b) deformed skull

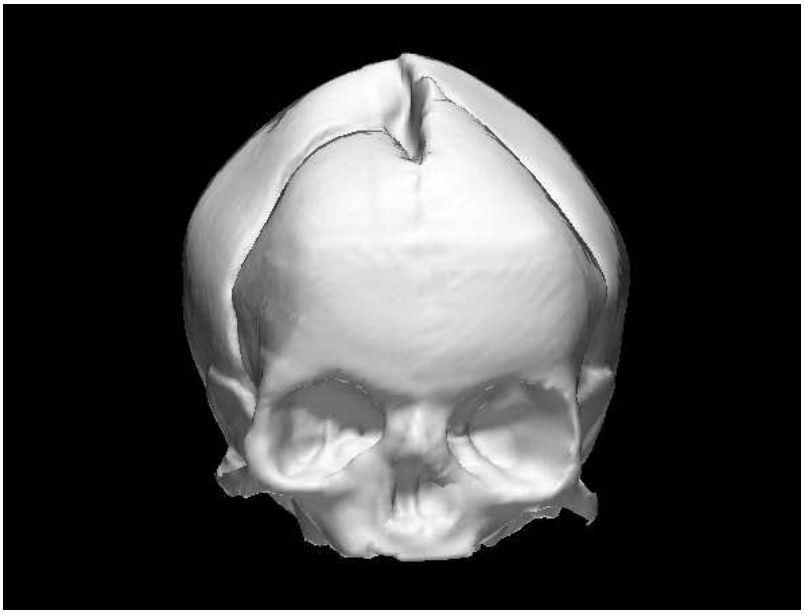

Figure 6.16: Front view of the foetal skull before and after moulding for model *III* - deformation magnification = 4. Note the lifting of the parietal bones which causes the *BPD* to decrease.

(a) undeformed skull

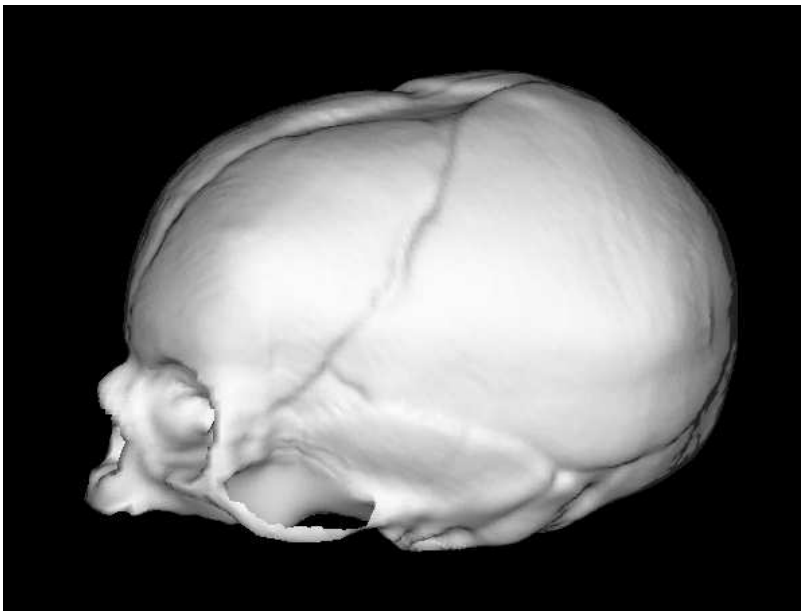

(b) deformed skull

Figure 6.17: Lateral view of the foetal skull before and after moulding for model *III* - deformation magnification = 4. The lifting of the left parietal bone is clearly visible. The same effect causes the *SOBD* to decrease. Note the upward bulging of the anterior fontanelle.

(a) undeformed skull

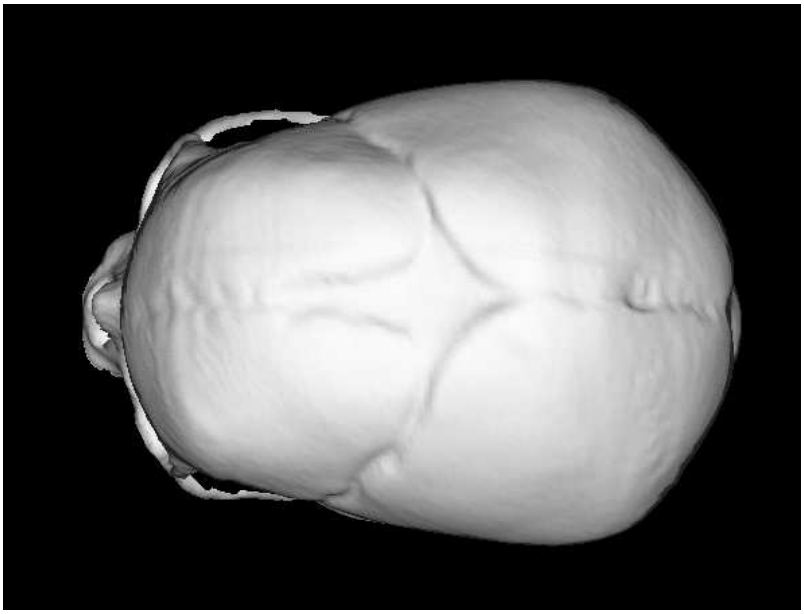

(b) deformed skull

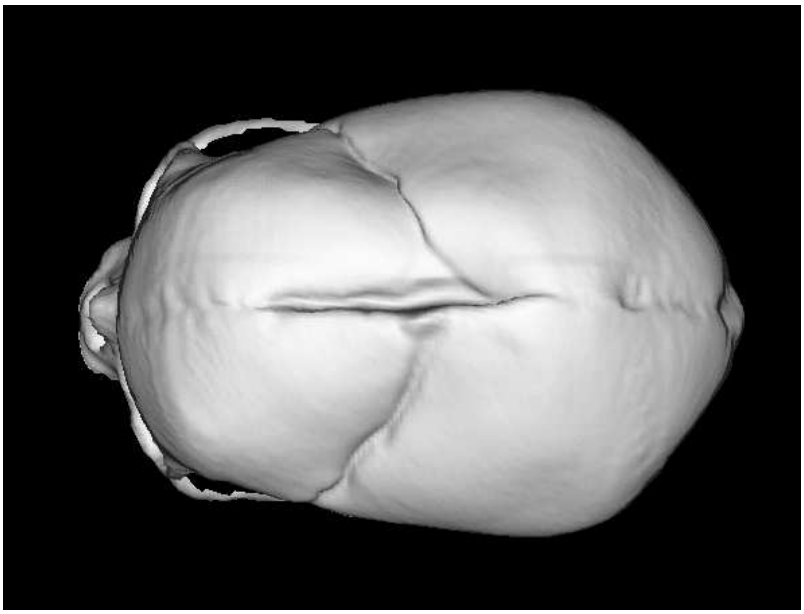

Figure 6.18: Top view of the foetal skull before and after moulding for model *III* - deformation magnification = 4. The anterior fontanelle is compressed, resulting in up- and downward displacements of its membranous structure.

Table 6.16: Analysis times (sec.) for three models as a solution to the convergence problem (* user interaction time is not included).

Time (sec.)	model *I*	model *II*	model *III**
User time	454.05	41218.	80294.
System time	85.690	4839.1	9392.2
Total CPU time	539.74	46057.	89686.
Wallclock time	878.00	67355.	131359.

Table 6.17: The modified moulding index, *MMI*, for three different models of foetal head moulding and from clinical experiments by Sorbe and Dahlgren [94] (* the *MMI*'s from Sorbe and Dahlgren are averages and corrected to account for the skin).

	Before	After	% moulding
Sorbe*	2.08	2.18	4.8
model *I*	2.10	2.13	1.4
model *II*	2.08	2.27	9.1
model *III*	2.10	2.23	6.2

Table 6.18: Relative diametral strains (%) for model *III* of experiment *III* (row 2) and corrected average diametral strains from Sorbe and Dahlgren (row 1) [94], for all diameters.

MaVD	*OrOD*	*OrVD*	*OFD*	*SOFD*	*SOBD*	*BPD*	*BFD*	*BTD*
+1.47	-	+1.85	-	-	-1.90	0.00	-	-
+1.10	+1.63	+1.04	+1.52	-0.75	-2.84	-0.92	-0.22	-0.02

and are not always consistent with the effects of the changes of the diameters. The latter was apparent from Kriewall's moulding index and was discussed in Section 5.4.1. Nonetheless, for the sake of completeness, Table 6.17 gives the modified moulding index, *MMI*, for all three models, before and after moulding and the values of Sorbe and Dahlgren [94]. Since there is a discrepancy in magnitude between Sorbe's values as reported in Table 5.8 and the author's values, because the former include the skin, a corrected *MMI* is calculated by taking the original diameters of the author in combination with the displacements from Sorbe and Dahlgren.
The percentage moulding (third column in Table 6.17) is calculated from:

$$\frac{MMI_a - MMI_b}{MMI_b} \times 100 \tag{6.2}$$

where MMI_b and MMI_a are the modified moulding indices before and after moulding respectively.
It is observed that model *II* and model *III* display higher degrees of moulding than model *I*. Model *III* shows the best agreement in terms of percentage moulding (6.2%) with the converted average value from Sorbe and Dahlgren (4.8%).

6.4 Discussion

Table 6.18 shows the relative diametral strains for model *III* of experiment *III*[8] and those from Sorbe and Dahlgren[9][94].
Comparison of the results in Table 6.18 shows relatively good agreement both in terms of the *shape after deformation* as the *degree of deformation*. One should not expect much better agreement considering the variance in the model parameters and the simplifications in the model, e.g. the omission of the second stage and soft structures of the foetal head (e.g. skin, membranes and brains). The order of magnitude of the strains is relatively constant and roughly ranges between 1-3% for the first seven diameters in the table. Relative diametral strains for experiment *I* - the parietal bone test - as shown in Table 6.6 for *NLG*, range between 2.5-7.5%. Despite some minor differences in the load distribution and the location of the diameters between the two experiments, this result shows that the parietal bone test displays unrealistically large strains. The main reason is the lack of stiffness because surrounding bones and fontanelles/sutures are missing. The boundary conditions, as specified by McPherson and Kriewall

[8]The largest absolute diametral strains from Table 6.15 are chosen when both left and right measurements are available.

[9]These values are corrected to account for the skin.

[72] can not normally compensate for this shortcoming. Thus, this result emphasises again the importance of analysing the entire skull rather than isolated parts of it.

6.5 Summary

This chapter presented a FE analysis, aimed at the assessment of foetal skull moulding during the first stage of labour. Experiment *I* involved a simple test on the parietal bones and was aimed at the evaluation of h- and p-refinement, first- and second-order elements and linear vs non-linear geometric analysis. The results of this test were in agreement with the findings of Kriewall and McPherson [72] and also showed that the use of first-order elements at the highest level of refinement and the assumption of non-linear geometry, was sufficient for high accuracy without excessive requirements of CPU time.
Experiment *II* evaluated the behaviour of the complete foetal skull, involving the parietal bones, the frontal bones, the occipital bone, the squamosal bones, the skull base and maxilla, the fontanelles and the sutures. The basic experiment assumed linear elastic behaviour of the fontanelles and sutures. The results were in agreement with clinical experimental results by Sorbe and Dahlgren [94] in terms of the *shape after deformation* but the *degree of deformation* was significantly smaller. Elaboration *I* aimed to assess the influence of several parameters in the model on the degree of moulding. It was found that the thickness of the fontanelles and sutures played a crucial role in the overall stiffness of the skull. Additionally to this finding, elaboration *II* assumed nonlinear, hyperelastic behaviour of the fontanelles and sutures. The more realistic material constants in this model resulted in a significant improvement of the elastic behaviour of the foetal skull. However, because of the higher and more realistic degree of deformation, convergence problems occurred during the analysis, due to excessive rotations of the incompressible fontanelle/suture elements. In experiment *III*, three models were suggested to solve this problem. The fastest approach involved a linear geometric model, model *I*, which showed poor realistic behaviour because of the generally non-linear nature of the problem. An alternative approach, i.e. model *II*, under the (correct) assumption of non-linear geometry, involved extrapolation of the results in case convergence failed for the application of 100% of the load. Although the behaviour of this model was more realistic, the accuracy of the results was found to be very sensitive to the order of the fitted polynomial and the percentage of load at which convergence stopped. Finally, model *III*, was based on user-interactive adaptation of the model during the analysis by removing, stiffening and refining

elements which showed excessive rotations. This model yielded the most realistic results when compared to the experimental results by Sorbe and Dahlgren [94], despite the longer CPU time and user-interaction time as compared to the other models.
Visualisation of the final model showed the lifting of the parietal bones when subjected to the pressure of the cervix. A finding which corresponds to the results from experiment *I* and the results from McPherson and Kriewall [72]. This phenomenon is also reported in [36] and is commonly known in the obstetric and paediatric community.

Chapter 7

Conclusions

7.1 Summary and conclusion

Foetal head moulding is a phenomenon with exhibits positive and negative characteristics in relation to the process of human childbirth. The positive aspect manifests itself during the birth process where the moulding of the skull allows the foetus to pass through the birth canal even when the dimensions of the latter are restricted. However, excessive head moulding may result into cranial birth injuries, which may affect the well-being of the infant at birth and possibly for the rest of its life. Thus, a realistic model of the behaviour of the foetal skull during delivery is of major importance to the obstetric and paediatric community. In obstetrics, the concept of a birth simulation for early diagnosis on the progress of labour has become popular during the last decade. In the early and mid 90's, several individual researchers and research groups did interesting preliminary work on the birth simulation but never covered the concept of foetal head moulding in depth. However, a simulation which does not involve foetal head moulding would have poor specificity since it would be more likely to recommend the need for Caesarian section even if vaginal delivery would be perfectly possible. In paediatrics, a realistic model of foetal head moulding is a major step towards the understanding of mechanical cranial birth injuries. Excessive moulding occurs when labour is prolonged, or when contractions are too forceful, or when there is malposition of the foetal head or inept instrumental interference. Displacements of the skull bones may cause bony lesions, dural membrane injury, intracranial hypertension with focal or general brain swelling and possibly with retinal haemorrhage, congestion of the Galenic venous system and direct injury of major intracranial vessels [36].

The objective of the research, as presented in this dissertation, was to contribute to the understanding of the foetal head moulding phenomenon by study-

ing the deformation of a human foetal skull when it is subjected to the forces of labour. Previous work on the biomechanics of foetal head moulding involved the assessment of the parietal bones only. The model, presented in this dissertation involves the static analysis of deformation of a complete foetal skull.

The fact that the cranial bones of the foetal skull are very thin as compared to their surface dimensions, justified the use of a shell-based surface model. A first attempt to recover the outer shape of a foetal skull required the acquisition of orthogonal images of a foetal skull and a 3D adult skull obtained from CT images. Specification of corresponding landmarks on both objects allowed us to warp the shape of the adult skull into the shape of a foetal skull. This model was eventually replaced by a more accurate model, acquired from laser-scanned data of a life-size model of a real foetal skull. The registration problem, to create a valid surface model from different acquisitions of laser-scanned data, was solved using least-squared error based matching of landmarks. Different triangulated patches of the object were subsequently connected using a combined technique of thin-plate spline interpolation and advancing front-based triangulation to generate a valid, compatible mesh for finite element analysis.

A biomechanical model of foetal skull moulding was designed, based on clinical research involving the assessment of material properties of structures of the foetal and adult skull and the measurements of intra-uterine and head-to-cervix pressures. Based on the nature of the available data from this research, it was decided to restrict the model to a static analysis of the first stage of labour, when the foetal head is in contact with the uterine cervix.

A first experiment involved the finite element analysis of the parietal bones of the foetal skull as an extension of the earlier work by McPherson and Kriewall [72]. The results of this experiment, though more accurate, were in agreement with their findings. Further evaluation of these results indicated the need of using the finest possible mesh to ensure the highest possible accuracy. It was also shown that at this level of refinement, the considerable excess of processing time needed when using second-order elements as opposed to first-order elements, was not worthwhile.

With this information in mind, the second experiment, involving the assessment of the entire skull, was performed. The complex nature of the finite element model, containing shell elements with orthotropic properties for foetal cranial bone, isotropic properties for the foetal skull base and hyperelastic properties for the fontanelle and suture structures, was shown to be sensitive to relatively small changes of the material properties of each of these components. Convergence problems did occur for higher degrees of deformation because of the excessive rotations of the fontanelle and suture structures which behave

like membranes and are thus incompressible. This problem was solved using three different models which were validated by comparing the change of principal diameters of the skull with results from clinical studies on the quantitative assessment of foetal head moulding as performed by Kriewall et al. [47] and Sorbe and Dahlgren [94].

The first model assumed linear geometry. In this case a solution is always found and the time needed for processing is short. However, the model is in general too stiff because of the non-linear nature of the problem.

The second model assumed non-linear geometry and results were extrapolated using polynomial regression in case the solutions failed to converge in a reasonable time and within preset error bounds, for full application of the load. This model required considerably more processing time than the first model but gave more realistic results. A major drawback of this model is that the extrapolated results can show significant variation, depending on the order of the fitted polynomial and the percentage of load applied when convergence failed.

Finally, a third model assuming non-linear geometry was suggested for which full convergence was achieved by adapting the model during the analysis, i.e. removing, stiffening or refining the elements which showed excessive rotations or tendency towards zero or negative stiffness. This model, though expensive in terms of processing and user interaction time, showed very good agreement with the clinical experimental results from Sorbe and Dahlgren [94]. Visualisation of the deformed models showed the lifting of the parietal bones, a phenomenon which was reported in [36, 72] and which is commonly known in the obstetric and paediatric community.

The biomechanical model of foetal head moulding as presented in this dissertation is a significant improvement as compared to the previously suggested model of the parietal bones by McPherson and Kriewall [72]. Despite the variation within the parameters involved in the birth process, the model shows good agreement with clinical experimental results on the quantitative assessment of foetal head moulding, both in terms of the *shape after deformation* as the *degree of deformation*. The model allows us to evaluate the biomechanics of foetal head moulding in a quantitative fashion and continuously across the geometry. Therefore, it can be used in the obstetric field, to improve the sensitivity of a computerised birth simulation, aimed at the early diagnosis of possible complications during vaginal delivery. In the paediatric field, it can be applied to investigate mechanical cranial birth injuries as well as congenital malformations such as hydrocephalus.

7.2 Elaborations and further research

The results of the absolute diametral strains in the experimental sections of Chapter 6 were presented with an accuracy of four digits. This accuracy was necessary to compare subtle changes as a result of different parameter settings. It would of course be foolish to assume that we have calculated the deformations of the moulded skull with such an accuracy, considering the fact that the parameters involved in the model, i.e. geometry of the skull, head-to-cervix pressures, intrauterine pressure, material properties of foetal bone and fontanelles and sutures, can vary significantly, depending on a wide range of factors. Intrauterine and head-to-cervix pressures depend on parity, gravidity, duration of labour, maternal position, rupture of the membranes, maternal physiological factors, size of the uterus, size, position and compressibility of the foetus, etc. Both the material properties and geometry of the foetal skull depend on morphogenetic processes such as biological growth and ossification. Gestational age was shown in [71] to be a major factor to the bending stiffness and general thickness of foetal cranial bone. Hence, this brief summation points out the variation present within the model parameters. In elaboration *I* of experiment *II*, presented in Chapter 6, the effect of the variation of these parameters on the degree of foetal skull moulding was evaluated. However, to perform an in-depth study on the variation of foetal head moulding, more comprehensive data on the model parameters is required. In the next sections, I will outline the feasibility and possible strategies to the successful acquisition of such data. Furthermore, involvement of other structural components of the skull model, such as skin, brains and membranes, the consideration of the second stage of labour and further improvements of geometric modelling and finite element analysis are suggested.

Shape and geometric modelling of the foetal skull

The skull model used throughout this research was obtained from laser-scanning a replica model of a real foetal skull. This resulted in an accurate model of the surface of the skull, an approximation which was reasonable under the assumption that the bones of the cranial vault can be considered as thin shells. However, the acquisition of a CT dataset of a foetal or newborn skull would simplify the process of modelling the geometry of the surface as well as providing the internal structures of the skull base and facial bones. It is however not clear how much the internal structures would influence the moulding of the skull in general. In elaboration *I* of experiment *II* (Chapter 6), the change of thickness of the temporal bones did not show a significant effect on the skull moulding.

Besides the ethical and political difficulties to obtain a complete CT dataset of a foetal or newborn skull, its availability would not provide sufficiently accurate data to model the thickness of the cranial vault bones. In [71], the average of the reported values of the parietal bone thickness was around 0.75 mm. The interplanar resolution of conventional CT scanners is about 1 mm. whilst the intraplanar resolution is of the order of 0.5 mm. To accurately model the thickness of the cranial vault bones, an accuracy of at least 0.1 mm. is required.

Shape variation of the model

The model as presented in this work involved the analysis of a single foetal skull. To investigate the sensitivity of foetal skull moulding to shape variations would require the availability of a number of skulls. However, as mentioned before, there are ethical problems related to this. An alternative solution could be based on warping using thin-plate spline interpolation. Variation of principal diameters could be obtained from measurements from a clinical experiment similar to the one as conducted by Kriewall et al. [47] and Sorbe and Dahlgren [94].

Mesh generation for biomechanical models

The mesh generation algorithms as described in Chapter 3 allow fast mesh creation for arbitrary complexity but are restricted to level or visible surfaces ($2\frac{1}{2}$D). A significant improvement would involve the extension to 3D surfaces and solids. This would avoid the time-consuming, user-interactive tessellation of the object into smaller level patches.

Material properties of the foetal skull

In the past, only Bylski et al. [14] and McPherson and Kriewall [71] investigated material properties of the structures of the foetal cranium. Although ethical issues would pose an even greater problem than the acquisition of CT data, more sophisticated experiments could provide more accurate data on the material properties.

Hyperelastic behaviour of the fontanelles and sutures

In this work, the Mooney-Rivlin (MR) model was used to model the hyperelastic properties of the fontanelles and sutures. It was not clear in how much this model was responsible for a more realistic behaviour of the deformation of the skull as opposed to the actual values used in the MR model as reported in

[14]. Bylski et al. [14] found a hyperelastic model, i.e. the Skalak, Tozeren, Zarda and Chien (STZC) model, which fitted the experimental data, from a biaxial tension test, better than the Mooney-Rivlin model. The assessment of this model in future work should be considered.

The involvement of skin, brains and membranes

In the current model, the skin, brains and membranes[1] were ignored.
Since *the brain* is virtually incompressible, the model should include a parameter to model deformation without change of volume.
Previous work on the biomechanics of brain tissue using a poroelastic model [81] and the biomechanics of hydrocephalus [77, 81] could be combined with the foetal head moulding model to investigate brain damage following excessive moulding.

Viscoelastic and plastic behaviour of the bones of the cranial vault

Experiments investigating possible viscoelastic behaviour of the skull bones of the foetal cranial vault have not been conducted as yet. The assumption of viscoelastic behaviour of the cranial vault bones is realistic considering the fact that articular cartilage is known to show this behaviour [32]. Consideration of viscoelasticity and more specifically, creep, into a model of foetal head moulding would show continuing deformation even when the load is held constant.
There must be some degree of plasticity as well considering the significant time it takes for restitution after moulding (i.e. about three days as reported in [47, 94]).
As mentioned before, more sophisticated experiments than those reported in [70, 71], to assess the properties of foetal cranial bone, are required.

Measurements of the intra-uterine and head-to-cervix pressures during the first stage of labour

It was pointed out in Chapter 5 that studies involving the measurements of the intra-uterine pressure and the head-to-cervix pressure showed significant inter-observer and intra-observer variation. None of the studies done so far have studied a significantly large sample nor did they take full account of correlated variables such as cervical dilatation, parity and gravidity, rupture of the membranes and progress of labour. Better controlled studies are necessary to

[1] The *membranes* imply here the protective membranes between the brains and the cranial vault such as the dura mater, not the *foetal membranes*.

provide reliable and sufficient data. These data could then be used in the foetal head moulding model, either directly or as a validation for an idealised model. Bell's model, as described in Chapter 5, assumes the lower pole of the foetal head/skull to be of a spherical shape. This assumption results in a relatively simple model which does agree satisfactorily with experimental values. The geometry of the lower pole of the head is however more complicated in reality. A better mathematical model could be sought after but care has to be taken not to go into overcomplex parameter specifications.

Static vs dynamic analysis

In this work, the analysis of deformation of the foetal skull is based on the application of a static load. The true process is dynamic, though it changes very slowly in time. It is likely that a dynamic analysis would improve the model only when viscoelastic properties of the cranial vault bones and the uterine cervix would be considered.

Viscoelastic properties of the cervix

Bell [10] pointed out that the dilatation of the cervix is not strictly linear in time, but oscillates around a linearly increasing average dilatation in time. This is due to the viscoelastic properties of the cervix. As mentioned in the previous paragraph, a dynamic analysis is required to take the viscoelastic behaviour of the cervix into account.

The involvement of the second stage of labour

The second stage of labour was left out at this stage since many parameters, needed for a successful simulation, are missing. One of these involves a realistic model of the pressure distribution on the head. Even though several researchers have measured the pressures on the foetal head during the second stage, it is difficult to model the pressure distribution because of the complex geometry of the birth canal which involves the *maternal pelvis* and *soft tissues*. The generation of a 3D solid mesh of the maternal pelvis was accomplished in [23] using Delaunay tetrahedrisation. Soft tissue modelling of the maternal birth canal could be aided by the current availability of MRI, CT and photographic images of the Visible Female (Visible Human Project). Current developments on the biomechanical behaviour of soft tissue have been covered amongst others in [32, 96, 108] and sections III and IV of [13]. Once the geometry is modelled, a *mechanical contact analysis* could be applied to model the interaction between the foetal head and the maternal birth canal.

Validation of foetal head moulding

Kriewall et al. [47] and Sorbe and Dahlgren [94] are the only researchers who performed quantitative assessment of foetal head moulding in the past. The study by Sorbe and Dahlgren covers a sufficiently large sample of 319 vaginal deliveries without any major complications. Better controlled experiments are needed though, preferably in combination with intra-uterine and head-to-cervix pressure measurements.

Finite element modelling for biological objects of complex geometry and structure

The final model on deformation of the foetal skull (model *III* in experiment *III* of Chapter 6) showed good agreement with the experimental results from Sorbe and Dahlgren [94]. However, the amount of time needed, i.e. processing time as well as user-interaction time, to arrive at this model was considerable. More complex models would require even more time hence more optimal solution strategies should be sought after. The ABAQUS software for FEA, which we used throughout this research, requires to stop analyses, evaluate results, change the model and restart the analysis. This procedure has to be repeated until full convergence is reached. A major and reasonably straightforward improvement could be the automatic adaptation of a model based on pre-specified conditions as set by the user.

Appendix A

An introduction to the Finite Element Method (FEM)

A.1 General concepts of the mechanics of deformable bodies

To analyse the mechanical behaviour of a deformable body we conventionally aim to establish [76]:

Force and moment equilibrium relating *stress* to applied forces or other stresses, whether there are applied forces or not. If *displacements* are small then the equations of equilibrium may considered to be linear.

Geometric compatibility relating *strain* to *displacements* and are purely geometrical arguments which depend on the definition of strain and the type of deformation and geometry of the particular structure. If the *displacements* are small then the strain-displacement relationships may considered to be linear.

Stress-strain relations or *constitutive* relations relating *stress* to *strain*. They are usually empirical thus depend on experimental evidence.

The set of equations obtained from these three conditions allows us to solve for displacements, stresses and strains.

A.1.1 Stress

Figure A.1 shows the stress components on a parallelepiped with infinitesimally small sides $\Delta x, \Delta y, \Delta z$. There are three *direct stress* components, $\sigma_{xx}, \sigma_{yy}, \sigma_{zz}$ and three independent *shear stress* components, $\sigma_{xy}, \sigma_{yz}, \sigma_{zx}$.
Index definitions and sign conventions are:

- For direct stress components the second index is basically redundant but it will be kept for conformity with shear stresses. The index denotes the direction of the face upon which the stress component acts. The sign of the resulting stress component is *positive* when a positively directed force component acts on a positive face OR when a negatively directed force component acts on a negative face.

- Shear stress components are described by two distinct indices: the first index denotes the direction of the face upon which the stress component acts. The second index denotes the direction of the shear force. The sign convention is as before.

It can be shown that $\sigma_{ij} = \sigma_{ji}$, for $j \neq i$ (the proof can be found in [21]).
Rather than representing stress by a two-dimensional tensor, it is more convenient to represent it by the column vector:

$$\sigma = \left[\begin{array}{cccccc} \sigma_{xx} & \sigma_{yy} & \sigma_{zz} & \sigma_{xy} & \sigma_{yz} & \sigma_{zx} \end{array} \right]^T \tag{A.1}$$

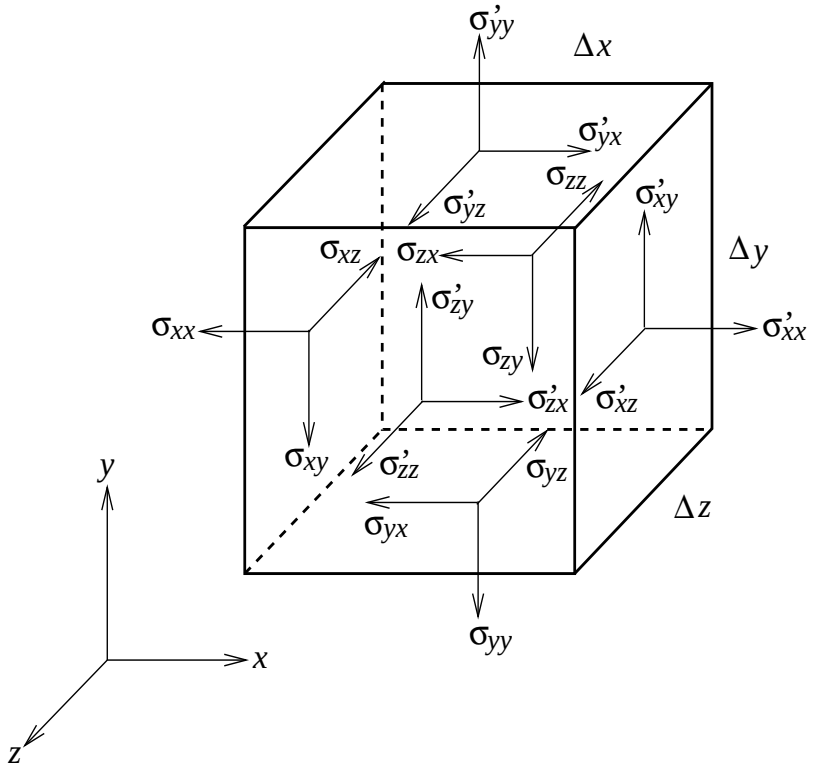

Figure A.1: Stress components acting on the six sides of an infinitesimally small parallelepiped. To guarantee moment and force equilibrium: $\sigma'_{ij} = \sigma_{ij} + \frac{\partial \sigma_{ij}}{\partial i}\Delta i$, for $i, j = x, y, z$.

A.1.2 Displacement - Deformation - Rigid body motion

Figure A.2 shows a body before and after displacement. The *displacement* of an individual point is the vector quantity:

$$\mathbf{u} = [\ u \quad v \quad w\ ] \tag{A.2}$$

The displacement of a continuous body consists of two distinct motions:

1. *Rigid body motion*: translation and rotation of the body as a whole.
2. *Deformation*: motion of points on the body, relative to each other.

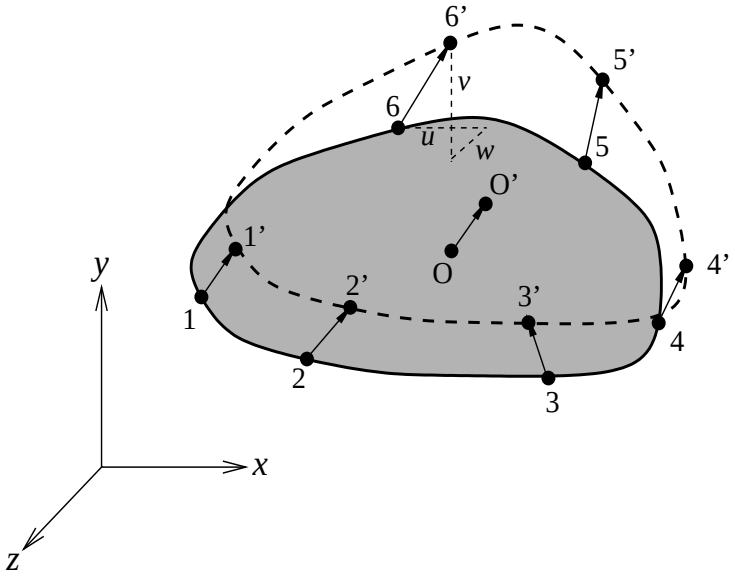

Figure A.2: An arbitrary 3D body before and after deformation.

A.1.3 Strain

Figure A.3 shows the deformation of an infinitesimally small element (in 2D, for ease of illustration).
Under the assumption that the strains are small as compared to unity, we can write the *normal* strain in the x-direction:

$$\begin{aligned} \epsilon_x &= \lim_{\Delta x \to 0} \frac{O'C' - OC}{OC} \\ &= \lim_{\Delta x \to 0} \frac{[\Delta x + (\partial u/\partial x)\Delta x] - \Delta x}{\Delta x} \\ &= \frac{\partial u}{\partial x} \end{aligned} \tag{A.3}$$

Similar reasoning yields the strains in the y-direction and in the z-direction after extending to 3D yields:

$$\epsilon_y = \frac{\partial v}{\partial y} \tag{A.4}$$

$$\epsilon_z = \frac{\partial w}{\partial z} \tag{A.5}$$

For the *shear* strain component in the x-y plane we can write:

$$\begin{aligned}
\epsilon_{xy} &= \lim_{\Delta x, \Delta y \to 0} (\angle COE - \angle C'O'E') \\
&= \lim_{\Delta x, \Delta y \to 0} \left(\frac{\pi}{2} - \angle C'O'E' \right) \\
&= \lim_{\Delta x, \Delta y \to 0} \left(\frac{\pi}{2} - \left(\frac{\pi}{2} - \frac{(\partial v/\partial x)\Delta x}{\Delta x} - \frac{(\partial u/\partial y)\Delta y}{\Delta y} \right) \right) \\
&= \frac{\partial v}{\partial x} + \frac{\partial u}{\partial y}
\end{aligned} \tag{A.6}$$

and for the shear strains in the y-z and z-x planes respectively:

$$\epsilon_{yz} = \frac{\partial w}{\partial y} + \frac{\partial v}{\partial z} \tag{A.7}$$

$$\epsilon_{zx} = \frac{\partial u}{\partial z} + \frac{\partial w}{\partial x} \tag{A.8}$$

Hence the strain vector in 3D becomes:

$$\boldsymbol{\epsilon} = \begin{bmatrix} \epsilon_x & \epsilon_y & \epsilon_z & \epsilon_{xy} & \epsilon_{yz} & \epsilon_{zx} \end{bmatrix}^T \tag{A.9}$$

A.1.4 The elastic stress-strain relations

The elastic stress-strain relations or *constitutive relations* for a linear-elastic isotropic 3D body are (in matrix notation):

$$\begin{bmatrix} \sigma_{xx} \\ \sigma_{yy} \\ \sigma_{zz} \\ \sigma_{xy} \\ \sigma_{yz} \\ \sigma_{zx} \end{bmatrix} = \frac{E}{(1-2\nu)(1+\nu)} \begin{bmatrix} 1-\nu & \nu & \nu & 0 & 0 & 0 \\ \nu & 1-\nu & \nu & 0 & 0 & 0 \\ \nu & \nu & 1-\nu & 0 & 0 & 0 \\ 0 & 0 & 0 & \frac{1}{2}-\nu & 0 & 0 \\ 0 & 0 & 0 & 0 & \frac{1}{2}-\nu & 0 \\ 0 & 0 & 0 & 0 & 0 & \frac{1}{2}-\nu \end{bmatrix} \begin{bmatrix} \epsilon_x \\ \epsilon_y \\ \epsilon_z \\ \epsilon_{xy} \\ \epsilon_{yz} \\ \epsilon_{zx} \end{bmatrix} \tag{A.10}$$

where E is Young's modulus and ν is Poisson's ratio. In the abbreviated notation the constitutive relations become:

$$\boldsymbol{\sigma} = \mathbf{E}\boldsymbol{\epsilon} + \boldsymbol{\sigma}_0 \tag{A.11}$$

where $\mathbf{E}$ is the material stiffness matrix and $\boldsymbol{\sigma}_0$ is the initial stress vector[1].

[1] For example, stress caused by temperature changes.

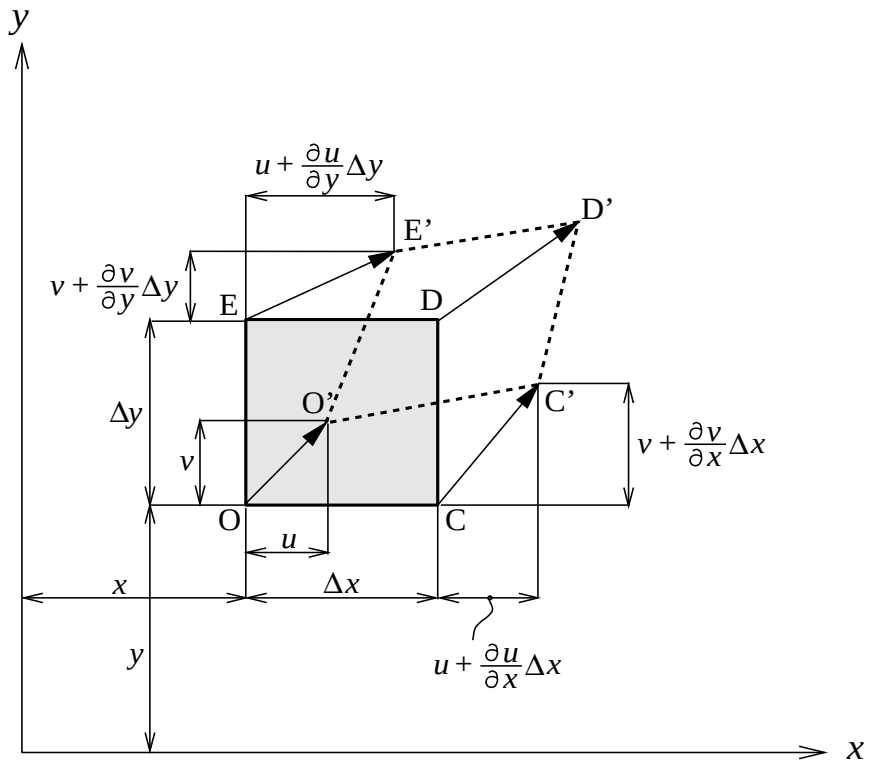

Figure A.3: Deformation of a small 2D element of a continuous body.

A.2 The Principle of Virtual Displacements (PVD)

In Section A.1 the three relationships of the analysis of a three-dimensional deformable body were outlined. At each point of the deformable body, equilibrium is expressed by six independent equations, i.e. translational equilibrium in each direction x,y,z and rotational equilibrium about each axis. The PVD is a single scalar equation which is able to enshrine these six equations for the whole body. Assume a particle subjected to forces $\mathbf{p}_i$ as is shown in Figure A.4. Now imagine the particle displaces by an imaginary or *virtual* displacement $\delta\mathbf{u}$. Under the assumption that virtual displacements are independent of the real forces, the *virtual work* δW is given by the scalar product:

$$\delta W = \sum_{i=1}^{n} \mathbf{p}_i.\delta\mathbf{u} \tag{A.12}$$

If the particle is in equilibrium, then $\sum_{i=1}^{n} \mathbf{p}_i = 0$ hence:

$$\delta W = 0 \tag{A.13}$$

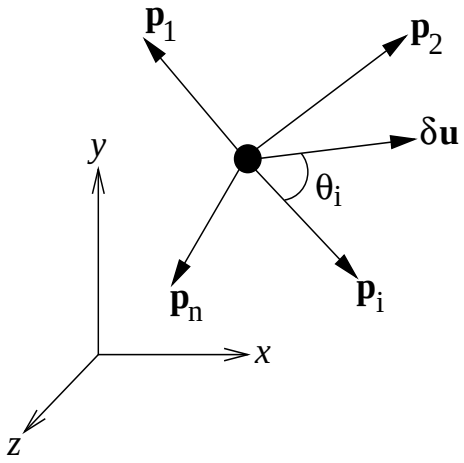

Figure A.4: A particle in 3D space subjected to n forces $\mathbf{p}_i$ and a virtual displacement $\delta\mathbf{u}$.

Alternatively, if equation A.13 is satisfied for arbitrary $\delta\mathbf{u}$, then the particle is in equilibrium[2].

A.3 Formulation of the displacement-based Finite Element Method for a general continuum

Figure A.5 shows a three-dimensional body of arbitrary shape. The body is placed in a fixed coordinate system with coordinates x, y, z. Any point on the surface has an outward-pointing surface normal $\mathbf{n}$ with components or *direction cosines* $\frac{\partial n}{\partial x}, \frac{\partial n}{\partial y}, \frac{\partial n}{\partial z}$.
The body is in general subjected to two types of external forces:

body forces - force per unit volume:

$$\mathbf{p}_b = [\ p_{b,x} \quad p_{b,y} \quad p_{b,z}\ ]^T \tag{A.14}$$

surface traction forces - force per unit area:

$$\mathbf{p}_s = [\ p_{s,x} \quad p_{s,y} \quad p_{s,z}\ ]^T \tag{A.15}$$

Application of the *PVD* and stating the equilibrium between the virtual (internal) strain energy, δU, and the virtual external work, δW_{ex}:

$$\delta W = \delta U - \delta W_{ex} = 0 \tag{A.16}$$

[2]Arbitrary, to exclude the case where $\sum \mathbf{p}_i$ and $\delta\mathbf{u}$ are orthogonal.

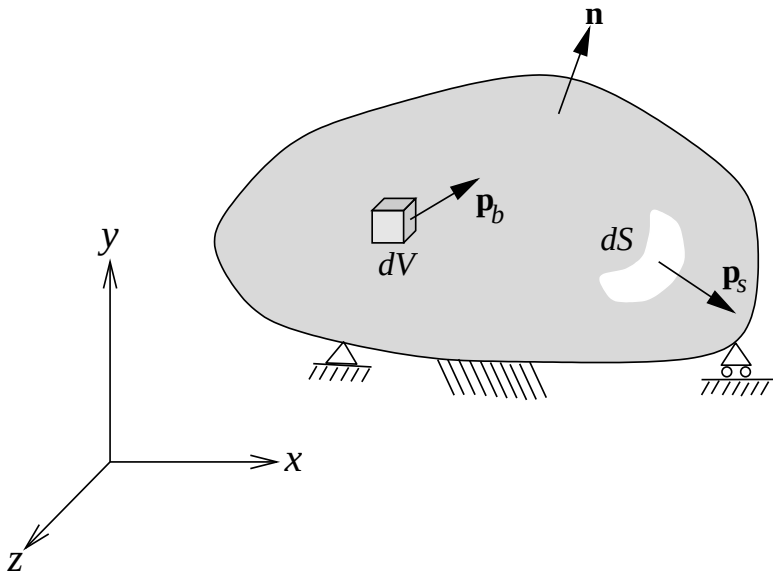

Figure A.5: An arbitrary 3D body, with prescribed boundary conditions, subjected to body forces, $\mathbf{p}_b$, and surface traction forces, $\mathbf{p}_s$.

Writing out equation A.16 yields:

$$\int_V \boldsymbol{\sigma}^T.\bar{\boldsymbol{\epsilon}}\, dV = \int_V \mathbf{p}_b.\bar{\mathbf{u}}\, dV + \int_S \mathbf{p}_s.\bar{\mathbf{u}}\, dS \tag{A.17}$$

where the $\bar{\mathbf{u}}$ are virtual displacements[3] (in global coordinates) and $\bar{\boldsymbol{\epsilon}}$ the corresponding virtual strains.
Finally, for an assembly of n elements, the PVD becomes:

$$\sum_{l=1}^{n} \int_{V\ l} \boldsymbol{\sigma}^T.\bar{\boldsymbol{\epsilon}}\, dV = \sum_{l=1}^{n} \left(\int_{V\ l} \mathbf{p}_b.\bar{\mathbf{u}}\, dV + \int_{S\ l} \mathbf{p}_s.\bar{\mathbf{u}}\, dS \right) \tag{A.18}$$

A.4 Example

Equation A.17 allows us to derive a finite element formulation for a variety of different element shapes. To stay within the realm of this work, we will illustrate the derivation of a solution for a second-order (linear strain) triangular plate element (LST) of thickness t.

A.4.1 Representation in barycentric coordinates

Barycentric coordinates or *area* coordinates were first introduced by F. Möbius in 1827 [27]. Consider the triangle $\triangle n_1 n_2 n_3$ in Figure A.6a. An arbitrary point, p, inside the triangle can always be specified using the barycentric combination:

[3] We will use this shorter notation in the further course of the text instead of $\delta\mathbf{u}$.

$$p = \sum_{i=1}^{3} \xi_i \mathbf{n}_i \tag{A.19}$$

where $\mathbf{n}_i$ are points in a general coordinate system and ξ_i are the *barycentric coordinates*. If equation A.19 is to be geometrically meaningful, we require that $\xi_1+\xi_2+\xi_3 = 1$. This implies that $\xi_i = A_i/A$, for $i = 1, \ldots, 3$, with $A = \sum_{i=1}^{3} A_i$ or the area of $\triangle n_1 n_2 n_3$.
We can also write (see Figure A.6b):

$$\xi_i = \frac{h_i}{H_i} \tag{A.20}$$

for $i = 1, \ldots, 3$.

A.4.2 Shape functions

For a single 2D element, the displacement vector is represented by:

$$\mathbf{u} = \begin{bmatrix} u & v \end{bmatrix}^T \tag{A.21}$$

The nodal displacements for a second-order triangular element l are given by:

$$\mathbf{d}_l = \begin{bmatrix} d_1 & d_2 & \ldots & d_{12} \end{bmatrix}^T \tag{A.22}$$

We can write then:

$$\mathbf{u} = \mathbf{N}\mathbf{d}_l \tag{A.23}$$

where

$$\mathbf{N} = \begin{bmatrix} N_1 & 0 & N_2 & 0 & N_3 & 0 & N_4 & 0 & N_5 & 0 & N_6 & 0 \\ 0 & N_1 & 0 & N_2 & 0 & N_3 & 0 & N_4 & 0 & N_5 & 0 & N_6 \end{bmatrix}$$

The shape functions are readily seen to be:

$$N_i = 2(\xi_i - \frac{1}{2})\xi_i$$

for $i = 1, \ldots, 3$

$$N_i = 4\xi_{i-3}\xi_{1+(i-3) \bmod 3}$$

for $i = 4, \ldots, 6$

A.4.3 The strain-displacement relation

The relation between strain and displacement is given by[4]:

[4]Remember that the terms involving a z-component in $\boldsymbol{\epsilon}$, as given in Equation A.9, are absent.

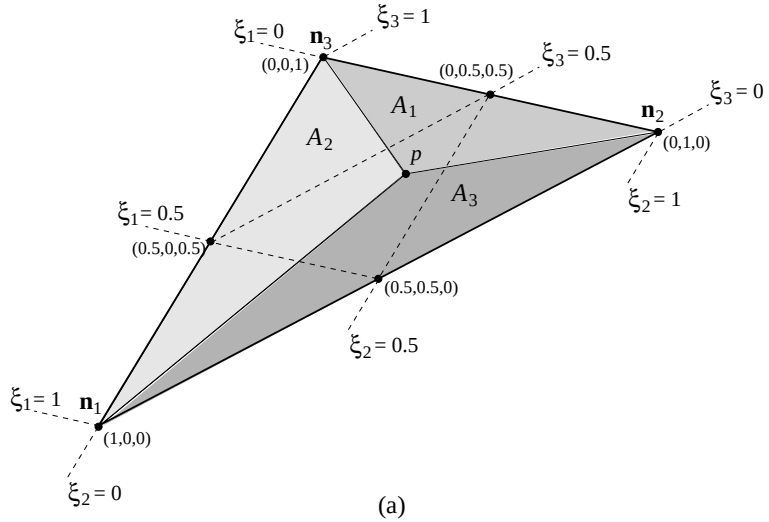

(a)

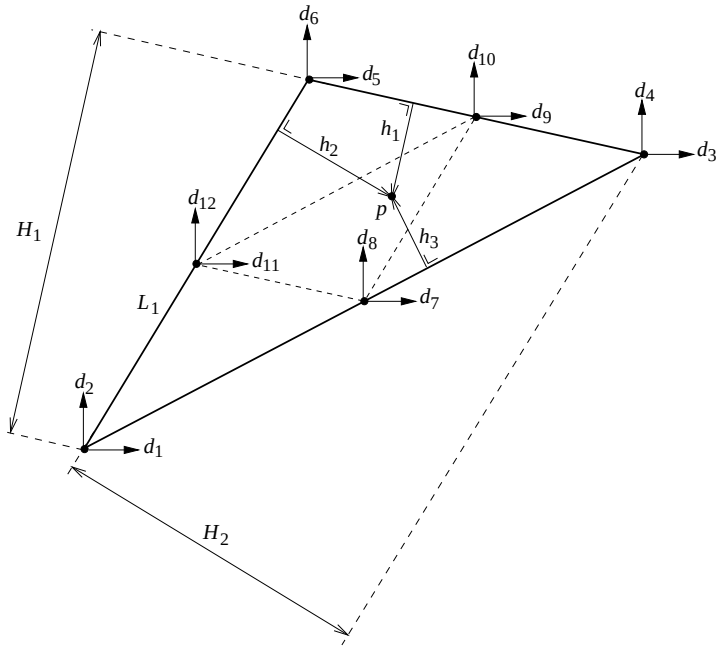

(b)

Figure A.6: Second-order (linear strain) triangular plate element (LST). Representation in barycentric coordinates to locate an arbitrary point, p, in the interior of the element.

$$\boldsymbol{\epsilon} = \boldsymbol{\partial}\mathbf{u} \tag{A.24}$$

with

$$\boldsymbol{\partial} = \begin{bmatrix} \frac{\partial}{\partial x} & 0 \\ 0 & \frac{\partial}{\partial y} \\ \frac{\partial}{\partial y} & \frac{\partial}{\partial x} \end{bmatrix}$$

We define the strain-displacement matrix:

$$\mathbf{B} = \boldsymbol{\partial}\mathbf{N} \tag{A.25}$$

combining equations A.23,A.24 and A.25 gives

$$\boldsymbol{\epsilon} = \mathbf{B}\mathbf{d}_l \tag{A.26}$$

A.4.4 Working it all out!

For a single element l, working out the lhs of Equation A.17 using Equations A.11[5] and A.25:

$$\begin{aligned} \int_{V\ l} \boldsymbol{\sigma}^T \bar{\boldsymbol{\epsilon}}\, dV &= \int_{A\ l} \boldsymbol{\epsilon}^T \mathbf{E}\bar{\boldsymbol{\epsilon}}\, t\, dA \\ &= \int_{A\ l} \mathbf{d}_l{}^T \mathbf{B}^T \mathbf{E}\mathbf{B}\bar{\mathbf{d}}_l\, t\, dA \\ &= \mathbf{d}_l{}^T \mathbf{k}_l \bar{\mathbf{d}}_l \end{aligned} \tag{A.27}$$

with the element stiffness:

$$\mathbf{k}_l = \int_{A\ l} \mathbf{B}^T \mathbf{E}\mathbf{B}\, t\, dA \tag{A.28}$$

One remaining problem is the conversion from barycentric coordinates to general coordinates to allow us to calculate $\mathbf{B}$, since $\boldsymbol{\partial}$ is a function of the general coordinates x, y.

For the second-order triangle we can write:

$$\begin{aligned} x &= \sum_{i=1}^{3} \xi_i\, x_i \\ y &= \sum_{i=1}^{3} \xi_i\, y_i \end{aligned} \tag{A.29}$$

[5] Omitting the initial stress $\boldsymbol{\sigma}_0$.

and after elimination of ξ_3:

$$\begin{aligned} x &= (x_1 - x_3)\xi_1 + (x_2 - x_3)\xi_2 + x_3 \\ y &= (y_1 - y_3)\xi_1 + (y_2 - y_3)\xi_2 + y_3 \end{aligned} \tag{A.30}$$

The conversion from the derivative operator in general coordinates $\boldsymbol{\partial}$ to the derivative in barycentric coordinates is given by:

$$\begin{bmatrix} \frac{\partial}{\partial \xi_1} \\ \\ \frac{\partial}{\partial \xi_2} \end{bmatrix} = \mathbf{J} \begin{bmatrix} \frac{\partial}{\partial x} \\ \\ \frac{\partial}{\partial y} \end{bmatrix} \tag{A.31}$$

where the two-dimensional *Jacobian*:

$$\mathbf{J} = \begin{bmatrix} \frac{\partial x}{\partial \xi_1} & \frac{\partial y}{\partial \xi_1} \\ \\ \frac{\partial x}{\partial \xi_2} & \frac{\partial y}{\partial \xi_2} \end{bmatrix} \tag{A.32}$$

Going back to our triangular element, we can write:

$$\begin{bmatrix} \frac{\partial}{\partial x} \\ \\ \frac{\partial}{\partial y} \end{bmatrix} = \frac{1}{2A} \begin{bmatrix} y_2 - y_3 & y_3 - y_1 \\ \\ x_3 - x_2 & x_1 - x_3 \end{bmatrix} \begin{bmatrix} \frac{\partial}{\partial \xi_1} \\ \\ \frac{\partial}{\partial \xi_2} \end{bmatrix} \tag{A.33}$$

with $2A = |\mathbf{J}|$
We can write for an infinitesimally small area of the triangle:

$$\begin{aligned} dA &= dh_2(dh_1 \frac{L_1}{H_1}) \\ &= H_2\, d\xi_2\, L_1\, d\xi_1 \\ &= 2A\, d\xi_1 d\xi_2 \end{aligned}$$

Incorporating this result into Equation A.28 yields the *isoparametric* formulation of the stiffness:

$$\mathbf{k}_l = \int_0^1 \int_0^1 \mathbf{B}^T \mathbf{E} \mathbf{B} |\mathbf{J}| t\, d\xi_1 d\xi_2 \tag{A.34}$$

The integrand in Equation A.34 is a collection of products of derivatives of $\mathbf{N}$ with respect to ξ. Because of the complexity, integration is mostly done by numerical integration (NI). A popular technique for numerical integration is the *Gauss quadrature* procedure (See [8],[19] for excellent coverage of this and

other NI techniques).
Returning to the PVD, we work out the rhs in Equation A.17:

$$\int_{V\ l} \mathbf{p}_b.\bar{\mathbf{u}}\, dV + \int_{S\ l} \mathbf{p}_s.\bar{\mathbf{u}}\, dS = \mathbf{P}_l^T \bar{\mathbf{d}}_l \tag{A.35}$$

after substitution of the lhs with $\bar{\mathbf{u}} = \mathbf{N}\bar{\mathbf{d}}_l$ and the kinematically equivalent force defined as:

$$\mathbf{P}_l = \int_{V\ l} \mathbf{N}^T \mathbf{p}_b\, dV + \int_{S\ l} \mathbf{N}^T \mathbf{p}_s\, dS$$

The individual element displacements are incorporated into the global displacement vector, $\mathbf{U}$, using the selection matrix, $\mathbf{a}_l$, which is for the case of a LST a $12 \times m$ matrix, for m dof for the entire assembly. The matrix consists of 12 unit elements and many zeroes. Writing this for the lth element:

$$\mathbf{d}_l = \mathbf{a}_l \mathbf{U} \tag{A.36}$$

Substitution of Equation A.36 into the rhs of Equation A.35 and into A.27 respectively, and summation over all elements yields:

$$\left[\mathbf{U}^T \sum_{l=1}^{n} \mathbf{a}_l^T \mathbf{k}_l \mathbf{a}_l\right] \bar{\mathbf{U}} = \left[\sum_{l=1}^{n} \mathbf{P}_l^T \mathbf{a}_l\right] \bar{\mathbf{U}} \tag{A.37}$$

The general formulation of an assembly of elements is then formulated as:

$$\mathbf{K}\mathbf{U} = \mathbf{R} \tag{A.38}$$

with the general stiffness matrix:

$$\mathbf{K} = \sum_{l=1}^{n} \mathbf{a}_l^T \mathbf{k}_l \mathbf{a}_l \tag{A.39}$$

and the transpose of global loading vector:

$$\mathbf{R}^T = \sum_{l=1}^{n} \mathbf{P}_l^T \mathbf{a}_l \tag{A.40}$$

Equation A.38 allows us to calculate the nodal displacements in $\mathbf{U}$ with given loading, as represented in $\mathbf{R}$, and after calculation of the stiffness matrix, $\mathbf{K}$, from the elements stiffnesses $\mathbf{k}_l$ (Equation A.34). Once the nodal displacements are known, the strains can be calculated from Equation A.26 and subsequently the stresses, from Equation A.11.
Equation A.38 assumes static behaviour of the structure. Extra terms involving

inertia and damping forces can be added to yield the statement of dynamic equilibrium:

$$\mathbf{M}\ddot{\mathbf{U}} + \mathbf{C}\dot{\mathbf{U}} + \mathbf{K}\mathbf{U} = \mathbf{R} \tag{A.41}$$

With the mass matrix, $\mathbf{M}$, and the damping matrix, $\mathbf{C}$.

In this appendix, a brief overview of the principles of the FE method was given using the example of a second-order triangular element. The theory of the FE method is vast and further elaborations are beyond the scope of this work. For an in-depth coverage of the FE method, we refer the interested reader to [8] and [76]. A more practical approach can be found in [19]. Finally, non-linear finite element analysis is covered in [41].

Appendix B

Anatomy of the foetal skull

1. **Anterior fontanelle**: the largest fontanelle located on the top of the cranial vault and slightly anterior. It is the point where frontal (5), coronal (6) and sagittal (8) sutures join.

2. **Posterior fontanelle**: located at the back of the skull. It joins the sagittal (8) and lambdoidal (9) sutures.

3. **Mastoidal fontanelle** or postero-lateral fontanelles - left and right: located at the side of the skull and slightly posterior. Joins the squamosal (7) and lambdoidal (9) sutures.

4. **Sphenoidal fontanelle** or antero-lateral fontanelles (left and right): located at the side of the skull and slightly anterior. Joins the coronal (6) and squamosal (7) sutures.

5. **Frontal suture**: connects the bridge of the nose and the anterior fontanelle (1).

6. **Coronal sutures** - left and right: connect the anterior fontanelle (1) and the sphenoidal fontanelle (4).

7. **Squamosal suture** - left and right: connects the mastoidal (3) and sphenoidal (4) fontanelle.

8. **Sagittal suture**: located in between the parietal bones (10) and connecting the anterior (1) and posterior fontanelles (2).

9. **Lambdoidal suture** - left and right: joins at the posterior fontanelle (2) at one end and diverging towards the mastoidal fontanelle (3) at the other end.

10. **Parietal bones**: the large bones at both sides of the vault and located slightly posterior.

11. **Frontal bones**: smaller than the parietal bones (10) and part of the neurocranium, though connecting to the viscerocranium at the orbits (20).

12. **Occipital bone**, external part: located at the back and slightly downwards.

13. **Occipital bone**, lateral part: located at the skull base.

14. **Squamosal temporal bone**: the bone which is directly connected to the zygomatic arch bone (16).

15. **Petrosal temporal bone**: the bone in between the occipital bone (12) and squamosal temporal bone (14).

16. **Zygomatic bone**: or zygomatic arch or jaw bone is connected to the squamosal temporal bone (14).

17. **Sphenoidal bone**: the bone which lies in between the maxilla (19) and the squamosal temporal bone (14).

18. **Mandible**

19. **Maxilla**: the facial bone of the skull, incl. the palate.

20. **Orbit**: the eye-socket.

21. **Tympanic Ring**

22. **Frontal tuberosity**: a protuberance of the frontal bone, respectively right and left.

23. **Parietal tuberosity**: a protuberance of the parietal bone. Frontal and parietal tuberosities disappear gradually during the first years of life.

24. **Occipital tuberosity**: a protuberance of the occipital bone. Doesn't necessarily vanish, hence can still be seen on the adult skull.

25. **Foramen magnum**

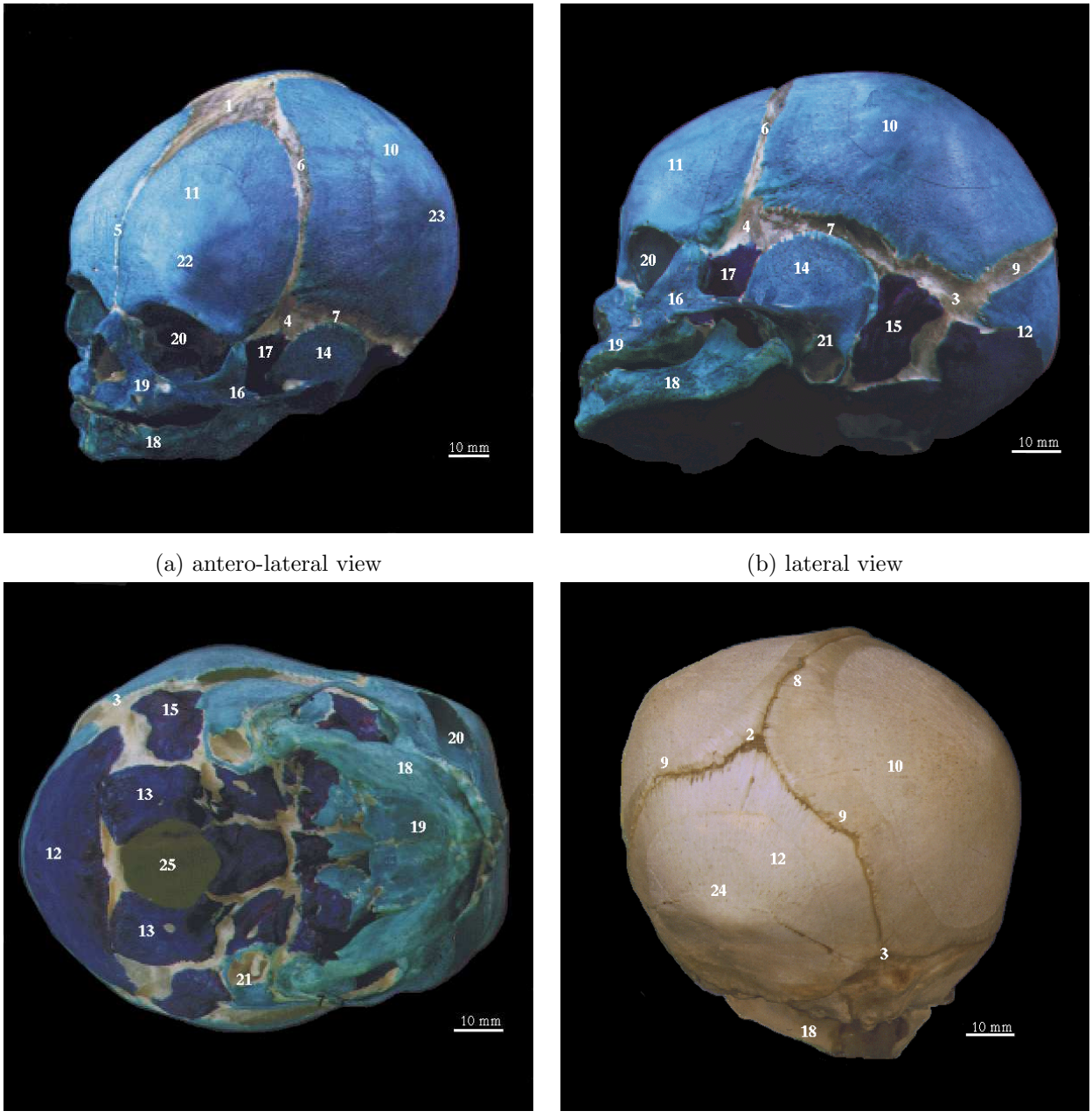

(a) antero-lateral view

(b) lateral view

(c) basal view

(d) posterior view

Figure B.1: Anatomy of the foetal skull. Source: *Life Before Birth* by M.A. England [26].

Appendix C

Main diameters and corresponding landmarks of the foetal head and skull

The main diameters of the foetal head/skull and the corresponding landmarks[1], for validation, are defined.
See Figures C.1 and C.2 for the location of landmarks and diameters on the foetal head and skull respectively.

Mentum - Pogonion (1) According to Riolo [88] the true mentum or menton is lower than the landmark which is used to specify the mento-vertical diameter (MVD).

Maxilla - Anterior nasal spine (2)

Orbit - Nasion (3) Located where the frontal suture meets the upper part of the bridge of the nose.

Front (4) The extremum of the sinciput[2] in the horizontal direction.

Front-high (5) Located in between the front (4) and bregma (6). I define this landmark as the intersection point of the line that connects the left and right frontal tuberosities (11) across the vault and the centerline of the frontal suture.

[1]The first explanatory term for a landmark is the one commonly used to specify the diameter. If present, the second explanatory term is the more correct term of the landmark as specified by Riolo et al. [88].

[2]The forepart of the head or skull.

Bregma (6) Located where the coronal, sagittal and frontal sutures meet. For a foetal or newborn skull, this is the centre of the anterior fontanelle.

Occiput - vertical (7) Is difficult to locate. The top vertex of the (triangular) posterior fontanelle (where sagittal and lambdoidal sutures meet) is taken.

Occiput (8) The extremum of the occiput in the horizontal direction.

Sub-occiput (9) The extremum of the occipital tuberosity.

Parietal tuberosity (10) Left and right.

Frontal tuberosity (11) Left and right

Temporal-squamosal landmark (12) See Figure C.2.

Orbito-vertical diameter - *OrVD* The distance from the orbit (3) to the occiput-vertical landmark (7).

Orbito-occipital diameter - *OrOD* The distance from the orbit (3) to the occiput (8).

Maxillo-vertical diameter - *MaVD* The distance from the maxilla (2) to the occiput-vertical landmark (7).

Mento-vertical diameter - *MVD* Also known as the occipito-mental diameter; the distance from the mentum (1) to the occiput-vertical landmark (7).

Occipito-frontal diameter - *OFD* The distance from the front (4) to the occiput (8).

Suboccipito-frontal diameter - *SOFD* The distance from the front-high landmark (5) to the sub-occiput (9).

Suboccipito-bregmatic diameter - *SOBD* The distance from the bregma (6) to the sub-occiput (9).

Biparietal diameter - *BPD* In theory measured between the left and right parietal tuberosities (10), in practise however, the largest diameter in a coronal plane which intersects the parietal bones.

Bifrontal diameter - *BFD* In theory measured between the left and right frontal tuberosities (11), in practise however, the largest diameter in a coronal plane which intersects the frontal bones.

Bitemporal diameter - *BTD* Reported by Kriewall [47], but not defined. The distance between two distinct landmarks (12) each on the left and right temporal squamosal bone, is taken. The landmarks are the typical dents emanating from the zygomatic bone upwards towards the squamosal suture.

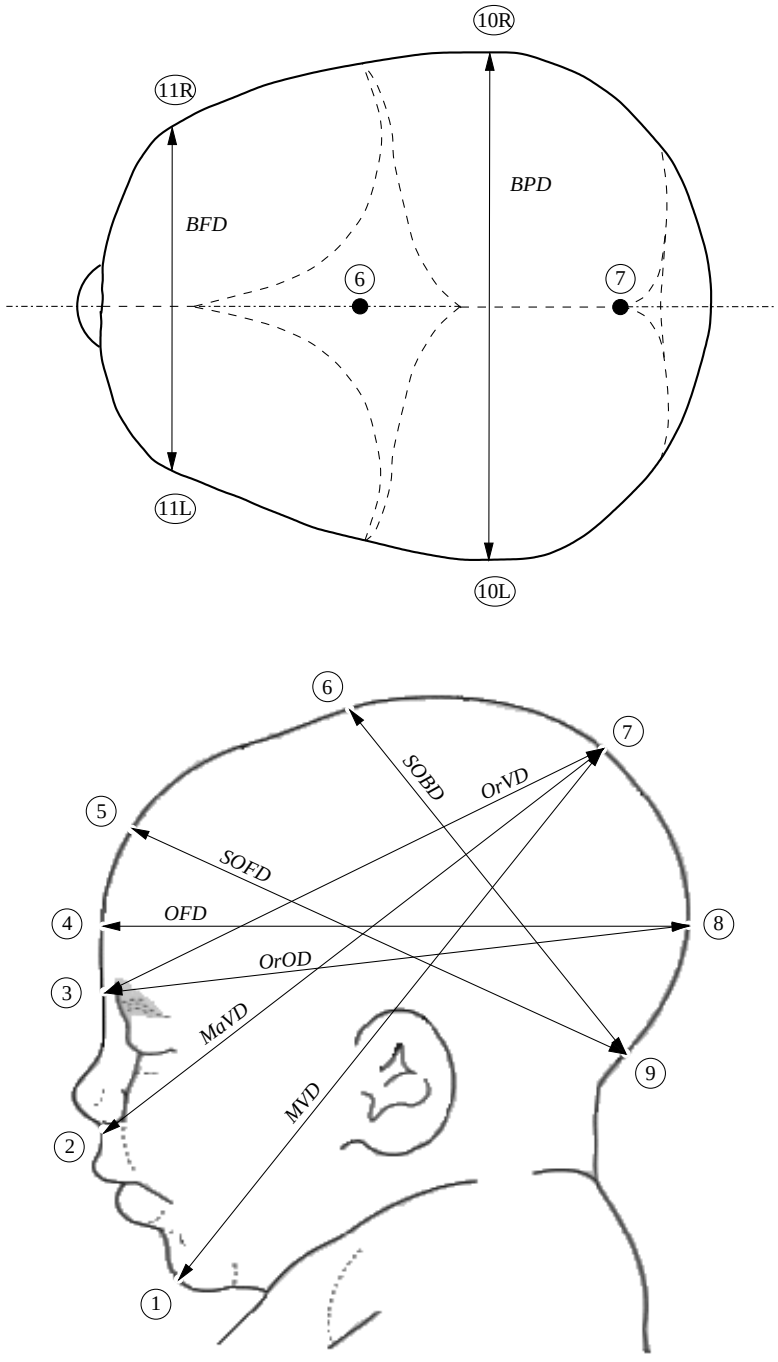

Figure C.1: Landmarks and diameters for evaluation of foetal head moulding: foetal head. Note that landmarks 1-9 lay on the centre-line across the head.

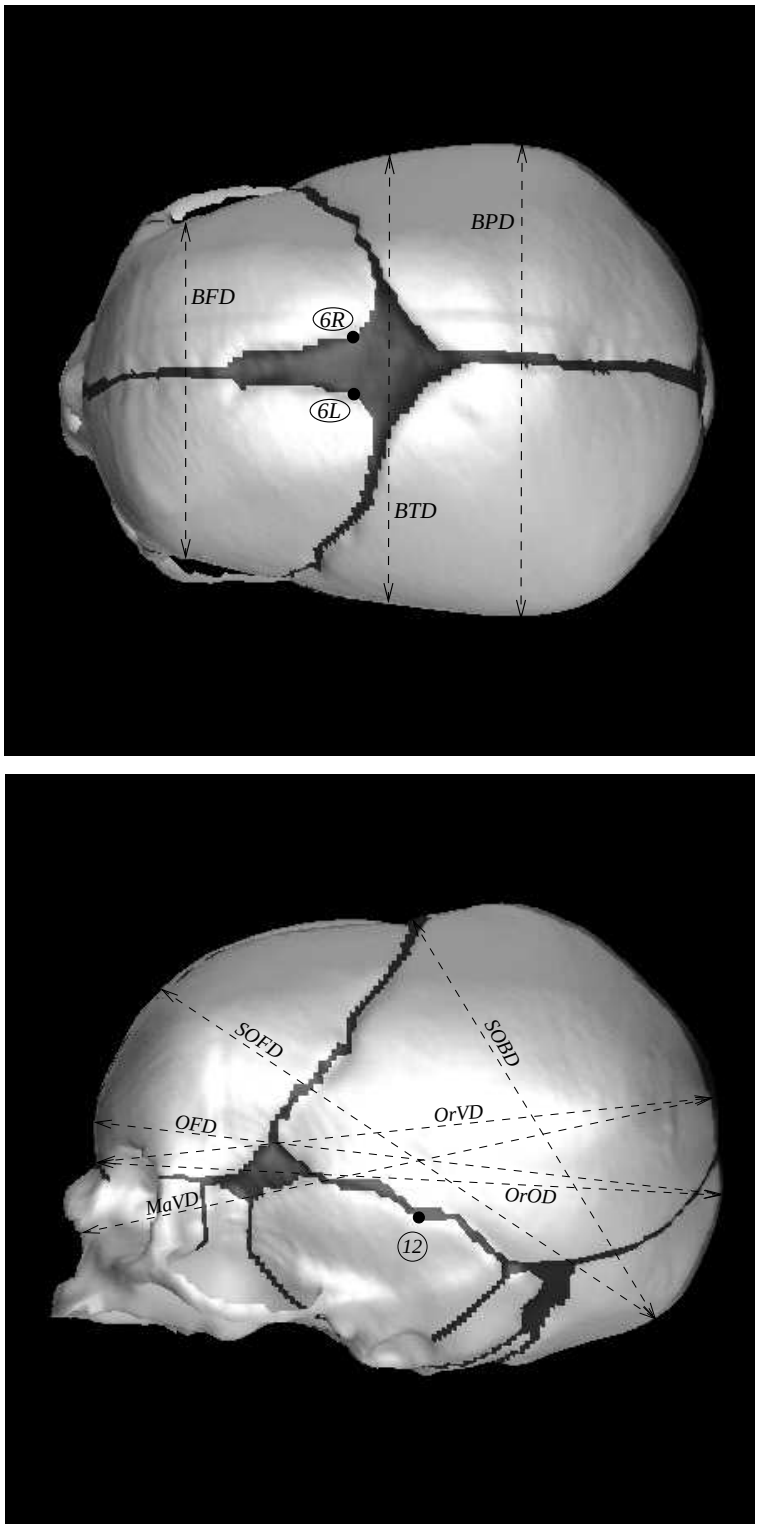

Figure C.2: Diameters for evaluation of foetal head moulding: foetal skull. Landmark 12 (left and right) is used to specify the BTD. Landmark 6L and 6R illustrate the use of left and right measurements when the original landmark (in this case the *bregma*) lies inside a fontanelle or suture.

Appendix D

Glossary of medical/obstetrical terminology

Sources to this glossary[1] are [1, 2, 17, 45, 83, 90, 98, 104] and Chapter 13 in [99].

Abortion The expulsion or extraction of all (complete abortion) or any part (incomplete abortion) of the placenta or membranes, without an identifiable foetus or with a foetus (alive or dead) weighing less than 500g. In the absence of known weight, an estimated duration of gestation of less than 24 completed weeks is taken.

Acidosis Any condition in which the hydrogen ion concentration of blood and body tissues is increased, thus the pH is lowered. *Respiratory* acidosis refers to acidosis resulting from carbon dioxide retention by the lungs. *Metabolic* acidosis implies either retention of non-volatile acids or loss of base.

Amniotic fluid The fluid contained within the amnion (see *membranes*) in which the foetus floats.

Apgar score Used to check the condition of the infant usually after 1, 5 and 10 minutes after birth. A score from 0-2 is given for five different signs. An Apgar score of 8-10 implies the infant is in best condition. See Table D.1.

Assisted vaginal delivery See *forceps delivery* and *vacuum extraction*.

[1] Slanted text is used to emphasise a word but does not necessarily imply that the word is an item in the glossary!

Table D.1: Apgar score. * using nasal catheter.

Sign	0	1	2
Heart rate	Absent	$<$ 100 bpm	$\geq$ 100 bpm
Respiratory effort	Absent	Slow, irregular	Good, crying
Muscle tone	Limp	Some limb flexion	Active
Response to stimulus*	Nil	Grimace	Vigorous cry
Colour	Blue, pale	Body pink, limbs blue	Pink

Arterial pH Is the pH measured from a foetal scalp blood sample or the umbilical arteries (see *umbilical cord pH*). The value of the pH should normally be greater than 7.25. Values lower than that may point at foetal acidosis.

Atlanto-occipital point The anatomical location where the base of the skull is connected to the spine.

Birth canal See *Vagina*

Bradycardia Abnormally slow heart rate, usually taken $\leq$ 60 bpm.

Calvaria *pl* of **Calvarium**: The vault of the skull.

Cartilage Is a tough, firm, animal skeletal tissue. There are several varieties but it basically consists of rounded cells, scattered in a resilient polysaccharide-containing matrix with numerous collagen fibres. It is important as a shock-absorbing material and is also the main pre-cursor tissue of bone and part of the body's growth mechanism. *Articular* cartilage forms the gliding surface of a joint (articulation).

Caesarian section Is the operation by which a potentially viable foetus is delivered through an incision in the abdominal wall and the uterus.

Cephalic presentation Occurs in about 95% of deliveries and is characterised by the head occupying the lower segment of the uterus.

Cephalo-pelvic (dis)proportion The geometric (dis)proportion between the foetal head and the maternal pelvis.

Cerebrum - *cerebral, cerebro*: The term applied either to the brain as a whole or to its uppermost portion made up of the two cerebral hemispheres.

Cervix or *cervix-uteri*. The lower barrel-shaped part of the *uterus*. Its lower end joins the *vagina* at an angle varying from 45-90 degrees. Its main function is during early pregnancy by retaining the embryo safely within the uterine cavity. The cervix becomes much softer and more congested as gestation progresses. It becomes shorter (*effaced*) and slightly *dilated* as term approaches. See Figures D.1, D.3, D.7 and D.8.

Cervical Dilatation The widening of the cervix during the first stage of labour caused by the foetal head pressing against the lower pole of the uterus and the traction within the the tissue of the lower uterine muscles. See Figures D.3 and D.8.

Cervical ostium or cervical os - internal and external. See Figures D.1 and D.7.

Cervical rim The external *cervical os*.

Cervical spine Upper part of the vertebral column or backbone, consisting of 7 vertebrae (out of 33 across the entire spine).

Conception The fertilisation of an ovum by a spermatozoon and the implantation of the resulting zygote.

Cortical bone or compact bone, is a dense type of bone, for example the shaft of long bone. A more spongy type of bone is found, for example at the articulating ends of long bones, which is called *cancellous* bone.

Cranium - *cranial*. The skull; the bones enclosing the brain.

Delivery The actual expulsion of the products of conception, including the *placenta*.

Dilatation See *Cervical Dilatation*

Dura mater The dura mater encloses the entire central nervous system. The cranial dura mater is firmly bound to the surrounding bones of the cranial vault. The dura mater exhibits three major folds: the tentorium cerebelli, the falx cerebri and the falx cerebelli. See Figure D.10.

Edema or *Oedema*. Is the excess fluid in the tissue spaces. A sufficient accumulation in the subcutanous tissues causes visible swelling. It may be localised due to local vascular causes or generalised, implying overall body retention of fluid and electrolytes.

Ectopic pregnancy or *extrauterine pregnancy* is one in which a fertilised ovum implants in an area other than the uterine cavity.

Effacement The shortening or *taken up* of the cervix prior to *dilatation*. See Figures D.3 and D.8.

False Labour Is quite common in late pregnancy and is characterised by irregular brief contractions of the *uterus* accompanied by mild back or abdominal pain but lack of progress. The presenting part does not descend.

Foetus The offspring of a viviparous animal while in the uterus. In man, the term is conventionally used during the period from 8 weeks after *conception* until delivery.

Foramen magnum The large hole in the occipital bone at the base of the skull through which the brainstem passes from the cranial cavity to become continuous with the spinal cord (see (25) in Appendix B).

Forceps delivery Is the process by which the baby is delivered using an obstetric forceps to extract the baby's head. The primary functions of the forceps are *traction* (for example, for assistance in the terminal phase of labour) and *rotation* (in cases in which there is no *cephalo-pelvic disproportion* but the head presents with an unfavourable diameter).

Galenic venous system Consists of the great vain of Galen (*vena cerebri magna Galeni*) and the internal cerebral vein (*vena cerebri interna* aka *vena cerebri parva Galeni*). The internal cerebral vein is together with the basal vein (*vena basalis*), the largest supply to the great vain of Galen. See Figure D.11.

Gestation See *Pregnancy*.

Gestational age Calculated from the last menstrual period (LMP) (rather than the date of conception) or from ultrasound measurements of for example the biparietal diameter.

Gravidity Refers to the total number of pregnancies, including abortions, ectopic pregnancies and normal intrauterine pregnancies.

Hypophysis or *Pituitary gland*. The gland is oval in shape and lies in the base of the skull in a depression of the *sphenoidal bone* (see (17) in Appendix B), called the pituitary fossa.

Hypoxaemia or *Hypoxemia*. A decrease in arterial oxygen tension.

Hypoxia Lack of oxygen supply.

Intracranial hypertension Raise of blood pressure above normal levels on the arterial side of the circulation, inside the cranium.

Ischemia or *Ischaemia*. Insufficient blood supply to an area of tissue or an organ, due to obstruction or functional constriction of one or more blood vessels or as a part of a more general circulatory failure.

Lower uterine pole The fictitious lowest point of the lower uterine segment of the uterus which is in contact with the foetal head (in case of cephalic presentation). Corresponds more or less to the location of the internal os (see Figure D.7).

Lower uterine segment The thin lower part of the uterus See Figure D.2.

Membranes or *foetal* membranes, protect the foetus and include the amnion, the chorion, allantois and the yolk sac. The *amnion* is the innermost membrane and surrounds the foetus.

Mesenchyme is embryonic connective tissue of the *mesoderm*, consisting of irregularly tracking cells in a jelly-like matrix. It gives rise to connective tissue, blood vessels, cartilage, bone, etc.

Mesoderm The middle of three germinal layers of the embryo, in between the ectoderm and endoderm. From it are derived muscle, cartilage, bone, blood, blood vessels, connective tissues and many other structures.

Mode of delivery Includes normal vaginal delivery, *Caesarian section*, *forceps delivery* and *vacuum extraction*.

Morphogenesis The origin and development of a part, organ or organism.

Multigravida(e) A woman who has been pregnant more than once.

Multipara(e) A woman who has delivered more than one offspring weighing 500g. or more, or of 24 weeks of gestation or more.

Nullipara A woman who has not delivered an offspring weighing 500g. or more, or of 24 weeks of gestation or more.

Obturator internus muscle of the pelvic diaphragm. See Figure D.6.

Occiput-anterior vertex presentation See *Vertex presentation*.

Occiput-posterior vertex presentation See *Vertex presentation*.

Ossification Is the formation of new bone which normally takes place in preexisting *cartilage* or fibrous tissue. The skeletal elements of the endoskeleton, i.e. the vertebral column, the skull base, shoulders, pelvic girdles and the limbs are preceded by cartilage models that form bones by *endochondral* ossification. The viscerocranium, i.e. the covering bones of the skull and the superficial elements of the shoulder girdle are derived from the exoskeleton and ossify *intramembranously* (dermally).

Parity The state of having given birth to an infant or infants weighing 500g. or more, alive or dead. If the weight is not known, an estimated length of gestation of 24 weeks or more may be used. Thus, a patient is parous if she has given birth, irrespective of the mode of delivery, at or beyond the 24th. week of pregnancy.

Pelvic floor Although not a part of the bony pelvis, the pelvic floor forms a part of the birth canal and thus plays an important role in the mechanism of labour. The *pelvic diaphragm* is the main support of the pelvic floor and is shown in Figure D.6. The two *levator ani* muscles form a gutter during the second stage of labour, with the opening of the vagina facing forward between the sides of the gutter (see Figure D.5).

Placenta Is the intimate apposition or fusion of foetal organs to maternal tissues for the purpose of physiologic exchange. At term it is circular in shape, forming a spongy disc about 20 cm. in diameter and about 3 cm. thick. Its weight is usually around 500g. but there is a direct relationship with the foetal weight. See Figures D.7 and D.9.

Pregnancy or *gestation*: The maternal condition of having a developing foetus in the body.

Primigravida(e) A woman who has been pregnant only once.

Primipara(e) A woman who has given birth to one offspring weighing 500g. or more, or of 24 weeks of gestation or more.

Prolonged labour Generally this implies the prolongation of the *first stage*, a condition which occurs most commonly in *primiparae*. Prolongation of the *second stage* of labour is usually referred to as *delay of labour*.

Retinal haemorrhage Haemorrhage of the retina, i.e. the light-sensitive structure of the eye.

Rupture of the membranes (ROM) The membranes may rupture at any time during labour, although this usually occurs towards the end of the first stage of labour. When the membranes rupture spontaneously near term it is probable that labour will begin within a short time, although sometimes the onset is delayed. Early rupture of the membranes is more likely to occur if the presenting part is not engaged or if there is a malpresentation, but it also occurs in many normal cases.

Septum An anatomical structure which serves as a dividing wall or partition.

Spines or **Ischial spines**: Anatomical location of the pelvis. They are used to determine the station of the foetus: 'zero' station implies the head has descended to the level of the spines (see Figure D.6).

Tentorium See Figure D.10.

True labour is accompanied by a regular sequence of uterine contractions, progressively stronger and closer together and resulting in *effacement* and *dilatation* of the *cervix* and, in the absence of malpresentation or *cephalo-pelvic disproportion*, descent of the presenting part.

Tuberosity A bony protuberance.

Umbilical cord The structure, containing the two umbilical arteries and the umbilical vain, together with supporting tissues, which connects the foetal circulation with the maternal placenta.

Umbilical cord pH Is the pH measured from a blood sample of the umbilical cord. This procedure is considered to be safer than foetal scalp blood sampling (see also *Arterial pH*).

Uterus The uterus is a pear-shaped, thick-walled, muscular organ, situated between the base of the bladder and the rectum. It is divided into two main portions, the larger portion or body above and the smaller *cervix* below. The body itself is divided into a thick upper segment and a thin lower segment (see Figure D.2). During pregnancy the uterus is adapted to contain the growing foetus and placenta, and it also undergoes changes in preparation for its task of expelling the foetus during labour. At term the uterus is about 35 cm. long and on the average 23 cm. in diameter. It weighs about 1 kg. in contrast to the unpregnant uterus which weighs roughly 65g. See Figures D.1 and D.7.

Uterine activity Uterine contractions. The uterus contracts irregularly and painlessly throughout pregnancy (Braxton-Hicks contractions). At the onset of labour, the contractions become regular and painful, enough to distract the woman from her usual activities and cause the *cervix* to be *taken up* and *dilated*.

Uterine fundus see Figure D.1.

Uterine tubes see Figure D.1.

Vacuum extraction The vacuum extractor or ventouse, introduced by Malmström in 1954, is designed to assist delivery by the application of traction to a suction cap attached to the foetal scalp. The instrument lacks the precision of the forceps and disregards the finer details of the pelvic architecture as well as the mechanism of labour.

Vagina Is a strong canal of muscle, on the average 7.5 cm. long, and extends from the *uterus* to the vestibule of the external genitalia. Because the *cervix* of the uterus projects into the upper portion, the anterior wall of the vagina is 1.5-2 cm. shorter than the posterior wall. See Figures D.2, D.6 and D.7.

Vascular Relating to the blood vessels.

Vertex presentation With a vertex presentation, the denominator is the occiput. It is conventional to describe four positions for each presentation:

- Left occipito-anterior position - See Figure D.4a,
- Right occipito-anterior position,
- Right occipito-posterior position - See Figure D.4b,
- Left occipito-posterior position.

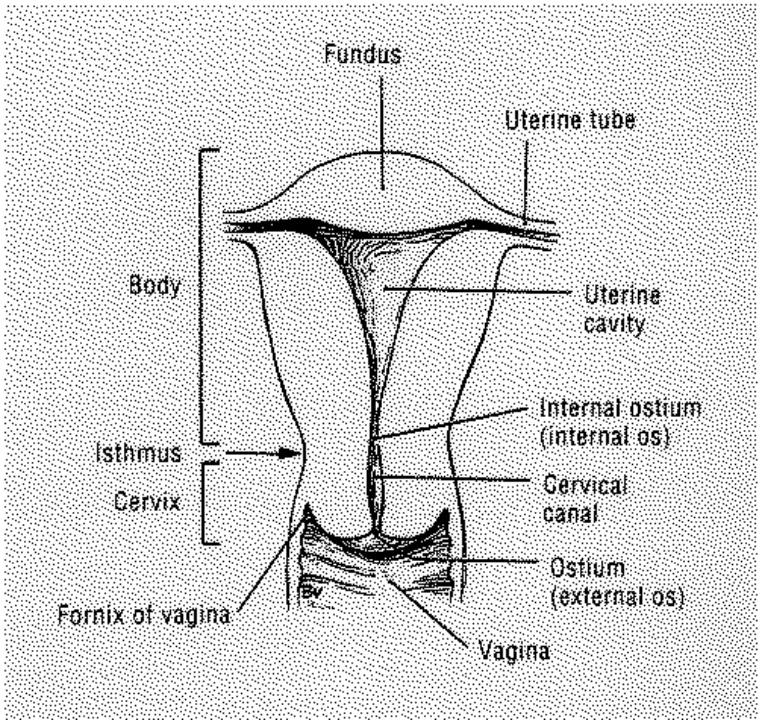

Figure D.1: The unpregnant uterus. Source: Grant's Atlas of Anatomy [1].

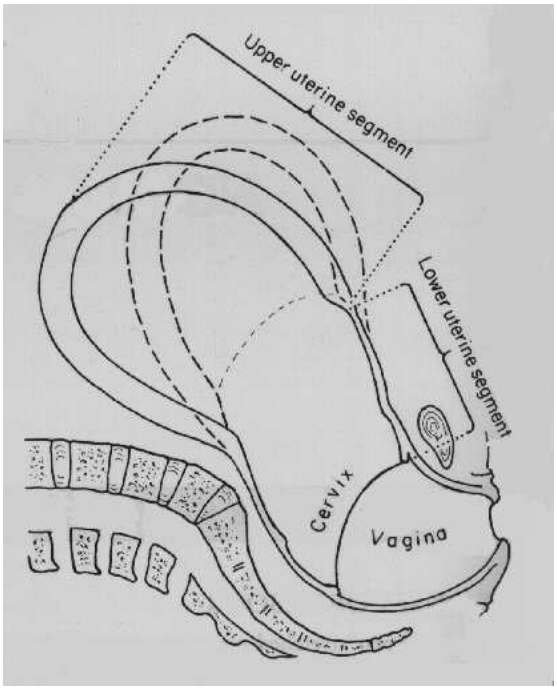

Figure D.2: The thick upper uterine segment and the thin lower uterine segment at the end of the first stage of labour. The dashed lines show the position of the uterus during contraction. Source: Obstetrics by Ten Teachers - Chamberlain [17].

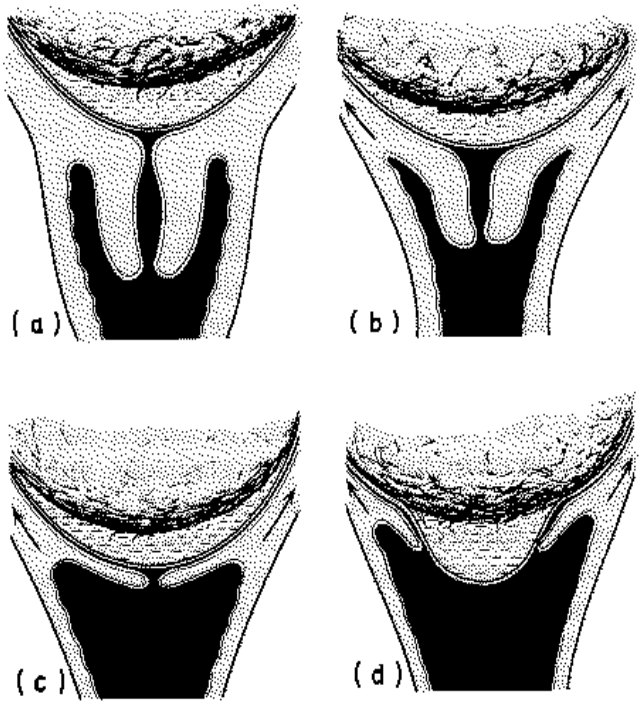

Figure D.3: Effacement (a-c) and dilatation (d) of the uterine cervix. The foetal head is in contact with the lower uterine pole. Note the bulging of the membranes creating the *forewaters*. Source: Obstetrics by Ten Teachers - Chamberlain [17].

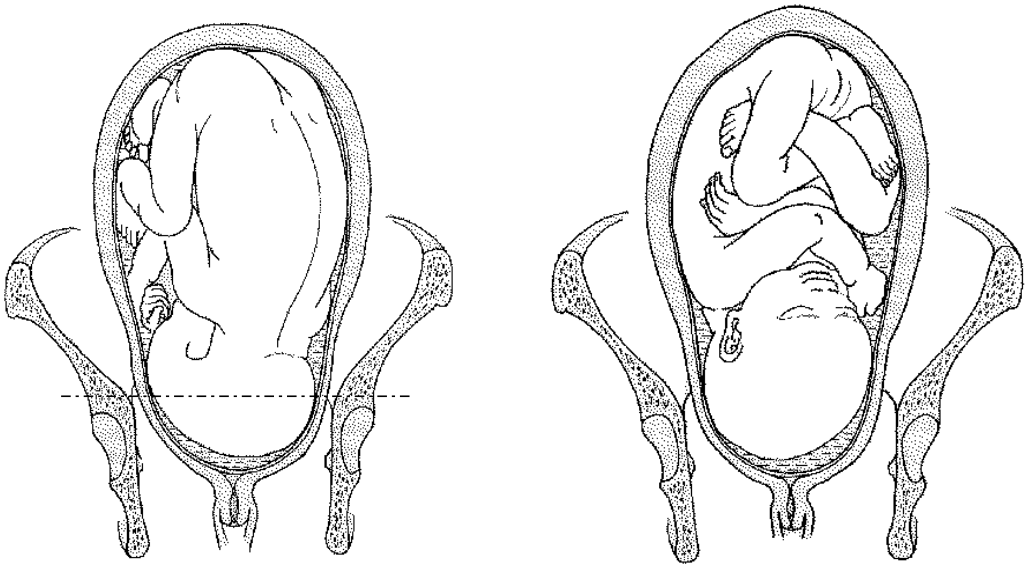

(a) Left occiput-anterior presentation (b) Right occiput-posterior presentation

Figure D.4: Vertex presentations. The dash-dotted line in (a) shows the orientation of the *SOB* plane. Source: Obstetrics by Ten Teachers - Chamberlain [17].

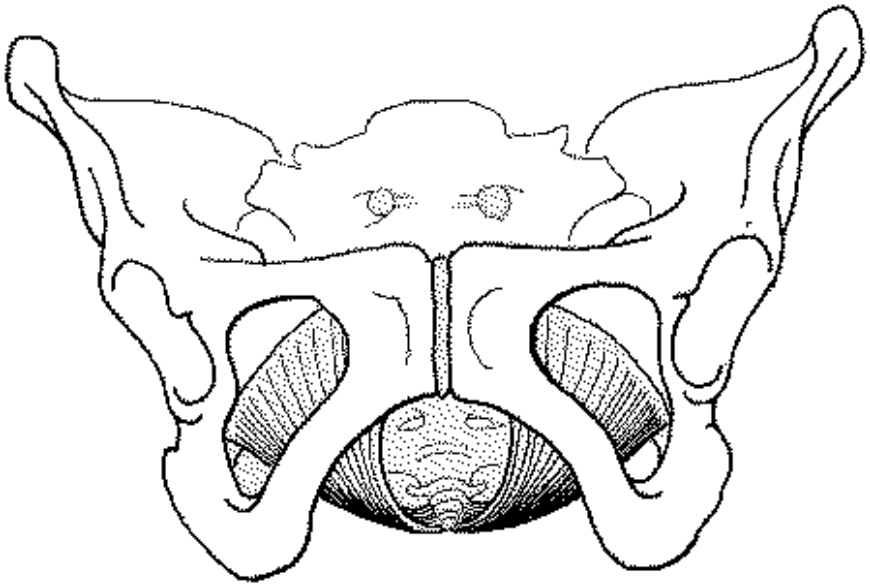

Figure D.5: The pelvic floor with levator ani sling. Source: Obstetrics by Ten Teachers - Chamberlain [17].

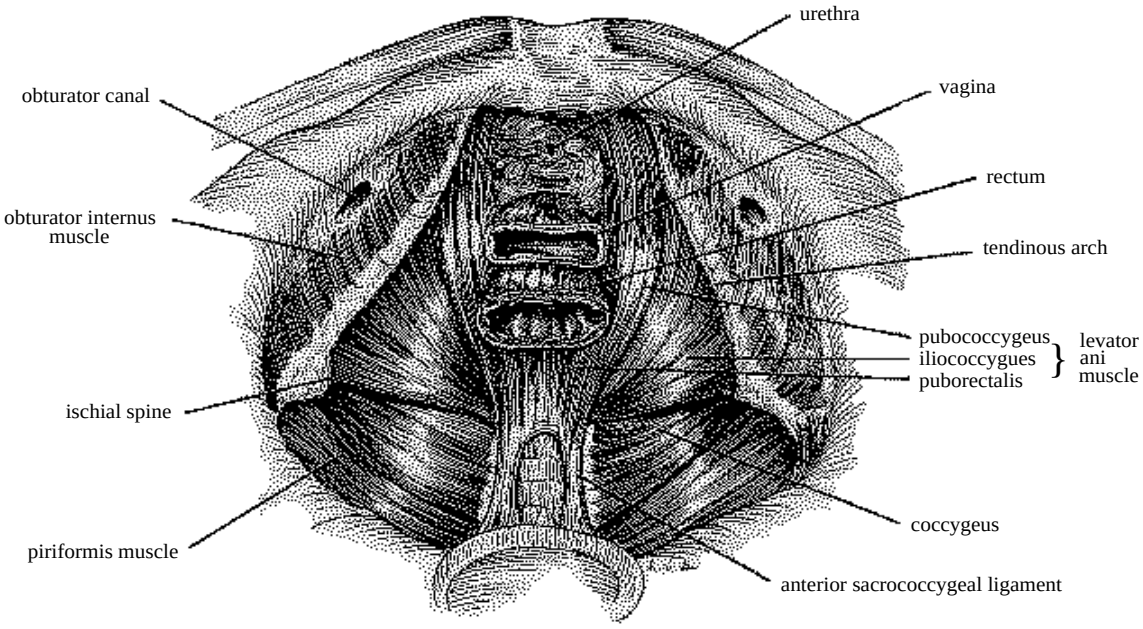

Figure D.6: Pelvic diaphragm, viewed from above. Source: Anatomy of the Female Reproductive System - Krantz [43].

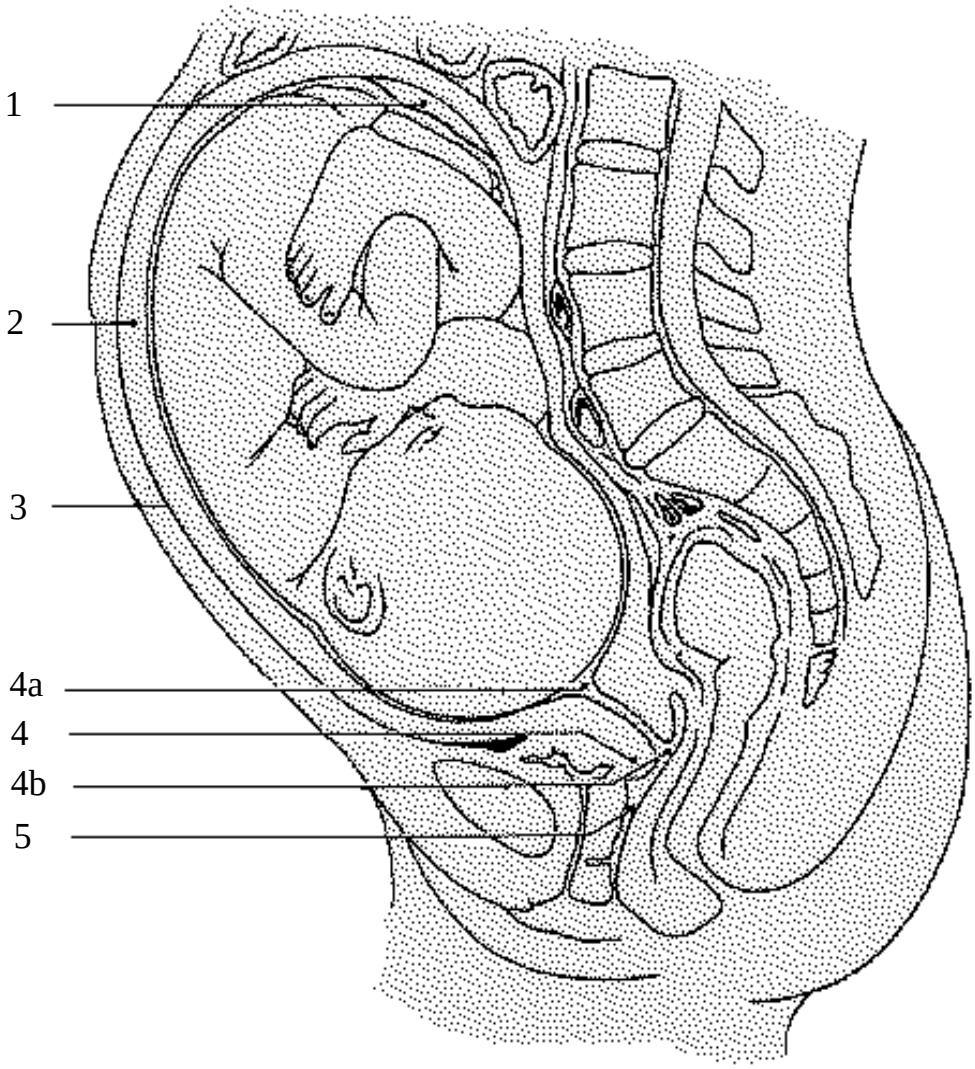

Figure D.7: A term baby in utero. 1 = placenta; 2 = uterus; 3 = peritoneum; 4 = cervix; 4a = internal os(tium); 4b = external os(tium); 5 = vagina. Source: The Human Body on File - Swan [98].

(a) Partial effacement of cervix

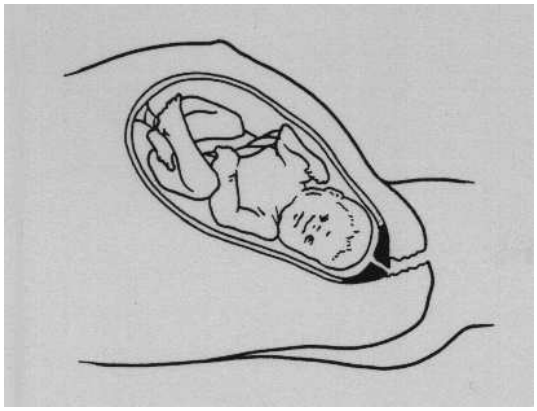

(b) Full effacement of cervix

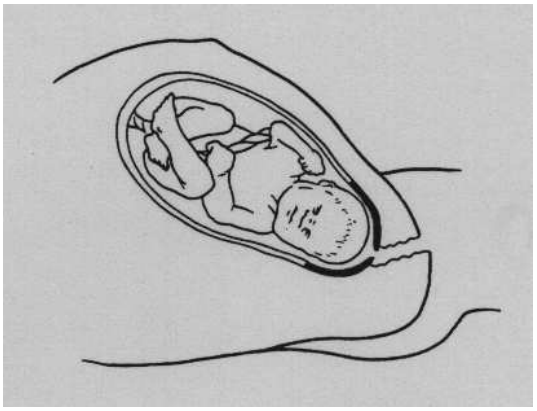

(c) Partial dilatation of cervix

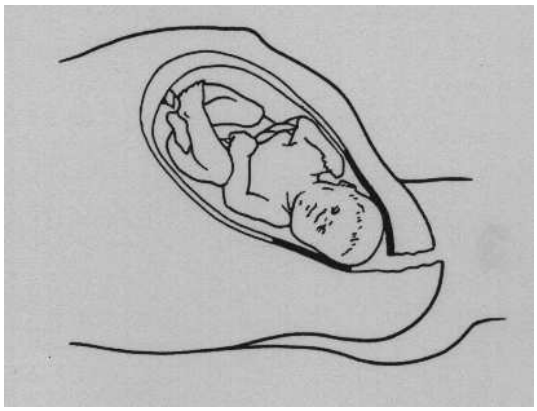

(d) Full dilatation of cervix

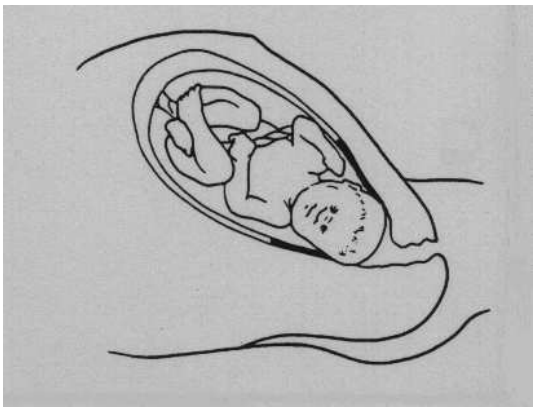

Figure D.8: First stage of labour. Source: The Human Body on File - Swan [98].

(a) Baby's head rotates, (internal rotation)

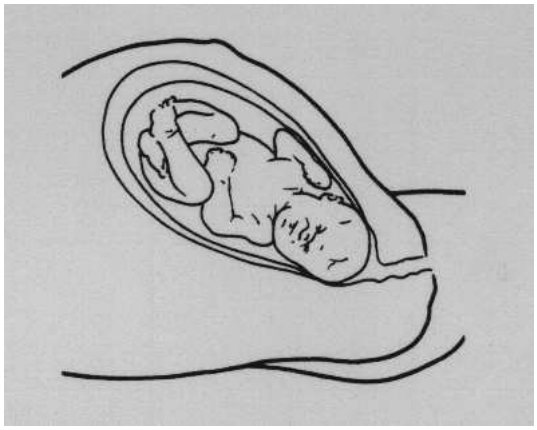

(b) Head rotates back to former angle, (restitution).

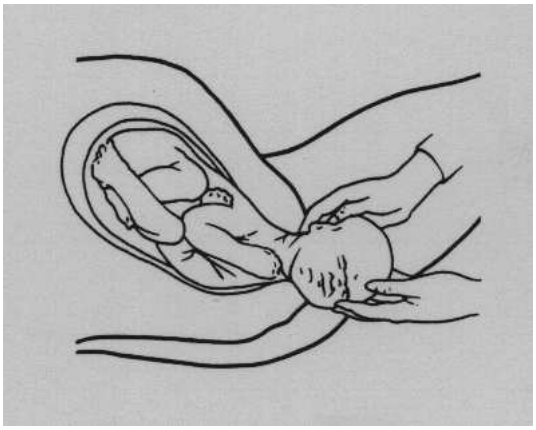

(c) Shoulders and rest of baby follow

(d) Third stage of labour (delivery of placenta)

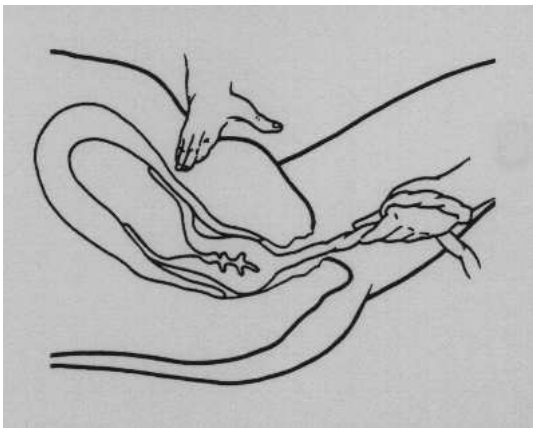

Figure D.9: Second and third stage of labour. Source: The Human Body on File - Swan [98].

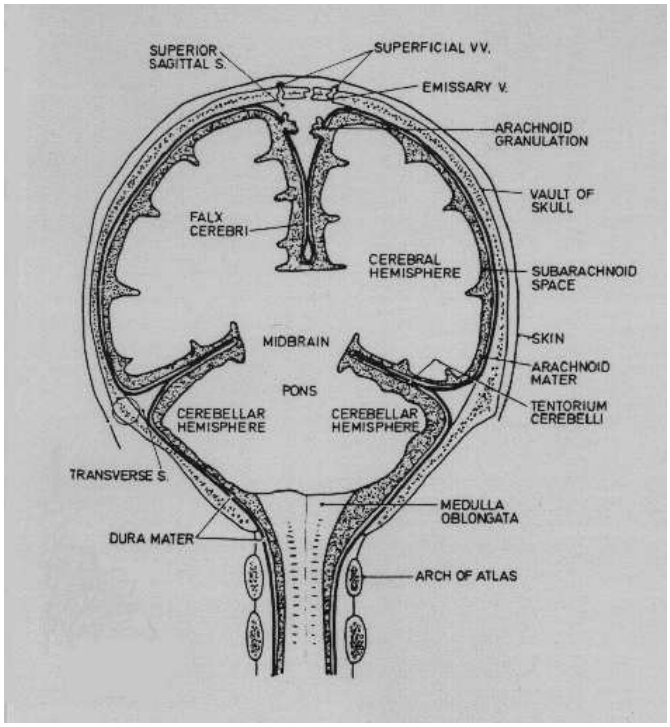

Figure D.10: Tentorium and falx. Source: The Oxford Medical Companion [104].

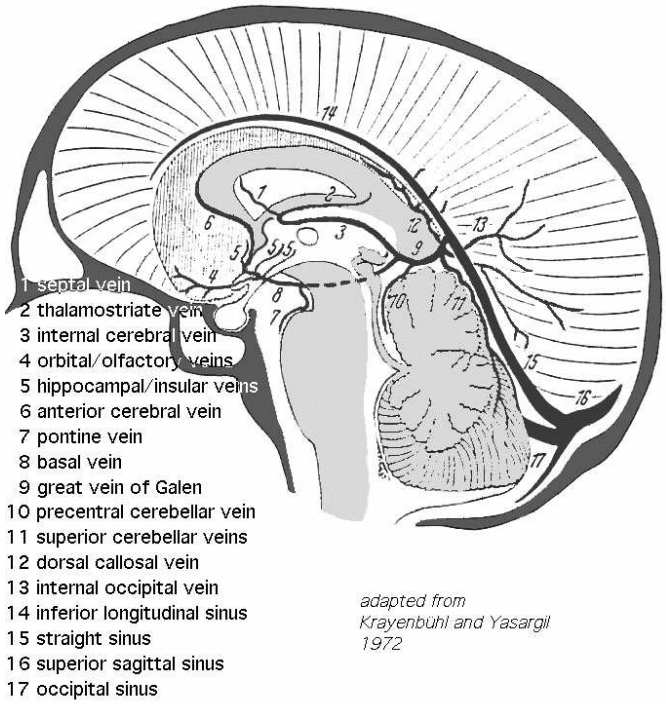

Figure D.11: Galenic venous system. Source: Radiological anatomy and topography of the cerebral veins - Krayenbuhl [45].

Bibliography

[1] A.M.R. Agur and M.J. Lee, editors. *Grant's Atlas of Anatomy*. Williams and Wilkins, Baltimore, ninth edition, 1991.

[2] F. Al-Azzawi. *Childbirth and Obstetric Techniques*. Mosby, London - UK, second edition, 1998.

[3] A.C.J. Allman, E.S.G. Genevier, M.R. Johnson, and P.J. Steer. Head-to-cervix force: an important physiological variable in labour. 2. Peak active force, peak active pressure and mode of delivery. *Br. J. Obstet. Gynaecol.*, 103(8):769–775, August 1996.

[4] C. Amiel-Tison, C. Sureau, and S.M. Shnider. Cerebral handicap in full-term neonates related to the mechanical forces of labour. *Baillière's Clinical Obstetrics and Gynaecology*, 2(1):145–165, 1988.

[5] M.C. Antonucci, M.C. Pitman, T. Eid, P.J. Steer, and E.S. Genevier. Simultaneous monitoring of head-to-cervix forces, intrauterine pressure and cervical dilatation during labour. *Med. Eng. Phys.*, 19(4):317–326, 1997.

[6] N. Arad, N. Dyn, D. Reisfeld, and Y. Yeshurun. Image warping by radial basis functions: Application to facial expressions. *CVGIP*, 56(2):161–172, March 1994.

[7] H.H. Barrett. Image reconstruction and the solution of inverse problems in medical imaging. In A.E. Todd-Pokropek and M.A. Viergever, editors, *Medical Images: Formation, Handling and Evaluation*, volume 98 of *NATO ASI Series F: Computer and Systems Sciences*. Springer-Verlag, Berlin, 1992.

[8] K-J. Bathe. *Finite Element Procedures*. Prentice-Hall, Englewood Cliffs, New-Jersey, 1996.

[9] J.M. Beazley. An approach to controlled parturition. *Am. J. Obstet. Gynecol.*, 133(7):723–732, April 1979.

[10] F. Bell. *Biomechanics of human parturition: A fundamental approach to the mechanics of the first stage of labour.* PhD thesis, University of Strathclyde - Glasgow, March 1972.

[11] F.L. Bookstein. Principal warps: Thin-plate splines and the decomposition of deformations. *IEEE Transactions on Pattern Analysis and Machine Intelligence*, 11(6):567–585, 1989.

[12] F.L. Bookstein. *Morphometric Tools for Landmark Data, Geometry and Biology.* Cambridge University Press, New-York, 1991.

[13] J.D. Bronzino, editor. *The Biomedical Engineering Handbook.* CRC Press, Florida - USA, 1995.

[14] D.L. Bylski, T.J. Kriewall, N. Akkas, and J.W. Melvin. Mechanical behavior of fetal dura mater under large deformation biaxial tension. *J. Biomechanics*, 19(1):19–26, 1986.

[15] J. Carr. *Surface Reconstruction in 3D Medical Imaging.* PhD thesis, University of Canterbury - New Zealand, February 1996.

[16] M.J. Castro-Diaz. Mesh refinement over triangulated surfaces. Technical Report No 2462, INRIA, October 1994.

[17] G.V.P. Chamberlain. *Obstetrics by Ten Teachers.* Arnold, Bath - UK, 1995.

[18] A.C.F. Colchester, J. Zhao, K.S. Holton-Tainter, C.J. Henri, N. Maitland, P.T.E. Roberts, C.G. Harris, and R.J. Evans. Development and preliminary evaluation of VISLAN, a surgical planning and guidance system using intra-operative video imaging. *Medical Image Analysis*, 1(1):73–90, 1996.

[19] R.D. Cook. *Finite Element Modeling for Stress Analysis.* John Wiley, USA, 1995.

[20] R. Courant. Variational methods for the solution of problems of equilibrium and vibrations. *Bulletin of the American Mathematical Society*, 49:1–23, 1943.

[21] S.H. Crandall, N.C. Dahl, and T.J. Lardner. *An Introduction to the Mechanics of Solids.* McGraw-Hill, Singapore, 1978.

[22] A. Csapo. The diagnostic significance of the intra-uterine pressure. I. *Obstet. Gynecol. Surv.*, 25(5):403–435, 1970.

[23] C.R. Dance, R.J. Lapeer, and R.W. Prager. 3D model of a female pelvis reconstructed from CT images. In *Proceedings of the Visible Human Project Conference*, 1996.

[24] P. Defoort. Instrumental delivery: the obstetric perspective. In P. Govaert, editor, *Cranial Haemorrhage in the Term Newborn Infant*, chapter 7. Mac Keith Press - Cambridge University Press, London, 1993.

[25] C.L. Dym. *Introduction to the Theory of Shells.* Hemisphere Publishing Corporation, USA, 1990.

[26] M.A. England. *Life Before Birth.* Mosby-Wolfe, London, second edition, 1996.

[27] G. Farin. *Curves and Surfaces for Computer-Aided Geometric Design - A Practical Guide.* Academic Press, London, fourth edition, 1990.

[28] P.A. Firby and C.F. Gardiner. *Surface Topology.* Ellis Horwood Ltd., New York, second edition, 1991.

[29] J.D. Foley, A. Van Dam, S.K. Feiner, and J.F. Hughes. *Computer Graphics, Principles and Practice.* Addison-Wesley, Reading-Massachusetts, second edition, 1997.

[30] E.A. Friedman. The graphic analysis of labor. *Am. J. Obstet. Gynecol.*, 68(6):1568–1575, 1954.

[31] Y.C. Fung. Stress-strain history relations of soft tissues in simple elongation. In Y.C. Fung, N. Perrone, and M. Anliker, editors, *Biomechanics, Its foundations and objectives*, pages 181–208. Prenctice-Hall, Englewood-Cliffs, NJ, 1972.

[32] Y.C. Fung. *Biomechanics: Mechanical Properties of Living Tissues.* Springer, New York, second edition, 1993.

[33] H. Furuya, T. Hashimoto, K. Kokuho, H. Kino, and K. Fukamauchi. Pressures on the human fetus during labor - intrauterine and on the fetal head. *Acta Obstet. Gynecol. Jap.*, 33(12):2173–2181, 1981.

[34] B. Geiger. *Three-dimensional modeling of human organs and its application to diagnosis and surgical planning.* PhD thesis, Ecole des Mines de Paris, April 1993.

[35] G.W. Gough, N.J. Randall, E.S. Genevier, I.A. Sutherland, and P.J. Steer. Head-to-cervix forces and their relationship to the outcome of labor. *Obstetrics & Gynecology*, 75(4):613–618, April 1990.

[36] P. Govaert. *Cranial Haemorrhage in the Term Newborn Infant.* Mac Keith Press - Cambridge University Press, London, 1993.

[37] J.G. Hall, U.G. Froster-Iskenius, and J.E. Allanson. *Handbook of Normal Physical Measurements.* Oxford University Press, Oxford, 1989.

[38] B. Haskell, M. Day, and J. Tetz. Computer-aided modeling in the assessment of the biomechanical determinants of diverse skeletal patterns. *Am. J. Orthod.*, 89(5):363–382, 1986.

[39] C.H. Hendricks, W.E. Brenner, and G. Kraus. Normal cervical dilatation pattern in late pregnancy and labor. *Am. J. Obstet. Gynecol.*, 106(7):1065–1082, 1970.

[40] Hibbitt, Karlsson and Sorensen Inc., Warrington, Cheshire UK. *ABAQUS Version 5.7 - Manuals*, 1997.

[41] E. Hinton, editor. *NAFEMS Introduction to Nonlinear Finite Element Analysis.* National Agency for Finite Element Methods and Standards, Glasgow, Schotland, 1991.

[42] J.D. Knoke, L.L. Tsao, M.R. Neumann, and J.F. Roux. The accuracy of intra-uterine pressure during labor: A statistical analysis. *Computers and Biomedical Research*, 9(2):177–186, 1976.

[43] K.E. Krantz. Chapter 2: Anatomy of the female reproductive system. In R.C. Benson, editor, *current Obstetric & Gynecologic Diagnosis & Treatment.* Lange Medical Publications, Los Altos, California, 1982.

[44] A.J. Krapohl, G.G. Myers, and R. Caldeyro-Barcia. Uterine contractions in spontaneous labor. A quantitative study. *Am. J. Obstet. Gynecol.*, 106(3):378–387, 1970.

[45] H. Krayenbühl and M.G. Yasargil. Radiological anatomy and topography of the cerebral veins. In P.J. Vinken and G.W. Bruyn, editors, *Handbook of Clinical Neurology*, volume 11, chapter 5, pages 102–117. Elsevier, Amsterdam, 1972.

[46] T.J. Kriewall, G.K. McPherson, and A.Ch. Tsai. Bending properties and ash content of fetal cranial bone. *J. Biomechanics*, 14(2):73–79, 1981.

[47] T.J. Kriewall, J.S. Stanley, and G.K. McPherson. Neonatal head shape after delivery: An index of molding. *J. Perinat. Med.*, 5(6):260–267, 1977.

[48] R.J. Lapeer and R.W. Prager. 3D shape recovery of a newborn skull using thin-plate splines. *Computerized Medical Imaging and Graphics*. In Press.

[49] R.J. Lapeer and R.W. Prager. Finite element model of a fetal skull subjected to labour forces. In A. Colchester and C. Taylor, editors, *MICCAI'99*, September 1999.

[50] R.J.A. Lapeer and R.W. Prager. 3D warping of homologous objects using thin-plate splines. Technical Report CUED/F-INFENG/TR292, Cambridge University Engineering Department, May 1997.

[51] J.K.T. Lee, S.S. Sagel, R.J. Stanley, and J.P. Heiken, editors. *Computed Body Tomography with MRI correlation*. Lippincott-Raven, Philadelphia, third edition, 1998.

[52] C.L. Lindgren and C.N. Smyth. Measurement and interpretation of the pressures upon the cervix during normal and abnormal labour. *J. Obstet. Gynaecol. Br. Cwlth*, 68(6):901–915, 1961.

[53] L. Lindgren. The effect of rupture of the membranes upon the mechanisms of labour. *Acta Obstet. Gynecol. Scand.*, 38:211–226, 1959.

[54] L. Lindgren. The causes of foetal head moulding in labour. *Acta Obstet. Gynecol. Scand.*, 39:46–62, 1960.

[55] L. Lindgren. The concept of pressure in biology and pressure transducers. *Acta Obstet. Gynecol. Scand.*, Suppl 66:87–123, 1977.

[56] L. Lindgren. The influence of pressure upon the fetal head during labour. *Acta Obstet. Gynecol. Scand.*, 56(4):303–309, 1977.

[57] L. Lindgren and D. Holmlund. Friction between the fetal head and uterine wall during normal labor and lower uterine spasm. *Am. J. Obstet. Gynecol.*, 103(7):939–941, 1969.

[58] L. Lindgren and H. Siener. Cervical tension during labour. *Am. J. Obstet. Gynecol.*, 95(3):414–420, 1966.

[59] A.D. Linney, S.R. Grindrod, S.R. Arridge, and J.P. Moss. Three-dimensional visualization of computerized tomography and laser scan data

for the simulation of maxillo-facial surgery. *Med. Inform.*, 14(2):109–121, 1989.

[60] A.D. Linney, A.C. Tan, R. Richards, A.M. Coombes, J. Gardener, and W.R. Lees. The acquisition, visualisation and applications of three dimensional data on the human body. Department of Medical Physics, University College London.

[61] Y. Liu, M. Scudder, and M.L. Gimovsky. CAD modeling of the birth process. Part II. In H. Sieburg, S. Weghorst, and K. Morgan, editors, *Health Care in the Information Age*, pages 652–666. IOS Press and Ohmsha, 1996.

[62] S.H. Lo. A new mesh generation scheme for arbitrary planar domains. *Int. J. Numer. Methods. Eng.*, 21(8):1403–1426, 1985.

[63] S. Lobregt and M.A. Viergever. A discrete dynamic contour model. *IEEE Transactions on Medical Imaging*, 14(1):12–24, 1995.

[64] W.E. Lorensen and H.E. Cline. Marching cubes: A high resolution 3D surface construction algorithm. *Computer Graphics*, 21(4):163–169, 1987.

[65] B. Ludwig, M. Brand, and P. Brockerhoff. Postpartum CT examination of the heads of full term infants. *Neuroradiology*, 20(3):145–154, 1980.

[66] A.I. Lurie. *nonlinear theory of elasticity*, volume 36 of *North-Holland Series in Applied Mathematics and Mechanics*. Elsevier, 1990.

[67] J.H. McElhaney. Dynamic characteristics of the tissues of the head. In *Perspectives in Biomedical Engineering*, pages 215–222. MacMillan Press, Ltd, London, 1973.

[68] J.H. McElhaney, J.L. Fogle, J.W. Melvin, R.R. Haynes, V.L. Roberts, and N.M. Alem. Mechanical properties of cranial bone. *J. Biomechanics*, 3(5):495–511, 1970.

[69] R.M.H. McMinn. *Color Atlas of Human Anatomy*. Mosby Year Book, Hong-Kong, third edition, 1993.

[70] G.K. McPherson. *Mechanical properties of fetal cranial bone and their influence on head molding in parturition*. PhD thesis, The University of Michigan, 1978.

[71] G.K. McPherson and T.J. Kriewall. The elastic modulus of fetal cranial bone: A first step towards an understanding of the biomechanics of fetal head molding. *J. Biomechanics*, 13(1):9–16, 1980.

[72] G.K. McPherson and T.J. Kriewall. Fetal head molding : An investigation utilizing a finite element model of the fetal parietal bone. *J. Biomechanics*, 13(1):17–26, 1980.

[73] J.W. Melvin, J.H. McElhaney, and V.L. Roberts. Development of a mechanical model of the human head - determination of tissue properties and synthetic substitute materials. In *Proceedings of the Fourteenth STAPP Car Crash Conference*, pages 221–240, New-York, 1970. Society of Automotive Engineers.

[74] A.S. Moolgaoker. A comparison of different methods of instrumental delivery based on electronic measurements of compression and traction. *Obstetrics & Gynecology*, 54(3):299–309, 1979.

[75] M.E. Mortenson. *Geometric Modeling*. John Wiley, Toronto, 1985.

[76] NAFEMS. *A Finite Element Primer*. National Agency for Finite Element Methods and Standards, Glasgow, Schotland, 1987.

[77] T. Nagashima, N. Tamaki, S. Matsumoto, B. Horwitz, and Y. Seguchi. Biomechanics of hydrocephalus: A new theoretical model. *Neurosurgery*, 21(6):898–904, 1987.

[78] A. Nahum, R. Smith, and C.C. Ward. Intracranial pressure dynamics during head impact. In *Proceedings of the Twenty First STAPP Car Crash Conference*, pages 339–366. Society of Automotive Engineers, 1977.

[79] T.R. Nelson, D.B. Downey, D.H. Pretorius, and A. Fenster. *Three-Dimensional Ultrasound*. Lippincott Williams & Wilkins, Philadelphia, 1999.

[80] J.K. Ousterhout. *Tcl and the Tk Toolkit*. Addison-Wesley, Reading-Massachusetts, 1994.

[81] A. Peña. *Theoretical Study of Brain Biomechanics via Poroelastic Theory and the Finite Element Method*. PhD thesis, Cambridge University, September 1996.

[82] J. Peraire, M. Vahdati, K. Morgan, and O.C. Zienkiewicz. Adaptive remeshing for compressible flow computations. *Journal of Computational Physics*, 72(2):449–466, 1987.

[83] M.L. Pernoll. Chapter 43: Maternal & perinatal statistics. In R.C. Benson, editor, *current Obstetric & Gynecologic Diagnosis & Treatment*. Lange Medical Publications, Los Altos, California, 1982.

[84] Mark Phillips. *Geomview Manual - Version 1.6.1*. The Geometry Center, 1996.

[85] A. Rempen and M. Kraus. Measurement of head compression during labor: Preliminary results. *J. Perinat. Med.*, 19(2):115–120, 1991.

[86] A. Rempen and M. Kraus. Pressures on the fetal head during normal labor. *J. Perinat. Med.*, 19(3):199–206, 1991.

[87] R.S. Rhodes and L.B. Cook. *Orthographic Projection in Basic Engineering Drawing*. Longman Scientific and Technical, Harlow, UK, 1990.

[88] M.L. Riolo, R.E. Moyers, J.S. McNamara, and W.S. Hunter. *An atlas of craniofacial growth*. Ann Arbor: Center for Human Growth and Development, University of Michigan, 1974.

[89] R.N. Rohling. *3D Freehand Ultrasound: Reconstruction and Spatial Compounding*. PhD thesis, Cambridge University, September 1998.

[90] K.P. Russell. Chapter 31: The course & conduct of normal labor & delivery. In R.C. Benson, editor, *current Obstetric & Gynecologic Diagnosis & Treatment*. Lange Medical Publications, Los Altos, California, 1982.

[91] H. Schulman and S.L. Romney. Variability of uterine contractions in normal human parturition. *Obstetrics & Gynecology*, 36(2):215–221, 1970.

[92] R.D. Shaw and R.G. Pitchen. Modification to the Suhara-Fukuda method of network generation. *Int. J. Numer. Methods Eng.*, 12(1):93–99, 1978.

[93] K.K. Shung, M.B. Smith, and B. Tsui. *Principles of Medical Imaging*. Academic Press, Inc., San Diego, California, 1992.

[94] B. Sorbe and S. Dahlgren. Some important factors in the molding of the fetal head during vaginal delivery - a photographic study. *Int. J. Gynaecol. Obstet.*, 21(3):205–212, 1983.

[95] D.D. Stark and W.G. Bradley, editors. *Magnetic Resonance Imaging*, volume I. Mosby, St.Louis, Missouri, 1999.

[96] C. Sumi, A. Suzuki, and K. Nakayama. Estimation of shear modulus distribution in soft tissue from strain distribution. *IEEE Transactions on Biomedical Engineering*, 42(2):193–202, 1995.

[97] L. Svenningsen, R. Lindemann, and K. Eidal. Measurements of fetal head compression pressure during bearing down and their relationship to the condition of the newborn. *Acta Obstet. Gynecol. Scand.*, 67(2):129–133, 1988.

[98] R. Swan, editor. *The Human Body on File*. Library Association, London, 1983.

[99] E.M. Symonds. *Essential Obstetrics and Gynaecology*. Churchill Livingstone, London, second edition, 1992.

[100] S.P. Timoshenko and S.W. Woinowsky-Krieger. *Theory of Plates and Shells*. McGraw-Hill, Singapore, second edition, 1959.

[101] A.C. Turnbull. Uterine contractions in normal and abnormal labour. *Am. J. Obstet. Gynecol.*, 64(3):321–333, 1957.

[102] M.J. Turner, R.W. Clough, H.C. Martin, and L.J. Topp. Stiffness and deflection analysis of complex structures. *J. Aero. Sc.*, 23(9):805–823, 1956.

[103] F. van der Heyden. *Image Based Measurement Systems, Object recognition and parameter estimation*. John Wiley, West Sussex - UK, 1994.

[104] J. Walton, J.A. Barondess, and S. Lock, editors. *The Oxford Medical Companion*. Oxford University Press, Oxford, 1994.

[105] C.C. Ward and G.K. Nagendra. Mathematical models: Animal and human models. In A.M. Nahum and J. Melvin, editors, *The Biomechanics of Trauma*, chapter 5. Appleton-Century-Crofts, Norwalk - Connecticut, 1986.

[106] B. Welch. *Practical Programming in Tcl and Tk*. Prentice Hall, New-Jersey, second edition, 1997.

[107] A. Wischnik, E. Nalepa, K.J. Lehmann, K.U. Wentz, M. Georgi, and F. Melchert. Zur prävention des menschlichen geburtstraumas I. mitteilung: Die computergestützte simulation des geburtsvorganges mit hilfe der kernspintomographie und der finiten-element-analyse. *Geburtshilfe und Frauenheilkunde*, 53(1):35–41, 1993.

[108] S.L.-Y. Woo, M.A. Gomez, and W.H. Akeson. Mechanical behaviors of soft tissue. In A.M. Nahum and J. Melvin, editors, *The Biomechanics of Trauma*, chapter 7. Appleton-Century-Crofts, Norwalk - Connecticut, 1986.

[109] J.L. Wood. Dynamic response of human cranial bone. *J. Biomechanics*, 4(1):1–12, 1971.

[110] W.C. Young. *Roark's Formulas for Stress and Strain.* McGraw-Hill, Singapore, sixth edition, 1989.